Hadronic resonance production with ALICE at LHC energies

A

THESIS

SUBMITTED TO THE
UNIVERSITY OF JAMMU
FOR THE AWARD OF DEGREE OF

DOCTOR OF PHILOSOPHY

IN
PHYSICS

BY

VIKASH SUMBERIA

Department of Physics
University of Jammu, Jammu
Jammu and Kashmir – 180006

January, 2025

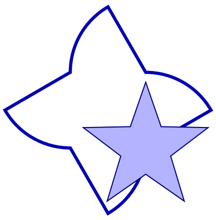

This thesis is dedicated to my parents,
for their endless love, support and encouragement...

DEPARTMENT OF PHYSICS
UNIVERSITY OF JAMMU
Jammu-180006

CERTIFICATE

It is certified that **Mr. Vikash Sumberia**, worked under my supervision and the work is worthy of consideration for the award of Ph.D. degree in Physics. It is further certified that:

i. the thesis embodies the work of the candidate himself. It is original and not copied from any other source.

ii. the candidate worked under my supervision for the prescribed period required under statues.

iii. the candidate has put in the required attendence in the Department of Physics, University of Jammu, Jammu during the period of research.

iv. the candidate has fulfilled all the requirements of the UGC-MSP-2016 regulations.

v. the candidate has fulfilled the statutory conditions as laid down in Section 18 of the statues governing the degree of Doctor of Philosophy.

17/01/2025

(Prof. Arun Bharti)
Head
Department of Physics
University of Jammu
Jammu

Head
Department of Physics
University of Jammu
Jammu-180006

17/01/2025

(Prof. Sanjeev Singh Sambyal)
Research Supervisor
Department of Physics
University of Jammu
Jammu

PLAGIARISM CERTIFICATE

I, **Vikash Sumberia**, S/O Sh. Girdhari Lal, hereby declare that the work reported in this thesis entitled **"Hadronic resonance production with ALICE at LHC energies"** has been done entirely by me under the supervision of Prof. Sanjeev Singh Sambyal, Department of Physics, University of Jammu, Jammu. The work undertaken by me in this thesis is original and has not been copied from any other sources without due acknowledgment. I also ascertain that no part of this thesis is presented elsewhere for the award of any degree or diploma of any University or Institution. Moreover, this thesis is having 8% degree of plagiarism as per the **Drillbit plagiarism detection software** analysis report.

Vikash Sumberia

(Vikash Sumberia)

Dated: 17/01/2025

17/01/2025

(Prof. Arun Bharti)

Head

Department of Physics

University of Jammu

Jammu

Head

Department of Physics

University of Jammu

Jammu-180006

17/01/2025

(Prof. Sanjeev Singh Sambyal)

Research Supervisor

Department of Physics

University of Jammu

Jammu

DrillBit

The Report is Generated by DrillBit Plagiarism Detection Software

No: DLJ/25/3309
Dt. 9-1-25

Submission Information

Author Name	Vikash Sumberia
Title	Ph.D
Paper/Submission ID	2968368
Submitted by	sahi_vikram@yahoo.com
Submission Date	2025-01-09 13:57:38
Total Pages, Total Words	149, 37668
Document type	Thesis

Result Information

Similarity **8 %**

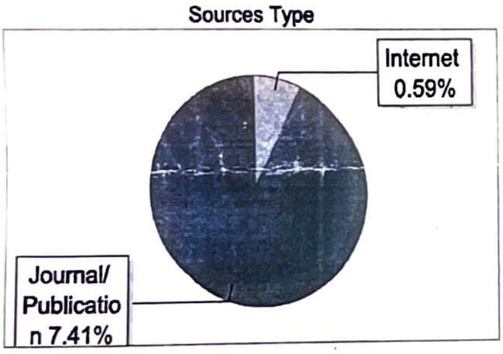

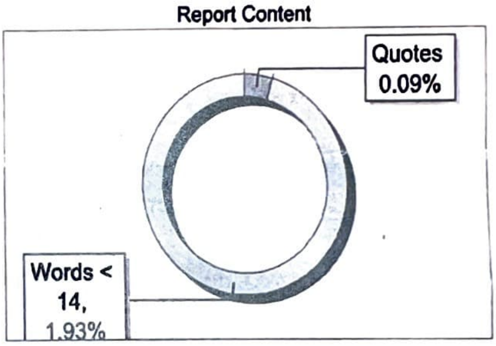

Exclude Information

Quotes	Excluded
References/Bibliography	Excluded
Source: Excluded < 14 Words	Excluded
Excluded Source	**0 %**
Excluded Phrases	Not Excluded

Database Selection

Language	English
Student Papers	Yes
Journals & publishers	Yes
Internet or Web	Yes
Institution Repository	Yes

A Unique QR Code use to View/Download/Share Pdf File

I/c LIBRARIAN
DHANVANTRI LIBRARY
UNIVERSITY OF JAMMU

Head
Department of Physics
University of Jammu
Jammu-180006

DECLARATION

I, **Vikash Sumberia**, S/O Sh. Girdhari Lal, hereby declare that the work reported in this thesis entitled **"Hadronic resonance production with ALICE at LHC energies"** has been done entirely by me under the supervision of Prof. Sanjeev Singh Sambyal, Department of Physics, University of Jammu, Jammu. The work undertaken by me in this thesis is original and has not been copied from any other sources without due acknowledgment. It has not been submitted fully or partially elsewhere for the award of any degree, diploma, fellowship or other similar titles of recognition to the best of my knowledge to anybody else in any other University or Institution.

Dated: 17/01/2025

Vikash Sumberia

(Vikash Sumberia)

17/01/2025

(Prof. Arun Bharti)

Head

Department of Physics

University of Jammu

Jammu

Head
Department of Physics
University of Jammu
Jammu-180006

17/01/2025

(Prof. Sanjeev Singh Sambyal)

Research Supervisor

Department of Physics

University of Jammu

Jammu

ACKNOWLEDGMENT

With profound reverence, I bow to Almighty *Lord Krishna*, whose blessings and grace provided me the strength, wisdom, and opportunity to embark on and complete this thesis. His divine guidance illuminated my path during challenging times and inspired me to persevere. I express my deepest gratitude to my supervisor, *Prof. Sanjeev Singh Sambyal*, whose mentorship and kindness have left an indelible mark on my academic and personal journey. Beyond being an exemplary guide, he is a compassionate and gentle human being whose personality and generosity have inspired me immensely. I sincerely thank the Almighty for blessing me with him as my research supervisor.

I would like to express my deepest respect and gratitude to *Prof. Anju Bhasin*, the Principal Investigator of the project "Indian Participation in the ALICE Experiment at CERN," under which I worked as a Project Associate. Despite her busy schedule with administrative work in the University, she always took the time to help me, not just with academic matters, but also by offering emotional support and financial assistance through project funding. Her guidance and encouragement allowed me to focus on my research and have been a key part of my academic journey. I also thank *Er. Anik Gupta* for his invaluable assistance in managing the lab's computing resources and for his helpful advice during this journey. My heartfelt thanks to *Prof. Ramni Gupta* for her support and care, *Dr. Rajendra Nath Patra* for insightful discussions and *Dr. Saroj Kanta Nayak*, *Er. Sanjay Mahajan*, and *Dr. Renu Bala* for their valuable guidance.

I sincerely thank *Prof. Arun Bharti*, Head of the Department, for his constant guidance and unwavering support throughout my Ph.D. His wonderful sense of humor and our shared connection to the same region made our conversations truly special. I will always cherish the moments we shared and his encouragement throughout this journey. I would also like to extend heartfelt thanks to my teachers in the department, *Prof. Naresh Padha*, *Prof. RajniKant*, *Prof. Vivek Gupta*, *Prof. K. K. Bamzai*, *Prof. Rani Devi*, and *Dr. Sandeep Arya*, for their invaluable academic support and constant encouragement throughout my journey. The non-teaching staff of the department have my deepest appreciation for their unwavering support and assistance, which played an essential role in the completion of this research. I am truly grateful to each one of them for their invaluable contributions.

To my labmates, I owe a deep sense of gratitude for fostering a supportive and intellectually enriching environment that made this journey truly special. I am especially thankful to my seniors, *Dr. Randhir Singh* and *Dr. Meenakshi Sharma*, for their insightful discussions on physics and their invaluable guidance. My heartfelt gratitude goes to *Mahima Sharma*, whose unwavering support provided strength and comfort during the highs and lows of this journey. Your presence added so much joy and I will always treasure our countless chess games over coffee - despite losing most of them! Thank you for always standing by me and for all the beautiful moments we shared along the way. I am equally grateful to *Nasir Mehdi Malik* for his thoughtful ideas on my research topic and for our engaging discussions over coffee. A special thanks to *Binti Sharma*, *Sheetal Sharma*, *Zarina Banoo*, *Pratibha Bhagat*, *Upasana Sharma*, *Mokshi Vaid*, *Salman K. Malik*, *Ashish Jalotra*, *Fakhar-Ul-Haider*, *Balwan Singh*, and *Touseef Ahangar* for creating a collaborative and friendly atmosphere in the lab. Your support and companionship made this journey even more enjoyable and meaningful. My heartfelt thanks also go to my dear friend Sahil for making this journey comfortable and joyful.

I am profoundly grateful to my conveners in the PWG-LF, including *Dr. Livio Bianchi*, *Dr. Alberto Calvia*, *Dr. Ramona Lea*, *Dr. Saurav Kundu*, and *Dr. Nicolo Jacazio*, as well as the PAG-Resonances conveners, including *Dr. Jihye Song*, *Dr. Enrico Fragiocomo*, *Dr. Bong-Hwi Lim*, and *Dr. Adrian Fereydon Nassirpour*, for their timely guidance throughout my research. A special mention goes to *Dr. Tapan K. Nayak* for the enriching discussions during my visit to CERN. I also express my heartfelt gratitude to *Dr. Klaus Werner* for his invaluable help with the technical details of the EPOS4 model.

I would also like to express my sincere gratitude to the people at NISER Bhubaneswar, including *Prof. Bedanga Das Mohanty*, *Dr. Ranbir Singh*, *Dr. Varchaswi Kashyap*, and *Dr. Dukhishyam Malik*, for their invaluable support and for making my visits to NISER a significant and enriching part of this research journey. I would like to acknowledge the *Department of Science and Technology, Govt. of India*, for providing me the necessary funds to carry out this research. Furthermore, I extend my thanks to the *CERN Grid Computing Center* for providing the computational facilities that were required to complete this work.

To my family, I owe everything I am today. My grandparents, *Smt. Sheelo Devi* and *Sh. Banarsi Dass*, whose blessings and hard work shaped the lives of us all; my parents, *Smt. Kamlesh Kumari* and *Sh. Girdhari Lal*, for their unwavering support and unconditional love; my aunts and uncles, *Smt. Sheetel Devi*, *Sh. Parveen Kumar*, *Smt. Shallu Chalotra*, and *Sh. Jeet Raj*, for their continuous encouragement and belief in my academic pursuits; my brother, *Sahil Sumberia*, for being my rock during this journey; my sister-in-law, *Anu Raina*, for bringing joy to our family; and the little ones, *Komal*, *Pragya*, *Anaya*, and *Aditi*, for their love and cheerfulness.

To my dear friends — *Mukhtar*, *Balwinder*, *Manav*, *Kanu*, *Khalil*, *Manmeet*, *Mulveer*, *Ishan*, *Sandeep*, *Naveen*, *Arun*, *Raman*, *Dinesh*, *Suhail*, *Mukesh*, *Anirudh*, *Yogeshwar*, *Aman*, *Amir*, and *Hritik* — your unwavering support and companionship have been invaluable.

Finally, I express my heartfelt apologies to anyone whose name I may have missed inadvertently. Your contributions have been equally valuable, and I am sincerely grateful for your support.

(Vikash Sumberia)

ABSTRACT

Quantum Chromodynamics (QCD), a subfield of Quantum Field Theory (QFT), is a fundamental theory in physics that describes the strong interaction between quarks and gluons. In QCD, quarks are the elementary particles that constitute neutrons, protons, and other hadrons, whereas gluons are the force carriers that mediate the strong nuclear force to hold the quarks together. The strong force is one of the four fundamental forces in nature, along with the electromagnetic, weak, and gravitational forces. The theory of QCD was developed in the 1970s, and it is now an essential part of Standard Model (SM) of particle physics, which describes the interactions between all known particles and the fundamental forces. One of the key features of QCD is its mathematical formulation in terms of a non-Abelian gauge theory based on a group of symmetries that describe the transformations that the quarks and gluons undergo when they interact. The non-Abelian nature of the theory makes the gluons interact with each other, resulting in the phenomenon of color confinement. Color, in the context of particle physics, refers to a property of quarks that is analogous to the electric charge in electromagnetism. However, it is important to note that this term has nothing to do with the colors that we see with our naked eyes. While photons, which mediate the electromagnetic force, do not carry any electric charge, gluons, which mediate the strong force, carry a color charge. This distinction is a key difference between the two forces and is crucial in developing a complete understanding of the behavior of subatomic particles. Quarks have six known flavors (up (u), down (d), charm (c), strange (s), top (t), and bottom (b)) and exist in three types of color charges, which are labeled red, green, and blue, whereas antiquarks have opposite color charges, which are labeled anti-red, anti-green, and anti-blue. Due to color confinement in QCD, hadrons are color-

less because they are composed of quarks and antiquarks whose color charges cancel each other out. Another important prediction of QCD is the phenomenon of asymptotic freedom, which means that at very high energies or short distances, the strong force between quarks and gluons becomes weaker, which allows for a perturbative description of the interactions.

At very high energies and temperatures, the quarks and gluons are no longer confined to individual hadrons, but instead form a deconfined state of quarks and gluons known as the quark-gluon plasma which is a hot, dense, and strongly interacting thermal medium, often described through the framework of relativistic hydrodynamics. Such a state of matter is believed to have existed for a few microseconds after the Big Bang around 13.8 billion years ago, and can be recreated in laboratory by carrying out ultra-relativistic heavy-ion collisions with the help of collider facilities such as Relativistic Heavy Ion Collider (RHIC) at Brookhaven National Laboratory (BNL) and Large Hadron Collider (LHC) at European Council for Nuclear Research (CERN). This new state, formed in these collisions, exists for a very short period of time and cannot be directly observed by detectors. However, there are several signatures that confirm the formation of quark-gluon plasma (QGP) in high-energy heavy-ion collisions. These include: Jet suppression, elliptic flow, enhanced production of strange particles, direct photon production, chiral symmetry restoration, quarkonia suppression, etc. Overall, the combination of these signatures provides strong evidence for the formation of the QGP in high-energy heavy-ion collisions. The enhancement in the production of strange quarks in heavy-ion collisions compared to nucleon-nucleon collisions is a key observable in heavy-ion physics and is considered one of the earliest signatures of QGP. In heavy-ion collisions, the gluon density saturates due to the formation of a thermalized QGP medium, leading to an enhancement in the yield of strange hadrons compared to pp collisions, where strange hadron production is suppressed due to canonical suppression. The study of strange to non-strange hadron ratios in both small and large system collisions provides valuable insights into the hot and thermalized medium formed in these collisions.

As the system expands and cools, it undergoes a phase transition from the QGP to the hadronic phase, where quarks and gluons recombine to form hadrons. After the phase transition, inelastic collisions among hadrons take place until they cease at chemical freeze-out, where the yields of various hadrons are fixed. Beyond this point, hadrons continue to interact elastically, altering their momenta while their yields remain unchanged. These elastic interactions exist until kinetic freeze-out, where the system cools enough that hadrons no longer interact, and both their momenta and yields get fixed. The timespan between the chemical and kinetic freeze-outs is called as hadronic phase. Hadronic resonances such as $\rho(770)^0$, $\mathrm{K}^*(892)^0$, $\Sigma(1385)^\pm$, $\Lambda(1520)$, $\Xi(1530)^0$ and $\phi(1020)$ (which may be denoted by ρ^0, K^{*0}, $\Sigma^{*\pm}$, Λ^*, Ξ^{*0}, and ϕ for simplicity) are produced before chemical freeze-out and play a key role in probing the dynamics of the hadronic phase, as their yields and properties can be modified through hadronic interactions of their decay daughters within the hadronic gas. The decay daughters of hadronic resonances can undergo rescattering or regeneration during the hadronic phase, which can either suppress or enhance the observed yields compared to those produced at chemical freeze-out. The modification in the yields of hadronic resonances depends on their lifetimes, interaction cross section of their decay daughters, and duration of the hadronic phase. The shorter the lifetime of hadronic resonance, the more interactions its decay daughters undergo within the hadronic gas, leading to a greater modification of their yields compared to those produced at chemical freeze-out. Experimental observations show that the yields of short-lived resonances, such as ρ^0 and K^{*0}, are suppressed in both small and large system collisions compared to stable hadrons with the same strangeness content. In contrast, resonances with relatively longer lifetimes, such as Λ^*, show suppression only in large system collisions, suggesting the existence of a brief hadronic phase in small system collisions. Resonances with even longer lifetimes, such as Ξ^{*0} and ϕ, are not suppressed, even in large system collisions, indicating an upper limit to the duration of the hadronic phase formed in such collisions. Thus, the lifetimes of hadronic resonances are exploited to estimate the duration of the hadronic phase in both small and large collision systems. The resonance Λ^* is particularly interesting for studying the properties of the hadronic phase in small systems, as its lifetime falls between those of the K^{*0} and ϕ resonances. Moreover, no measurements of Λ^* have yet been made in collisions p–Pb at $\sqrt{s_{\mathrm{NN}}} = 8.16$ TeV, the highest energy available in this collision system with A Large Ion Collider Experiment (ALICE) at LHC. Given that the p–Pb system serves as an intermediate between the pp and Pb–Pb systems in terms of both system size and particle production, it helps disentangle initial and final state effects in large collision systems. Furthermore, for meaningful comparisons, measurements of Λ^* production are also not performed in pp collisions at $\sqrt{s} = 8$ TeV, the closest available energy to the p–Pb collisions at $\sqrt{s_{\mathrm{NN}}} = 8.16$ TeV.

In this work, the production yield of the Λ^* resonance is analyzed in p–Pb collisions at $\sqrt{s_{\mathrm{NN}}}$ = 8.16 TeV across four V0A multiplicity classes (excluding minimum bias non-single diffractive (NSD) events) and in inelastic pp collisions at $\sqrt{s}$ = 8 TeV, using data from ALICE. The invariant yield of Λ^* is calculated and the yields are compared to the results published at lower energies. The p_{T}-integrated yield and average p_{T} are obtained by fitting the p_{T} spectra with the Levy-Tsallis function, which behaves exponentially in the low-p_{T} region while following a power law in the high-p_{T} region. The nuclear modification factor (R_{pPb}) for Λ^* is calculated in p–Pb collisions at $\sqrt{s_{\mathrm{NN}}}$ = 8.16 TeV and compared to R_{pPb} of other hadrons at the same energy. The yield ratios of the resonances to the stable hadrons (Λ^*/Λ and $\mathrm{K}^{*0}/\mathrm{K}^0_{\mathrm{S}}$) are calculated and also compared with the other available results. To interpret the results, comparisons are made with the EPOS3 hydrodynamical model, where around 3 million events are simulated with and without the hadronic afterburner (UrQMD).

To further advance our understanding of the properties of the QGP medium and the hadronic phase in heavy-ion collisions, we exploited the EPOS4 hydrodynamical model. EPOS4 is an updated version of EPOS3, featuring improvements in both primary (parton-level) and secondary (hadronic-level) scatterings. At the primary scattering level, EPOS4 introduces a saturation scale that ensures proper factorization and binary scaling, correcting violations seen in EPOS3. At the secondary scattering level, the model enhances the core-corona procedure by dividing string segments based on energy loss and incorporating improved methods for managing energy-momentum flow during freeze-out. Using EPOS4, the particle yields and yield ratios are calculated for the pp system at $\sqrt{s} = 13.6$ TeV and the PbPb system at $\sqrt{s_{\mathrm{NN}}} = 5.36$ TeV in the mid-rapidity region ($|y| < 0.5$), with and without the hadronic afterburner (UrQMD). For the pp system, 5 million events are generated for each UrQMD setting, while for the PbPb system, 1.5 million events are generated for each setting. These energies align with current LHC collision energies, providing a basis for future comparisons with experimental data.

The entire thesis, compiled into six chapters, is organized as follows:

Chapter 1: This chapter introduces high-energy physics, or particle physics, a field dedicated to understanding the fundamental building blocks of matter and the forces that govern their interactions. It traces key breakthroughs in particle physics, from the discovery of protons, neutrons, and electrons to quarks at the most fundamental level and the discovery of the Higgs boson at the LHC in 2012, which confirmed a crucial aspect of the Standard Model. The Standard Model remains the most successful theory describing the interactions of elementary particles via the electromagnetic, weak, and strong forces. The chapter then focuses on QCD, the theory of strong interactions, which explains how quarks and gluons interact via the "color" charge, a quantum property analogous to the electric charge in Quantum Electrodynamics (QED). Unlike QED, QCD allows for gluon self-interactions, where gluons act as massless mediators of the strong force. Quarks and gluons are always confined within color-neutral hadrons, which are categorized into mesons (quark-antiquark pairs) and baryons (three-quark systems). The discussion moves to the QCD phase transition, where matter transforms from a state of confined hadrons to a deconfined phase of quarks and gluons. This transition is characterized by temperature and energy density, similar to phase transitions in QED, such as the change from solid to liquid or gas. At extremely high temperatures or energy densities, quarks and gluons exhibit asymptotic freedom, where the interaction between them weakens, leading to the formation of QGP. The chapter then explores the formation of QGP in heavy-ion collisions at the LHC and RHIC and highlights the various signatures indicating the formation of QGP. Next, the chapter discusses the production of hadronic resonances in collisions at LHC and RHIC at various center-of-mass energies. The yields of these resonances are sensitive to the interactions of their decay daughters in the hadronic phase, the period between chemical and kinetic freeze-outs. Resonances with short lifetimes, such as ρ^0 (1.335 fm/c) and K^{*0} (4.15 fm/c), are suppressed in high-multiplicity pp, p–Pb, and central Pb–Pb or Au–Au collisions compared to peripheral collisions. In contrast, resonances with longer lifetimes, like ϕ (46.26 fm/c), show no significant evolution in yield with multiplicity. The Λ^{*} resonance, with a lifetime around 12.54 fm/c, lies between the resonances K^{*0} and ϕ and provides insight into the properties of the hadronic phase. In Pb–Pb and Au–Au collisions, the yield of Λ^{*} is suppressed in the most central collisions compared to peripheral collisions, but no multiplicity dependence has been observed in small systems. The chapter concludes by presenting the motivation for this analysis, which is to study the production yield of the Λ^{*} resonance in p–Pb collisions at $\sqrt{s_{\mathrm{NN}}}$ = 8.16 TeV and in pp collisions at $\sqrt{s}$ = 8 TeV using data from the ALICE detector at the LHC.

Chapter 2: This chapter focuses on relativistic kinematics, which is crucial for understanding particle collisions at high energies, a key aspect of modern particle physics. High energies are required in this field because they allow us to probe the fundamental structure of matter at increasingly smaller scales. According to the principles of quantum mechanics and the uncertainty principle, higher-energy collisions enable the study of shorter wavelengths, allowing particles to be investigated at subatomic levels. These energies also facilitate the production of new particles, such as those predicted by the Standard Model and beyond, which are often too massive to exist under ordinary conditions. Relativistic kinematics becomes necessary because particles in high-energy physics experiments, such as those conducted at LHC, often travel at velocities close to the speed of light. In these conditions, classical mechanics no longer provides accurate predictions and special relativity must be employed. The chapter begins by introducing the concept of four-vectors, mathematical objects that combine space and time components into a unified framework, allowing for the consistent description of particle behavior in different reference frames. Lorentz transformations are then introduced, which describe how physical quantities, such as position and momentum, change between observers moving at constant velocities relative to each other. The energy-momentum four-vector and its conservation during particle collisions are also covered. The conservation laws of energy and momentum in relativistic frameworks are fundamental to predicting the outcomes of high-energy particle interactions, such as the creation of new particles or the decay of existing ones. The chapter further delves into key kinematic variables used to describe collision processes, such as rapidity, pseudorapidity, and transverse momentum. These variables allow physicists to analyze particle trajectories and energies in a way that accounts for relativistic effects. For instance, rapidity is preferred over velocity at relativistic speeds because it transforms linearly under Lorentz transformations, making it a more practical quantity for comparing particle motion across different reference frames.

Chapter 3: The chapter begins with an overview of LHC at CERN, Geneva, Switzerland, and introduces its key experimental setups. The four major experiments at the LHC where the data from the collisions is recorded are ALICE, Compact Muon Solenoid (CMS), Large Hadron Colider beauty (LHCb), and A Toroidal LHC ApparatuS (ATLAS). The ALICE experiment, designed to explore the properties of QGP formed in heavy-ion collisions, is discussed in detail. The ALICE detector consists of the central barrel, the forward detectors and a muon spectrometer. For this analysis, central barrel detectors, including Inner Tracking System (ITS), Time Projection Chamber (TPC), Time-of-Flight (TOF), and VZERO (V0) detectors, play a significant role. The ITS is crucial for reconstructing primary and secondary vertices with high precision near the interaction point, whereas the TPC and TOF are essential for charged-particle tracking and particle identification, respectively. The VZERO detectors are key for triggering minimum-bias events and determining collision centrality in heavy-ion collisions. The chapter also discusses other subsystems in ALICE such as the Transition Radiation Detector (TRD), which is used for electron and jet identification, the Electromagnetic Calorimeter (EMCal) for measuring high-energy particles like photons and jets, and the Photon Spectrometer (PHOS), which is focused on detecting electromagnetic radiation from the QGP. Additionally, the chapter covers the ALICE experiment's data acquisition and computing infrastructure for both online and offline data processing and analysis.

Chapter 4: This chapter provides a comprehensive outline of the techniques used for reconstructing the Λ^{*} resonance, with methods that can be generalized to other resonances as well. The reconstruction process begins by identifying the decay products, a proton and a kaon, which are detected using the ITS, TPC, and TOF subsystems in ALICE. The chapter offers a detailed description of the steps involved, including the particle identification algorithms based on energy loss $\mathrm{d}E/\mathrm{d}x$ and time-of-flight measurements, track reconstruction using the Kalman filter, and the criteria for event selection to optimize the signal-to-background ratio. The invariant mass distribution of unlike-charged proton-kaon pairs from the same events is obtained by adding their four-momenta. This distribution contains both the signal peak of the Λ^{*} resonance and the combinatorial background, which arises from uncorrelated proton and kaon pairs. The combinatorial background is estimated using like-sign and event-mixing techniques, which are discussed in detail in the chapter. After estimating the background, it is subtracted from the unlike-charged pair distribution, leaving behind the signal of the Λ^{*} resonance along with a residual background. A fitting procedure is then applied to extract the resonance signal. This involves fitting the invariant mass distribution with a Voigtian function, which is a convolution of Breit-Wigner and Gaussian functions for the signal peak, and a second-order polynomial for the residual background. To determine the raw yield of Λ^{*}, the bin-counting method is employed, as described in detail in the chapter. The chapter also includes calculations for detector efficiency and acceptance, using the Monte Carlo simulations. These simulations are used to account for the inefficiencies in detecting all Λ^{*} resonances decaying into protons and kaons. The loss of signal due to event and track selection cuts is accounted for and thoroughly discussed. Additionally, the method for calculating systematic uncertainties is covered in detail. The chapter then presents the corrected transverse momentum (p_T) spectra of the Λ^{*} resonance, measured in inelastic pp collisions at $\sqrt{s} = 8$ TeV and in p–Pb collisions at $\sqrt{s_{\mathrm{NN}}} = 8.16$ TeV across four multiplicity classes defined by the V0A detector. These spectra are also compared to minimum-bias event classes to investigate any multiplicity dependence. Furthermore, a comparison of the p_{T} spectra obtained in p–Pb collisions at $\sqrt{s_{\mathrm{NN}}}$ = 8.16 TeV with previously published results at $\sqrt{s_{\mathrm{NN}}}$ = 5.02 TeV is presented, allowing for a study of energy-dependent effects on Λ^{*} production. The chapter also discusses the p_{T}-integrated yield and the average transverse momentum ($\langle p_{\rm T} \rangle$) of the Λ^*, which provide insight into the overall production rates and momentum distributions of the resonance in different collision systems and multiplicity classes. The nuclear modification factor ($R_{\rm pPb}$) for Λ^* is calculated to disentangle the cold nuclear matter (CNM) effects from hot QCD effects, and the results are compared to other hadrons, such as Λ, $\rm K^0_S$, and $\rm K^{*0}$, to explore production mechanisms of baryons and mesons. Finally, the resonance to non-resonance yield ratios, specifically for Λ^* and $\rm K^{*0}$, are discussed, providing insights into the hadronic interactions in the late stages of p–Pb collisions which affect short-lived resonances differently according to the lifetime of resonance particle and interaction cross-section of its decay daughters.

Chapter 5: In this chapter, we provide a comprehensive overview of the EPOS4 hydrodynamical model, a general-purpose framework designed to study various observables in relativistic collisions across different systems and energies. The core concept underlying EPOS4 is parallel scattering, which accounts for multiple parton-parton scatterings occurring simultaneously during high-energy collisions. Understanding the dynamics of heavy-ion collisions is crucial compared to smaller system collisions, due to a significant difference in the volume of the system, making the EPOS4 model an optimal choice for this analysis. This chapter explores the foundational framework of EPOS4 and highlights key differences from its predecessor, EPOS3. We utilized the EPOS4 model to investigate the dynamics of both large and small system collisions, focusing on the production yields of strange and resonance particles. The enhancement of strange hadron yields in central Pb–Pb collisions, compared to pp and peripheral Pb–Pb collisions, suggests the formation of a medium in central Pb–Pb collisions. We can distinguish the hydrodynamical evolution of the medium produced in different collision systems by measuring the average transverse momentum of hadrons formed in these events. The influence of late-stage hadronic interactions on the differential yield of resonances is analyzed using the ratio UrQMD ON / UrQMD OFF, where UrQMD ON represents the activation of late-stage hadronic interactions, while UrQMD OFF represents their absence. The chapter also discusses the integrated yield ratios of various strange hadrons to pions, both with and without UrQMD, revealing that the strangeness enhancement is an early-stage effect rather than a late-stage one. Additionally, we measure and discuss the resonance to non-resonance yield ratios for ρ^0, K^{*0}, $\Sigma^{*\pm}$, Λ^*, Ξ^{*0}, and ϕ, where the resonance yields are suppressed in central Pb–Pb collisions compared to both pp and peripheral Pb–Pb collisions, particularly for resonances with shorter lifetimes. Finally, the lifetime measurements of the hadronic phase have been performed using the ratios $\mathrm{K}^{*0}/\mathrm{K}$, ρ^0/π, and Λ^*/Λ with EPOS4 when UrQMD is ON, comparing these results with the ALICE data, all of which are discussed in detail in this chapter.

Chapter 6: This chapter provides a summary of the main findings presented in the thesis, focusing on the analysis of the Λ^* resonance in inelastic pp collisions at $\sqrt{s}$ = 8 TeV and in p–Pb collisions at $\sqrt{s_{\mathrm{NN}}}$ = 8.16 TeV across four V0A multiplicity classes and the minimum-bias class using data from the ALICE detector. The key results are discussed in comparison with other available measurements of the Λ^* resonance and other hadrons with ALICE data, as well as predictions from the EPOS3 and EPOS4 models.

Contents

Appendix

List of Figures

List of Tables

List of Acronyms

AGS	Alternating Gradient Synchrotron
ALICE	A Large Ion Collider Experiment
ATLAS	A Toroidal LHC ApparatuS
Au	Gold
BNL	Brookhaven National Laboratory
CERN	European Council for Nuclear Research
CGC	Color Glass Condensate
CMS	Compact Muon Solenoid
CNM	cold nuclear matter
DESY	Deutsches Elektronen-Synchrotron
ITS	Inner Tracking System
LHC	Large Hadron Collider
LHCb	Large Hadron Colider beauty
NSD	non-single diffractive
Pb	Lead
PHENIX	Pioneering High Energy Nuclear Interaction eXperiment
QCD	Quantum Chromodynamics
QED	Quantum Electrodynamics
QFT	Quantum Field Theory
QGP	quark-gluon plasma
RHIC	Relativistic Heavy Ion Collider
SM	Standard Model

STAR	Solenoidal Tracker at RHIC
STR	Special Theory of Relativity
TOF	Time-of-Flight
TPC	Time Projection Chamber

Chapter 1

Introduction

In the field of high-energy physics, scientists aim to investigate the universe at its smallest and largest levels, delving into the fundamental workings of matter to find new discoveries from subatomic particles all the way up to galaxies, which are light years away. This leads to the study of elementary particle physics, which is focused on identifying the fundamental building blocks of matter and energy. With a better understanding of these building blocks, scientists hope to unlock a deeper understanding of the natural world around us. These findings in elementary particle physics matter to everyone on Earth, but they are also fundamental to understanding the rest of the universe. By studying the fundamental principles that underlie the cosmos, scientists are trying to uncover the mysteries of the universe's origins and how it has evolved over billions of years while continuing to operate in the present day. According to current scientific understanding, the QGP, a state of matter composed of free quarks and gluons [1], existed for only a few microseconds after the Big Bang before the universe cooled enough and eventually evolved into the diverse range of particles that we observe in the universe today. An outline of the critical stages of the evolution of the universe, starting from the Big Bang about 13.8 billion years ago till today, is presented visually in Figure 1.1. Scientists can recreate these conditions in the laboratory using particle accelerators, such as the LHC at CERN, Geneva, Switzerland. Despite decades of ongoing research, many fundamental principles of particle physics remain a mystery. For example, scientists have yet to fully explain the nature of dark matter and dark energy, which together make up about 95% of the universe's total matter-energy content. Even though particle physics encounters numerous challenges today, it has produced significant knowledge and technology that have revolutionized our comprehension of the surrounding world. For example, particle physics has led to the discovery of many new particles, including the discovery of the Higgs boson in 2012 [2, 3], significantly contributing to the understanding of how particles acquire mass [4]. This discovery has deepened our understanding of the fundamental nature of matter and offers the potential for further breakthroughs in the field.

The journey to understand the fundamental building blocks of matter and to verify theories in particle physics has been marked by the development and use of giant particle accelerators throughout the world. Initially, atoms were believed to be the smallest indivisible particles of matter. However, this notion was challenged by experiments conducted by Ernest Rutherford in 1909-1911, which led to the discovery of the nucleus [5]. The subsequent discovery of protons [6] and neutrons [7] improved our understanding of the composition of the atom. In the late 1960s and early 1970s, experiments on deep inelastic scattering conducted at the Stanford Accelerator Center uncovered the presence of quarks within protons

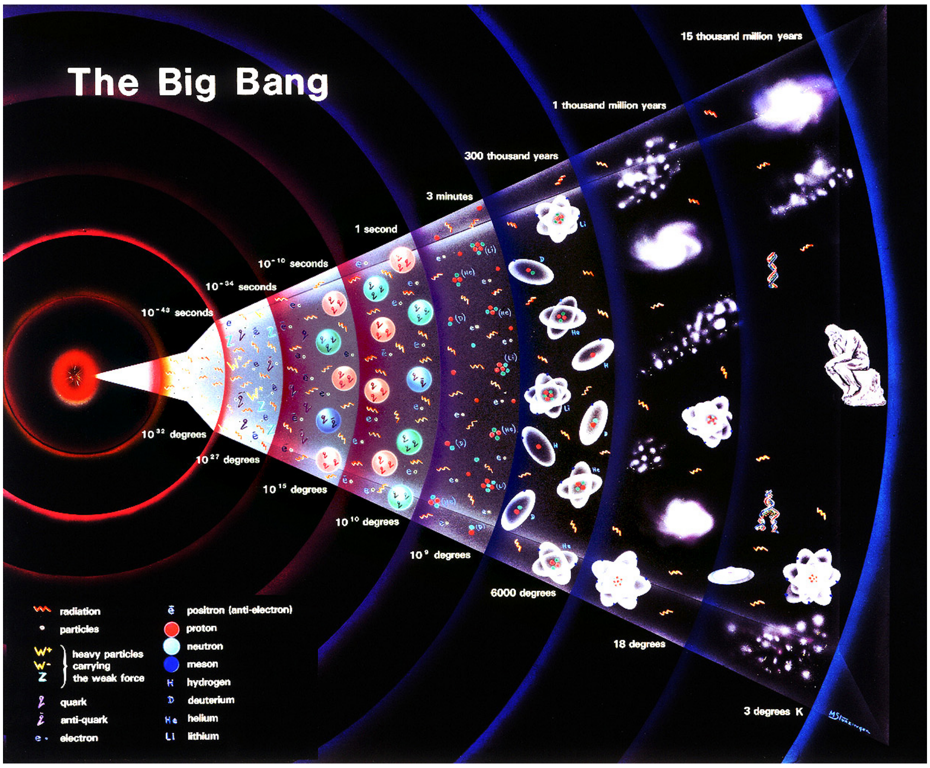

Figure 1.1: Diagram outlining the critical stages of evolution of the Universe from the Big Bang to the present.

and neutrons [8, 9]. By bombarding nucleons with high-energy electrons, these experiments provided strong evidence that quarks are elementary particles. Currently, quarks are regarded as fundamental particles that cannot be split further. Unlike free particles, quarks are not observed independently but are instead confined within composite particles known as hadrons, because of the strong force that holds them together. This process, called quark confinement, is a key aspect of QCD, the theory explaining the strong interaction [10]. In 1979, at the Deutsches Elektronen-Synchrotron (DESY) laboratory in Germany, e^+e^- annihilation experiments led to the groundbreaking discovery of the gluon, marking a significant achievement in particle physics [11]. Conducting high-energy collisions between electrons and positrons, these experiments first uncovered the existence of gluons. As carriers of the strong force, gluons are responsible for mediating interactions among quarks. This discovery not only provided empirical support for the theoretical construct of QCD but also reinforced our understanding of the strong interaction and the confinement of quarks within hadrons. Today, particle accelerators such as the LHC at CERN continue to push the boundaries of our knowledge in particle physics. These powerful machines allow scientists to probe the subatomic world with ever-increasing precision, seeking new particles, studying their properties, and unraveling the mysteries of the universe at its most fundamental level. The pursuit of understanding the fundamental building blocks of matter and the exploration of the strong force and quark confinement remain at the forefront of scientific research, driving us towards deeper insights into the nature of our universe.

Through centuries of exploration and countless experiments, a remarkable theoretical framework known as SM of particle physics has emerged. This model stands as the pinnacle of scientific achievement, providing us with a deep understanding of the building blocks of matter and the fundamental interactions that govern their behavior [12]. According to SM, there are two main types of particles: fermions and bosons. Fermions have half-integer spin and are the building blocks of matter. They include quarks and leptons. Quarks are incredibly tiny particles that participate in the strong nuclear force and make protons and neutrons, the building blocks of atomic nuclei. There are six types, or flavors, of quarks: up (u), down (d), charm (c), strange (s), top (t) and bottom (b). Each quark flavor possesses a unique set of characteristics, such as mass, charge, and interaction properties. Quarks possess fractional electric charges. The up quark has a charge of +2/3, while the down quark has a charge of -1/3. The combination of different quark charges within a hadron determines its overall electric charge. Leptons, on the other hand, do not experience the strong nuclear force. There are three known types, or generations, of leptons: electron and its associated neutrino (first generation), muon and its neutrino (second generation), and tau and its neutrino (third generation). Each generation of leptons has a distinct mass and behaves differently in various interactions. Bosons, on the other hand, are particles that mediate the fundamental forces of nature and have integer spin. They carry and exchange forces between particles. The Standard Model includes four types of bosons. The photon is the particle of light and electromagnetism. The $W^{\pm}$ and Z bosons are responsible for the weak nuclear force, which is involved in processes such as radioactive decay. The gluon is the mediator of the strong nuclear force, which holds quarks together inside protons and neutrons. Lastly, the Higgs boson is associated with the Higgs field and gives mass to other particles. Figure 1.2 provides a visual representation of the SM of particle physics, illustrating the fundamental particles and their interactions within the framework of this theory.

The SM describes three fundamental forces: the electromagnetic force, the weak nuclear force, and the strong nuclear force. The electromagnetic force is responsible for the interactions between charged particles. The weak nuclear force is involved in processes such as radioactive decay and neutrino interactions. The strong nuclear force holds atomic nuclei together by binding quarks within protons and neutrons. Whereas, the SM has been successful in explaining a wide range of experimental observations, it is not a complete theory. It does not include gravity and does not account for phenomena like dark matter and dark energy. Scientists are actively working on extending the model to address these open questions and discover new physics beyond the SM.

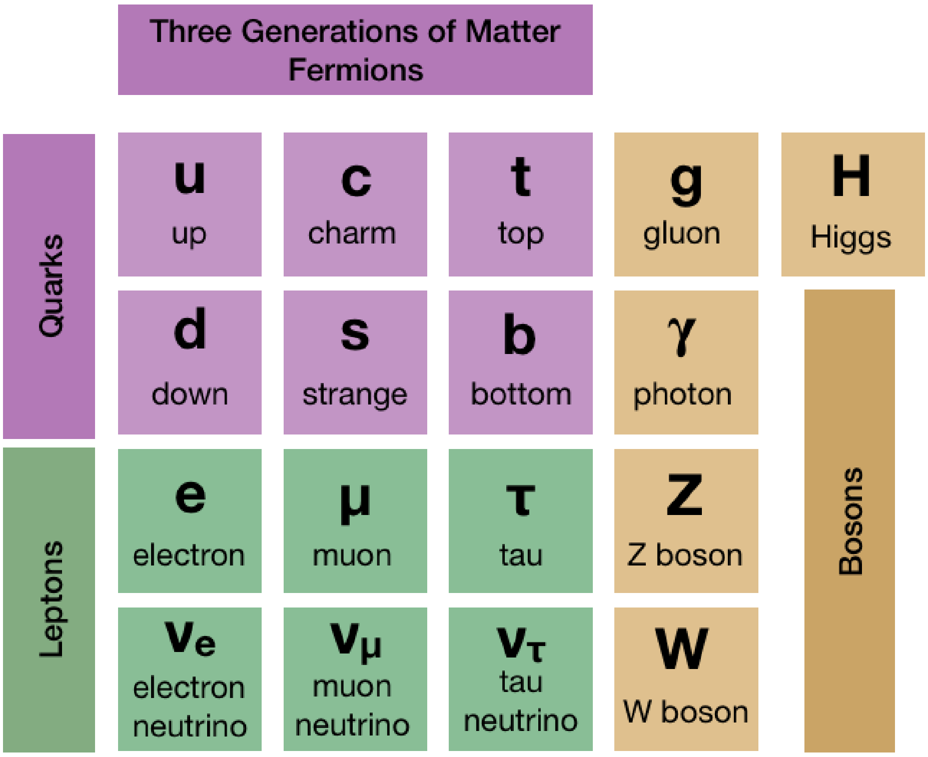

Figure 1.2: The Standard Model of elementary particles in visual form showing the 12 fundamental fermions and the 5 bosons.

1.1 Quantum Chromodynamics (QCD)

Quantum chromodynamics (QCD) is the theoretical framework governing strong interactions, illuminating the behavior of quarks and gluons. This theory introduces color quantum numbers, analogous to the electric charge in QED, as the fundamental descriptors of these interactions. In the context of QCD, ‘color’ represents an abstract property, serving as a distinctive quantum attribute, rather than having any relation to the colors we perceive in our everyday environment. Quarks and gluons, the building blocks of matter in QCD, carry color charges, and what sets QCD apart is its unique feature: the allowance for self-interactions among these particles. Within this intricate framework, massless gluons act as mediators, similar to photons in the QED, facilitating the exchange of color charge information among quarks. Notably, gluons exhibit eight distinct color charge states, a departure from two electric charge states in QED, adding depth and complexity to QCD. In practical terms, quarks are always bound within composite particles, called hadrons, which include mesons and baryons. These hadrons, whether they take the form of mesons or baryons, emerge as color-neutral entities composed of quarks and gluons. Mesons are composed of a quark and an antiquark, whereas baryons are formed by the binding of three quarks. Antibaryons, on the other hand, consist of three antiquarks. This absence of free quarks is a testament to the extraordinary strength of the strong force and highlights the unique and enigmatic nature of the subatomic world described by QCD. According to QCD, the potential for interaction between quarks and gluons is as follows:

$$V_{QCD}(r) = \frac{-4}{c}\frac{\alpha_s}{r} + kr \tag{1.1}$$

where, 'α_s' represents running coupling constant, 'r' is the distance between two interacting partons (quarks and gluons) and k is color string tension constant. The strong coupling constant [13] which depends on momentum transfer Q^2 between partons is described as:

$$\alpha_s(Q^2) = \frac{12\pi}{(11N_c - 2N_f)\ln(Q^2/\lambda_{QCD}^2)} \tag{1.2}$$

where, N_c is the number of color charges, N_f is the number of quark flavors, λ_{QCD} is the scale parameter in the QCD calculations, which is about $\sim$ 200 MeV [14]. In Figure 1.3, we observe the behavior of the strong coupling constant, α_s, as a function of the momentum transfer denoted as Q. Figure 1.3 and Equation 1.1 offer insight into two distinctive characteristics of QCD: color confinement and asymptotic freedom. Equation 1.2, representing the QCD potential, reveals the phenomenon of color confinement, indicating that isolated quarks cannot exist in nature. The first term in Equation 1.2 bears a resemblance to the Coulomb potential seen in QED and dominates at small values of the separation distance, 'r'. However, as the distance between quarks increases, a linear term begins to dominate. This implies that the amount of energy needed to separate the quarks increases with the increase in distance between them. Consequently, as the quarks move apart, they create flux tubes of color field lines between them. Eventually, when a threshold energy is reached, this energy transforms into the creation of a quark and anti-quark pair rather than allowing for the existence of free quarks. The parameter α_s, often referred to as the running coupling constant, is not a fixed value, but rather depends on the momentum transfer, as outlined in

Equation 1.2. This phenomenon is key to understanding the behavior of quarks and gluons within QCD. In Figure 1.3, we observe that at small momentum transfers (where Q^2 $<<$ λ^2_{QCD}) or large distance scales, the running coupling constant of QCD becomes significantly large. Consequently, quarks and gluons remain confined within hadrons rather than existing as free particles. This particular aspect of QCD is known as quark or color confinement, and it is the regime where non-perturbative QCD methods are applicable. Conversely, at large momentum transfers (where $Q^2 >> \lambda^2_{QCD}$) or small distance scales, the QCD coupling constant weakens. In the limit as Q^2 approaches infinity, quarks and gluons become free within the QCD vacuum. This is referred to as asymptotic freedom, and in this regime, perturbative QCD techniques are valid. Figure 1.3 impressively demonstrates the agreement between predictions from QCD-based models and experimental data gathered from various systems over a broad range of momentum transfers, providing strong support for the theory's validity. David Gross and Frank Wilczek [15, 16], in 1973, discovered asymptotic freedom in the realm of QCD. At the same time, David Politzer [17] conducted groundbreaking independent research that aligned with the findings of Gross and Wilczek. In recognition of their profound contributions to our understanding of interactions between the fundamental particles, Gross, Wilczek, and Politzer were jointly honored with the Nobel Prize in Physics in the year 2004.

1.2 QCD Phase transition and QGP

A phase transition is a well-established phenomenon in which matter undergoes a transformation from one state to another, typically characterized by a specific set of order parameters. These order parameters are variables used to differentiate between the different phases or states that a substance can assume. An illustrative example of phase transition can be found in the realm of QED, in the well-known phase diagram of water [18], where temperature and pressure serve as order parameters that characterize the transitions between solid ice, liquid water, and gaseous steam. Similarly, phase transitions are anticipated to occur in QCD sector as well. In this context, the transition is defined as a transformation

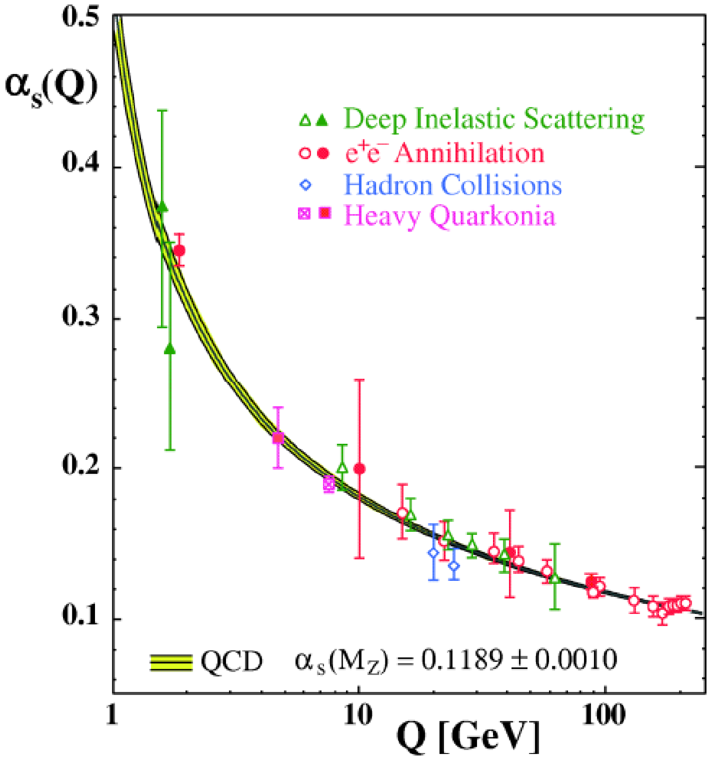

Figure 1.3: The QCD running coupling constant measurement from various experiments are compared in wide range of momentum transfer [13].

from a state where hadrons are bound together to a state where quarks and gluons exist in a deconfined, liberated form. As the QCD exhibits asymptotic freedom under conditions of high momentum transfer or small distance scales, it implies that at large energies or temperatures, the interactions between quarks and gluons weaken, or in other words, the running coupling constant becomes significantly small at large energies and high temperatures. In 1974, T. D. Lee [19], J. C. Collins , and M. J. Perry [20] postulated that by achieving a high energy density, it might be feasible to generate a densely packed nuclear matter consisting of quarks or gluons in a state of asymptotic freedom. Such dense nuclear matter containing asymptotically free quarks or gluons, spanning volumes larger than typical nucleonic scales, is referred to as quark-gluon plasma (QGP). Theoretical investigations, including lattice QCD calculations [21, 22, 23, 24], have indicated the potential existence of a QGP medium at high temperatures. In Figure 1.4, we observe the energy density (ε/T^4), pressure density ($3p/T^4$), and entropy density ($3s/T^4$) as functions of temperature, as determined by lattice QCD calculations for a system with (2+1) quark flavors at zero baryon chemical

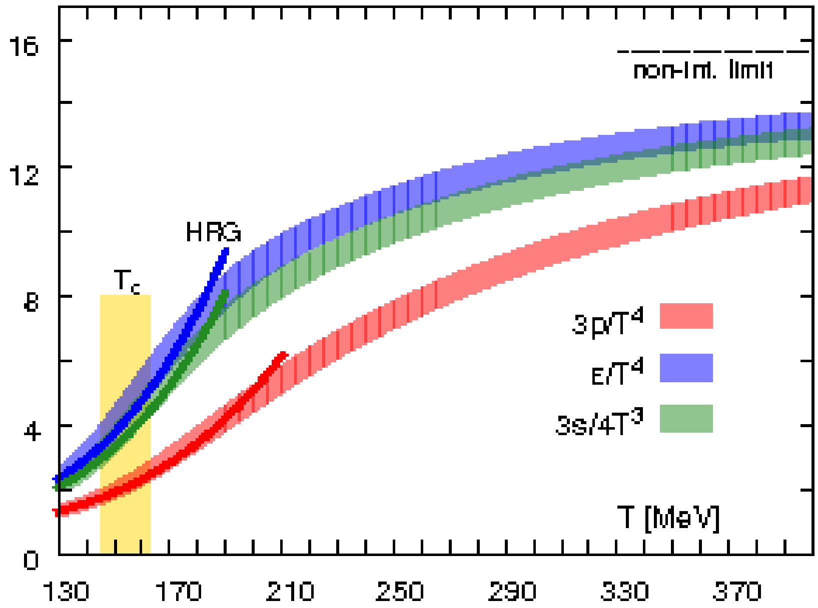

Figure 1.4: Normalised energy density (ε/T^4), pressure density ($3p/T^4$), entropy density ($3s/T^4$) as a function of temperature from Lattice QCD calculation of (2+1) flavor at zero baryon chemical potential ($\mu_B = 0$), as represented by different color bands. At lower temperatures, the solid lines in distinct colors, corresponds to outcomes derived from the Hadron Resonance Gas (HRG) model, while the dashed lines at higher temperatures corresponds to a non-interacting Hadron Resonance Gas. This regime is often referred to as the Stefan-Boltzmann ideal gas limit [21].

potential ($\mu_B = 0$). Here, μ_B quantifies how the energy of a system changes in response to variations in the number of baryons. A nonzero baryon chemical potential would indicate an excess of baryons over anti-baryons or vice versa, implying a net baryon density in the system. The division by T^4 reflects the expected scaling in the high-temperature regime, where the thermodynamic quantities approach the Stefan-Boltzmann limit of an ideal gas of relativistic particles. In this limit, the densities of energy, pressure and entropy scale as T^4, allowing a direct comparison of the QCD system with the behavior of the ideal gas. In particular, the energy density shows a pronounced increase around a critical temperature, denoted as $T_c = 156.5 \pm 1.5$ MeV [21]. This distinct change suggests an increase in the number of degrees of freedom within the system, hinting at a significant transition. Specifically, this transition marks the shift from a state characterized by hadronic matter to a new phase of asymptotically free quarks and gluons.

The QCD phase diagram shown in Figure 1.5 is a graphical representation that helps us understand how different phases of strongly interacting matter behave under varying conditions of temperature (T) and baryon chemical potential (μ_B). This phase diagram is particularly crucial for exploring the properties of matter under extreme conditions, such as those that existed in the early universe and inside dense objects like neutron stars. In this diagram, there are two primary axes: temperature (T) and baryon chemical potential (μ_B). The $\mu_B = 0$ axis represents conditions in which the baryon chemical potential is zero, which means that there is no net excess of baryons over antibaryons in the system. This axis has been extensively studied using lattice QCD simulations [22, 23, 24, 25]. At low temperature and chemical potential, the phase of matter we encounter is the hadronic phase. This phase consists of color-neutral bound states, primarily composed of protons, neutrons, and other hadrons. In this regime, quarks and gluons are confined within these hadronic structures. As the temperature increases and reaches a critical point, there is a transition to a phase called quark-gluon plasma (QGP) [26]. This phase transition is characterized by the deconfinement of quarks and gluons and is of great interest for understanding the early universe. The transition between the hadronic matter and the QGP is not a sudden change but rather a smooth crossover, especially at low and zero chemical potential. For finite temperatures and higher values of baryon chemical potential (μ_B), QCD lattice calculations predict that the crossover transition between hadronic matter and the QGP phase changes into a first-order phase transition [27]. The exact location of this critical point is the subject of active research and is being explored through heavy-ion collision experiments and theoretical calculations. At very large chemical potentials, further intriguing phenomena are anticipated, including the possibility of a color superconducting phase [28]. Advancements in the lattice QCD phase diagram synchronize closely with the expanding realm of experimental data. Presently, experimental results from heavy-ion collision experiments are primarily generated by two key facilities: the Large Hadron Collider (LHC) in Geneva, Switzerland, which provides data at lower densities and high temperatures, and the Relativistic Heavy Ion Collider (RHIC) at the Brookhaven National Laboratory in New York, USA, offering insights into larger chemical potentials. Notably, upcoming facilities such as the Nuclotron based Ion Collider fAcility (NICA), and the Facility for Anti-proton and Ion Research (FAIR), are expected to explore even higher density regimes, expanding our understanding of the

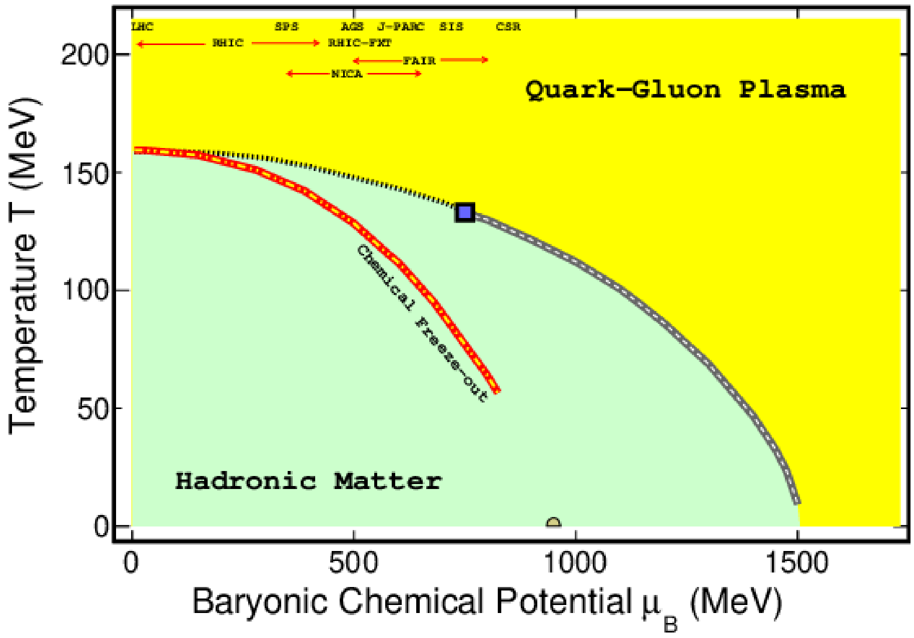

Figure 1.5: QCD phase diagram featuring temperature (T) against baryon chemical potential (μ_B). The black solid line shows the first-order phase transition, separating the hadronic and quark-gluon phases at high μ_B. The critical point, marking the endpoint of this transition, is denoted by a solid square marker. The red-yellow dotted line corresponds to the chemical freeze-out determined from particle yields in heavy-ion collisions using a thermal model. At T = 0 and $\mu_B \sim 925$ MeV, the diagram represents the ground state of nuclear matter along the x-axis [29].

QCD phase diagram.

1.3 Heavy-ion collisions and their space-time evolution

The experimental exploration of QCD thermodynamics is intimately linked with heavy-ion collision experiments, necessitating a brief examination of the evolution of these collisions in both space and time as illustrated in Figure 1.6. Various types of nuclei can be employed in heavy-ion collisions, with prominent examples being Gold (Au) at RHIC and Lead (Pb) at LHC. When two beams of these nuclei, accelerated to relativistic velocities in opposite directions, collide, they give rise to a nonthermalized state characterized by strongly interacting fields, which is called a glasma and is commonly treated in the color glass condensate framework [30, 31] due to its nonthermal behavior. This glasma comprises partons originating from the colliding nuclei and sea quarks, which emerge due to the extreme conditions during the collision. Given the highly nonthermal nature of the glasma, traditional

Lattice QCD calculations are inapplicable. Moreover, the diverse momenta of the particles within the glasma present a formidable challenge for their study.

In the subsequent stage, the partons further fragment into quarks and gluons, resulting in the formation of the quark-gluon plasma (QGP). This is a highly interacting state featuring deconfined quarks and gluons. Initially anticipated to resemble an electromagnetic plasma, it is now firmly established that the QGP behaves more like a strongly interacting fluid, often described through the framework of relativistic hydrodynamics. As the quark-gluon plasma expands and simultaneously cools, it approaches temperatures near the QCD transition temperature, at which point the deconfined quarks and gluons must recombine to form color-neutral hadrons. This phase transition marks the determination of the chemical composition of the hadrons, and the associated temperature is referred to as the chemical freeze-out temperature. After the chemical freeze-out, hadrons continue to interact with one another, exchanging energy and momentum, until they reach a specific point in space-time where the distances between them increase significantly. At this time, they become too far apart to engage in further interactions, marking the point known as kinetic freeze-out. Subsequently, the particles are detected by the particle detector.

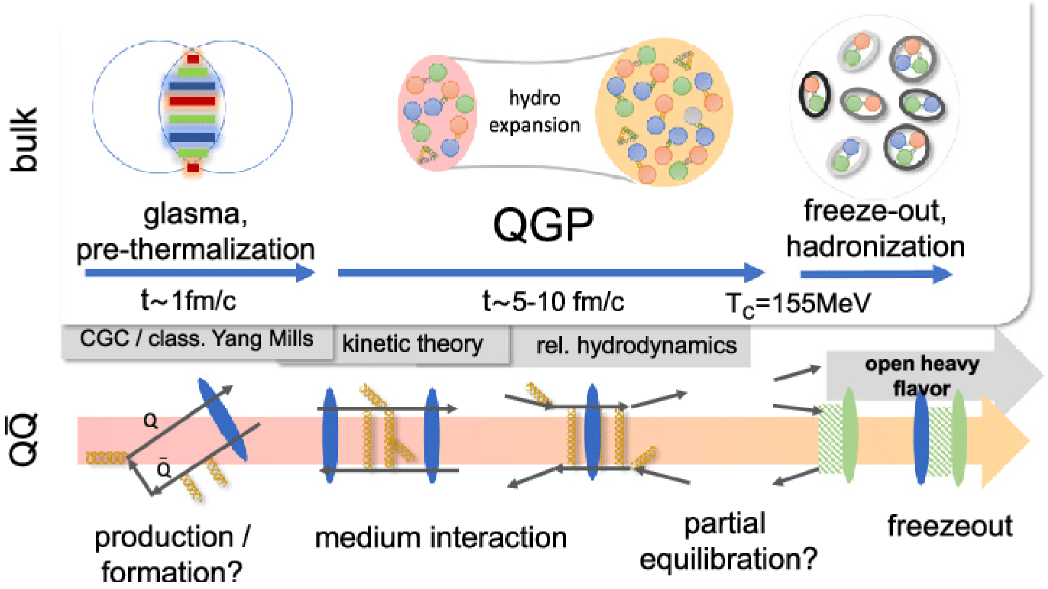

Figure 1.6: An overview of the various stages of a heavy-ion collision is provided. The diagram highlights the different effective theories employed to describe these distinct stages, depicted in grey [32].

1.4 QGP and its signatures

In the preceding few sections, we discussed QGP, the predicted state of nuclear matter at temperatures resembling those that were prevalent in the early universe during the first few microseconds after the Big Bang explosion. Since the QGP exists only for a very brief moment after heavy-ion collisions, it cannot be detected directly by the detectors. Therefore, we rely on various tell-tale signs or signatures to confirm its existence and study its properties. The signatures of the formation of QGP during the initial stages in the evolution of heavy-ion collisions are discussed in the following subsections.

1.4.1 Strangeness Enhancement

The saturation of strangeness in the QGP is a consequence of the abundance of thermal gluons within this unique state of matter [33]. This saturation means that there is a significant presence of strange quarks and antiquarks in the QGP due to the intense heat and energy. Consequently, when the QGP undergoes the process of hadronization, where it transforms into ordinary hadronic matter, it is anticipated that the production of hadrons containing strange quarks will occur in a manner that reflects a state of chemical equilibrium [34, 35]. To understand this, there is a prevailing viewpoint, which suggests that the equilibrium state achieved by different types of quarks within the QGP, often referred to as flavor equilibrium, persists as the QGP evolves into ordinary particles during hadronization. In simpler terms, this viewpoint implies that the equilibrium state of quarks within the QGP remains unchanged as it moves into different forms of particles. It is like saying that if things were mixed evenly at one point, they stay that way as they change into different forms. The initial confirmation of these expectations came from the WA97 experiment [36]. They observed a remarkable 20-fold increase in the production of Ω and $\bar{\Omega}$ hyperons during central fixed-target Pb–Pb collisions at $\sqrt{s_{\mathrm{NN}}} = 17.3$ GeV, when compared to predictions based on p–Pb collisions. Subsequent validation of these findings came from the NA57 experiment [37]. Moreover, a similar observation was made at the higher energy levels of RHIC, specifically $\sqrt{s_{\mathrm{NN}}} = 200$ GeV, as demonstrated by the Solenoidal Tracker at RHIC

(STAR) experiment[38]. To assess the saturation of strange flavor in emitted hadrons, ther-

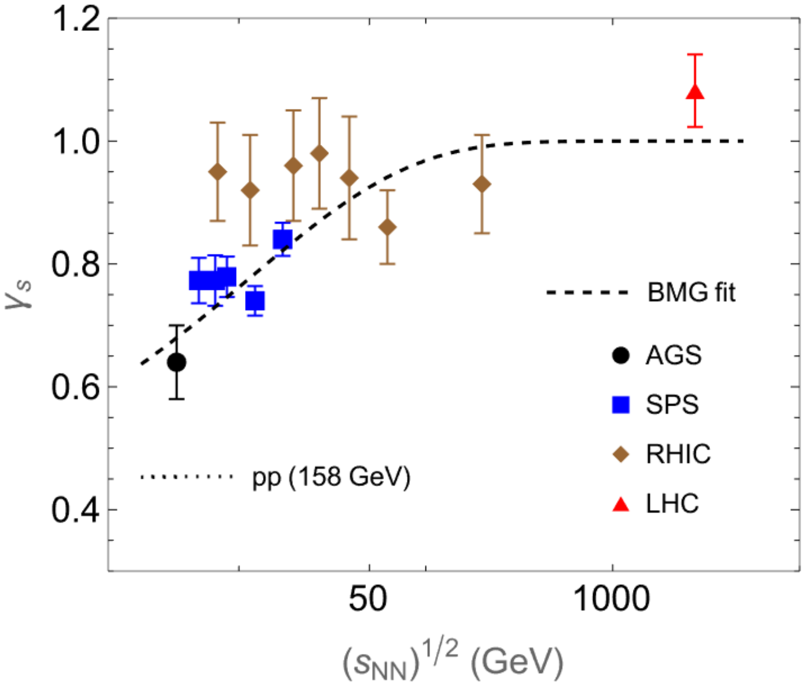

Figure 1.7: Evolution of the strangeness fugacity γ_s as a function of $\sqrt{s_{\mathrm{NN}}}$ in central Au−Au or Pb−Pb collisions based on chemical fits using the grand canonical ensemble [39, 40, 41]. The dashed curve provided in [39] shows the analytic fit to $\gamma_s(\sqrt{s_{\mathrm{NN}}})$.

mal fits are used with parameters such as temperature (T_c), chemical potentials (μ_B and μ_S) for baryon number and strangeness, and strangeness fugacity (γ_s). When γ_s is less than 1, indicating under-saturation as typically seen in pp collisions, strangeness is not fully saturated. Figure 1.7 shows γ_s evolving with collision energy from Alternating Gradient Synchrotron (AGS) to LHC levels. The dashed curve in the figure represents an analytical fit provided in [39], revealing that as the collision energy increases, γ_s approaches unity. This confirms the complete saturation of the strange quark density during hadronization at the highest RHIC and LHC energies, in accordance with the anticipated strangeness behavior. Both strangeness saturation and the duration of QGP are intricately linked to the size of the colliding nuclei and the energy of the collision. The size of the colliding particles, often represented by the mass number (denoted as A), directly influences the initial conditions and volume of the QGP fireball formed during the collision. A larger colliding nucleus results in a larger fireball. Simultaneously, the collision energy, expressed as $\sqrt{s_{\mathrm{NN}}}$, determines the energy density and the overall evolution of the QGP. According to data provided by ALICE as in Ref. [42], there is a correlation between system size and the enhancement of strange hadrons in various collision systems, revealing a systematic rise in the production yield of multi-strange baryons relative to charged pions, and furthermore, the yield ratio of strange hadrons to pions increases at a higher rate as the number of strange valence quarks within the hadron increases.

1.4.2 Quarkonium suppression

Quarkonium suppression refers to the phenomenon observed in relativistic heavy-ion collisions, where the production of quarkonium states such as J/Ψ $(c\bar{c})$ and Υ $(b\bar{b})$ is reduced compared to what would be expected in the absence of a QGP medium. This suppression is primarily caused by color screening effects within the QGP [43]. It is worth noting that the Υ states (composed of $b\bar{b}$ quarks) are expected to dissociate at different QGP temperatures compared to the J/Ψ states (composed of $c\bar{c}$ quarks) due to variations in their binding energies. Initially, it was believed that suppression would be most pronounced at low quarkonium momenta, where the quark-antiquark pair is closely embedded in the QGP and experiences strong color screening. In contrast, at high transverse momentum (p_{T}), it was anticipated that suppression would weaken as quarkonium formation occurs outside the QGP due to relativistic time delay, resulting in minimal screening effects. However, further investigations have revealed additional mechanisms contributing to quarkonium melting, including non-static factors like thermal ionization and contributions from higher-energy quarkonium states. Additionally, cold nuclear matter (CNM) effects play a role, including nuclear shadowing, momentum broadening of initial-state partons, and absorption by spectator nucleons, all of which impact the degree of quarkonium suppression. Together, these mechanisms create the observed sequential suppression pattern in heavy-ion collisions. In particular, the suppression of J/Ψ at the LHC energy is less pronounced compared to RHIC, and this difference cannot be solely explained by gluon shadowing. This suggests the presence of new production mechanisms for J/Ψ at higher collision energies, such as the possibility of regeneration through the coalescence of charm quark pairs generated during the initial phase of the collision. Furthermore, the suppression of high p_{T} quarkonia, including J/Ψ, is expected to be similar to that of open-charm mesons due to the substantial energy loss experienced by the color-octet precursor state within the QGP [44].

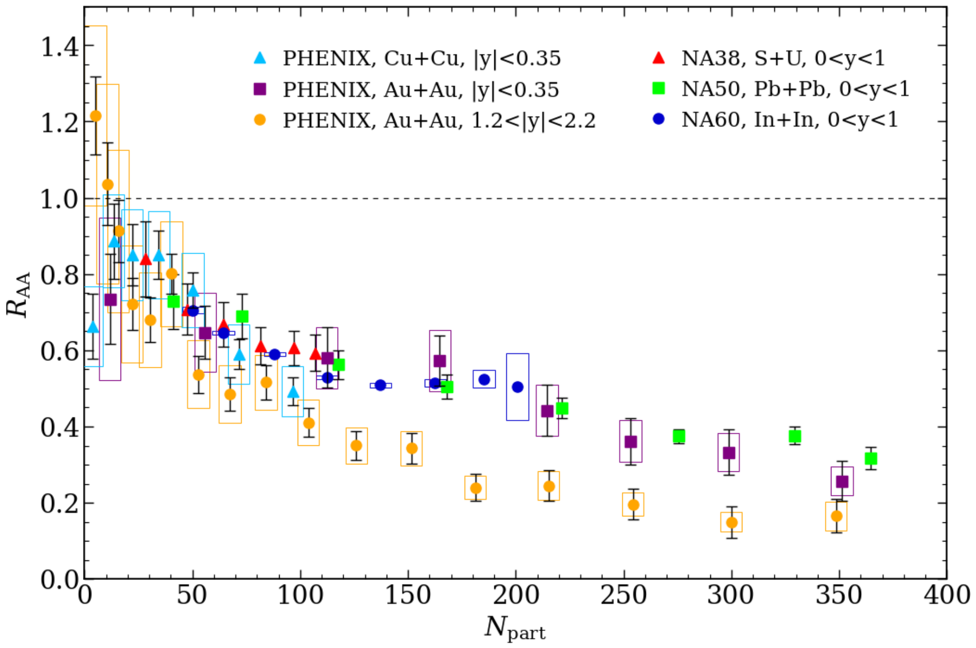

Figure 1.8: The nuclear modification factor R_{AA} (J/Ψ) as a function of the number of participating nucleons N_{part} at mid-rapidity from NA38, NA50, NA60 and PHENIX. Collision system, rapidity window and centrality are given for each in the legend.

At extremely high collision energies, a substantial abundance of $c\bar{c}$ pairs is generated, allowing for significant regeneration of charmonium states during the subsequent hadronization process [45, 46]. The yields of charmonium at such large collision energies are expected to follow the same thermal equilibrium principles that govern other hadron yields. However, the overall production of charmonium states is primarily affected by the production cross section for $c\bar{c}$ pairs within the nuclear collision. This observation serves as compelling evidence for the occurrence of deconfinement. Importantly, this regenerative process is most effective at lower transverse momenta (p_{T}), where the density of $c\bar{c}$ pairs is maximum. To assess quarkonium suppression quantitatively, one common measure exploited is the nuclear modification factor R_{AA}, which computes the ratio of inclusive yields per unit rapidity in A−A collisions relative to those in proton-proton collisions, normalized by the number of binary nucleon-nucleon interactions taking place in the nuclear collision:

$$R_{AA}(p_{\mathrm{T}}) = \frac{dN_{AA}/dp_T dy}{< T_{AA} > d^2\sigma_{pp}/dp_T dy} \tag{1.3}$$

where $< T_{AA} >$ is the longitudinally integrated nuclear density averaged over the experimentally selected events in a certain collision centrality window. A value $R_{\mathrm{AA}} < 1$ implies suppression in the nuclear collision relative to the extrapolation from independent proton-proton collisions. The R_{AA} (J/Ψ) dependence on the number of participating nucleons (N_{part}) in the nuclear collision was first observed at the CERN SPS in experiments NA38 [47], NA50 [48, 49] and NA60 [50]. A clear pattern of suppression in the yeild of J/Ψ is observed above $N_{part} \sim 100$, increasing steadily up to the most central collisions of $N_{part} > 350$ as illustrated in the figure. These new findings were further verified by the Pioneering High Energy Nuclear Interaction eXperiment (PHENIX) at RHIC [51] at higher energies than at SPS.

1.4.3 Temperature measurements

Temperature measurements play a crucial role in providing quantitative evidence for the formation of a quark-gluon plasma (QGP) in relativistic heavy-ion collisions. The equation of state of QCD matter can be determined by measuring the temperature as a function of the deposited energy. The change in the number of effective degrees of freedom in the QGP leads to a change in the entropy density at a given temperature, which is closely related to the energy density. Thermal slopes, which can be derived from the transverse-momentum spectra of emitted particles, offer one approach to measuring this temperature, often referred to as the chemical freeze-out temperature. Another valuable method involves analyzing the invariant-mass spectrum of lepton pairs, particularly in the intermediate-mass region (IMR) between the ϕ-meson and J/ψ, otherwise the spectrum is distorted by decay of vector mesons which gives false measurements of the temperature. This approach provides insights into the time-averaged temperature of the emitting medium. However, these temperature measurements come with challenges. Collective flow effects and background contributions, such as those arising from semi-leptonic charm decays, can obscure the accurate determination of temperature in such collisions. The first and still most accurate measurement of temperature in heavy-ion collisions has been carried out by NA60 fixed target In+In collisions at $\sqrt{s_{\mathrm{NN}}} = 17.3$ GeV, which reported the slope of the di-muon invariant mass spectrum as a measurement of temperature [52]. The STAR experiment has recently presented their findings on electron-pair invariant mass spectra in Au+Au collisions at center-of-mass energies of $\sqrt{s_{\mathrm{NN}}} = 27$ and 54.4 GeV [53]. They used thermal fits of the form $M^{3/2}\ \exp(-M/T)$ to analyze the intermediate-mass region (IMR). The results indicate temperatures of $T_{IMR} = 301 \pm 60$ MeV and $T_{IMR} = 338 \pm 59$ MeV for the respective collision energies. These results are presented in Figure 1.9, where they are compared to the values of $(T_c,\ \mu_{B,c})$ during chemical freeze-out (shown as blue dots) and the initial thermalization conditions $(T_{ini},\ \mu_{B,ini})$. Interestingly, it is observed that the temperature measurements from the dilepton invariant-mass spectra are higher than the estimated initial thermalization temperatures of the QGP, implying the presence of contributions from pre-equilibrium processes in the measured mass range. However, when focusing on the mass region around the ρ-meson, known as the low-mass region (LMR), the temperatures extracted from thermal fits align with those obtained from chemical freeze-out analyses [52, 53]. These results are also shown in Figure 1.9. The study of temperature as a signature of QGP formation continues to be an active area of research in the field of relativistic heavy-ion collisions.

1.4.4 Direct photons

Direct photons are theoretically valuable in providing insight into the temperature of QGP during heavy-ion collisions. However, their practical analysis is complicated due to several factors. Firstly, the temperature of the QGP evolves over time during the collision, making it challenging to pinpoint a single temperature value. Secondly, the photon spectrum is altered by a blue-shift effect caused by the transverse expansion velocity of the matter emitting the photons. Lastly, there can be contributions to the photon spectra from photons radiated by the hadron gas in the final stages of the collision. Consequently, any meaningful interpretation of the measured photon spectra relies on complex modeling and is influenced by various factors. To address this, the PHENIX collaboration has collected extensive data from collisions at RHIC and LHC, examining how the yield of direct photons depends on collision energy and system size over a wide range [54]. The Figure 1.10

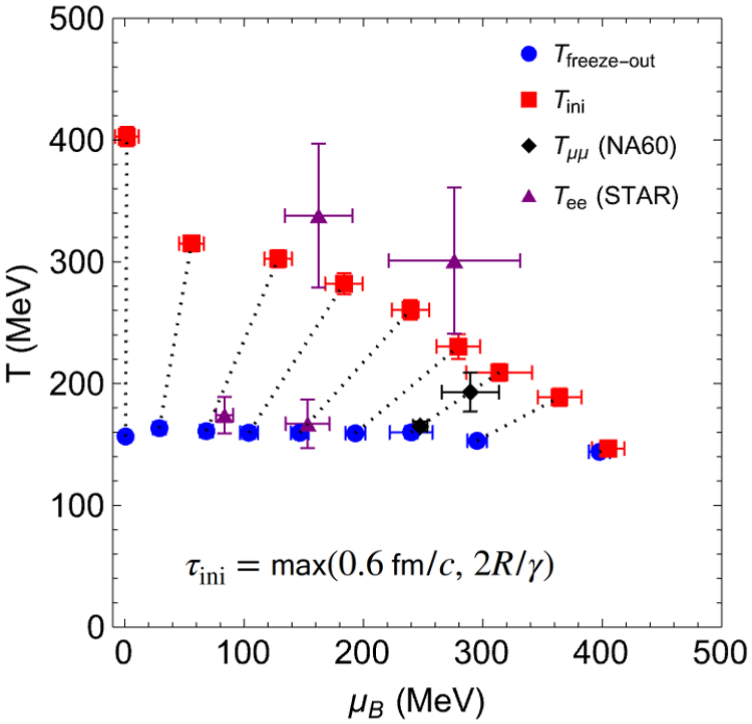

Figure 1.9: The QCD phase diagram is illustrated with several key points: the locations of chemical freeze-out (represented by blue circles), the average initial temperatures and chemical potentials (represented by red squares), and the effective temperatures obtained from thermal fits applied to the intermediate and low-mass regions within dilepton invariant-mass spectra. Additionally, dotted lines are included to indicate constant T/μ_B lines, which correspond to regions with approximately consistent entropy per baryon in the QGP phase [53].

shows un-subtracted direct photon spectra from ALICE for Pb–Pb collisions at a center-of-mass energy of $\sqrt{s_{\text{NN}}} = 2.76$ TeV [55], in three different centrality ranges. Additionally, the figure presents the background of direct photons in pp collisions, which has been computed using next-to-leading-order perturbative QCD and scaled with the average N_{Coll} (nuclear collisions) for each centrality group. Exponential fittings have been applied to the low transverse momentum ($p_{\text{T}} < 2.1$ GeV/c) segment of the spectrum after subtracting the perturbative QCD background. These fittings have yielded thermal slopes of $T_{eff} = (297 \pm 12 \pm 41)$ MeV for the $0-20\%$ centrality window and $T_{eff} = (410 \pm 84 \pm 140)$ MeV for the 20-40% window. The reason behind the significant larger slope parameter for the less central window isn't entirely clear, but one possibility could be that the data used in the fitting process begin at a slightly higher p_{T} value, influencing the result. Overall, direct photon measurements offer a promising avenue for probing the properties of the QGP and

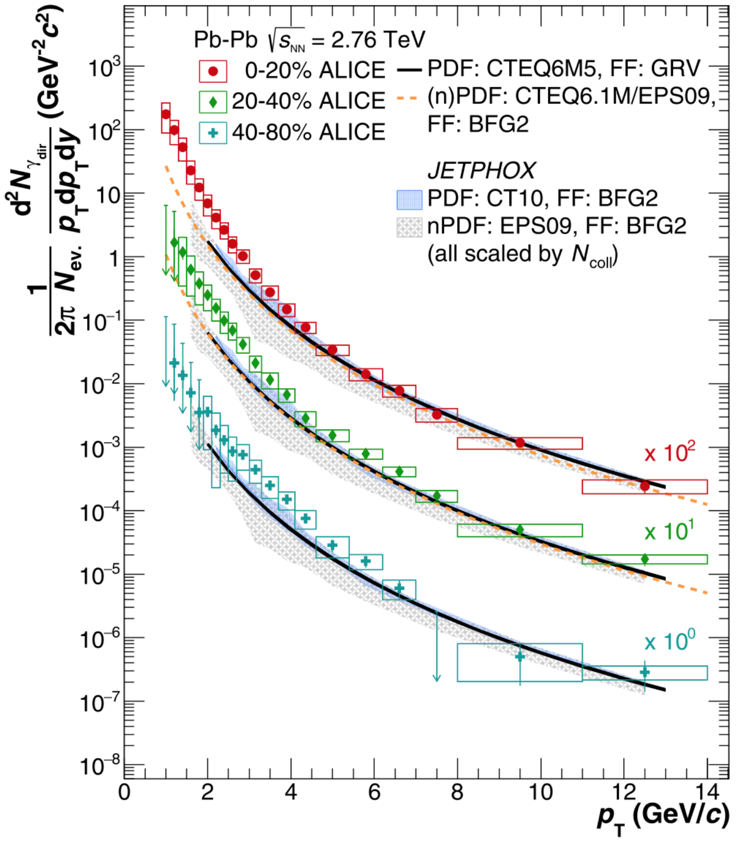

Figure 1.10: The transverse momentum (p_T) spectra of direct photons in Pb−Pb collisions at $\sqrt{s_{NN}}$ = 2.76 TeV are presented for three centrality ranges: 0–20% (scaled by a factor of 100), 20–40% (scaled by a factor of 10), and 40–80%. These spectra are compared to next-to-leading order perturbative QCD predictions for direct photon yields in pp collisions at the same energy, which are further scaled by the number of binary nucleon collisions corresponding to each centrality window [55].

continue to be a subject of active research in the field of high-energy nuclear physics. Further investigations and refinements in both experimental techniques and theoretical models are expected to provide even deeper insights into the nature of the QGP and the conditions prevailing in heavy-ion collisions.

1.4.5 Chiral symmetry restoration

In the vacuum and at low temperatures, the quark condensate $\langle 0|q\bar{q}|0\rangle$ exhibits a persistent nonzero expectation value, resulting in the spontaneous breakdown of chiral symmetry. This manifests itself through a substantial mass discrepancy between chiral partner mesons, such as $\rho(770)$ and $a_1(1260)$, characterized by an approximate 500 MeV gap [56]. There are expectations for the restoration of chiral symmetry at higher temperatures and baryon densities. Lattice-QCD calculations indicate melting of the quark condensate with increasing temperature [57], ultimately leading to its disappearance, a key indicator of chiral symmetry restoration. This gradual dissolution of the quark condensate is expected to coincide with the emergence of degeneracy among chiral partner hadrons. Consequently, the masses of ρ and $a1$, or more generally, the relevant vector and axial vector spectral functions, are expected to converge with increasing temperature and achieve degeneracy upon the full restoration of chiral symmetry. While probing the axial vector channel seems challenging, the vector channel can be explored through the measurement of emitted lepton pairs, either e^+e^- or $\mu^+\mu^-$. In the QGP phase, the ρ-meson peak in the spectral function, already collision-broadened in hot or dense hadronic matter, undergoes complete disappearance. This signifies quark deconfinement and the consequent deconfinement of associated hadron states above T_c [58, 59]. Precise measurements of the lepton pair spectrum, particularly in the $\mu^+\mu^-$ channel for Indium-Indium (In+In) collisions at $\sqrt{s_{\mathrm{NN}}} = 17.3$ GeV at CERN-SPS by the NA60 experiment [52, 60, 61, 62, 63], revealed a significantly diminished peak at the ρ-meson mass corresponding to final-state decays of ρ-mesons within a dilute hadronic medium, superimposed on a broad background which is consistent with expectations from models of in-medium resonance broadening [64]. The production of low-mass electron pairs has been experimentally investigated in collisions $\sqrt{s_{\mathrm{NN}}} = 200$ GeV Au + Au at RHIC energies through measurements carried out by PHENIX [65] and STAR [66]. The observed features in the data share similarities with those obtained from SPS energies in the In+In system, with a reduced level of statistical significance. In particular, dielectron data from Pb+Pb collisions at the LHC are currently limited to peripheral and semi-peripheral collision scenarios [67].

1.5 Hadronic resonances in high energy collisions

The hadronic resonances are formed during hadronization in the evolution of high-energy particle collisions. These resonances have very short lifetimes, a few fm/c, and they decay as soon as they are produced. The lifetime of these resonances is comparable to the duration

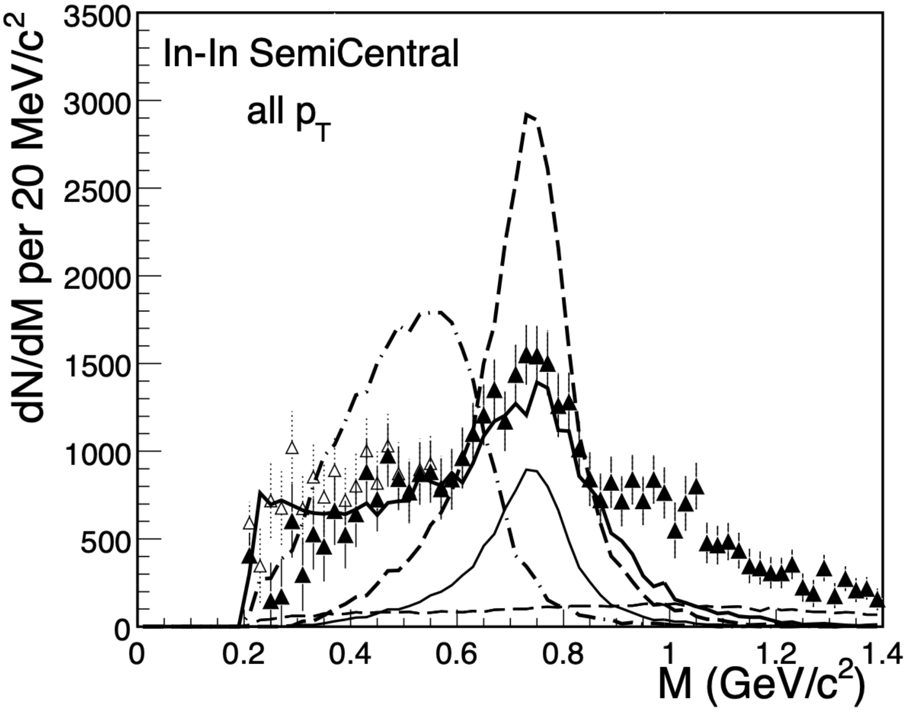

Figure 1.11: Excess $\mu^+\mu^-$ mass spectrum for the semi-central bin in 158 GeV/c In+In collisions in comparison with model predictions. The curves show: "Cocktail" ρ (thin solid), unmodified ("vacuum") ρ (dashed), in-medium broadening ρ (thick solid), in-medium shifted ρ (dashed-dotted). The errors are purely statistical [60].

of the hadronic phase [68, 69, 70, 71, 72, 73, 74] that is the timespan between the chemical and kinetic freeze-outs that occur during the evolution of high-energy collisions. At chemical freeze-out, the inelastic interactions among the partons cease, and the yield of hadrons becomes fixed i.e. there is no new particle production after chemical freeze-out. However, these particles continue to undergo elastic interactions until the hadronic gas expands to a volume where the average distance between the hadrons becomes large enough so that they do not interact elastically with one another, and their momenta become fixed. This specific moment in spacetime is referred to as kinetic freeze-out. Due to their very short lifetimes, few of these resonances decay within the hadronic phase. The decay daughters of these resonances interact with the surrounding hadronic gas, thus their momenta undergo changes. Consequently, the reconstruction of the original resonance particle is not possible through its decay daughters due to their altered momenta, a phenomenon known as the re-scattering effect. Thus, the measured yield of resonance particles is suppressed compared to original yield produced before chemical freeze-out. Another phenomenon, referred to as regeneration, comes into play within the hadronic gas, leading to an enhancement in the yield of the resonances. This enhancement occurs because hadrons inside the hadronic gas can sometimes re-generate a resonance because of pseudo-elastic interactions. These effects of rescattering or regeneration are dominant at low p_{T}. The extent to which these effects influence the resonance yield depends on factors such as the lifetime of resonance particle, the duration of the hadronic phase following the collision, and the interaction cross-section of the decay daughters of resonances. Table 1.1 lists some of the measured hadronic resonances and their properties, including decay channels, branching ratios, and lifetimes. The table includes shorthand notations that will be used to represent these resonances throughout this thesis. The schematic view of the rescattering and regeneration processes for the resonances K^{*0} and ϕ in the hadronic gas is shown in Figure 1.12. The production yields of the hadronic resonances along with their stable particles are an important tool for understanding the evolution of the relativistic high-energy particle collisions. It is worth mentioning here that the stable particles selected for the yield ratios should have the same strangeness quantum number as the resonance particle, ensuring that any strangeness effects in the ratio are canceled out. The measurements of the p_{T}-integrated yield ratios of resonances to ground-state particles by ALICE [76, 77, 78, 79, 80, 81, 82, 83, 84, 85] and STAR [86] are presented in Figure 1.13. It can be observed from Figure 1.13 that

Table 1.1: Properties of hadronic resonances, including their decay channels, branching ratios, and lifetimes in their rest frames [75].

Resonance	Shorthand	Decay Channel	Branching Ratio	Lifetime (fm/c)
$\rho(770)^0$	ρ^0	$\pi^+ + \pi^-$	1.0	1.335
$\mathrm{K}^*(892)^0$	K^{*0}	$\pi^- + K^+$	0.67	4.16
$\phi(1020)$	ϕ	$K^+ + K^-$	0.492	46.26
$\Delta^{++}(1232)$	Δ^{++}	$\pi^+ + p$	1.0	1.69
$\Sigma(1385)^+$	Σ^{*+}	$\pi^+ + \Lambda$	0.870	5.48
$\Sigma(1385)^-$	Σ^{*-}	$\pi^- + \Lambda$	0.870	5.01
$\Lambda(1520)$	Λ^*	$K^- + p$	0.225	12.54
$\Xi(1530)^0$	Ξ^{*0}	$\pi^+ + \Xi^-$	0.67	22

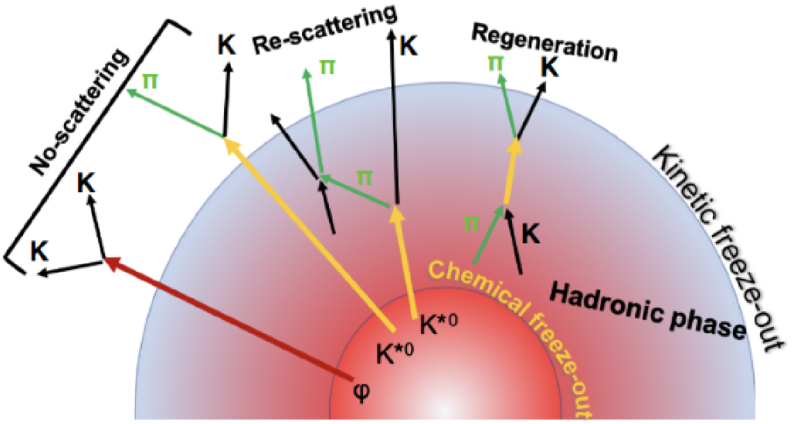

Figure 1.12: Schematic view of rescattering and regeneration processes in the hadronic gas.

in Pb–Pb collisions, the yields of ρ^0, K^{*0}, $\Sigma^{*\pm}$ and Λ^* exhibit suppression with collision centrality. However, this suppression is not observed in the case of the ϕ and Ξ^{*0} resonances due to their longer lifetimes compared to the duration of the hadronic phase formed in such collisions. This varying degree of suppression among these resonances, influenced by their lifetimes, is often exploited to estimate the lifetime of hadronic phase formed in such collisions. In small system collisions such as pp and p–Pb, the suppression in the yield with multiplicity is evident only for ρ^0 and K^{*0} resonances. This observation suggests that the duration of the hadronic phase is dependent on the colliding systems, with longer lifetimes associated with larger colliding systems. Another intriguing parameter in the study of resonances is the nuclear modification factor, denoted as R_{AA} and R_{pA}. The nuclear modification factor compares the p_{T} spectra in A$-$A or p$-$A collisions to those in pp collisions, with the A$-$A or p$-$A spectra scaled by the number of binary nucleon-nucleon collisions. These factors allow us to measure the extent of energy loss experienced by the particles as they traverse the medium formed during A$-$A and p$-$A collisions compared to pp collisions and also to disentangle cold nuclear matter (CNM) effects from hot initial-state effects. Consequently, the yield measurements of various hadronic resonances, characterized by different lifetimes, masses, quark content, and quantum numbers, provide important information for understanding several aspects, including the p_{T}-spectra shapes, the duration of the hadronic phase, strangeness production, parton energy loss, rapidity yield asymmetry, and radial flow effects. Moreover, recent studies by ALICE [87] have revealed intriguing phenomena related to vector mesons (spin $= 1$). In peripheral heavy-ion collisions, the system possesses significant angular momentum, which can be observed through vector mesons due to net polarization of their spins, aligning with the direction of $\vec{L}$ or $\vec{B}$. Thus, studying hadronic resonances not only shed light on the properties of the hadronic phase but also provides insights into the initial conditions of nucleus-nucleus collisions.

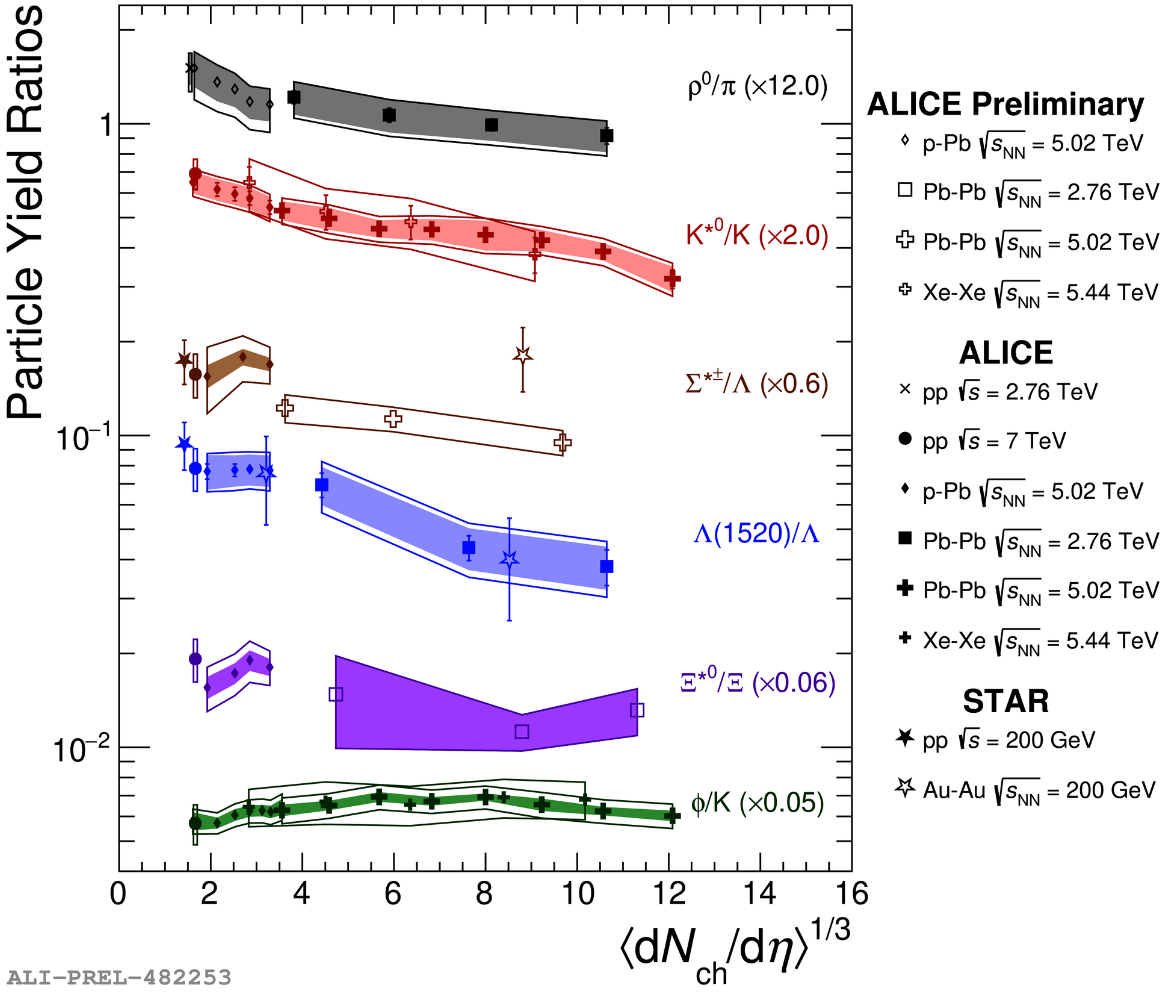

Figure 1.13: The p_{T}-integrated yield ratios of different resonances compared to their stable counterparts across various systems and collision energies with STAR [86] and ALICE [76, 77, 78, 79, 80, 81, 82, 83, 84, 85]. The uncertainty is expressed as bars for statistical errors and boxes for systematic errors.

1.6 Motivation

The distinct lifetimes of hadronic resonances serve as a valuable tool for investigating the characteristics of the hadronic phase, as previously discussed. ALICE has conducted studies on the K^{*0} and ϕ resonances, revealing significant suppression in the final yield of K^{*0} in the most central Pb–Pb collisions and high multiplicity pp and p–Pb collisions. In contrast, no such suppression is observed for the ϕ yield. This difference in the yield alteration of these two resonances arises primarily from the fact that the lifetime of K^{*0} is either comparable to or shorter than the duration of the hadronic phase in such collisions, causing its decay products to undergo rescattering and regeneration within the hadronic phase. Undoubtedly, the rescattering effect prevails in the case of K^{*0}, resulting in its overall suppression with centrality or multiplicity. However, the ϕ resonance has a lifetime longer than the duration of the hadronic phase in such collisions, resulting it to decay after the hadronic phase ends and its decay daughters do not interact with the hadronic gas. Consequently, this leads to the flat behavior of the yield ratio of ϕ resonance to kaon. These observations provide hints for the finite lifetime of the hadronic phase in large collision systems. To further refine our understanding of the properties of hadronic phase, ALICE has extended its measurements to Λ^* resonance, which possesses a lifetime that lies between that of the K^{*0} and ϕ resonances, in small and large collision systems. It is worth mentioning here that the Λ^* resonance is the excited state of the Λ baryon, featuring identical strangeness quantum number but differing in mass, spin and parity. The J^P of Λ^* is $\frac{3}{2}^-$, while that of Λ is $\frac{1}{2}^+$. The measurements on the ratio of Λ^* to ground-state Λ show some suppression in its yield in Pb–Pb collisions but no such suppression is observed in small system collisions. This indicates that either there is no hadronic phase formed in the small system collisions, or the duration of the hadronic phase is extremely brief, causing the Λ^* to decay shortly after it ends. However, the former scenario appears less likely, as the significant suppression of K^{*0} and ρ^0 in high-multiplicity pp and p–Pb collisions confirms the existence of hadronic phase in these smaller collison systems. This makes Λ^* an interesting candidate to get insights into the properties of hadronic phase. The measurements with ALICE on the Λ^* in small systems are in pp collisions at $\sqrt{s}$ = 7 TeV and in p$-$Pb collisions at $\sqrt{s_{\mathrm{NN}}}$ = 5.02 TeV. There are no measurements of Λ^* available at higher energies in the p–Pb system at LHC with ALICE. With the increase in the energy of collisions, the initial energy density available for particle production increases, leading to the creation of a hotter and denser medium, enhancing the likelihood of forming a QGP medium and enabling the production of heavier particles and resonances, as well as modifying the relative particle yields and their kinematic properties. Thus, studying Λ^* in p–Pb system at the highest collision energy of $\sqrt{s_{\mathrm{NN}}}$ = 8.16 TeV available with ALICE becomes intriguing.

Furthermore, understanding of the results in heavy-ion (AA) experiments is significantly dependent on comparing them with the results from smaller collision systems such as proton-proton (pp) or proton-nucleus (p−A). In terms of system size and the quantity of the produced particles, proton-nucleus (p−A) collisions serve as an intermediate scenario between proton-proton (pp) and nucleus-nucleus (A−A) collisions. At the LHC, the multiplicity of charged particles produced in p−A collisions reaches a level comparable to that in semi-peripheral Au−Au and Cu−Cu collisions at the RHIC such that the presence of final state dense matter effects cannot be ignored anymore in p−A collisions. Moreover, p−A collisions offer insights into the fundamental properties of QCD under conditions of exceptionally low fractional parton momentum (x) and high gluon densities [88]. In this regime, phenomena such as parton shadowing and saturation, explained in the framework of Color Glass Condensate (CGC), may also become apparent.

1.7 Organisation of thesis

This thesis investigates the production yield of Λ^* resonance in pp and p–Pb collisions at $\sqrt{s}$ = 8 TeV and $\sqrt{s_{\mathrm{NN}}}$ = 8.16 TeV, respectively with the ALICE detector. It also includes an analysis of various hadronic resonances and strange hadrons using the EPOS4 hydrodynamical model with and without hadronic afterburner. The work in this thesis has been structured into six chapters as follows:

Chapter 1 provides an overview of the SM of particle physics, emphasizing the discovery of the Higgs boson at the LHC in 2012 and introducing the QCD phase diagram. It discusses LHC, formation of hot and dense QGP medium, resonances in high-energy particle collisions, and outlines the motivation for the thesis which is to study the production yield of Λ^* resonance in pp and p–Pb collisions at $\sqrt{s}$ = 8 TeV and $\sqrt{s_{\mathrm{NN}}}$ = 8.16 TeV, respectively.

Chapter 2 delves into relativistic kinematics, which is required to understand the dynamics of high-energy particle collisions. It begins with four vectors and their properties, followed by a discussion about Lorentz transformation, which relates different reference frames in uniform motion relative to each other. The chapter further discusses key kinematic variables like rapidity, pseudorapidity and the invariant yield of the particles produced in high-energy nuclear collisions.

Chapter 3 begins with an overview of LHC in CERN and its four major experiments: ALICE, CMS, LHCb, and ATLAS. It focuses on the ALICE experiment, designed to study the QGP medium formed in heavy-ion collisions. The key subdetectors of the ALICE used in this analysis include the Inner Tracking System (ITS), Time Projection Chamber (TPC), Time-Of-Flight (TOF) and VZERO (V0A), which are used for tracking, particle identification and calculation of the multiplicity of collisions. Other detectors such as the Transition Radiation Detector (TRD) and Electromagnetic Calorimeter (EMCal) are also discussed, along with the data acquisition and processing infrastructure used in ALICE.

Chapter 4 delves into the techniques used to reconstruct the resonance Λ^*. The chapter provides details on how the invariant mass distribution of proton-kaon pairs is used to measure the Λ^* signal, while the combinatorial background is estimated by using similar signal and event mixing techniques. Subsequently, the chapter addresses the subtraction of this background, fitting the signal with a Voigtian function, and extracting the raw yield using the bin-counting method. Detector efficiency and acceptance are calculated using Monte Carlo simulations. In addition, the chapter explores methods to determine the systematic uncertainties associated with these measurements. It provides the corrected p_{T} spectra of Λ^* for inelastic pp collisions at $\sqrt{s}$ = 8 TeV and p–Pb collisions at $\sqrt{s_{\mathrm{NN}}}$ = 8.16 TeV, across various V0A multiplicity classes. Then it compares these spectra with the spectra at lower energy in the p–Pb system to analyze the energy dependence of the Λ^* p_{T} spectra. The discussion includes the p_{T}-integrated yield and the average p_{T} of Λ^*. Moreover, the nuclear modification factor (R_{pPb}) of Λ^* is calculated and compared with R_{pPb} of other hadrons such as Λ, K^{*0}, and ϕ. Finally, the chapter measures resonance to non-resonance particle yield ratios, suggesting the formation of a short-lived hadronic phase in p–Pb collisions at $\sqrt{s_{\mathrm{NN}}}$ = 8.16 TeV.

Chapter 5 explores the production of resonances and strange hadrons in pp collisions at $\sqrt{s}$ = 13.6 TeV and Pb–Pb collisions at $\sqrt{s_{\mathrm{NN}}}$ = 5.36 TeV using the EPOS4 hydrodynamic model, both with and without the UrQMD hadronic afterburner. The chapter provides an overview of the key concepts underlying EPOS4 and highlights its improvements over its predecessor, EPOS3. The chapter discusses various particle yield ratios to analyze the production of resonances and strange hadrons. The predictions for the hadronic phase lifetime in the EPOS4 model have been discussed and compared with existing ALICE data. Additionally, the simultaneous occurrence of strangeness enhancement and baryon-antibaryon annihilation processes is addressed.

Chapter 6 summarizes the key findings from the analysis of the Λ^* resonance using data from the ALICE detector in inelastic pp collisions at $\sqrt{s}$ = 8 TeV and p–Pb collisions at $\sqrt{s_{\mathrm{NN}}}$ = 8.16 TeV across various V0A multiplicity classes, and also provides a summary of the analysis of hadronic resonances and strange hadrons using EPOS4 with and without the UrQMD hadronic afterburner.

Chapter 2

Relativistic kinematics in high energy particle physics

2.1 Why high energies?

We present two justifications for the necessity of high energies for understanding matter at its fundamental level. The initial rationale stems from our desire to investigate elementary particles that behave as point-like entities. In order to achieve this, an extremely small de Broglie wavelength ($\lambda = h/p$) is required for the probing beam, where p denotes the momentum and h stands for Planck's constant. This concept can be interpreted by considering the resolution (Δr) of the probing beam, which is the distance between two elementary objects separated by a distance Δr [89]. The large momentum in the probing beam corresponds to enhanced resolution, enabling the exploration of finer structures and even probing quarks within the protons and neutrons.This is in analogy with the resolution offered by an optical microscope, as expressed by $\Delta r \approx \lambda / \sin\theta$, where θ denotes the angular aperture of the light beam used to view the structure of an object. The larger the angle θ and the smaller the wavelength λ of the incident beam, the finer the resolution achieved.

The second rationale that requires high energies in experimental particle physics is straightforward: There are many elementary particles that exhibit substantial mass, and the energy mc^2 required for their creation is correspondingly high. The heaviest elementary particle identified to date, the ’top’ quark (which must be produced as a pair with its antiparticle), possesses $mc^2 \approx 175,\mathrm{GeV}$, nearly 200 times the mass of a proton.

2.2 Units used in high energy physics

The fundamental units in physics (length, mass, and time) are conventionally expressed in the SI system as meters, kilograms, and seconds. However, these units are often impractical in the realm of high-energy physics, where typical lengths and masses are on the order of $10^{-15}\,\mathrm{m}$ and $10^{-27}\,\mathrm{kg}$, respectively. In high-energy physics, the unit of length commonly used is $femtometer$ or $fermi$, denoted as $1\,\mathrm{fm} = 10^{-15}\,\mathrm{m}$. For example, the root mean square radius of the charge distribution of a proton is $0.8\,\mathrm{fm}$. Similarly, the unit of energy in high-energy physics is the *gigaelectronvolt* (GeV), which is convenient because of its alignment with the typical mass-energy mc^2 of strongly interacting particles. For example, the rest-mass energy of a proton is $M_p c^2 = 0.938\,GeV$.

In high-energy physics calculations, the quantities $\hbar$ (reduced Planck constant) and c (speed of light) frequently appear, sometimes at high powers. To simplify these expressions, natural units are often employed. In natural units, Planck’s constant ($\hbar$), the speed of light (c), and the Boltzmann constant (k_B) are set to unity. The length and time scales are then expressed in units of GeV^{-1}, while the mass or energy are measured in GeV. To convert observables from SI units to natural units, a conversion factor is used: $\hbar c = 0.1975\,\mathrm{GeV\,fm}$.

2.3 Special Theory of Relativity and invariants

In the domain of high-energy physics, particles collide at relativistic speeds, resulting in the production of particles that are boosted along the beam direction. As a result, Special Theory of Relativity (STR) is necessary for explaining high-energy physics phenomena, which differ from low-energy physics that follows Newton’s laws in classical mechanics. The STR is based on two key principles:

- The velocity of light remains invariant in all inertial frames.

- Physical laws maintain their invariant form in any inertial frame of reference, necessitating expression in terms of Lorentz tensors within the mathematical domain.

In order to switch between different inertial frames, specific transformations are needed. Examples include the Galilean and Lorentz transformations. The Lorentz transformation is particularly important because it ensures that the speed of light remains constant in all inertial frames, making it the preferred transformation for transitions between these frames.

2.3.1 Lorentz transformation

Consider an inertial frame of reference S where the space coordinates of an event happening at time t are x, y, and z. If an observer is situated in a different inertial frame S', moving at a constant velocity v with respect to S (assumed to be in the $+x$ direction), they will observe the same event happening at time t' with coordinates x', y', and z'. The transformation between the measurements x, y, z, t and x', y', z', t' is precisely addressed by the Lorentz transformation. In the matrix form, the Lorentz transformation can be expressed as follows:

$$\begin{bmatrix} x^{0'} \\ x^{1'} \\ x^{2'} \\ x^{3'} \end{bmatrix} = \begin{bmatrix} \gamma & \beta\gamma & 0 & 0 \\ \beta\gamma & \gamma & 0 & 0 \\ 0 & 0 & 1 & 0 \\ 0 & 0 & 0 & 1 \end{bmatrix} \times \begin{bmatrix} x^0 \\ x^1 \\ x^2 \\ x^3 \end{bmatrix} \tag{2.1}$$

where, x^0, x^1, x^2, x^3 represent t, x, y, z in frame S, while the primed quantities ($x^{0'}$, $x^{1'}$, $x^{2'}$, $x^{3'}$) represent the same in frame S'. Furthermore, $\beta = v/c$ and $\gamma = \frac{1}{\sqrt{1-\beta^2}}$.

The matrix of equations presented here was first derived by the Dutch physicist H. A. Lorentz. He demonstrated that the fundamental formulae of electromagnetism exhibit physical consistency across all inertial frames only when these specific equations are used to make the transition. The full significance of Lorentz's findings became apparent several years later when Einstein made further revelations. Furthermore, it should be noted that the Lorentz transformation converges to the Galilean transformation in scenarios where the relative velocity v is considerably smaller than the speed of light. More details on the Lorentz transformations can be found in [89].

2.3.2 4-momentum vector

The relativistic equation relating the total energy E, the 3-momentum vector $\mathbf{p}$ (with Cartesian components p_x, p_y, p_z), and the rest mass m for a free particle is given by:

$$E^2 = p^2c^2 + m^2c^4 \tag{2.2}$$

or, in terms of natural units:

$$E^2 = p^2 + m^2 \tag{2.3}$$

The components p_x, p_y, p_z, E can be expressed as components of an energy–momentum 4-vector p_μ, where $\mu = 1,2,3,4$. In the Minkowski convention adopted in this text, the three momentum (or space) components are considered real, and the energy (or time) component is treated as imaginary:

$$p_1 = p_x, \qquad p_2 = p_y, \qquad p_3 = p_z, \qquad p_4 = \imath E$$

So that:

$$p^2 = \sum p_\mu^2 = p_1^2 + p_2^2 + p_3^2 + p_4^2 = \mathbf{p}^2 - E^2 = -m^2 \tag{2.4}$$

Thus, p^2 is a relativistic invariant, with a value of $-m^2$, where m is the rest mass that remains constant across all reference frames. The Minkowski notation for 4-vectors defines the metric, which is the square of the 4-vector momentum $p = (\mathbf{p}, \imath E)$:

metric = (4-momentum)^2 = (3-momentum)^2 – (energy)^2

In analogy to space-time components, the components $p_{x,y,z}$ of the 3-momentum are referred to as spacelike, while the energy component E is timelike. For the 4-momentum transfer q in a reaction ($q = p - p'$, where p and p' are the initial and final 4-momenta), the following cases arise:

$q^2 > 0$ is spacelike, for instance, in a scattering process,

$q^2 < 0$ is timelike, such as the squared mass of a free particle.

At times, to avoid dealing with negative quantities, redefinitions may be necessary. In deep inelastic electron scattering, q^2 is spacelike and negative, leading to the common practice of defining the positive quantity $Q^2 = -q^2$. This underscores the notion that the sign of the metric is a matter of convention and does not impact the physical results.

2.3.3 Comparative analysis of fixed target and colliding beam accelerators

Demonstrating the application of 4-vector notation, we explore the energy available for particle production in both fixed-target and colliding-beam accelerators. Let us consider an incident particle with mass m_A, total energy E_A, and momentum $\mathbf{p}_A$, colliding with a target particle of mass m_B, energy E_B, and momentum $\mathbf{p}_B$. The squared total 4-momentum of the system is expressed as:

$$p^2 = (\mathbf{p}_A + \mathbf{p}_B)^2 - (E_A + E_B)^2 = -m_A^2 - m_B^2 + 2\mathbf{p}_A \cdot \mathbf{p}_B - 2E_A E_B \qquad (2.5)$$

The center-of-mass system (CMS) is defined as the reference frame where the total 3-momentum is zero. If E^* denotes the total energy in the CMS, then $p^2 = -E^{*2}$. Assume that the target particle (m_B) is at rest in the laboratory system (LS), where $\mathbf{p}_B = 0$ and $E_B = m_B$, while E_A represents the energy of the incident particle in the LS. In this scenario:

$$E^{*2} = -p^2 = m_A^2 + m_B^2 + 2m_B E_A \qquad (2.6)$$

Consider the case where the incident and target particles move in opposite directions, as seen in an e^+e^- or $p\bar{p}$ collider. With p_A and p_B denoting the absolute values of the 3-momenta, the equation 2.5 becomes:

$$E^{*2} = -p^2 = 2(E_A E_B + p_A p_B) + (m_A^2 + m_B^2) \simeq 4E_A E_B \qquad (2.7)$$

This approximation holds for $m_A, m_B \ll E_A, E_B$, and it applies to a head-on collision scenario. Considering beams crossing at an angle θ, the equation 2.7 would become $E^{*2} = 2E_A E_B(1+\cos\theta)$. Remarkably, the center-of-mass energy available for new particle production in a collider with equal beam energies E increases linearly with E, approximated by $E^* \simeq 2E$. In contrast, for a fixed-target experiment, the center-of-mass energy increases as the square root of the incident energy ($E^* \simeq \sqrt{2m_B E_A}$). Consequently, the highest achievable energies for creating new particles are attained at colliding-beam accelerators. For example, the center-of-mass energy of the Tevatron $p\bar{p}$ collider at Fermilab is E^* = 2 TeV = 2000 GeV. To achieve the same center-of-mass energy with a fixed target accelerator, the energy of the proton beam that collides with a target nucleon would need to be $E_A = E^{*2}/(2m_B) \simeq 2 \times 10^6$ GeV = 2000 TeV. Thus, the Colliders, with their unique ability to bring particles into head-on collisions at lower energy thresholds, showcase remarkable efficiency in exploring new realms of particle interactions compared to the fixed-target experiments which necessitate significantly higher energy levels to attain comparable outcomes.

2.3.4 Rapidity variable

The rapidity variable, represented by the symbol y, is a dimensionless quantity that plays a crucial role in particle physics in the study of high-energy particle collisions where relativistic effects become significant. Unlike velocity or momentum, rapidity has a unique advantage: it adds up easily under Lorentz transformations when objects move at relativistic speeds. This property makes it particularly useful for studying different particles in various frames of reference. The formula for rapidity is,

$$y = \frac{1}{2}\ln\left(\frac{E+p_z c}{E-p_z c}\right) \tag{2.8}$$

where, E is the particle energy, p_z is the momentum component along the beam direction, and c is the speed of light.

When making a transition from CMS to LS, the rapidity distribution remains unchanged, except for a shift in the y-scale by an amount equal to y_{cm}. This property, expressed as

$y = y^* + y_{cm}$, emphasizes the consistency of the rapidity distribution between different reference frames. The rapidity of the center-of-mass in the LS, y_{cm}, is given by

$$y_{cm} = \frac{1}{2}\ln\left(\frac{1+\beta_{cm}}{1-\beta_{cm}}\right), \tag{2.9}$$

where, β_{cm} is the velocity of the center-of-mass in the LS.

The additivity of rapidity simplifies the description of particle dynamics in different reference frames. In non-relativistic scenarios, rapidity reduces to longitudinal velocity (β), highlighting its role as a relativistic measure of velocity. For rapidity distributions in symmetric and non-symmetric systems, let us take the example of two identical particles colliding in a symmetric system. Figure 2.1 shows the rapidity distribution of charged particles in central Pb–Pb collisions, recorded by ALICE at $\sqrt{s_{\rm NN}} = 5.02$ TeV [90]. In symmetric collisions like this, the rapidity distribution is typically balanced around the center-of-mass rapidity. However, in non-symmetric systems, where the colliding particles differ significantly in mass, the rapidity distribution becomes asymmetric [79]. Experimental analyses of rapidity distributions in various collision systems provide valuable insights into the dynamics of particle production and interactions at high energies.

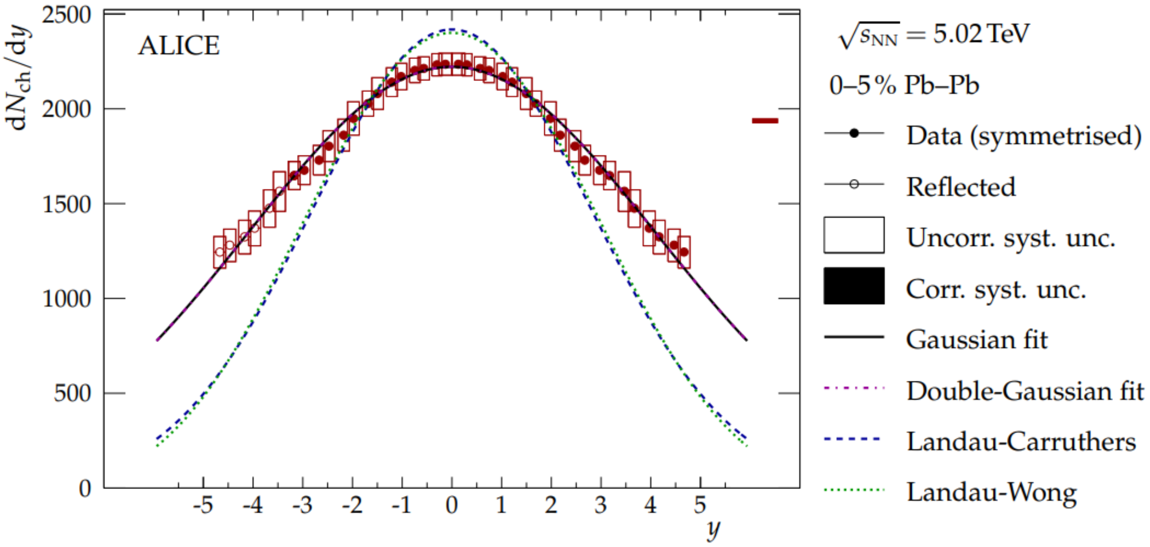

Figure 2.1: Estimate of $dN_{\rm ch}/dy$ in the most central (0–5%) Pb–Pb collisions at $\sqrt{s_{\rm NN}}$ = 5.02 TeV. Also shown are the Landau–Wong, Landau–Carruthers, Gaussian, and double–Gaussian distributions [90].

2.3.5 Pseudorapidity variable

Pseudorapidity is a concept used in particle physics to describe the angular distribution of particles in a high-energy collision system. Pseudorapidity, denoted by η, is defined in terms of the polar angle θ as:

$$\eta = -\ln\left[\tan\left(\frac{\theta}{2}\right)\right] \tag{2.10}$$

Pseudorapidity is also a dimensionless quantity like rapidity, making it a convenient parameter for describing particle trajectories in various collision experiments. The tangent function in the formula can take values between $-\infty$ and $+\infty$, and the natural logarithm (ln) of these values results in a pseudorapidity that spans the entire real number line. Particles close to the beam pipe, with θ near 0 or π, have pseudorapidities close to $-\infty$ and $+\infty$ respectively. This is a consequence of the mathematical properties of the pseudorapidity formula. The choice of pseudorapidity is motivated by its approximately invariant behavior under Lorentz boosts along the beam axis in the high-energy particle collisions which is advantageous particularly where relativistic effects become significant. Pseudorapidity is often used instead of rapidity because of its simpler geometric interpretation and ease of experimental measurement. Figure 2.2 presents the pseudorapidity distribution of charged particles in Pb–Pb collisions recorded with ALICE at $\sqrt{s_{\mathrm{NN}}}$ = 5.02 TeV [90]. In the region where $y \geq 0$, the rapidity distribution ($\frac{dN}{dy}$) and the pseudorapidity distribution ($\frac{dN}{d\eta}$), representing the p_{T}-integrated values (see Figures 2.1 and 2.2), are nearly identical. However, a small depression in the $\frac{dN}{d\eta}$ distribution compared to $\frac{dN}{dy}$ emerges around $y \approx 0$ and this dip is absent for massless particles such as photons.

In the CMS, where the distribution peaks at $y \approx \eta \approx 0$, the η-distribution is suppressed by a factor $\sqrt{1 - \frac{m^2}{\langle m_T^2 \rangle}}$. In the LS, where the maximum occurs around half of the beam rapidity ($\eta \approx y_b/2$), the suppression factor is $\sqrt{1 - \frac{m^2}{\langle m_T^2 \rangle}\cosh^2(y_b/2)}$, approximately equal to unity. Despite the frame of reference, the peak value of the pseudorapidity distribution is lower than the peak of rapidity distribution due to this suppression factor. In particular, at SPS energies, this suppression factor is approximately $\sim 0.8 - 0.9$. The dip in $\frac{dN}{d\eta}$ is attributed to the transformation from rapidity to pseudorapidity, introducing these effects

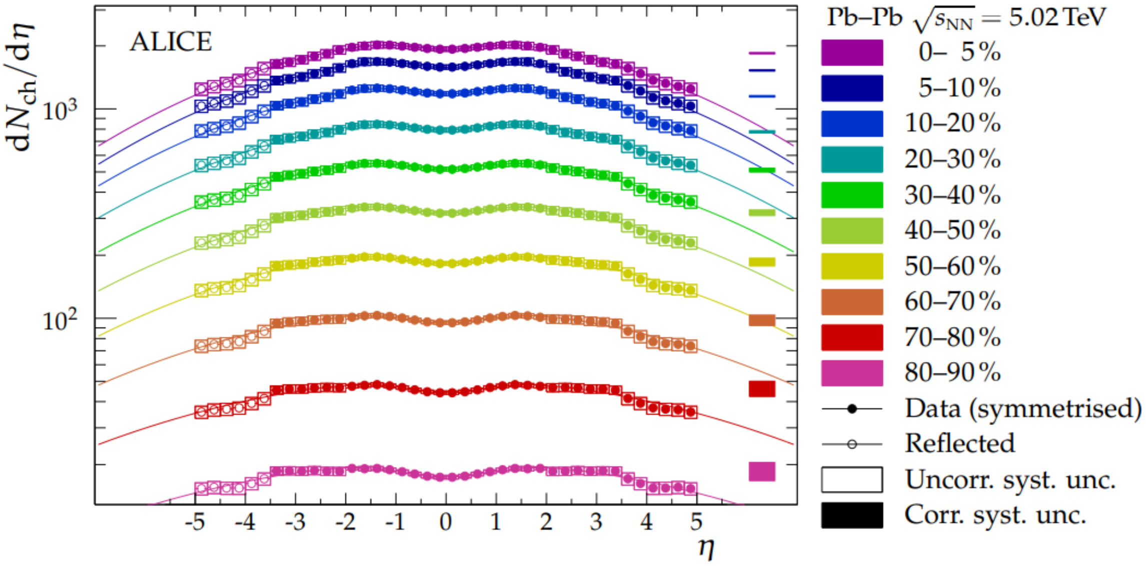

Figure 2.2: The charged particle pseudorapidity density distribution in Pb–Pb collisions at $\sqrt{s_{NN}} = 5.02$ TeV for ten centrality classes. Data points, representing total uncertainties, are enclosed in boxes, while filled squares indicate correlated uncertainties (evaluated at $\eta = 0$). Statistical errors, smaller than markers, are deemed insignificant. Values in $3.5 < \eta < 5$ are reflected around $\eta = 0$ (open circles). The line corresponds to fits of the difference between two Gaussians centered at $\eta = 0$ [90].

in the distribution. Moreover, it is observed from Figure 2.2 that the production of charged particles increases with the centrality of the collisions.

2.3.6 Invariant mass

The invariant mass of a system of particles is an important concept in particle physics, providing a measure of the total mass of a system that remains unchanged, regardless of the reference frame in which it is measured. It is calculated from the energy and momentum of the particles involved using the relation:

$$M^2 = E_i^2 - \mathbf{p}_i^2$$

where, E_i and $\mathbf{p}_i$ are the energy and momentum of the individual particles, respectively, and the sums are taken over all particles in the system.

Invariant mass is particularly useful in high-energy physics experiments, such as those conducted at particle colliders, because it allows for the identification of resonances and other short-lived particles that do not reach the detector's active material. When particles decay, their invariant mass can be reconstructed by adding the four-momentum vector of decay products, providing insights into the properties of the parent particles. For example, in the study of the $\mathrm{K}^*(892)^0$ resonance, the invariant mass of the decay products (typically a kaon and a pion) is analyzed to identify the presence of $\mathrm{K}^*(892)^0$ and to study its properties, such as its mass and width. By studying the invariant mass distributions of various particles, physicists can gain valuable information about the underlying processes and interactions occurring within the system.

2.3.7 Invariant yield

In high-energy particle collisions, measurement of particle yield is a fundamental aspect of understanding the underlying physics. The quantity used to serve this purpose is the invariant yield, an important concept in relativistic physics that remains invariant under Lorentz transformations. It provides a robust measure of particle production, accounting for relativistic effects.

The invariant yield ($E\frac{d^3N}{dp^3}$) is obtained by integrating over the azimuthal angle (ϕ), where ϕ is defined as $\tan^{-1}(p_y/p_x)$. This expression is further simplified using relationships such as $dp_x dp_y = dp_\mathrm{T}$ and $dy = dp_z/E$. The mathematical formulation is versatile, allowing the invariant yield to be expressed in terms of transverse momentum (p_T) or transverse mass ($m_T = \sqrt{p_\mathrm{T}^2 + m^2}$) experimentally.

$$E\frac{d^3N}{dp^3} = E\frac{d^3N}{dp_x dp_y dp_z} = E\frac{d^3N}{p_\mathrm{T} dp_\mathrm{T} d\phi dp_z} = \frac{d^3N}{p_\mathrm{T} dp_\mathrm{T} d\phi dy} = \frac{1}{2\pi}\frac{d^2N}{p_\mathrm{T} dp_\mathrm{T} dy} \tag{2.11}$$

In experimental settings, this translates into expressions like:

$$E\frac{d^3N}{dp^3} = \frac{1}{2\pi N_\mathrm{evt}}\frac{d^2N}{p_\mathrm{T} dp_\mathrm{T} dy} = \frac{1}{2\pi N_\mathrm{evt}}\frac{d^2N}{m_\mathrm{T} dm_\mathrm{T} dy} \tag{2.12}$$

where, N_evt represents the number of events, and N is the total number of particles produced.

These formulations help us to describe the invariant yield in terms of experimentally measurable quantities. The concept of invariant yield provides a common framework for comparing results across different collision experiments. Understanding the invariant yield is key to reveal the properties of matter under extreme conditions. It provides insights into the temperature, density, and thermodynamic properties of the created medium, while also helping probe particle production mechanisms and explore the nuclear matter phase diagram.

2.4 Particle decay

Consider the simple case of a particle that decays into two particles and calculate the various quantities involved. For a reaction of the type:

$$M \to A + B$$

i.e., a particle of mass M disintegrates into particles A and B with masses m_A and m_B, respectively. In the zero-momentum frame (where the initial and final momentum of the system is zero), $\vec{p}_A = -\vec{p}_B$, and thus $p_A^2 = p_B^2$. If E_A and E_B are the energies of the emergent particles in the considered frame, then for the decay process:

$$M = E_A + E_B \tag{2.13}$$

Clearly, if $M > m_A + m_B$, the particle fragments spontaneously; otherwise, for the case $M < m_A + m_B$, an amount of energy equal to or greater than the mass difference of the products and the particle is required to cause the fragmentation. This energy is called the binding energy. To calculate the energies of the product particles E_A and E_B, use $p_A^2 = p_B^2$ and substitute for each momentum $E^2 - m^2$:

$$E_A^2 - m_A^2 = E_B^2 - m_B^2 \tag{2.14}$$

Solving equations 2.13 and 2.14 for E_A and E_B, we get the following:

$$E_A = \frac{M^2 + m_A^2 - m_B^2}{2M}, \; E_B = \frac{M^2 + m_B^2 - m_A^2}{2M} \tag{2.15}$$

These equations ensure that both energy and momentum are conserved in the decay process and are particularly useful because they provide a straightforward method to calculate the individual energies of the decay products directly from their masses and the mass of the parent particle. This is very useful in high-energy physics experiments for identifying particles and understanding the dynamics of decay processes.

2.4.1 Decay rate

To calculate the decay rate or lifetime of a particle that decays into two daughter particles, the process is statistically modeled so that at any instant, the number of particles decaying is proportional to the number of particles remaining. Based on this assumption, we have

$$-\frac{dN(t)}{dt} \propto N(t) \tag{2.16}$$

and upon integration, the expression becomes:

$$N(t) = N_0 e^{-\frac{t}{\tau}} \tag{2.17}$$

where τ is the lifetime of the particle, and its inverse $\Gamma = \frac{1}{\tau}$ is called the decay rate. The lifetime of a particle is defined in its proper reference frame, which is the frame attached to the particle itself, measuring the proper time. In a boosted frame of reference, the lifetime of a particle appears to be longer because of time dilation.

A classic example of this phenomenon is the observation of cosmic-ray muons in the upper atmosphere. Muons have a proper lifetime of approximately 2.2 μs [91]. However, because of their high velocities, time dilation allows them to travel considerable distances before decaying, enabling them to reach the Earth's surface. Another example is the neutral kaon (K^0), which exhibits different lifetimes for its short-lived (K_S^0) and long-lived (K_L^0) states. The K_L^0 has a proper lifetime of about 51 ns [91], but in high-energy collisions, the time dilation effect can significantly extend its observed lifetime.

2.4.2 Breit-Wigner's non-relativistic formula

The wave function of a particle that decays according to the exponential law described in equations 2.16 and 2.17 is expressed as:

$$\psi(t) = \psi(0)e^{-\Gamma t/2} \tag{2.18}$$

The square modulus of this wave function, which represents the probability density, is:

$$|\psi(t)|^2 = |\psi(0)|^2 e^{-\Gamma t} \tag{2.19}$$

To determine the energy dependence of these states, we perform a Fourier transform with respect to the angular frequency ω, converting it to energy space:

$$\psi(E) = \int \psi(t)e^{iEt}\,dt = \frac{K}{(E-M)-i\Gamma/2} \tag{2.20}$$

In this context, K is a constant and M represents the mass or the central value of the energy (due to Einstein's mass-energy equivalence). The energy dependence of the decay rate is thus given by:

$$|\psi(E)|^2 \propto \frac{1}{(E-M)^2+(\Gamma/2)^2} \tag{2.21}$$

More generally, the Breit-Wigner formula is derived from the analysis of three-dimensional scattering theory using partial-wave analysis. The l-th partial wave amplitude is given by:

$$a_l = e^{i\delta_l}\sin\delta_l = \frac{1}{\cot\delta_l - i} \tag{2.22}$$

This expression is known as the optical theorem. In this case, the phase shift $\delta_l = \pi/2$ when the energy E equals the central energy value M. Expanding $\cot\delta_l$ in a Taylor series results in the same form as in equation 2.20. The contribution of each component of the angular momentum (partial wave) to the scattering amplitude is described by equation 2.21. This is essential for analyzing and predicting the results of scattering experiments. The phase shift $\delta_l = \pi/2$ at energy $E = M$ indicates a resonance, a peak in the scattering cross-section at a particular energy. Understanding phase shifts helps to identify resonances and study their properties. The Breit-Wigner's formula (equation 2.21) describes the shape of resonances, providing information about their width (related to Γ) and central energy M. These formulas are used to fit experimental data, allowing physicists to extract parameters such as masses, lifetimes, and decay rates of short living particles or resonances.

Chapter 3

The ALICE experiment at the LHC

The Large Hadron Collider (LHC) exemplifies human creativity and collaborative effort, standing as a peak in particle physics research. Constructed from 1998 to 2008 by CERN in collaboration with global institutions, the LHC is more than just a machine; it symbolizes global collaboration in the quest for scientific understanding. Since its 2009 launch, this engineering marvel has accelerated proton and lead (Pb) ion beams to center-of-mass collision energies up to 13.6 TeV for proton-proton and 5.36 TeV for Pb-Pb collisions, enabling pioneering experiments that explore the universe's earliest stages. Among the four main experiments at the LHC, the A Large Ion Collider Experiment (ALICE) is dedicated to study the physics of strongly interacting matter under extreme temperature and energy density conditions that result from heavy-ion collisions. This chapter presents an overview of the LHC and its key experiments, alongside a concise description of the experimental setup within the ALICE detector and its sub-detectors. Additionally, a brief examination of the online and offline computing systems used for data analysis is included.

3.1 The Large Hadron Collider (LHC)

The Large Hadron Collider (LHC) is an extraordinary engineering achievement, situated underground on the France-Switzerland border near Geneva. It forms a massive ring over 27 kilometers in circumference and descends to depths between 50 and 175 meters below the ground. The LHC's core components include a series of powerful superconducting magnets and accelerating structures that elevate particle energies. The CERN accelerator complex, illustrated in Figure 3.1, stands as the epicenter of this groundbreaking technology and research. This complex comprises various accelerator systems such as the Super Proton Synchrotron (SPS), Proton Synchrotron (PS), Antiproton Decelerator (AD), CERN Linear Electron Accelerator for Research (CLEAR), Advanced WAKefield Experiment (AWAKE), Isotope mass Separator On-Line DEvice (ISOLDE), Low Energy Ion Ring (LEIR), and LINer ACcelerator (LINAC). These systems synergize to elevate particle energy before feeding them into the colossal LHC ring, reaching unprecedented energy levels. Protons for the proton-proton (pp) collisions derive from hydrogen gas, which, when subjected to an electric field, loses electrons, leaving only protons. Starting at LINAC2, the protons achieve an energy of 50 MeV, then proceed through the PS Booster (PSB), Proton Synchrotron (PS), and Super Proton Synchrotron (SPS), incrementally increasing their energy to 450 GeV. Eventually, they enter the LHC rings, circulating in both directions, where their energy is augmented for collisions. Likewise, the lead (Pb) ion beam originates from heated lead vapor at 500°C, derived from a pure 2 cm, 500 mg lead sample. Electric fields remove some electrons, forming Pb ions. These ions are initially accelerated by LINAC 3 to 4.2 MeV per nucleon and further stripped of electrons within the same accelerator. The ions then move to the Low Energy Ion Ring (LEIR), reaching 72 MeV per nucleon. These initial stages are specific to heavy-ion collisions. The Pb ions continue their acceleration in the PS and SPS, where, in the PS, their energy increases to 5.9 GeV per nucleon, with any remaining electrons removed. In the SPS, the Pb beam is further upgraded to 177 GeV per nucleon before being injected into the LHC ring to travel in both directions. In Figure 3.2, Points 2 and 8 are marked as injection points where particles are introduced into the LHC ring, each allowing movement in a different direction. The acceleration of the particle beam occurs at Point 4 using the Radio Frequency (RF) system. The main experiments—ATLAS, ALICE, CMS, and LHCb—are positioned at locations 1, 2, 5, and 8, the intersections of the two beams. At Points 3 and 7, the collimation system acts to purify the beam by removing beam bunches that are significantly offset from the center. The beam dumping is executed at Point 6. Figure 3.2 shows a schematic view of the operational points within the LHC. Currently,

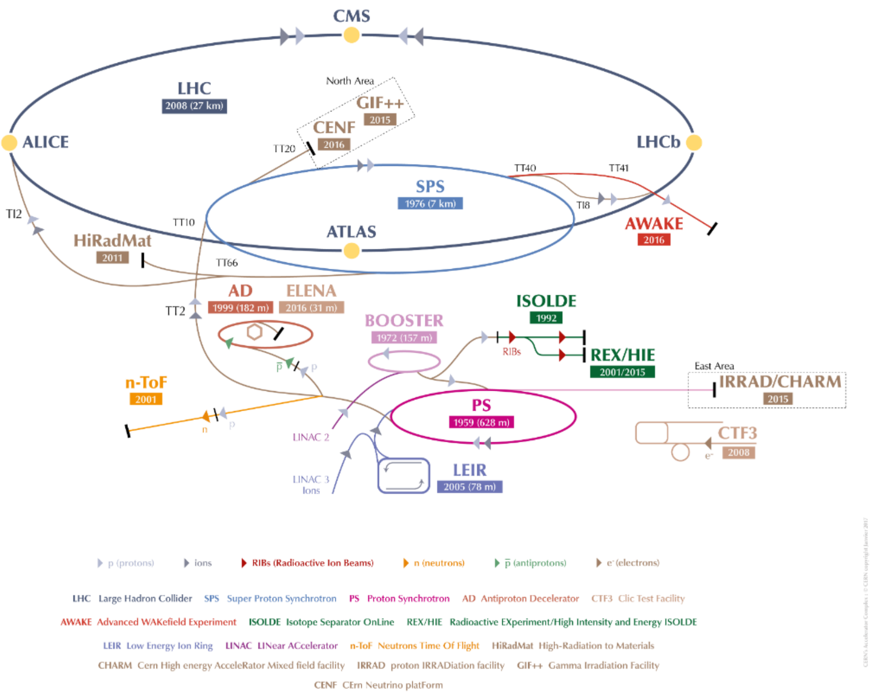

Figure 3.1: The CERN accelerator complex, alongside the locations of the PS and SPS, features four significant LHC experiments—ALICE, CMS, LHCb, and ATLAS—situated around the LHC ring [92].

the LHC's accelerator infrastructure can achieve a maximum center-of-mass energy of 14 TeV for pp collisions and 5.5 TeV per nucleon for heavy-ion collisions.

3.2 The ALICE experiment

The ALICE experiment is primarily dedicated to exploring heavy-ion physics within the LHC environment. It is specifically engineered to examine the properties of strongly interacting matter under extreme temperature and energy density conditions, leading to the formation of quark-gluon plasma (QGP). Although ALICE serves as a general purpose detector, its core objective is to analyze the QGP characteristics. The ALICE apparatus, which measures 26 meters in length, 16 meters in height, and 16 meters in width, has an approximate weight of 10,000 tons. It is situated within a spacious cavern approximately 56 meters below the surface close to the St Genis-Pouilly village in France and features 19 sub-detectors, as depicted in Figure 3.3. With remarkable tracking and particle identification (PID) capabilities over a broad momentum range ($10^{-2} - 10^{2}$ GeV/c), the ALICE

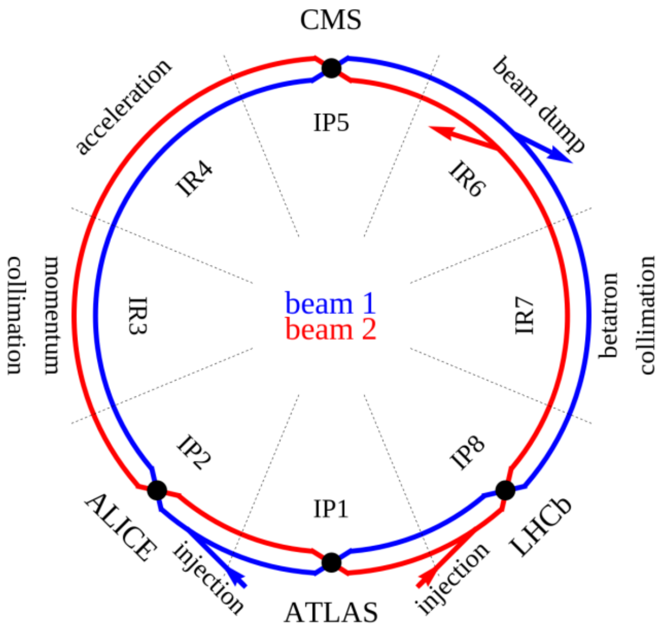

Figure 3.2: Schematic view of LHC accelerator complex [93].

detector enables the study of phenomena ranging from soft physics to the generation of jets and high-p_{T} particles. Furthermore, it is expertly built to accommodate high densities of charged particle multiplicity, notably observed at mid-pseudorapidity in central Pb–Pb collisions, which can surpass conventional proton-proton (pp) interactions by as much as three orders of magnitude at identical energy levels. In addition, this particle multiplicity can be between two and five times greater than the highest multiplicities recorded at the RHIC.

The ALICE detector employs a specific coordinate system that is important for precisely mapping particle paths and interactions within the device. It adopts a right-handed system, with its origin at the nominal interaction point (0,0,0). The z-axis, serving as its primary axis, runs parallel to the beam direction, extending through the beam pipe, with its positive direction facing away from the muon spectrometer. The x-y plane, positioned perpendicularly to the z-axis, defines the transverse plane, where the x-axis is directed towards the center of the LHC ring, and the y-axis points vertically upwards. The azimuthal angle (ϕ) is measured relative to the x-axis, while the polar angle (θ) is determined from the z-axis towards the x-y plane. The ALICE detector encompasses three major parts: the central barrel detectors, forward detectors, and the muon spectrometer. Key components such as the ITS, TPC, TOF, and V0 within the central barrel detectors are pivotal in the analysis discussed in this thesis. The following sections provide succinct overviews of these along with other sub-detectors. Furthermore, Table 3.1 presents comprehensive details regarding the position, η, and ϕ acceptance, and the functions of the ALICE detector subsystems.

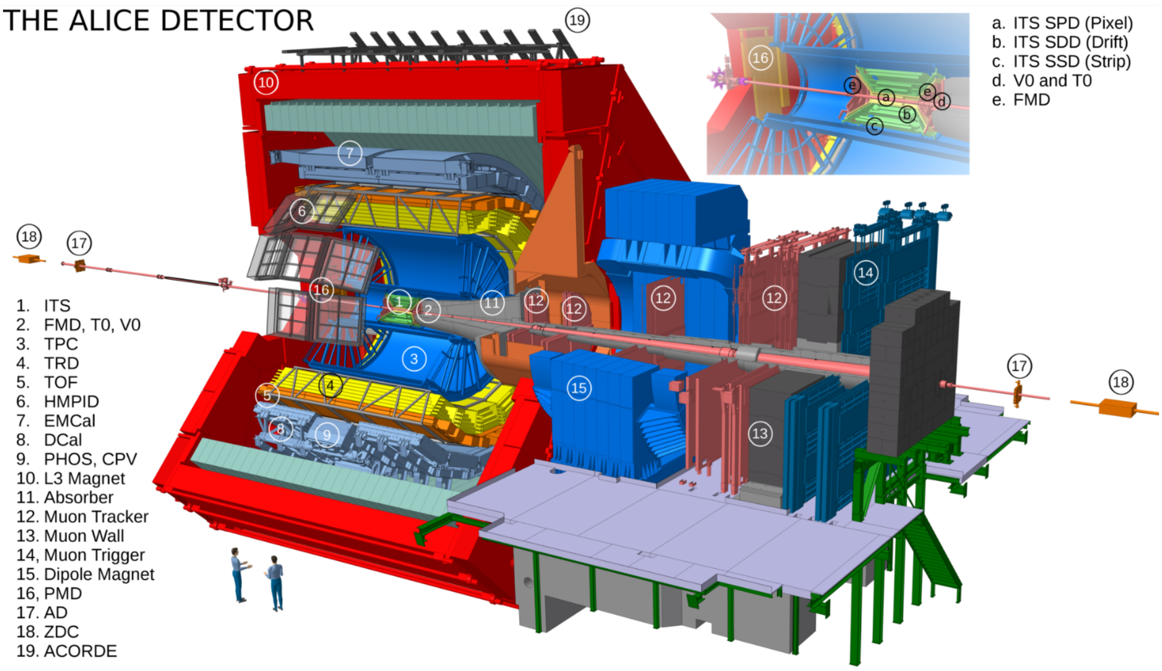

Figure 3.3: Schematic diagram illustrating the ALICE detector systems [94].

3.2.1 Central barrel detectors

3.2.1.1 Inner Tracking System (ITS)

The Inner Tracking System (ITS) serves as the innermost segment of the ALICE experiment, consisting of six layers of cylindrical silicon detectors that surround the beam pipe within the central barrel, as depicted in Figure 3.4. The very first layer is set 3.9 cm away from the nominal beam line, while the outermost layer is positioned 43 cm from this axis. Designed for both lightness and fragility, the ITS utilizes lightweight materials. It uses three separate technologies, pixel, drift and strip, with two layers each: namely the Silicon Pixel Detector (SPD), Silicon Drift Detector (SDD) and Silicon Strip Detector (SSD), covering the pseudorapidity range $|\eta| < 0.9$. The key purpose of the ITS is to accurately reconstruct primary and secondary vertices with resolutions better than 100 μm, thus boosting the tracking capabilities of ALICE around the interaction point. Furthermore, ITS helps

Table 3.1: Summary of the positions, η and ϕ acceptances and purposes of ALICE detector subsystems [95]

Detector	Position (in *cm*)	η acceptance	ϕ acceptance (in ^{o})	Purpose
Central barrel detector				
SPD	r= 3.9	$\|\eta\| < 2.0$	$0^o < \phi < 360^o$	tracking, vertex
	r= 7.6	$\|\eta\| < 1.4$	$0^o < \phi < 360^o$	tracking, vertex
SDD	r= 15.0	$\|\eta\| < 0.9$	$0^o < \phi < 360^o$	tracking, particle identification
	r= 23.9	$\|\eta\| < 0.9$	$0^o < \phi < 360^o$	tracking, particle identification
SSD	r= 38.0	$\|\eta\| < 1.0$	$0^o < \phi < 360^o$	tracking, particle identification
	r= 43.0	$\|\eta\| < 1.0$	$0^o < \phi < 360^o$	tracking, particle identification
TPC	$85 < r < 247$	$\|\eta\| < 0.9$	$0^o < \phi < 360^o$	tracking, particle identification
TRD	$290 < r < 368$	$\|\eta\| < 0.8$	$0^o < \phi < 360^o$	tracking, $e^{\pm}$ identification
TOF	$370 < r < 399$	$\|\eta\| < 0.9$	$0^o < \phi < 360^o$	particle identification
PHOS	$460 < r < 478$	$\|\eta\| < 0.12$	$220^o < \phi < 320^o$	photons
EMCAL	$430 < r < 455$	$\|\eta\| < 0.7$	$80^o < \phi < 187^o$	photons
HMPID	$r = 490$	$\|\eta\| < 0.6$	$1^o < \phi < 59^o$	particle identification
ACORDE	$r = 850$	$\|\eta\| < 1.3$	$30^o < \phi < 150^o$	cosmics
Forward detector				
PMD	$z = 367$	$2.3 < \eta < 3.9$	$0^o < \phi < 360^o$	photons
FMD	$z = 320$	$3.6 < \eta < 5.0$	$0^o < \phi < 360^o$	charged particles
	$z = 80$	$1.7 < \eta < 3.7$	$0^o < \phi < 360^o$	charged particles
	$z = -70$	$-3.4 < \eta < -1.7$	$0^o < \phi < 360^o$	charged particles
V0	$z = 329$	$2.8 < \eta < 5.1$	$0^o < \phi < 360^o$	charged particles
	$z = -88$	$-3.7 < \eta < -1.7$	$0^o < \phi < 360^o$	charged particles
T0	$z = 370$	$4.6 < \eta < 4.9$	$0^o < \phi < 360^o$	time, vertex
	$z = -70$	$-3.3 < \eta < -3.0$	$0^o < \phi < 360^o$	time, vertex
ZDC	$z = \pm 11300$	$\|\eta\| > 8.8$	$0^o < \phi < 360^o$	forward neutrons
ZDC	$z = \pm 11300$	$6.5 < \|\eta\| < 7.5$	$\|\phi\| < 10^o$	forward protons
ZDC	$z = \pm 730$	$4.8 < \eta < 5.7$	$\|2\phi\| < 32^o$	photons
Muon spectrometer				
MCH	$-1420 < z < -540$	$-4.0 < \eta < -2.5$	$0^o < \phi < 360^o$	muon tracking
MTR	$-1710 < z < -1610$	$-4.0 < \eta < -2.5$	$0^o < \phi < 360^o$	muon trigger

to track and classify charged particles with a low threshold p_{T} (p_{T} = 80 MeV/c), while improving momentum resolution at high p_{T}, and allowing more precise determinations of momentum and angle in the time projection chamber detector (TPC).

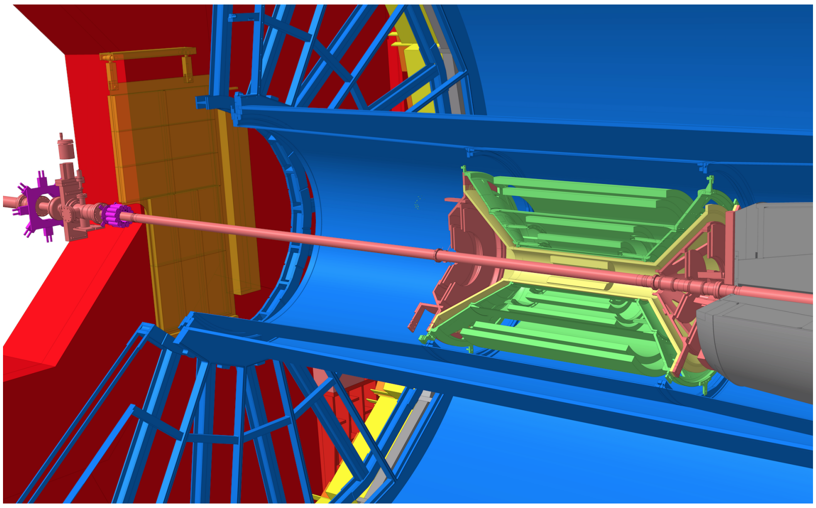

Figure 3.4: Systematic representation of the Inner Tracking System (ITS) detector within the ALICE experiment [96].

The primary component of the ALICE SPD is a ladder, which includes a matrix of pixel detectors that is flip-chip bonded to 8 front-end chips. Each pixel detector matrix contains 256 × 256 individual cells, each cell measuring 50 μm in the $r\phi$ direction and 300 μm in the z direction. The dimensions of this detector ladder are 13.8 mm ($r\phi$) by 82 mm (z). The use of high granularity allows for accurately determining the positions of charged tracks passing through the detector. The SPD's inner and outer layers are situated 3.9 cm and 7.6 cm from the beam axis, respectively, and extend 282 mm along the beam's length. To protect the heat-sensitive SDD layers, an Al-coated carbon fiber external shield encases the SPD barrel. The SDDs themselves are installed on linear supports known as ladders, with radial placements ranging from 14.9 cm to 23.8 cm from the beam axis, and extending 443 mm to 593 mm in the z direction, respectively. The inner layer comprises 14 ladders while the outer layer has 22. Each ladder supports six detectors for the inner layer and eight for the outer layer, ensuring complete coverage for particles produced from the vertices within the interaction region $\pm 1\sigma$. Much like in gaseous drift detectors, the ionization-induced charged cloud drifts at a constant speed within an electric field, facilitating the measurement of impact-point coordinates. Low-capacitance readout anodes are used to ensure excellent energy resolution. The SSD detectors consist of double layers of silicon strips, with layer 5 containing 782 strips and layer 6 containing 988 strips, aligned at a stereo angle of 35 *mrad*. As a result, a particle passing through any SSD layer triggers signals in both strip layers, allowing for detection at the intersection point. The information about energy loss (dE/dx) is obtained from the charge carriers gathered in the SSD. Each strip is 40 mm long and tilted at an angle of 17.5 *mrad* relative to the detector's short edge, which supports the formation of a stereo pair for reconstructing 2D track positions. The SSD layers are situated 38 cm (inner) and 43 cm (outer) away from the beam axis, with longitudinal extents of 86 cm and 98 cm, respectively. Figure 3.5 illustrates the energy loss by various particles as they move through the active material of the ITS.

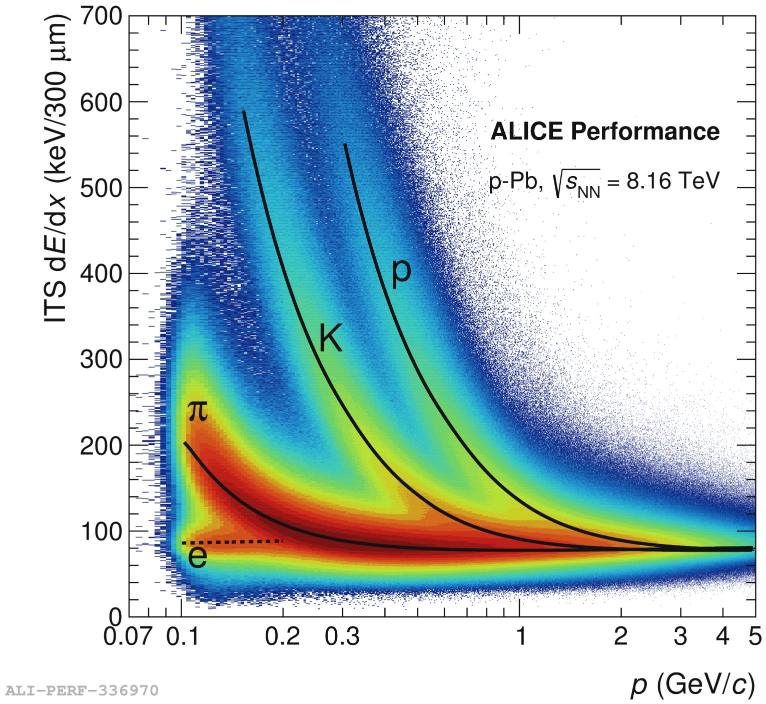

Figure 3.5: The energy loss (dE/dx) of particles traversing the Inner Tracking System (ITS) detector is depicted as a function of momentum in p–Pb collisions at $\sqrt{s_{NN}}$ = 8.16 TeV. Theoretical predictions are represented by solid lines [97].

3.2.1.2 Time Projection Chamber (TPC)

The Time Projection Chamber (TPC), a primary detector in the ALICE central barrel, is important for identifying and tracking charged particles. Figure 3.6 shows a 3D representation of the TPC's field cage. By integrating charged particle track data from the TPC, ALICE

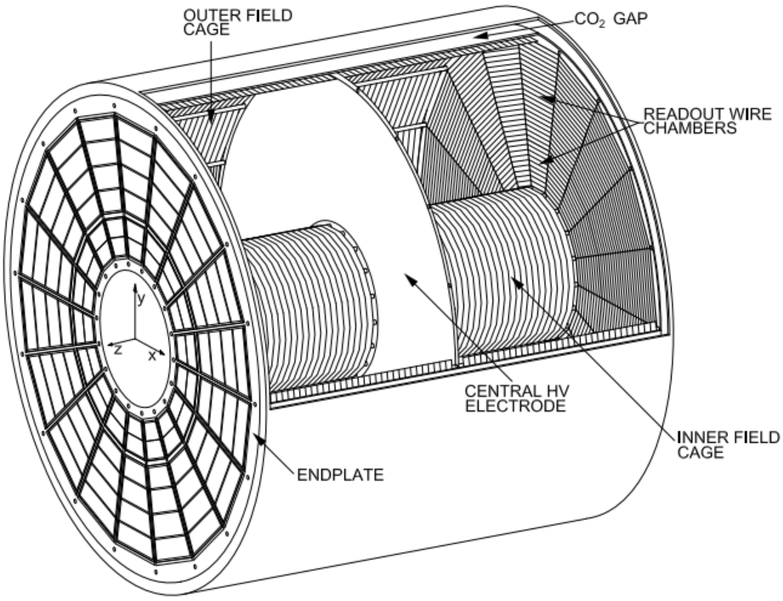

Figure 3.6: The three-dimensional representation of the TPC field cage depicts the high voltage electrode situated centrally within the drift region. Illustrated are the endplates, each comprising 18 sectors and featuring 36 readout chambers at both ends [98].

Transition Radiation Detector (TRD), and the ITS, studies on vector meson resonances and ‘charm’ and ‘beauty’ particles through their leptonic decay channels are feasible. The TPC features a cylindrical shape and is filled with a conductive gas mix of $\mathrm{Ne}-\mathrm{CO}_2-\mathrm{N}_2$. Its inner and outer radii measure 85 and 250 cm, respectively. The TPC is situated within a 0.5 T solenoidal magnetic field aligned with the beam axis, facilitated by the L3 solenoidal magnet. The TPC consists of two drift regions divided by a central high-voltage (HV) electrode situated axially. This electrode is charged to 100 kV and, together with voltage-dividing networks on both the inner and outer surfaces of the cylinder, creates an axial electric field of 400 V/cm. The TPC covers the pseudo-rapidity range $|\eta| < 0.9$ and the full azimuthal (2π) angle, allowing gas ionization along the paths of charged particles in its active volume. The ionized electrons produced drift towards the endplate of the cylinder due to the electric field. By measuring precise cylindrical plane coordinates at the endplates, the trajectory of charged particles is accurately reconstructed. This trajectory is inferred from detailed measurements of the arrival time in relation to the LHC beam collision and the cylindrical coordinates. The TPC distinguishes charged particles by assessing their specific ionization loss $(\mathrm{d}E/\mathrm{d}x)$ and momentum in the gas, using $\mathrm{d}E/\mathrm{d}x$ to differentiate between particle types.

For reliable $\mathrm{d}E/\mathrm{d}x$ measurements, it counts the number of clusters (n_{cl}) associated with the track, requiring $n_{cl} > 50$ from a maximum of 159 rows of TPC pads. The mean energy loss of charged particles is described by the Bethe-Bloch equation. For heavy charged particles, the Bethe-Bloch equation is given by

$$-\mathrm{d}E/\mathrm{d}x = \frac{4\pi e^4}{m_0}\frac{z^2}{v^2} N Z \ln\left\{\frac{2m_0 v^2\gamma^2}{I} - \beta^2 - \delta^2 - \frac{2C}{Z}\right\} \tag{3.1}$$

where,

$z =$ Charge of the primary particle

$m_0 =$ Rest mass of the electron

$v =$ Velocity of charged particle

$N =$ Number density of absorber material

$Z =$ Atomic number of the absorber material

$I =$ Mean excitation potential

$\beta = v/c$, $c =$ Velocity of light

$\gamma = \frac{1}{\sqrt{1-\beta^2}}$

$\delta =$ Density correction factor

$C =$ Shell correction factor

Electrons and positrons, due to their relatively low masses, follow a unique pattern described by a modified Bethe-Bloch equation, in which bremsstrahlung predominates as the primary mechanism of energy loss. The energy loss ($\mathrm{d}E/\mathrm{d}x$) is expressed as a function of momentum for certain charged particles, as shown in Figure 3.7. Within the TPC, charged particles are distinctly identifiable at low momenta, yet differentiation becomes difficult at intermediate and high momentum levels. To aid in particle identification at moderate momentum, data from the Time-Of-Flight (TOF) detector is used.

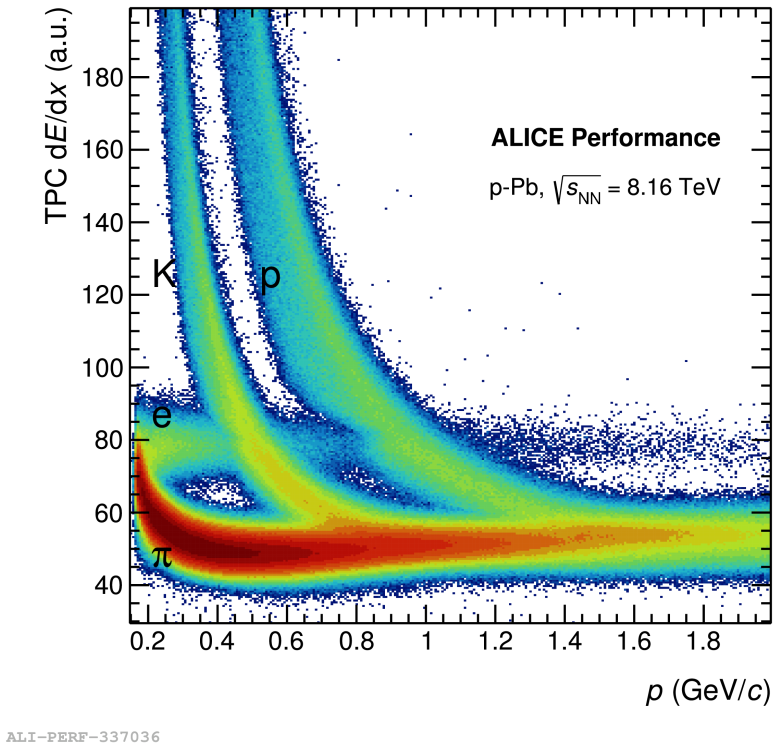

Figure 3.7: The energy loss (dE/dx) of particles in the TPC, plotted against momentum in p–Pb collisions at $\sqrt{s_{\mathrm{NN}}}$ = 8.16 TeV [99].

3.2.2 Transition Radiation Detector (TRD)

The Transition Radiation Detector (TRD) is an essential element of ALICE, tasked with identifying and triggering on electrons and jets, delivering a rapid trigger decision in about 7 microseconds. Designed to identify electrons with momenta above 1 GeV/c, it excels at differentiating electrons from pions, achieving a 90% electron efficiency [100, 101]. The TRD structure is made up of 522 detectors spread over 18 azimuthal sectors, each sector containing 5 stacks of 6 layers, forming a cylindrical shape approximately 7 meters in both diameter and length. Using a gas mixture of xenon and CO_2, the TRD improves the identification of electrons within the central barrel of the ALICE, especially for particles with transverse momentum (p_{T}) above 1 GeV/c, where the electron-pion separation ability diminishes. By detecting transition radiation from charged particles passing through, the TRD significantly improves the reconstruction of both light and heavy vector mesons. Its provision of spatially resolved space points ($\sim 600\,\mu m$ resolution) enables track extension beyond the TPC, enhancing momentum resolution. The TRD's configuration inside the ALICE central barrel, shown in Figure 3.8, outlines its inner and outer radii from the beam axis at 290 cm and 368 cm, respectively, encompassing the TPC. It consists of 540 modules over 18 sectors (super-modules), each featuring a 4.8 cm thick radiator and a multi-wire proportional chamber. Covering the complete azimuth within the mid-rapidity region ($-0.84 < \eta < 0.84$), and offering a quick response, the TRD effectively triggers on charged particles. It is particularly useful for particles with Lorentz factors (γ) greater than 1000, allowing effective separation of electrons from pions for momenta between 1 and 100 GeV/c.

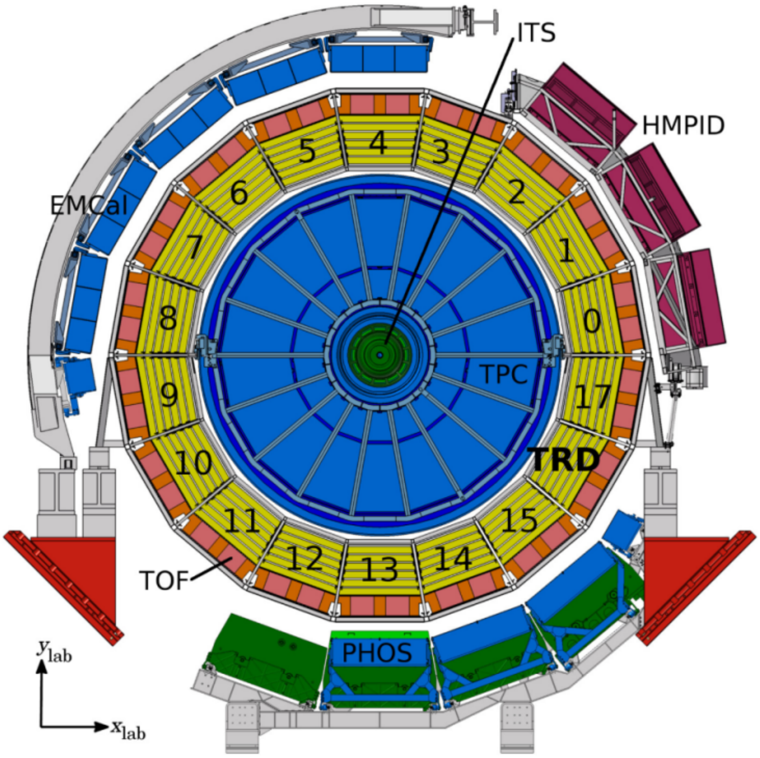

Figure 3.8: Illustrative cross-sectional view of the ALICE central barrel detector, oriented perpendicular to the LHC beam path [102].

3.2.2.1 Time-Of-Flight (TOF)

The Time-Of-Flight (TOF) detector is pivotal for identifying particles within the low to intermediate transverse momentum range. This cylindrical gas detector consists of Multigap Resistive Plate Chambers (MRPCs) [103]. The detector spans an area of 150 m^2 and is filled with a gas mixture made up of 90% $C_2H_2F_4$, 5% C_4H_{10}, and 5% SF_6. Each MRPC is constructed with a ten-layer double-stack configuration and achieves a time resolution of roughly 40 ps. Arranged into 18 sectors within a cylindrical layout, these MRPCs surround the transition radiation detector (TRD). The TOF has an inner radius of 3.7 m, an outer radius of 3.99 m, and provides coverage for $|\eta| < 0.9$ with a ϕ acceptance of 2π. Upon a charged particle's passage through the TOF detector, it ionizes the gas, instigating avalanche electrons to move towards the electrode, where they are impeded by the resistive plate gaps, ultimately forming a collective signal. The TOF detector utilizes time-of-flight analysis for particle identification. The time-of-flight (t) represents the duration for a particle to travel from the interaction point to the TOF detector over a known distance (L). Positioned on both sides of the interaction point, the T0 detector provides the initial time reference (t_0) [95]. With a time resolution of around 80 ps, the ALICE TOF allows for precise experimental determination of particle mass. This is achieved by integrating the time-of-flight data from the TOF with particle momentum (p) measured by the TPC, according to the following equation:

$$m = p \times \sqrt{\frac{t^2}{L^2} - 1} \tag{3.2}$$

The TOF β, representing the ratio of a particle's velocity to that of light, is depicted in Figure 3.9. Under typical operating conditions, an average total TOF time resolution of 80 ps is achievable, allowing for clear separation of K/π and p/K up to 3σ at p_T up to 2.5 and 4.0 GeV$/c$ respectively, where σ denotes the time resolution of the TOF detector.

3.2.2.2 ElectroMagnetic CALorimeter (EMCal)

The ALICE experiment is now equipped with an advanced ability to detect high-energy particles, including photons, electrons, neutral pions, and jets, along with their correlations, facilitated by the ElectroMagnetic Calorimeter (EMCal) [105]. The EMCal, a shashlik-type lead-scintillator sampling calorimeter, is composed of 4416 modules organized into twenty Super Modules (SM), totaling 17664 towers. Each tower utilizes wavelength-shifting fibers connected to Avalanche PhotoDiodes (APDs) for optical readouts. The triggering system in both the EMCal and the Di-Jet Calorimeter (DCal) supports effective signal detection by grouping nearby towers into 44 sets, which are then analyzed using a peak finding tech-

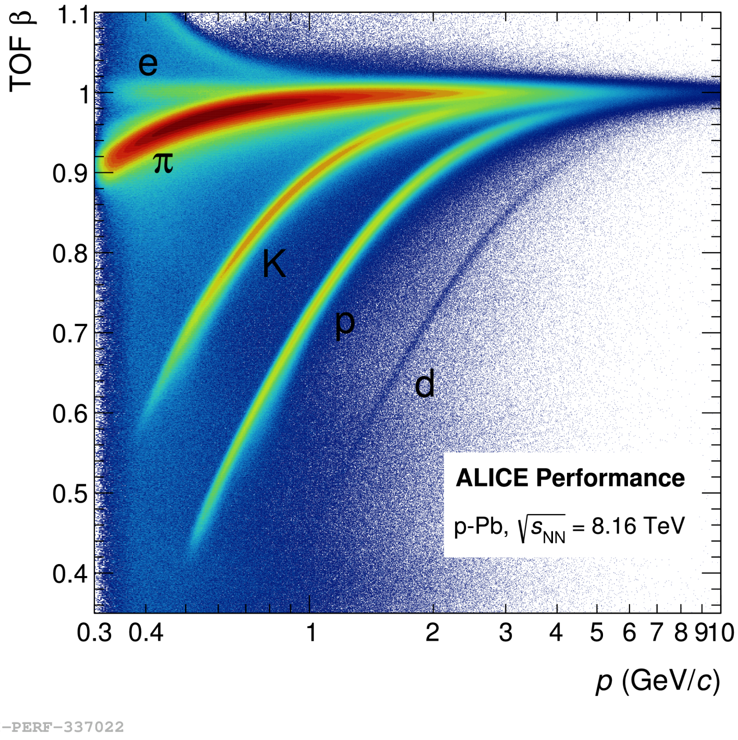

Figure 3.9: The TOF β distribution as a function of momentum in p–Pb collisions at $\sqrt{s_{\mathrm{NN}}}$ = 8.16 TeV [104]

nique. This process generates L0- and L1-level triggers for the ALICE Central Trigger Processor, allowing for the real-time selection of energetic particles such as photons and electrons. Covering an azimuthal angle of 107 degrees, the EMCal is situated approximately 4.5 meters from the vacuum tube with a longitudinal extension of 700 cm. It is engineered to study jet quenching and can evaluate the energy of charged particles, photons, and neutral mesons' photonic decays. The DCal, a supplementary component to the EMCal, spans a 70-degree azimuthal angle and is positioned to facilitate back-to-back jet measurements, thereby augmenting ALICE's precision in particle physics investigations.

3.2.2.3 PHOton Spectrometer (PHOS)

The PHOton Spectrometer (PHOS) [106] is an essential element of the ALICE experiment, tasked with detecting electromagnetic radiation from hot, strongly interacting matter in high-energy nucleus-nucleus collisions. It also enables the study of hadron spectra through radiative decays. With its 17280 detector channels, PHOS is placed 460 cm from the interaction point to ensure precise particle detection. It covers a pseudorapidity range from -0.12

to 0.12 and an azimuthal angle span from 220° to 320°. As a high-resolution electromagnetic calorimeter, PHOS excels in identifying photons and neutral mesons. Lead-tungstate crystals are used to reconstruct neutral mesons by observing their decay into two photons, while direct photons from the medium created in heavy ion collisions offer crucial insights into the medium's properties. Spanning 60° in azimuth and maintaining a pseudorapidity range of $|\eta| < 0.12$, PHOS significantly enhances our understanding of the complex dynamics in high-energy particle interactions.

3.2.2.4 High Momentum Particle Identification Detector (HMPID)

The ALICE High Momentum Particle Identification Detector (HMPID) [107] plays a critical role in differentiating between charged particles such as pions, kaons, and protons, especially at high momenta. Utilizing Ring Imaging Cherenkov (RICH) technology, the HMPID significantly enhances the particle identification (PID) capabilities of ALICE, allowing for π/K and K/p separation up to momenta of 3 and 5 GeV/c, respectively. Situated 5 meters from the beamline within the ALICE solenoid, the HMPID consists of seven RICH counters, extending over a pseudorapidity range of $|\eta| < 0.6$ and an angular span from 1.2° to 58.8°. Key components include a radiator medium and a photon detector, which detect Cherenkov radiation caused by charged particles exceeding the speed of light in the medium. By analyzing the angles of Cherenkov rings along with momenta gathered by other ALICE detectors such as the ITS and TPC, the HMPID enables accurate identification of charged particles at high momenta.

3.2.3 Forward detectors

3.2.3.1 Photon Multiplicity Detector (PMD)

The PMD detector [108, 109] serves to measure the multiplicity distribution of inclusive photons, primarily originating from the decay of π^0, within the forward pseudorapidity region ($2.3 < \eta < 3.7$, covering full azimuth). Constructed with two gas chambers or planes, the Preshower plane and the Charged Particle Veto (CPV) plane, with a lead converter sandwiched between them, this detector comprises numerous cells, each functioning as a gaseous proportional counter. Positioned at the rear of the lead plates, the Preshower plane is complemented by the CPV located closer to the interaction point. The CPV technique is employed to refine the analysis of photon characteristics in the detector's operational domain.

3.2.3.2 Forward Multiplicity Detector (FMD), T0 Detector

The FMD system is predominantly used to gather accurate offline information on the multiplicity of charged particles within the pseudorapidity range of $-3.4 < \eta < -1.7$ and $1.7 < \eta < 5.0$ [110]. Consisting of 51,200 silicon strip channels distributed across five ring counters, each featuring 20 and 40 sectors in azimuthal angle, the FMD, in conjunction with the ITS pixel system, offers comprehensive particle multiplicity distributions across all collision types within the range of $-3.4 < \eta < 5.0$. Moreover, the FMD facilitates the examination of multiplicity fluctuations on an event-by-event basis and enables flow analysis through azimuthal segmentation.

On the other hand, the T0 detector comprises two arrays of PMTs equipped with Cherenkov radiators, positioned on opposite sides of the Interaction Point (IP). Primarily, T0 provides crucial rapid timing signals for the L0 trigger in ALICE, initiates a wake-up signal for TRD, and furnishes collision-time references for the TOF detector. Covering the pseudo-rapidity range of $-3.3 < \eta < -2.9$ and $4.5 < \eta < 5$, the T0 detector boasts a trigger time resolution that exceeds 50 ps and can precisely determine IP location with an accuracy better than 1.5 cm. Comprising two arrays, T0-A and T0-C, located, respectively, at 3.6 m and 70 cm from the IP, each with specific pseudorapidity ranges, the T0 detector offers precise collision start-up times, online vertex position measurement, and multiplicity assessment of charged particles produced in hadron collisions. Additionally, it serves as an alternative Minimum Bias trigger detector.

3.2.3.3 VZERO (V0) detector

The VZERO (V0) detectors are plastic scintillator detectors strategically placed on either side of the interaction point [111]. Referred to as VZERO-A (V0-A) in the forward direction and VZERO-C (V0-C) in the backward direction, they cover the pseudorapidity range of $2.8 < \eta < 5.1$ (V0-A) and $-3.7 < \eta < -1.7$ (V0-C) with full azimuthal coverage, as depicted in Figure 3.10. Each detector comprises two arrays of 32 scintillator counters distributed across 4 rings, with each ring subdivided into 8 sectors. Primarily employed for triggering and filtering out beam-gas events based on their timing information, the V0 detectors exhibit a time resolution of approximately 1 ns. Within ALICE, these detectors play a crucial role as dedicated triggers for minimum bias events during data acquisition in pp, p–Pb, and heavy-ion collisions. They provide trigger information based on particles originating from the primary vertex of collisions and secondary interactions within the vacuum chamber elements, particularly for central barrel detectors. Furthermore, they contribute to determining the centrality of the collision in heavy-ion collisions and estimating the multiplicity in pp and p–Pb collisions.

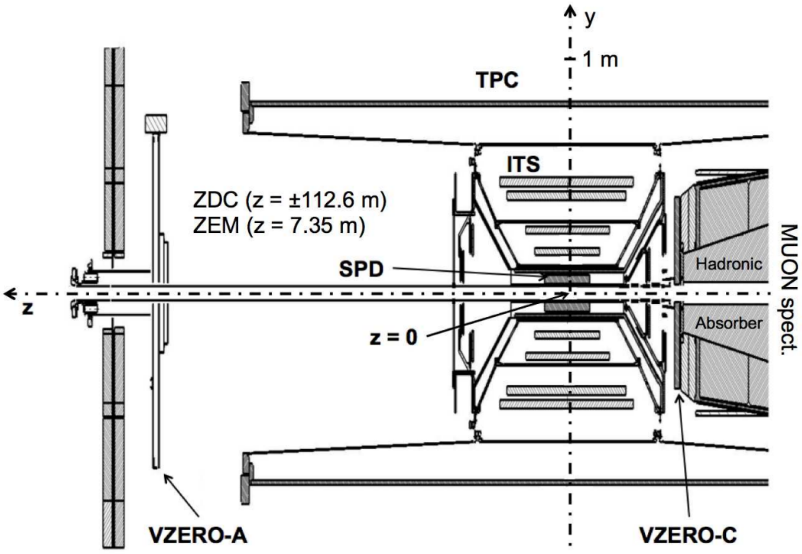

Figure 3.10: Position of the two VZERO arrays, and of the few detectors quoted in the text, within the general layout of the ALICE experiment [111].

3.3 The ALICE Framework

The ALICE detector comprises 18 distinct sub-detectors, each capable of operating independently in a standalone mode or as part of global partitions, which combine multiple sub-detectors for coordinated operation. The ALICE experiment employs an integrated framework of online and offline services to seamlessly manage its operations, spanning from particle collisions to the analysis of the resulting data.

3.3.1 ALICE online operations

The ALICE experiment relies on five central systems to manage its data collection activities. The *Data Acquisition System* (DAQ) configures and operates detectors during data taking by interfacing with the *Central Trigger Processor* (CTP) and the *High-Level Trigger* (HLT), which filters and compresses data in real time. The *Detector Control System* (DCS) oversees the experimental equipment, ensuring safe and stable operations, particularly during beam conditions. The *Experiment Control System* (ECS) coordinates these processes, managing communications between the DAQ, HLT, and DCS while overseeing detector partitions. The CTP distributes trigger signals for physics events, enabling efficient and organized data collection. Together, these systems ensure seamless data acquisition and processing for physics analysis.

3.3.1.1 The Data Acquistion System

The Data Acquisition (DAQ) system in ALICE is responsible for collecting, processing, and storing the large volumes of data generated during high-energy collisions at the LHC. It operates in conjunction with the Central Trigger Processor (CTP) and the High-Level Trigger (HLT), which select events based on predefined physics observables. The system efficiently handles both common and rare triggers: common triggers, such as central and semi-central collisions, are allocated significant bandwidth for precise capture, while rare triggers, like dielectron or dimuon events, use less bandwidth but are constrained by luminosity and detector live time. Data from the detectors is transmitted to the DAQ Readout Receiver Cards (D-RORC) via Detector Data Links (DDL). After passing through stages of local data concentration, sub-event assembly, and full event construction by Global Data Collector (GDC) computers, the data is stored in Transient Data Storage (TDS) before being transferred to Permanent Data Storage (PDS) for offline analysis. The system must operate efficiently under the high collision rates of proton-proton (pp) and the lower, but more complex, rates in lead-lead (Pb-Pb) collisions. Its architecture ensures a fair distribution of resources among various detector partitions, enabling the simultaneous study of multiple physics observables.

The flow chart in Figure 3.11 illustrates the sequence of operations, beginning with the decision of the CTP to trigger, which determines within 1 μs whether to record a collision event. This decision is passed through the Trigger and Timing Control (TTC) system to the Local Trigger Unit (LTU), which transmits it to the front-end electronics (FEE) of each detector. The data from the detectors is then routed through the DDL to the D-RORC for processing. Sub-events are sent to GDC computers, where they are assembled into complete events in ROOT format. These events are stored in TDS before being moved to PDS for archiving and later analysis.

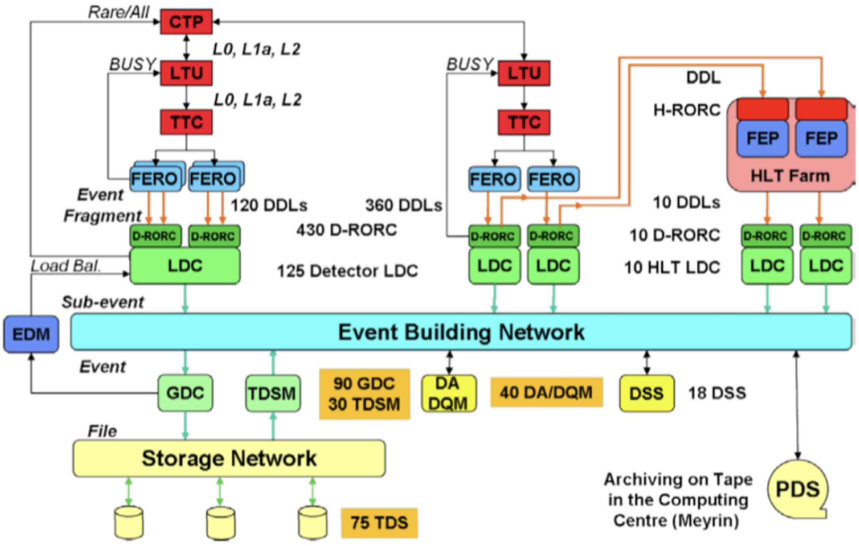

[h!]

Figure 3.11: The ALICE DAQ architecture, depicting the sequence from trigger decision to data storage.

3.3.1.2 The Central Trigger Processor

The main features of the ALICE Central Trigger Processor (CTP) are detailed in the technical design report [112]. The CTP is designed to manage trigger decisions for up to 24 detectors which are organized into six programmable trigger clusters, with each cluster capable of receiving independent trigger signals. This flexibility allows the CTP to dynamically group detectors based on specific physics requirements. The trigger system operates at three hierarchical levels to ensure a precise and timely data acquisition. The fastest level, Level 0 (L0), has a latency of 1.2 μs and provides an initial strobe signal to detectors with fast electronics while initiating BUSY signals for affected clusters. However, due to incomplete trigger inputs at this stage, the L0 trigger achieves only limited rate reduction. Level 1 (L1), arriving at 6.5 μs, incorporates most of the trigger inputs, enabling significant rate reductions and the storage of event data in multi-event buffers. The final trigger level, Level 2 (L2), arrives after 88 μs to account for the longest sensitive periods in detectors, such as the Time Projection Chamber (TPC), and finalizes the decision-making process.

The CTP uses 60 trigger inputs distributed across the three levels: 24 for L0, 24 for L1, and 12 for L2. Logical combinations of inputs, such as AND, are supported, while selected classes can use complementary signals. For a subset of inputs (4 L0 inputs), a lookup table enables the application of arbitrary logic functions, improving trigger efficiency, particularly for low-multiplicity interactions. The system also incorporates past-future protection to reduce pileup effects by analyzing interactions within two time windows: ± 88 μs for the TPC and ± 10 μs for the ITS. These programmable circuits generate output based on thresholds applied to interaction signals within defined time windows.

To handle rare triggers, the CTP employs a dynamic system that reserves bandwidth for low-frequency events. When data acquisition buffers reach a high occupancy level (high water mark), the CTP restricts non-rare trigger classes, prioritizing rare triggers. Once the buffer occupancy decreases below a low water mark, non-rare triggers are reactivated. This mechanism ensures that rare events are not overshadowed by high-frequency triggers, maintaining efficient bandwidth utilization. Trigger classes define the input requirements, output clusters, and veto conditions for events. Events are processed only if their trigger class requirements are satisfied, and no veto conditions—such as BUSY signals or past-future protection—are active. Multiple trigger classes can be activated simultaneously, but if all classes are vetoed, the event is dropped. Additionally, the CTP monitors hardware statuses, such as power supply voltages and fuse conditions, transmitting this information to the ALICE Detector Control System (DCS) via an independent I^2C link. This robust architecture allows the CTP to efficiently handle high-multiplicity events, rare phenomena, and varying collision conditions, ensuring optimized data acquisition for ALICE.

3.3.1.3 The High Level Trigger

In a single central nucleus-nucleus collision, the Time Projection Chamber (TPC) alone generates approximately 75 MB of data, assuming $\frac{dN_{\rm ch}}{d\eta} = 8000$ at mid-rapidity, as indicated by simulation studies. While many events may have low physical relevance, the total data rate across all detectors following trigger selection can easily reach 25 GB/s. However, the DAQ system can only archive data at a rate of about 1 GB/s. To address this discrepancy, the High-Level Trigger (HLT) system plays a crucial role by performing online processing to select relevant events or sub-events and compress data without compromising its physical content.

The HLT is designed to accept or reject events based on real-time online analysis. For accepted events, the HLT uses advanced compression algorithms to reduce the data size to levels manageable by the DAQ and storage systems. This ensures that critical physics information is retained while lowering the data transfer and storage requirements. The HLT collects raw data from the Local Data Concentrators (LDCs), performs fast local tracking and pattern recognition, identifies the primary vertex, and constructs a global event view. Following a trigger decision, the event's summary and compressed data are sent back to the DAQ through the HLT DDL output.

To achieve these tasks efficiently, the HLT utilizes a cluster of approximately 1000 multi-processor computers, enabling rapid processing of high-volume collision data. This architecture ensures real-time performance for online tracking, pattern recognition, and data compression, which are essential for handling the high data rates produced by the detectors during heavy-ion collisions.

The primary functionalities of the HLT can be categorized as follows:

- **Trigger**: Accept or reject events by performing extensive online analysis as a trigger decision mechanism.
- **Select**: Identify and focus on specific physics regions of interest within an event by conducting partial readouts.

- **Compress**: Apply sophisticated compression algorithms to approved and selected data to significantly reduce event size without any loss of critical physics information.

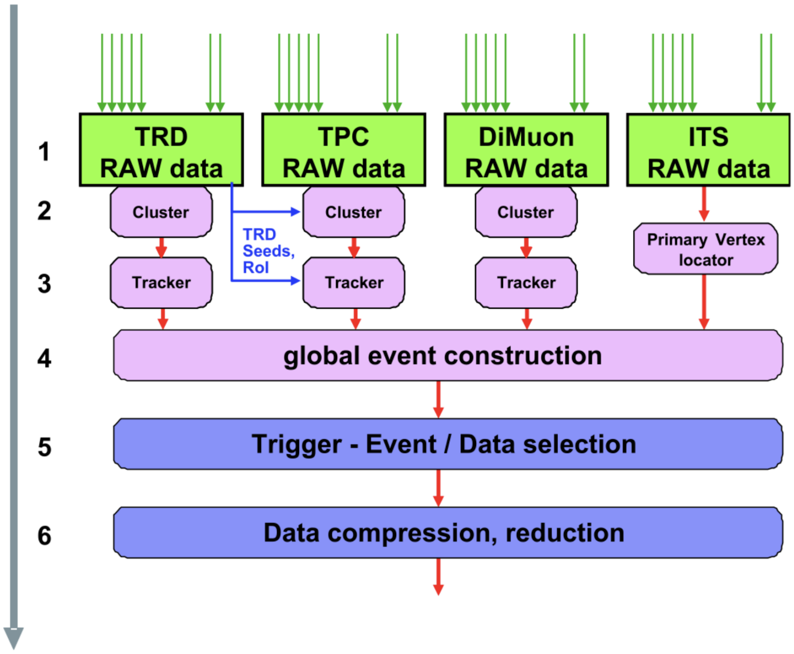

Figure 3.12: The six architectural layers of the HLT.

The HLT is not just a filtering system; it is a powerful tool for enhancing the efficiency of the data acquisition process. By performing real-time data analysis and reduction, the HLT bridges the gap between the high data rates generated by the detectors and the DAQ system's archiving capacity, enabling ALICE to capture and analyze the most relevant physics events while optimizing resource usage. The High-Level Trigger, as depicted in Figure 3.12, is a critical component for ensuring that ALICE meets its physics goals under the challenging conditions of heavy-ion and proton-proton collisions. Its capabilities in real-time processing and compression make it indispensable for addressing the high data rate demands of the experiment.

3.3.1.4 The Detector Control System

The primary responsibility of the ALICE Detector Control System (DCS) is to ensure the proper and safe operation of the ALICE experiment. The DCS facilitates remote control and monitoring of all experimental equipment through a dedicated set of operator panels, allowing the experiment to be efficiently managed and operated from the ALICE Control

Room (ACR) at LHC Point 2. The system is designed to provide optimal operating conditions, ensuring that data collection yields the best possible results. One of the key goals of the ALICE DCS is to minimize downtime and maximize the operational efficiency of the experiment.

To ensure efficient data analysis, the DCS continuously monitors and controls all relevant parameters, maximizing the operational availability of channels while data recording. The system is designed to integrate new components seamlessly, maintaining a coherent and unified monitoring and control framework across the entire experiment. This adaptability allows the DCS to evolve alongside the experiment, supporting scalability and long-term expansion as new detectors or modifications are introduced. The DCS also accommodates various operating modes, enabling independent operation of multiple detectors or sub-detectors while ensuring they function concurrently. This flexibility is crucial during different operational phases, such as data collection, maintenance, or shutdown periods. The system remains fully operational at all times, facilitating smooth transitions between stages and ensuring the readiness of all components for data acquisition and analysis.

In addition to managing the experiment's equipment, the ALICE control system is essential for fault detection and recovery. By continuously monitoring the status of detectors and associated subsystems, the DCS can quickly identify issues and initiate corrective actions to minimize disruptions. The system is designed for high availability, ensuring that it can handle unexpected events without significant loss of data or functionality.

3.3.1.5 The Experimental Control System

The Experiment Control System (ECS) plays a central role in coordinating the operations of the "online systems" within the ALICE experiment. These "online systems" enable the partitioning of the experiment, allowing groups of detectors to operate independently while still interacting with each other. In its final configuration, the detectors primarily work together to collect physics data, and the ECS ensures that all operations are synchronized across different partitions. The ECS allows multiple operators to work simultaneously on different sections of the experiment by coordinating the functions of the "online systems" for all detectors within each partition. It receives status updates from these systems and issues commands through Finite-State Machine (FSM) interfaces, ensuring smooth communication between components. The ECS also employs access control mechanisms to regulate permissions between the system and the "online systems," defining which actions can be performed.

While the ECS typically manages the "online systems," certain systems may operate independently, sending status information to the ECS without receiving direct commands. The ECS is made up of four main components: the Detector Control Agent (DCA), Partition Control Agent (PCA), Detector Control Agent Human Interface (DCAHI), and Partition Control Agent Human Interface (PCAHI), each playing a vital role in maintaining system functionality and communication.

3.3.2 ALICE offline operations

3.3.2.1 ALICE Grid

Due to the immense and unprecedented volume of data generated at the LHC, processing and storage resources must be distributed across multiple computing facilities. This distributed approach is both natural and effective, given the collaboration among institutes and universities participating in the experiment. To facilitate this, a global distributed computing project known as the Grid was initiated in 2000.

To enable seamless access to the Grid’s worldwide distributed computing resources, the ALICE Experiment developed the ALICE Environment (AliEn) architecture. The Grid allows participating institutions and universities to share and optimize their computing resources. It is organized into hierarchical levels called Tiers, based on the MONARC (Models of Network Analysis at Regional Centers for the LHC Experiment) model:

- **Tier 0 (CERN)**: Stores the raw data directly produced by the experiments.
- **Tier 1**: Comprises the largest external centers, responsible for maintaining a second copy of the data and performing event reconstruction.

- **Tier 2**: Includes regional centers that contribute to Monte Carlo simulations and prepare data in formats suitable for individual user analysis.

AliEn serves as the interface for ALICE users to interact with the Grid middleware. Through the AliEn User Interface, users can access data, submit analytical and simulation jobs, and monitor their progress. The architecture ensures transparent access to distributed resources, enabling efficient analysis and collaboration across the global ALICE community. This robust infrastructure underscores the importance of advanced computing frameworks in managing the complexity and scale of LHC experiments.

3.3.2.2 AliRoot framework

Figure 3.13 provides a schematic overview of the ALICE offline framework, AliRoot [113]. AliRoot serves as the primary software framework for simulation, reconstruction, and analysis in the ALICE experiment. The framework leverages the AliEn system for access to the computational Grid and is built using Object-Oriented programming techniques with the ROOT system [114] as its supporting foundation. This approach enables the creation of a unified software environment written entirely in C++, with minimal reliance on external (user-hidden) FORTRAN applications. AliRoot is specifically designed to handle the enormous volume of data generated in high-energy physics experiments. It provides tools to analyze both simulated and experimental data, encompassing features such as detector geometries and their responses to particle interactions. The framework integrates various Monte Carlo transport programs, including GEANT3 [115], GEANT4 [116], and FLUKA [117], for modeling particle interactions with detectors. Additionally, Monte Carlo event generators, such as PYTHIA [118] and HERWING [119] for pp collisions, and HIJING [120] and DPMJET [121] for proton-nucleus and nucleus-nucleus collisions, are employed to simulate events. These simulations are essential for evaluating detector efficiency and optimizing reconstruction algorithms.

The left side of the schematic representation in Figure 3.14 illustrates the process of event simulation, starting from Monte Carlo event generation to the production of raw data. Event generators produce a kinematic tree that includes information about particle-level

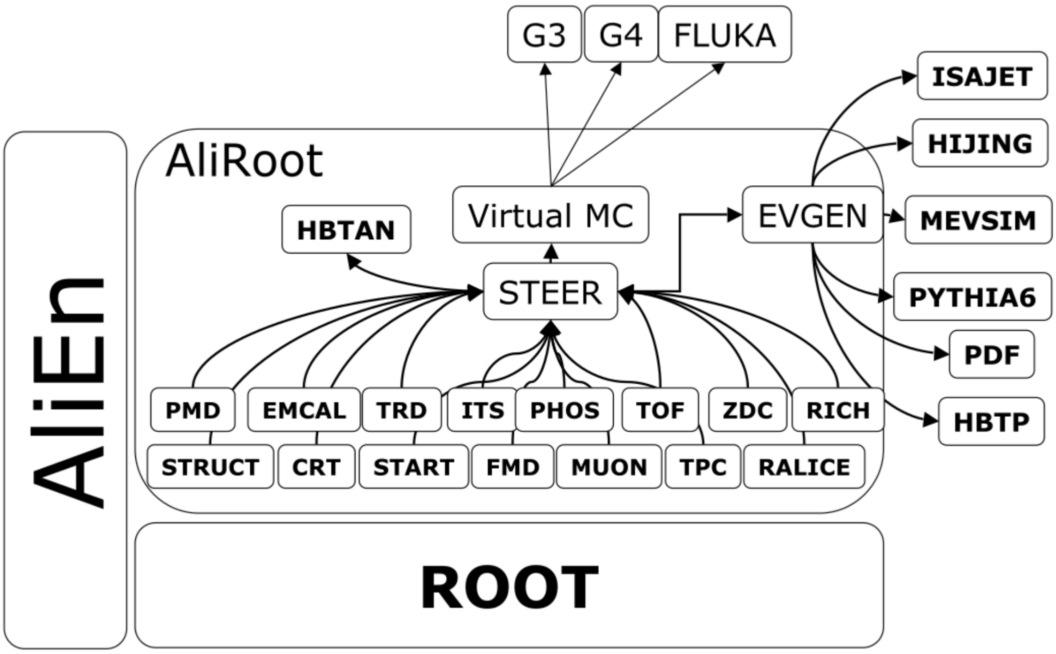

Figure 3.13: The AliROOT framework.

physics processes and fragmentation products (primary particles). This data contains detailed information about generated particles, such as their momentum, charge, type, and mother-daughter relationships. Simulated interactions between particles and detectors are also modeled, with "hits" (energy depositions at specific points and times) recorded for each detector. Trail references, or locations where particles cross predefined reference planes, are appended as supplementary data. The detector and electronics response functions are applied to convert hits into digitized signals, which are then saved as raw data in hardware-specific formats. The right side of the schematic outlines the reconstruction process, which is common for both real and simulated data. The reconstruction chain begins with local reconstruction at the detector level, including clustering of hits, followed by track reconstruction using Kalman filter-based algorithms [122]. This process starts with a seeding procedure and proceeds to global tracking. AliRoot also supports vertex reconstruction, tracking, and comprehensive analysis for the entire detector apparatus.

To ensure the accuracy and reliability of the framework, simulated events undergo the full simulation-reconstruction cycle. Reconstructed particles are systematically compared with the Monte Carlo truth data, allowing performance validation for both the software and the detectors. The iterative refinement of these tools is critical to achieving the precision

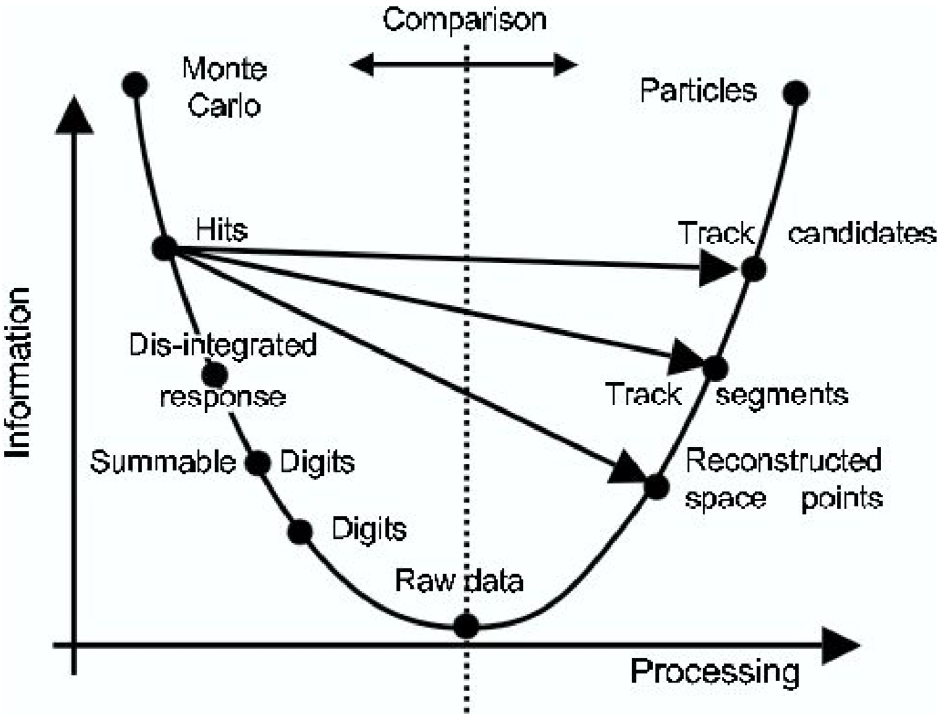

[h!]

Figure 3.14: Data processing framework

required in high-energy physics experiments.

Chapter 4

Λ^* production at mid-rapidity in pp and p–Pb collisions

The hadronic resonances have very short lifetimes, a few fm/c, which are comparable to the lifetime of the hadronic phase formed in the heavy-ion collisions. Some of these resonances decay while travelling through the medium and their decay daughters undergo rescattering or regeneration in the hadronic gas. Consequently, their yields change from the original ones produced before the chemical freeze-out, a phase where inelastic interactions stop, and hadron yields become fixed, with only elastic interactions occurring afterwards. Therefore, studying the production yields of hadronic resonances offers insight into the properties of the hadronic phase in the evolution of various collision systems. More specifically, the lifetimes of hadronic resonances are exploited to gain an understanding of the characteristics of the hadronic phase. Additionally, the particle production in p–Pb system is sensitive to the early-stage nuclear effects, unlike pp system. Given the intermediate volume of the system generated in p–Pb collisions compared to pp and Pb–Pb collisions, it is anticipated that the final stage effects on particle production in p–Pb will be similar to those observed in peripheral Pb–Pb collisions. Thus, the role of the initial and final state effects in particle production can be understood from the measurement of particle p_{T} spectra in different collision systems together. The Λ^* resonance is characterized by a mass of 1519.5 ± 1.0 MeV/c^2, a width of 15.6 ± 1.0 MeV/c^2, and a lifetime of 12.6 ± 0.8 fm/c. It decays into a proton-kaon pair with a branching ratio of 22.5% [56]. As a strange baryon with a net strangeness of -1, the Λ^* resonance has a lifetime roughly three times longer than the K^{*0} and about one-fourth that of the ϕ resonance. Studying its production yield is therefore important for estimating the duration of the hadronic phase and examining medium effects on resonance production. In this chapter, we present the measurements performed for Λ^* resonance in the inelastic pp collisions at $\sqrt{s}$ = 8 TeV and in p–Pb collisions at $\sqrt{s_{\mathrm{NN}}}$ = 8.16 TeV in non-single diffractive (NSD) class and different V0A multiplicity classes with the ALICE detector. The Λ^* resonance yield is extracted from the invariant mass distributions of proton-kaon pairs as a function of transverse momentum. Moreover, the invariant mass spectra of pK^- and $\bar{\mathrm{p}}\mathrm{K}^+$ were merged to minimize the statistical uncertainties. Consequently, throughout this chapter, unless specified, Λ^* refers to $\Lambda^* + \bar{\Lambda}^*$. The results obtained are compared with the published data and various theoretical models to understand the underlying physics in particle production.

4.1 Analysis details

The production of Λ^* is measured in pp collisions using data from LHC Run 2 in 2012 at a center-of-mass energy of $\sqrt{s}$ = 8 TeV, and in minimum-bias and across four V0A multiplicity classes for p–Pb collisions recorded in 2016 at $\sqrt{s_{\mathrm{NN}}}$ = 8.16 TeV. The details of the datasets and run numbers are provided in the Appendix A. The Λ^* resonance is reconstructed via its decay daughters using the invariant mass technique. The decay channel pK^- ($\bar{\mathrm{p}}\mathrm{K}^+$) with a branching ratio of 22.5% is explored for these analyses. In the p–Pb configuration, collisions occur between a ^{208}Pb beam with an energy of 2.56 TeV per nucleon and a proton beam with an energy of 6.5 TeV, resulting in a nucleon-nucleon center-of-mass energy of $\sqrt{s_{\mathrm{NN}}}$ = 8.16 TeV. Due to the significant mass difference between the proton and lead beams, an asymmetry exists in the p–Pb system, causing the center of mass to shift towards the heavier particle. Consequently, the rapidity of produced particles in the center-of-mass frame is shifted in the direction of proton beam by -0.465, relative to the lab system [123]. In contrast, the pp system is symmetric, resulting in the coincidence of the center-of-mass and lab systems. Therefore, there is no rapidity shift in the center-of-mass system relative to the lab system. Each proton beam has an energy of 4 TeV, resulting in a total energy of 8 TeV per pp collision. Measurements in the pp system are performed within the rapidity range $-0.5 < y_{\mathrm{cm}} < 0.5$, while in the p–Pb system, measurements cover the rapidity range $0 < y_{\mathrm{cm}} < 0.5$, corresponding to the mid-rapidity regions for both systems. In the pp system, measurements are performed in the inelastic collisions, whereas in the p–Pb system, measurements are performed in the NSD events and across four V0A multiplicity classes (0–20%, 20–40%, 40–60%, and 60–100%).

4.2 Event selection

Approximately 35 million events comprise the p–Pb sample, while the pp sample consists of around 58 million events after implementing all the event selection cuts. Selection of minimum-bias events is done by using the kINT7 trigger (inelastic trigger), which is configured to capture only those events which have a coincidence signal in both the V0A and V0C. The V0 detector system consists of two arrays of 32 scintillator detectors, each placed on opposing sides of the interaction point, covering the entire azimuthal angle within the pseudorapidity ranges $2.8 < \eta < 5.1$ (V0A) and $-3.7 < \eta < -1.7$ (V0C). By implying the timing information from V0 and ZDC detectors, background events originating from beam-gas interactions and other machinery-induced background collisions are effectively filtered out. The determination of the primary vertex of a collision involves reconstructing charged tracks in the ITS and TPC. Events are selected based on the primary vertex position (V_{z}), which represents the point where the collision occurs, ensuring it falls within ± 10 cm of the nominal interaction point along the beam axis. The normalized V_{z} distributions of the events in p–Pb and pp systems are shown in the Figure 4.1. In the p–Pb system, the multiplicity estimation is based on the V0A amplitude, while for the pp system, the sum of the amplitudes of V0A and V0C is used. This sum is proportional to the ionization energy deposited in the detector within the pseudorapidity ranges of V0A and V0C. The selection of charged particles in these η regions avoids the self-correlation effects with the central η regions

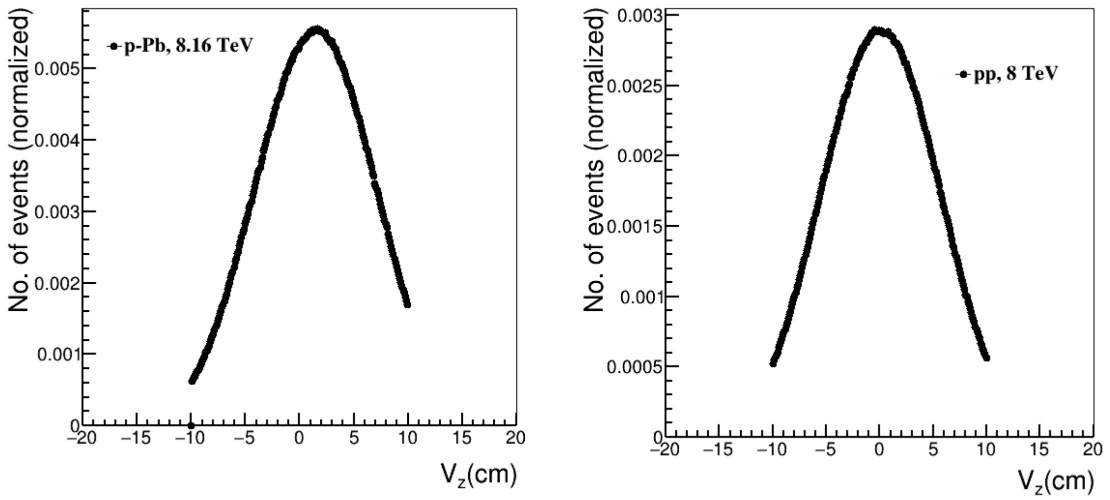

Figure 4.1: The normalized z-vertex distribution of events in the p–Pb collisions (left) at $\sqrt{s_{\rm NN}}$ = 8.16 TeV and in the pp collisions (right) at $\sqrt{s_{\rm NN}}$ = 8 TeV with the ALICE detector.

where the actual measurements of the resonances are made. Since this analysis focuses on minimum-bias pp collisions, only the p–Pb collisions are divided into various V0A multiplicity classes. For this, the V0A amplitude obtained from the p–Pb collisions is subjected to a fitting procedure using a Glauber model convoluted with a Negative Binomial Distribution (NBD) [124, 125]. The distribution of V0A amplitude fitted with NBD-Glauber is depicted in Figure 4.2. Following the implementation of multiplicity selection, the number of events as a function of multiplicity is illustrated in Figure 4.3.

The yield of Λ^* is measured in inelastic pp collisions with minimum-bias at $\sqrt{s_{\rm NN}}$ = 8 TeV. In the case of p–Pb collisions at $\sqrt{s_{\rm NN}}$ = 8.16 TeV, the yield is calculated across four V0A defined multiplicity classes (0–20%, 20–40%, 40–60%, and 60–100%), and also in the multiplicity integrated class (0–100%). The mean charged-particle pseudorapidity density ($\langle {\rm d}N_{\rm ch}/{\rm d}\eta \rangle$) corresponding to each multiplicity class, measured within the pseudorapidity region $|\eta| < 0.5$ in the lab frame, is provided in Table 4.1. Several additional event selection criteria are applied in this analysis. Pileup events, identified as those with multiple vertices during reconstruction, are excluded using `AliAnalysisUtils::IsPileUpEvent()`. A correlation check between the number of SPD clusters and tracklets is performed using `AliAnalysisUtils::IsSPDClusterVsTrackletBG()` with default parameters. Events with a primary vertex reconstructed using the SPD detector are retained, while those with

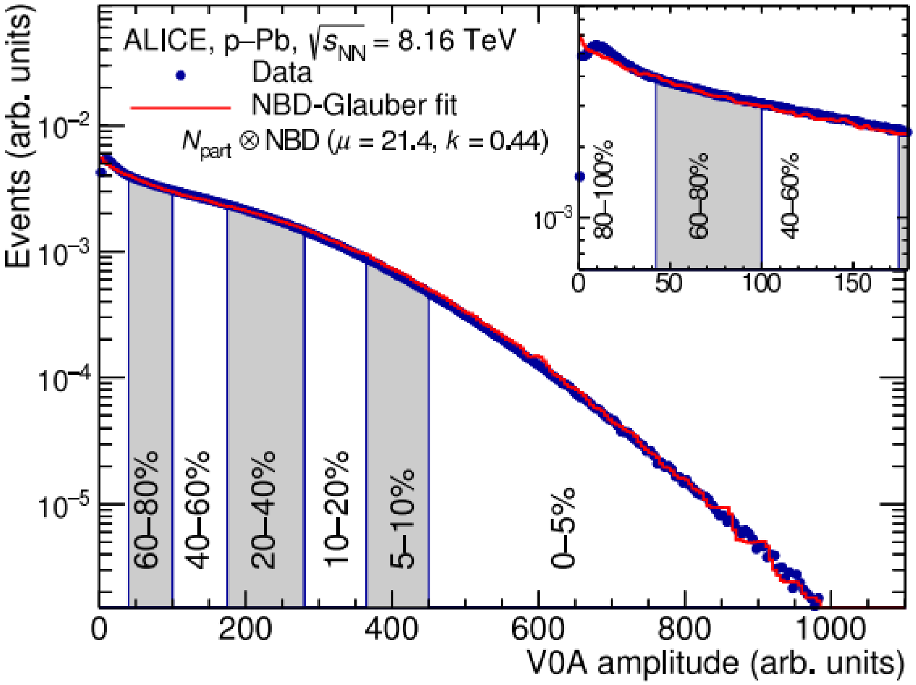

Figure 4.2: The V0A amplitude distribution measured in p–Pb collisions at $\sqrt{s_{NN}}$ = 8.16 TeV, divided in various multiplicity classes. The distribution is fitted with a Gluaber model function [126].

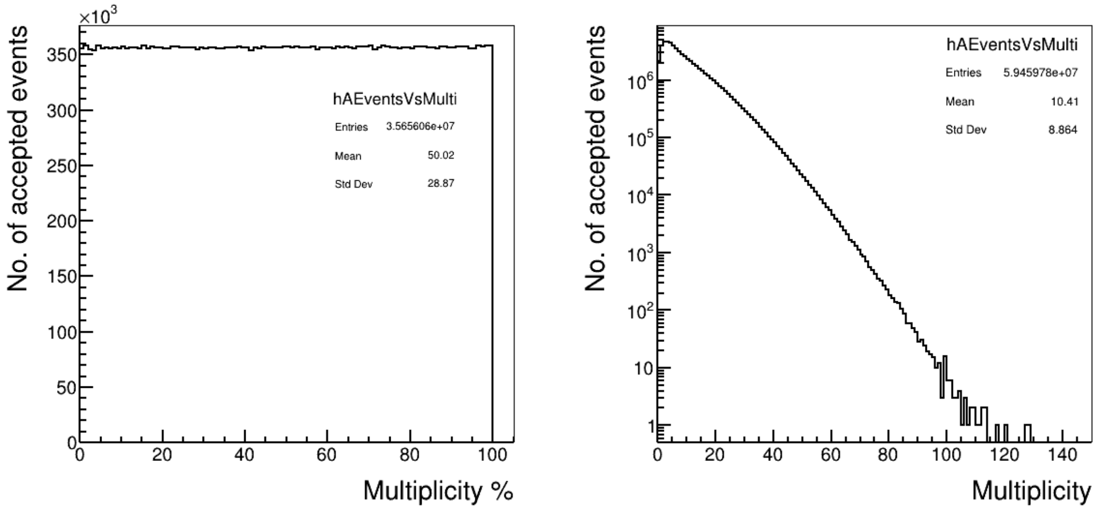

Figure 4.3: The multiplicity percentile distribution of accepted events using V0A in p–Pb collisions at $\sqrt{s_{NN}}$ = 8.16 TeV (left panel) and the accepted events vs charged particle multiplicity from V0A + V0C in pp collisions at $\sqrt{s_{NN}}$ = 8 TeV (right panel).

an SPD vertex-z resolution exceeding 0.25 cm, crucial for successful track matching between the ITS and TPC, are discarded. Additionally, events with an SPD vertex dispersion greater than 0.04 or a z-position difference between the track and SPD vertex exceeding 0.5 cm are rejected.

Table 4.1: The average charged particle multiplicity densities ($\langle \mathrm{d}N_{\mathrm{ch}}/\mathrm{d}\eta \rangle$) measured in pseudorapidity range $|\eta| < 0.5$ in the lab frame, corresponding to the various multiplicity classes defined using the V0 detector in p–Pb system at $\sqrt{s_{\mathrm{NN}}}$ = 8.16 TeV [126].

V0A percentile (%)	$\langle \mathrm{d}N_{\mathrm{ch}}/\mathrm{d}\eta \rangle_{\lvert\eta_{\mathrm{lab}}\rvert<0.5}$
0 – 20	41.65 ± 0.80
20 – 40	26.89 ± 0.70
40 – 60	18.39 ± 0.48
60 – 100	7.63 ± 0.24

4.3 Track selection

Charged tracks originating from the primary vertex are selected within the pseudorapidity interval $|\eta| < 0.8$, ensuring a uniform acceptance for the central barrel detectors, with a transverse momentum (p_{T}) greater than 0.15 GeV/c. A Kalman filter algorithm is employed for reconstructing primary tracks using data from the ITS and TPC detectors [122]. These tracks are refitted from the outermost layer of the TPC to the innermost layer of the ITS and extended up to the primary vertex, and vice versa. Additionally, tracks are required to have a signal in at least one of the SPD layers, where the track is reconstructed from hits in the detector. To ensure accuracy and reliability, the reconstructed primary tracks are fitted with a set of measurements, and the resulting χ^2 per cluster is required to be less than 36. These selection criteria are similar to those employed in previous measurements (Ref. [84]) to ensure the selection of high-quality tracks. The Λ^* resonance is then reconstructed from charged tracks that traverse at least 70 out of a maximum of 159 horizontal segments along the transverse readout plane of the TPC. To reduce contamination from secondary tracks arising from weak decays and beam background events, a selection based on the distance of closest approach to the primary vertex in the transverse plane ($\mathrm{DCA}_{\mathrm{xy}}$) and along the longitudinal direction ($\mathrm{DCA_z}$) is applied. Furthermore, a transverse momentum (p_T)-dependent cut of $\mathrm{DCA_{xy}(p_T)} < (0.0105 + 0.035 \times \mathrm{p_T}^{-1.1})$ cm is utilized, ensuring that it remains within 7 times its resolution. Additionally, the track's $\mathrm{DCA_z}$ is required to be less than 2 cm. These track selection criteria effectively reduce contamination, thereby enhancing the purity of the reconstructed Λ^* signal.

4.4 Particle identification

Particle identification of the daughter particles of Λ^*, namely protons and kaons, is done by using the TPC and TOF detectors. In TPC, identification of the daughter particles of Λ^* is based on measuring their specific energy loss ($\mathrm{d}E/\mathrm{d}x$) as they traverse the active medium of the detector, while identification in TOF is done by time of flight information. To reduce particle contamination and minimize combinatorial background for Λ^*, the momentum of the decay daughters is predominantly restricted within the TPC. Consequently, for protons, the maximum momentum allowed in the TPC is 1.1 GeV/c, and for kaons, it is limited to 0.6 GeV/c. In the case of pp collisions, these maximum momentum thresholds are slightly different, with the maximum momentum for protons in the TPC set to 1.0 GeV/c and for kaons it is up to 0.5 GeV/c. Additionally, a particle identification (PID) cut of 2σ (where σ represents the resolution) is applied for particle identification in the TPC (3σ in the case of pp collisions). If the momenta of the decay daughters exceed the respective momentum thresholds, they are then selected from the TOF detector, subject to a resolution cut of 3σ and a 5σ veto from the TPC. The term σ_TPC represents the resolution of the energy loss in the TPC and is defined as:

$$n\sigma_\mathrm{TPC} = \frac{\mathrm{d}E/\mathrm{d}x_\mathrm{measured} - \mathrm{d}E/\mathrm{d}x_\mathrm{expected}}{\sigma_\mathrm{TPC}} \tag{4.1}$$

where, $\mathrm{d}E/\mathrm{d}x_\mathrm{measured}$ denotes the average energy loss of the daughter tracks in the TPC, and $\mathrm{d}E/\mathrm{d}x_\mathrm{expected}$ represents the expected energy loss of the daughter tracks, determined using the modified Bethe-Bloch function [127].

In the Time-Of-Flight (TOF) detector, the combined information of time measurement from TOF, momentum, and track length from the tracking detectors (TPC and ITS) is used to determine the particle mass or identify the particle. The T0 detector is employed to measure the start time (collision time) for each event. The quantity $n\sigma_{\mathrm{TOF}}$ is expressed as:

$$n\sigma_{\mathrm{TOF}} = \frac{t_{\mathrm{measured}} - t_{\mathrm{expected}}}{\sigma_{\mathrm{TOF}}} \tag{4.2}$$

where, t_{measured} represents the flight time of the particles measured in the TOF detector, while t_{expected} denotes the expected time measured from the momentum and track length of the daughter particles of the Λ^*. Figures 4.4(a) and 4.4(b) show the σ distribution of the proton and kaon tracks in the data and Monte Carlo. The black lines show the area from which PID selection is done. The σ distribution of tracks in different momentum bins, fitted with a Gaussian function, along with the obtained mean and standard deviation, are provided in Appendix D.

4.5 Raw yield extraction

This section outlines the procedure for extracting Λ^* yield from the invariant mass distribution of the daughter particles in various p_{T} bins.

4.5.1 Invariant mass distribution: Signal extraction

The invariant mass distribution (M_{inv}) is obtained by combining primary protons and kaons with different charges originating from the same event, adding the four-momenta of daughter particles. The invariant mass distribution, expressed in terms of energy and momentum, is given by:

$$M_{pK} = \sqrt{(E_{\mathrm{p}} + E_{\mathrm{K}})^2 - (P_{\mathrm{p}} + P_{\mathrm{K}})^2} \tag{4.3}$$

where, E represents the energy and P denotes the momentum of the daughter particles. Separate distributions for pK^- and $\bar{\mathrm{p}}\mathrm{K}^+$ are obtained for Λ^* and $\bar{\Lambda}^*$, respectively. These distributions are then merged bin by bin to obtain the total signal for Λ^* + $\bar{\Lambda}^*$. It is important to note that not all protons and kaons originate from Λ^*, leading to the presence of

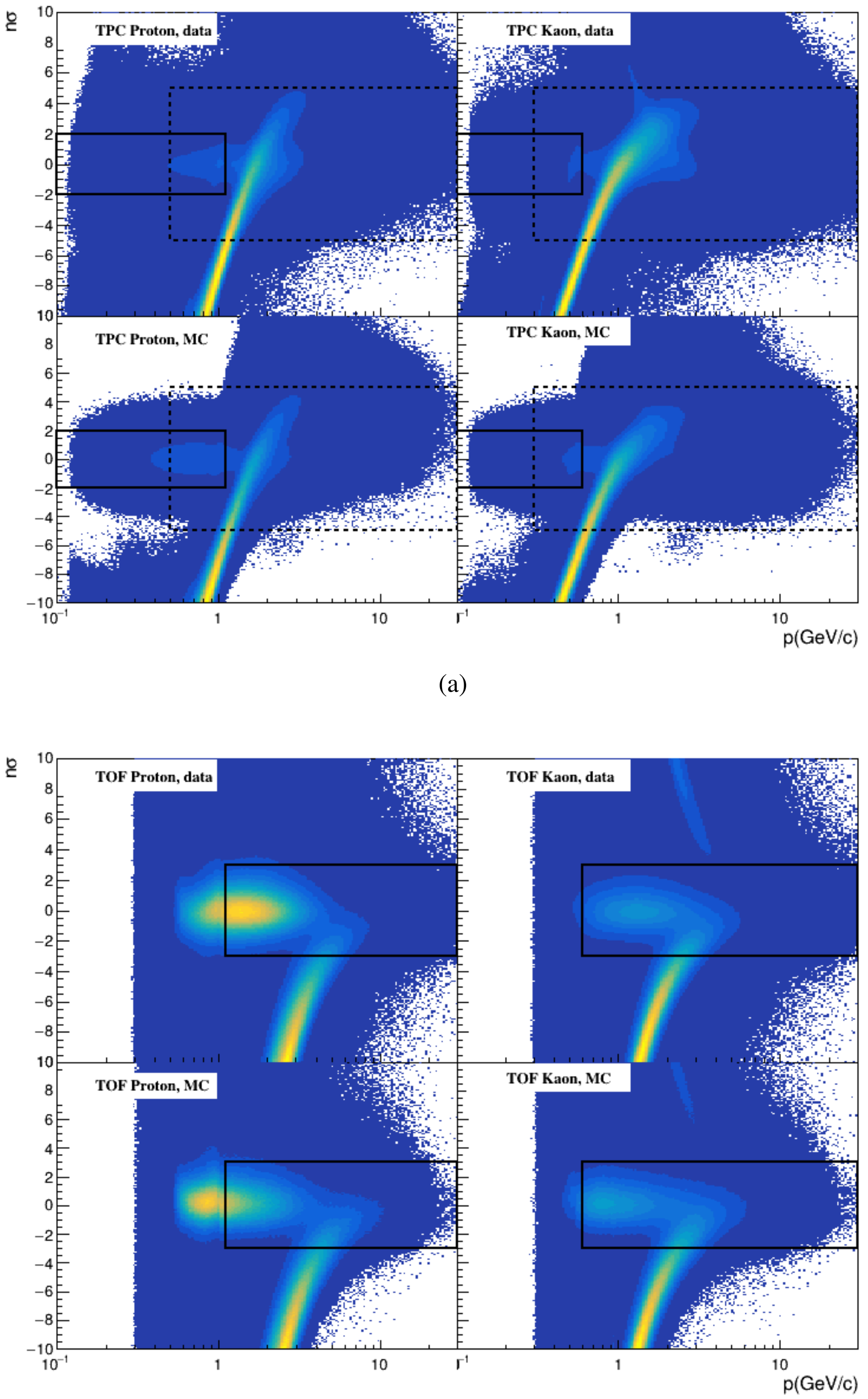

(a)

(b)

Figure 4.4: **a)** n_σ distributions of the daughter tracks identified using the TPC detector. The upper panels correspond to experimental data, while the lower panels represent Monte Carlo simulations. The left panels show distributions for protons, and the right panels for kaons. **b)** n_σ distributions of the daughter tracks identified using the TOF detector. The solid black lines indicate the regions used for PID selection, while the dotted black lines mark the regions where the TPC is utilized as a veto.

a significant combinatorial background. This background is estimated using event-mixing and like-sign techniques, as detailed in the following subsection. The Λ^* signal is extracted from eight p_{T} bins (0.6–1.0, 1.0–1.4, 1.4–1.8, 1.8–2.2, 2.2–2.6, 2.6–3.0, 3.0–4.0, and 4.0–6.0 GeV/c) for non-single diffractive events and four multiplicity classes (0–20%, 20–40%, 40–60%, and 60–100%) in p–Pb collisions at $\sqrt{s_{\mathrm{NN}}} = 8.16$ TeV. Similarly, for minimum-bias pp collisions at $\sqrt{s} = 8$ TeV, the signal is extracted from nine p_{T} bins (0.5–0.8, 0.8–1.0, 1.0–1.2, 1.2–1.5, 1.5–1.8, 1.8–2.1, 2.1–2.7, 2.7–3.5, and 3.5–4.5 GeV/c).

4.5.2 Combinatorial background

The event-mixing and like-sign techniques used for estimating the combinatorial background are explained below:

1. Event-mixing: In the event-mixing technique, unlike-sign charged kaons and protons from 10 different events are combined to construct the combinatorial background. Specifically, protons are selected from one event, while kaons are chosen from nine other events. To reduce the potential mismatches arising from differences in acceptance and to ensure a consistent event structure, particles from events with similar vertex positions z (with a difference $\Delta z < 1.0$ cm) and track multiplicities n (with a difference $\Delta n < 5$) are selected for mixing. Since the statistical significance of the mixed event distribution is ten times higher than that of the unlike-charge distribution, it is necessary to normalize the mixed event distribution to match the integral of the unlike-charge distribution. The normalization region is specifically chosen as $1.75 < M_{\mathrm{pK}}(\mathrm{GeV}/c^2) < 1.85$, which is away from the signal peak. This normalization process ensures a consistent comparison between the background and signal distributions.

2. Like-sign: In the like-sign technique, invariant-mass distributions are computed using protons and kaons with the same charge originating from the same event. For each invariant-mass bin, the value of the like-charge combinatorial background is determined as $\sqrt{\mathrm{n}_{--} \times \mathrm{n}_{++}}$, where n_{--} (n_{++}) represents the number of $\bar{\mathrm{p}}\mathrm{K}^-$ (pK^+) pairs in the bin. The invariant mass distribution of unlike-charged proton-kaon pairs, along with the estimated

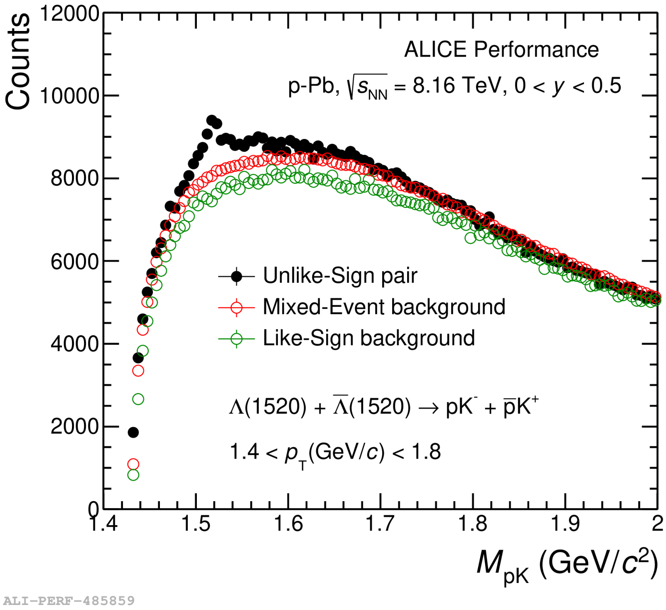

Figure 4.5: The unlike-sign charged particle pair invariant mass distribution of proton and kaon (black solid circles) extracted from the $1.4 < p_T < 1.8$ bin, in non-single diffractive p–Pb collisions at $\sqrt{s_{NN}}$ = 8.16 TeV at midrapidity, with normalized mixed-event background (open red circles) and like-sign background (open green circles).

combinatorial background obtained using the mixed-event and like-sign methods, at midrapidity for the $1.4 < p_T < 1.8$ GeV/c bin in non-single diffractive p–Pb collisions at $\sqrt{s_{NN}}$ = 8.16 TeV, is shown in Figure 4.5. Only the background estimated using the mixed-event technique is used to calculate the Λ^* signal (shown in the Figure 4.6), as the mixed-event combinatorial background—obtained by mixing particles from different events—is more uncorrelated compared to the like-sign background, which is obtained from particles within the same event.

4.5.3 Λ^* peak fits

After subtraction of the combinatorial background, a residual background is still present in the vicinity of the Λ^* peak. This residual background arises primarily from the misidentification of the kaons and protons within TPC. This misidentification becomes apparent when examining the dE/dx bands for charged particles in TPC. At lower momentum values, the dE/dx bands for charged particles are clearly distinct, allowing easy identification of protons and kaons without contamination. Nevertheless, as momentum increases, these bands start to converge, leading to some other charged particles being mistakenly recognized as protons and kaons. Consequently, this contributes to the residual background that persists even after subtracting the combinatorial background. The invariant-mass distributions are

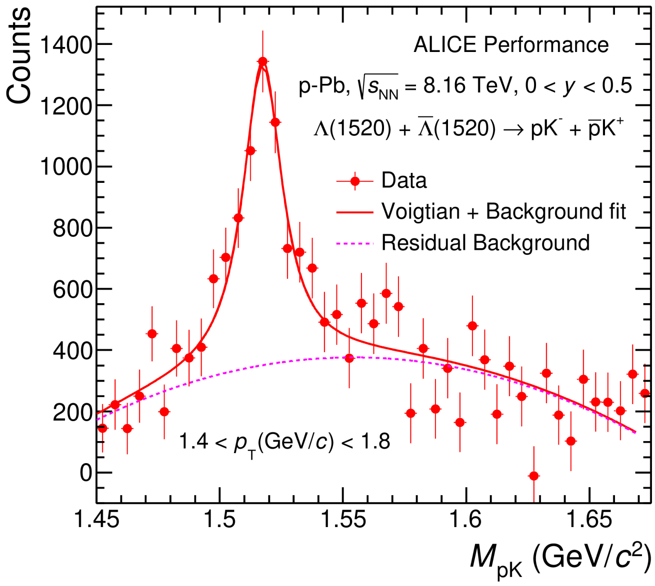

ALI-PERF-485863

Figure 4.6: The Λ^* signal after subtracting the combinatorial background (estimated using the mixed-event technique) from the unlike-sign charged particle pair invariant mass distribution for the $1.4 < p_{\mathrm{T}} < 1.8$ GeV/c bin, in non-single diffractive p–Pb collisions at $\sqrt{s_{\mathrm{NN}}} = 8.16$ TeV at midrapidity. The signal peak is fitted by a Voigtian function (solid red line), and the residual background is fitted by a second-order polynomial (dashed magenta line).

subsequently fitted with a Voigtian function combined with a second-order polynomial. The Voigtian, formed by convolving Breit-Wigner and Gaussian functions, characterizes the signal peak, whereas the polynomial denotes the residual background. The Gaussian part of the Voigtian function accounts for the mass resolution due to the detector's limitations, which is calculated from Monte-Carlo simulations and is discussed in the following sections. The range selected to fit the signal peak and the residual background in each p_{T} bin spans $1.45 < M_{\mathrm{inv}} < 1.65$ GeV/c^2. This interval effectively encompasses the signal region, facilitating accurate peak shape fitting and consistent subtraction of residual background. The fitting function with the residual background is given by

$$\frac{\Gamma/2\pi}{(m_0-m)^2+\Gamma^2/4}\,\frac{e^{-(m-m_0)/2\sigma^2}}{\sigma/\sqrt{2\pi}}+Am^2+Bm+C \tag{4.4}$$

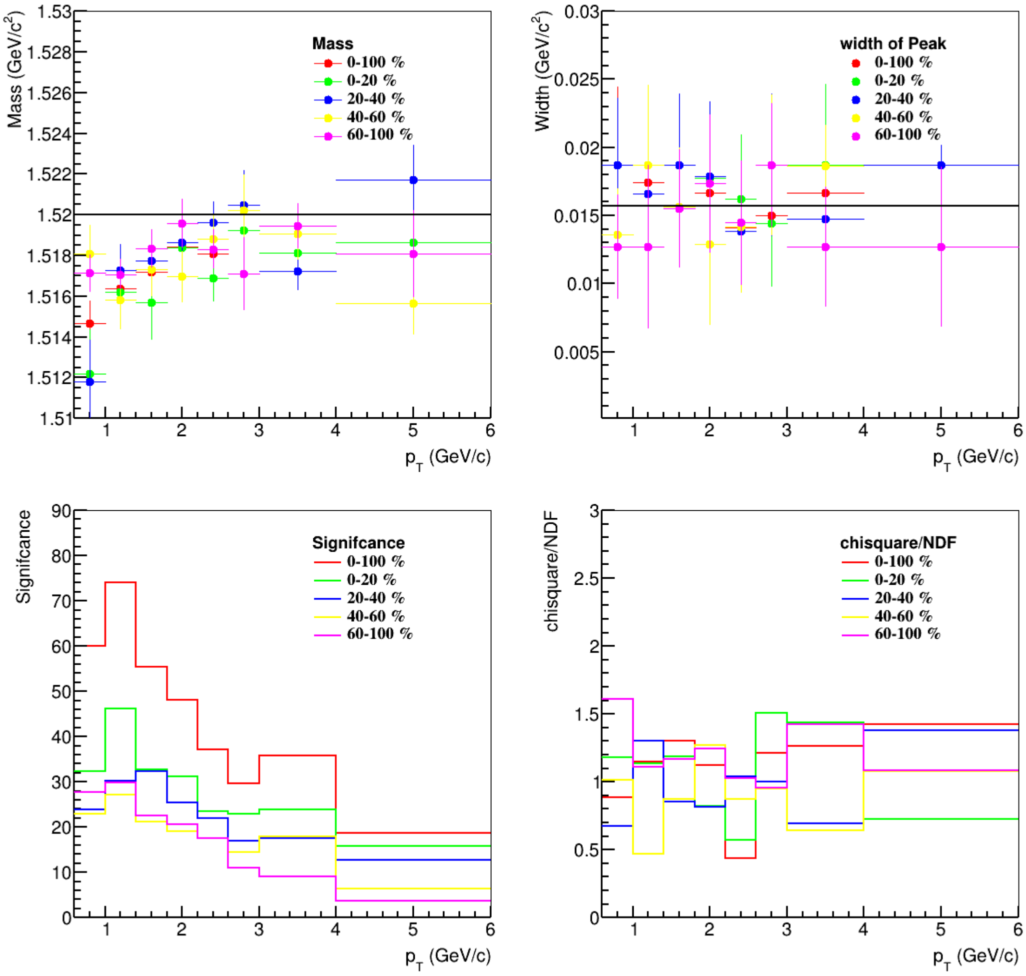

Figure 4.7: The mass, width, significance, and χ^2/ndf, as obtained from the Voigtian fit of Λ^* signal, are shown for p–Pb collisions at $\sqrt{s_{\mathrm{NN}}}$ = 8.16 TeV across various V0A multiplicity classes. In the top panel, the solid black lines indicate the PDG values for the mass and width of Λ^*.

where, m_0, Γ, and σ are the parameters used in the fitting process, representing the position of the mass peak, the full width at half maximum of the signal peak, and the detector-induced mass resolution, respectively. Figure 4.6 presents the invariant mass distribution after the removal of the combinatorial background. The distribution is fitted using a Voigtian along with a second-order polynomial. The mass, width, significance ($\frac{\text{signal}}{\sqrt{\text{signal+bkg}}}$), and χ^2/ndf values of the Λ^* signal, derived from the fit, are shown in Figure 4.7. The detector's mass resolution, obtained through Monte Carlo simulations, is used as a fixed parameter in the Voigtian fitting of the invariant mass spectra for Λ^* within different p_{T} intervals. To measure the detector's mass resolution, the differences between the generated mass (M_{Gen}) and the reconstructed mass (M_{Reco}) are computed by Monte-Carlo simulations and stored in a one-dimensional histogram. Gaussian functions are fitted to these distributions for each p_{T} bin, covering a range of $(-0.0045, +0.0045)$ GeV/c^2 (equivalent to approximately three times the RMS of the distributions). The standard deviations derived from these Gaussian fits serve as the default resolution values for Λ^* within their respective p_{T} bins. Moreover, the resolution values are directly determined from the histogram using `TH1::GetRMS()`. Another approach involves fitting the Monte-Carlo generated Λ^* signal with a Breit-Wigner

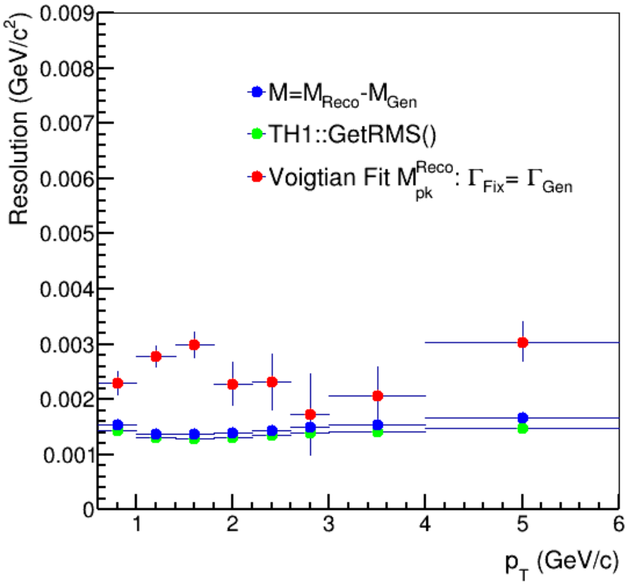

Figure 4.8: The detector's mass resolution, as determined through Monte-Carlo simulations, in minimum-bias p–Pb collisions at $\sqrt{s_{\mathrm{NN}}} = 8.16$ TeV.

function in each p_{T} bin, assuming no detector resolution. The width obtained from this fit is subsequently used as a fixed parameter to fit the reconstructed signal with a Voigtian function, where the resolution is treated as a variable parameter. The resolution parameters derived from these methods are illustrated in Figure 4.8. The peak of the Λ^* signal is observed within the p_{T} range from 0.6 GeV/c to 6 GeV/c in the case of the p–Pb system, while for the pp system, the peak of the signal is observed within the p_{T} range from 0.5 GeV/c to 4.5 GeV/c. The determination of these lower and upper limits is attributed to the lower significance of the signal observed below or above these respective values of p_{T}. This observation is evident in the significance plot in Figure 4.7.

4.5.4 Λ^* raw yield

The Λ^* raw yield is evaluated using two separate techniques: Bin Counting and Function Integration. Bin Counting serves as the default method, whereas Function Integration is employed for systematic studies. In the case of the p–Pb system, the width of the signal peak was left free while the invariant mass spectra were fitted in each p_{T} bin. Consequently, a systematic uncertainty is added to the final spectra while keeping the width fixed. Conversely, for the pp system, the width was fixed during fitting, and the systematic uncertainty is added while keeping the width free.

Bin Counting (Y_{BC}): The yield is obtained by integrating the invariant-mass histogram over the range $I_{\mathrm{min}} < m_{\mathrm{inv}} < I_{\mathrm{max}}$ and subtracting the integral of the residual background portion of the fit function (normalized by the bin width) over the same interval. The yields for the regions $(M_{\mathrm{K}} + M_{\mathrm{p}}) < m_{\mathrm{inv}} < I_{\mathrm{min}}$ and $m_{\mathrm{inv}} > I_{\mathrm{max}}$ are extracted from the peak fit and added to the yield calculated from the histogram. The statistical uncertainties of the yields in the tail regions are assumed to be fully correlated with each other and with the statistical uncertainty of the yield calculated from the histogram. Here, $I_{\mathrm{min}} = m_{\Lambda^*} - 2\Gamma$ and $I_{\mathrm{max}} = m_{\Lambda^*} + 2\Gamma$, where $m_{\Lambda^*} = 1519.54 \pm 0.17$ MeV/c^2 and $\Gamma = 15.73 \pm 0.29$ MeV/c^2 are the PDG values for the mass and width of Λ^* baryon, respectively. The raw yields, N_{raw}, are calculated as:

$$N_{\mathrm{raw}} = N_{\mathrm{counts}} - N_{\mathrm{poly2}} \tag{4.5}$$

where:

- N_{counts} represents the total number of counts in the histogram within the range $I_{\mathrm{min}} = m_{\Lambda^*} - 2\Gamma$ to $I_{\mathrm{max}} = m_{\Lambda^*} + 2\Gamma$.
- N_{poly2} is the integral of the second-degree polynomial (background fit) over the same range as N_{counts}.

The uncertainty in N_{raw} is determined through the use of the error propagation formula:

$$\sigma_{N_{\mathrm{raw}}} = \sqrt{\sigma^2_{N_{\mathrm{counts}}} + \sigma^2_{N_{\mathrm{poly2}}}} \tag{4.6}$$

where:

- $\sigma_{N_{\text{counts}}}$ is the statistical error associated with N_{counts}.
- $\sigma_{N_{\text{poly2}}}$ is the statistical error associated with N_{poly2}.

The error $\sigma_{N_{\text{poly2}}}$ is calculated as:

$$\begin{aligned}\sigma_{N_{\text{poly2}}} = \texttt{TF1::IntegralError}(&x_{\text{min}}, x_{\text{max}},\\ &\texttt{bg} \rightarrow \texttt{GetParameters()},\\ &\texttt{covGerr} \rightarrow \texttt{GetMatrixArray()})\end{aligned}$$

Here, the last argument is the Covariance Matrix, and 'bg' is the residual background function. The tail contribution from the peak fit function in the mass regions $(M_{\text{K}} + M_{\text{p}}) < m_{\text{inv}} < I_{\text{min}}$ and $m_{\text{inv}} > I_{\text{max}}$ is estimated as:

$$N_{\text{low}} = \int_{M_{\text{K}}+M_{\text{p}}}^{m_{\Lambda^*}-2\Gamma} \text{fit}(m_{\text{inv}})\,dm$$

$$N_{\text{high}} = \int_{m_{\Lambda^*}+2\Gamma}^{\infty} \text{fit}(m_{\text{inv}})\,dm$$

Thus, the final yield is expressed as:

$$Y_{BC} = N_{\text{low}} + N_{\text{raw}} + N_{\text{high}} \tag{4.7}$$

Function Integration (Y_{FI}): The yield is obtained by integrating the peak fitting function (Voigtian only) over the range $(M_{\text{K}} + M_{\text{p}}) < m_{\text{inv}} < \infty$:

$$Y_{FI} = \int_{M_{\text{K}}+M_{\text{p}}}^{\infty} \text{fit}(m_{\text{inv}})\ dm \tag{4.8}$$

The upper panel of Figure 4.9 illustrates the Λ^* raw yield as a function of p_{T} for minimum-bias and across four V0A multiplicity classes in p–Pb collisions at $\sqrt{s_{\text{NN}}}$ = 8.16 TeV, while the below panel of Figure 4.9 displays raw yield for minimum pp collisions at $\sqrt{s}$ = 8 TeV.

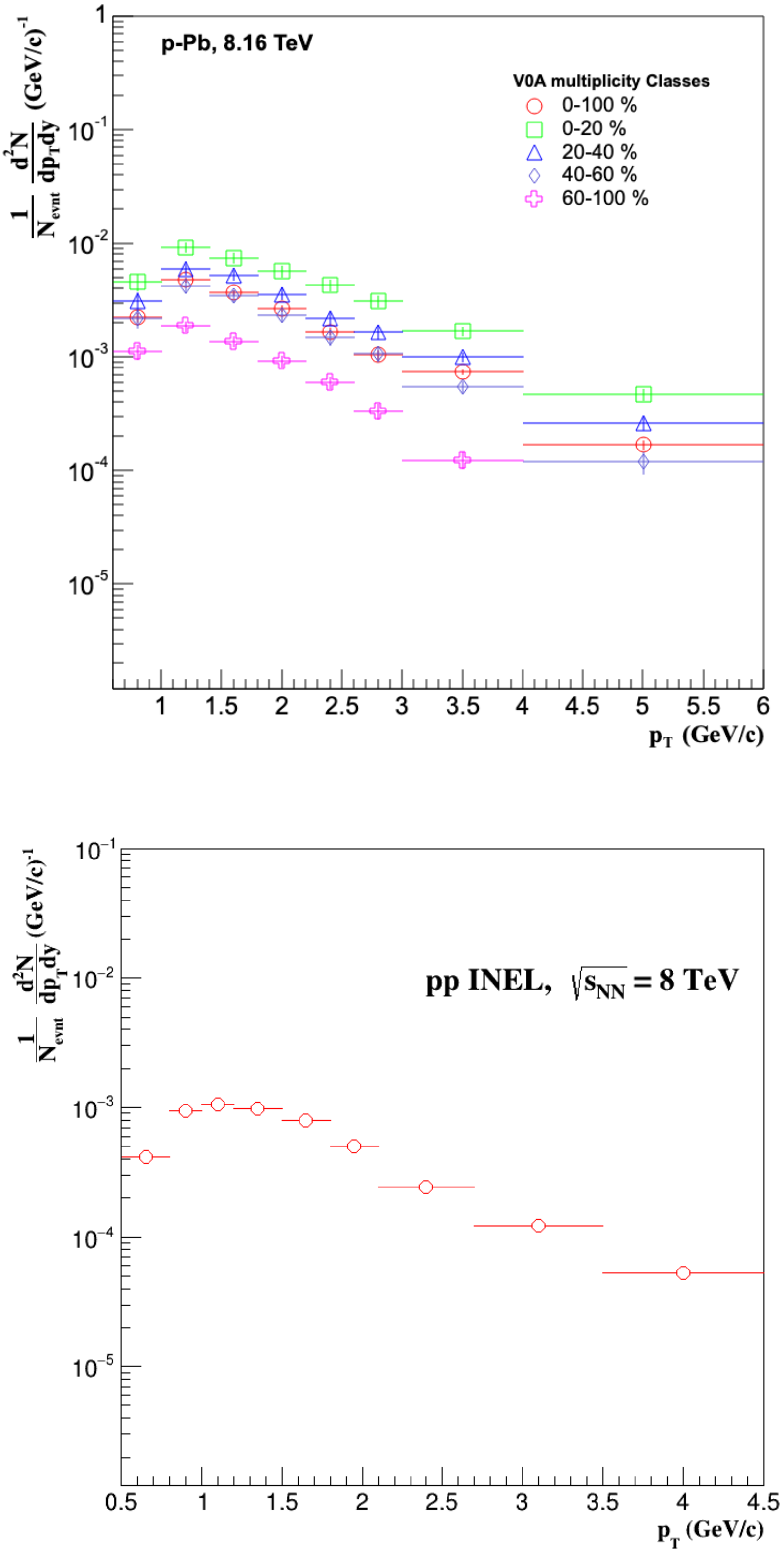

Figure 4.9: The Λ^* raw yield as a function of p_T for minimum-bias and across different V0A multiplicity classes in p–Pb collisions at $\sqrt{s_{NN}}$ = 8.16 TeV (upper panel) and in pp collisions at $\sqrt{s}$ = 8 TeV (lower panel).

4.6 Raw yield correction

The raw spectra undergo normalization by dividing by the number of events in each multiplicity class (N_{evt}), the efficiency of detector reconstruction and its acceptance ($A \times \varepsilon_{\mathrm{rec}}$), the branching ratio, and the factor for the rapidity window (dy). In the p-Pb collision system, with a rapidity window of (0,0.5), dy is assigned a value of 0.5, whereas for the pp collision system, with a rapidity window of (-0.5,0.5), dy is set to 1. The formula used for calculating the normalized corrected spectra is:

$$\frac{d^2N(\Lambda^*)}{dp_{\mathrm{T}}dy} = \frac{N_{\mathrm{rawCounts}}}{N_{\mathrm{evt}} \times BR \times dp_{\mathrm{T}} \times dy \times \varepsilon_{\mathrm{rec}}} \times f_{\mathrm{norm}} \times f_{\mathrm{SL}} \times f_{\mathrm{vtx}} \tag{4.9}$$

The factor f_{norm} acts as the correction factor to normalize non-single diffractive (NSD) events in minimum-bias p–Pb collisions and serves as the normalization factor for inelastic interactions in pp collisions. In the p–Pb system, the assigned value for f_{norm} is 0.992 [123], while in pp collisions it is fixed at 0.77 ± 0.02 [128]. The factor f_{SL} is a p_{T}-dependent parameter that compensates for the loss of signal due to the kINT7 trigger and event selection cuts, and is significant in low p_{T} regions. The factor f_{vtx} compensates for vertex loss by indicating the ratio of events with a successfully reconstructed vertex to the total of triggered events. For p–Pb collisions, f_{vtx} has a value of 1, and for pp collisions, it is set to 0.972 [123, 128].

4.6.1 Efficiency × Acceptance

Due to the detector's inability to fully reconstruct all generated Λ^* particles produced during collisions, correction factors such as efficiency and acceptance are calculated to adjust the measured Λ^* yield accordingly. Since these factors cannot be directly obtained from real data, a simulated dataset is used to measure the Λ^* reconstruction efficiency multiplied by the acceptance. This study employs the DPMJET-based event generator of periods LHC17l7a2_cent and LHC17l7a2_fast1 for p−Pb collisions, and PHOJET-based event generators, namely the periods LHC15h2a, LHC15h2b, LHC15h2c, LHC15h2d, LHC15h2f, LHC15h2h, and LHC152i for pp collisions. These generators simulate particle production and decay. Subsequently, GEANT3 is used to simulate particle interactions with the ALICE detector. Both real and simulated data undergo the same event selection and track quality cuts. In this context, particles generated by the event generator, without any detector effects, are termed as “generated particles". These particles serve as input for the GEANT3 detector simulation and subsequent track and signal reconstruction algorithms. The tracks identified by the reconstruction algorithms and that meet the track selection and PID criteria are referred to as “reconstructed tracks". A reconstructed Λ^* baryon is identified when both daughter tracks have been successfully reconstructed. The

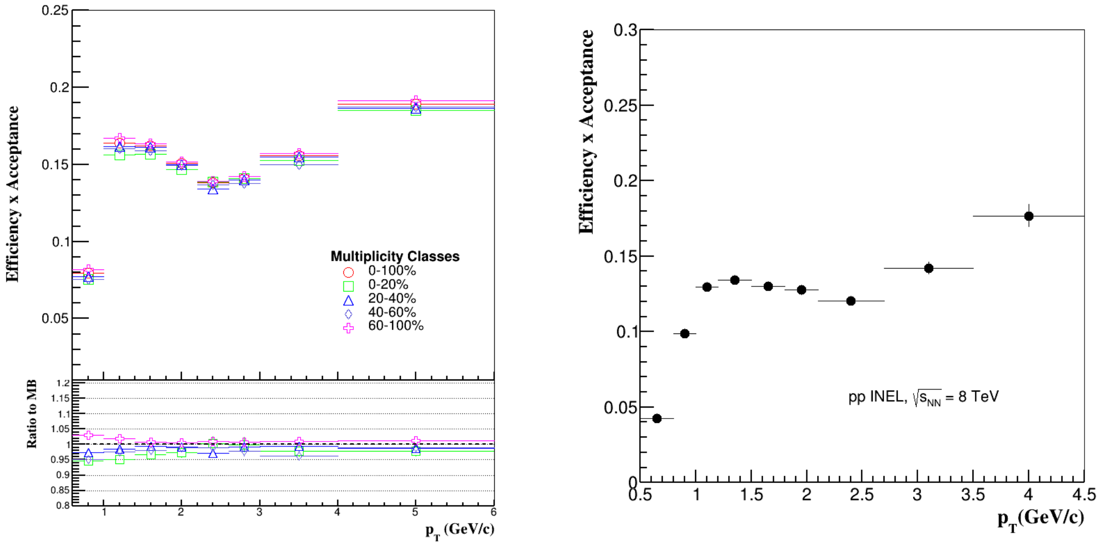

Figure 4.10: The Λ^* baryon reconstruction efficiency × acceptance as a function of $p_{\rm T}$ for different V0A multiplicity classes in p–Pb collisions at $\sqrt{s_{\rm NN}}$ = 8.16 TeV (left pannel) and for inelastic pp collisions at $\sqrt{s}$ = 8 TeV (right panel).

Λ^* reconstruction efficiency ($\varepsilon_{\rm rec}$) is defined as the ratio of the number of reconstructed Λ^* baryons, identified via their decay daughters after passing the same track and PID cuts applied to real data, to the number of generated Λ^* particles in the mid-rapidity region for both collision systems:

$$\varepsilon_{\rm rec} = \frac{N_{\rm reconstructed}}{N_{\rm generated}} \tag{4.10}$$

Here, $N_{\rm generated}$ represents the number of Λ^* baryons in the mid-rapidity region that decayed to $\rm pK^-$ pairs, and $N_{\rm reconstructed}$ denotes the number of Λ^* baryons in the mid-rapidity region for which decay daughters are successfully reconstructed.

The left and right panels of Figure 4.10 respectively show the product of detector efficiency and acceptance as a function of p_{T} for different multiplicity classes in p–Pb collisions at $\sqrt{s_{\mathrm{NN}}} = 8.16$ TeV and in inelastic pp collisions. The uncertainty in $\varepsilon_{\mathrm{rec}}$ is calculated using a Bayesian method, where the standard deviation of an efficiency $\varepsilon = k/n$, with k as a subset of the total n, is determined as:

$$\sigma_{\varepsilon} = \sqrt{\frac{k+1}{n+2}\left(\frac{k+2}{n+3} - \frac{k+1}{n+2}\right)} \tag{4.11}$$

The efficiency for the combined period is computed by taking the weighted average of efficiencies from individual data periods:

$$\mathrm{Efficiency}_{\mathrm{all\_data\_periods}}(\varepsilon) = \sum_{i} w_i \varepsilon_i(p_{\mathrm{T}}) \tag{4.12}$$

$$\sigma_{\varepsilon} = \sqrt{\sum_{i} w_i^2 \sigma_{\varepsilon_i}^2(p_{\mathrm{T}})} \tag{4.13}$$

Here, w_i represents the ratio of accepted events in the data period i to the total accepted events. The generated Λ^* spectra may exhibit a different shape compared to the measured (corrected) spectra. To address this, we implement a reweighting procedure for both the generated and reconstructed spectra obtained from simulations. The net effect of reweighting is more pronounced at low p_{T} compared to high p_{T} and procedure applied for reweighting is explained in Appendix E.

4.6.2 Signal and event loss correction

To account for the loss of Λ^* baryons due to event selection via the kINT7 trigger - which requires at least one hit in both the V0A and V0C detectors - instead of considering every inelastic event, the signal loss correction factor is determined. This is done through the following procedure:

Two sets of event selection criteria are established, labeled A and B:

Criterion A: Implement a cut solely on the generated $|v_z, Gen| < 10$ cm (without additional cuts).

Criterion B: Apply standard regular event-selection cuts.

The correction factor for signal loss, which indicates the fraction of signal lost due to event and trigger selection cuts, is computed as the ratio of two generated spectra, where:

Numerator: Particle p_{T} spectrum obtained with event selection A.

Denominator: Particle p_{T} spectrum obtained with event selection B.

Similarly, the event loss correction is calculated as the ratio:

Numerator: Number of events obtained with event selection B.

Denominator: Number of events obtained with event selection A.

In the p–Pb collision system, signal loss correction involves normalizing both the numerator and the denominator by their respective number of events, thus accounting for event loss. After correction, minimum-bias p–Pb collisions are termed as non-single diffractive (NSD) events. A constant function is fitted, and its value is used as the signal loss correction factor. In contrast, in pp collisions, this correction factor varies with p_{T} and peaks at low p_{T}, suggesting that events that do not meet the kINT7 selection criteria have softer p_{T} spectra compared to those with average and high p_{T} spectra. The error associated with this factor is computed as $\frac{|1-f_{SL}|}{2}$. The left panel of Figure 4.11 illustrates the signal loss correction for minimum-bias p–Pb collisions at $\sqrt{s_{\mathrm{NN}}}$ = 8.16 TeV. Corrections for other V0A multiplicity classes are detailed in the Appendix F. Table 4.2 lists the constant values from fits for minimum-bias events and various multiplicity classes in the p–Pb system. The

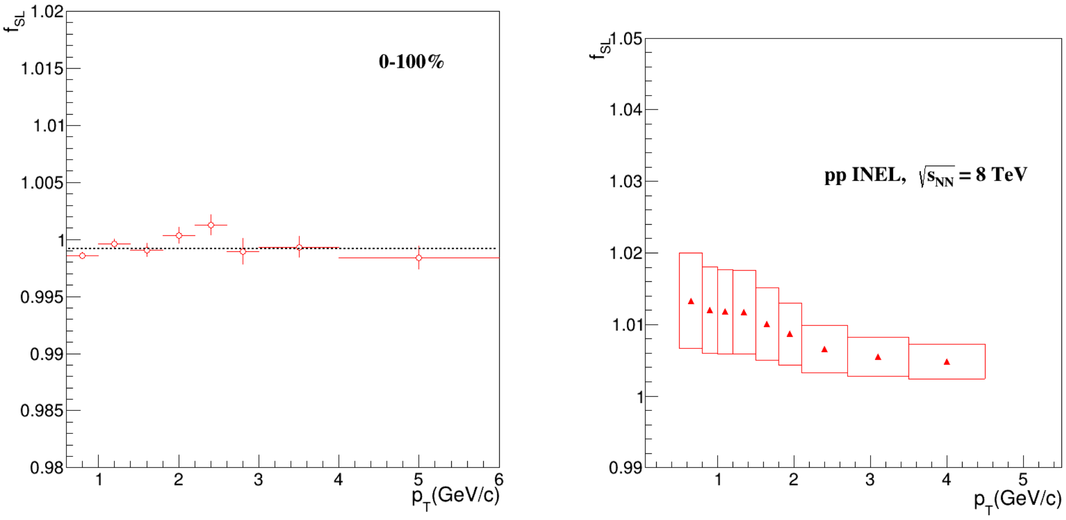

Figure 4.11: **Left panel:** Correction factors for signal loss in minimum-bias (0−100%) p–Pb collisions at $\sqrt{s_{\mathrm{NN}}}$ = 8.16 TeV. The dashed black line denotes a constant fit function. **Right panel:** Correction factor for signal loss in pp collisions at $\sqrt{s_{\mathrm{NN}}}$ = 8 TeV.

Table 4.2: The signal loss correction factor obtained from a constant fit to minimum-bias events (0-100%) and various V0A multiplicity classes in p–Pb collisions at $\sqrt{s_{\mathrm{NN}}}$ = 8.16 TeV.

V0A multiplicity classes (%)	f_{SL}
0–20	0.99985
20–40	0.99990
40–60	1.00051
60–100	0.99983
0–100	0.99916

signal loss correction for pp collisions at $\sqrt{s}$ = 8 TeV is shown in the right panel of Figure 4.11. After accounting for signal and event loss corrections, pp collisions are termed inelastic collisions.

4.7 Systematic uncertainties

The process for calculating systematic uncertainties is described as follows: Let y_{def} be the yield calculated using the set of default parameters, with associated statistical uncertainty σ_{def}. The yield of a systematic variation is represented by y_{sys}, with its statistical uncertainty σ_{sys}. The difference in yield is expressed as $\Delta = y_{\mathrm{def}} - y_{\mathrm{sys}}$, and the combined statistical uncertainty is calculated as $\sigma = \sqrt{\sigma_{\mathrm{def}}^2 - \sigma_{\mathrm{sys}}^2}$. Barlow consistency checks are performed for each systematic variation [129]. These checks determine whether a variation is a true source of systematic uncertainty or merely a result of statistical fluctuations. This involves computing the ratio $n = \Delta/\sigma$ for every p_{T} bin, and generating a distribution of n. Typically, two consistent measurements should have a mean near 0 and a standard deviation close to 1, with 68% (95%) of the data falling within $|\Delta/\sigma| < 1$ ($|\Delta/\sigma| < 2$). In this analysis, a variation is labeled as a source of systematic uncertainty if the standard deviation of the $n = \Delta/\sigma$ distribution exceeds 1.

The default parameters chosen for Λ^* measurements in these analyses include the following: Combinatorial background estimation is performed through the mixed event technique. The normalization region is selected outside the Λ^* baryon invariant mass peak, specifically in the range $1.75 < m_{\text{inv}} < 1.85$ GeV/c^2. A default fit region is defined as 1.45 $< m_{\text{inv}} < 1.65$ GeV/c^2. The residual background is modeled using a polynomial of 2^{nd} order (pol2). Signal peak fitting is done with Voigtian + pol2, where the width parameter is kept free, except for pp collisions where it is fixed in the default configuration. The resolution is fixed based on simulations. The Λ^* yield extraction relies on the bin counting method. Particle identification in the TPC and TOF detectors is done as follows: For daughter particles not detected in the TOF system, with momenta below 1.1 GeV/c for protons and 0.7 GeV/c for kaons, particle identification ensures $|N\sigma_{\text{TPC}}| < 2.0$. In the case of proton and kaon identification in pp collisions, the momentum thresholds are adjusted to below 1.0 GeV/c for protons and 0.6 GeV/c for kaons, with a $|N\sigma_{\text{TPC}}| < 3.0$ requirement. For daughter particles detected in the TOF system with momenta exceeding these limits, identification criteria are: $|N\sigma_{\text{TOF}}| < 3.0$ alongside $|N\sigma_{\text{TPC}}| < 5.0$ as a veto. The track selection cuts employed are `StandardITSTPCTrackCuts2011`.

4.7.1 Systematics due to signal extraction

In the systematic study pertaining to signal extraction, various parameters involved in the Λ^* measurement are systematically varied to assess their impact on the results. Firstly, the fitting range is explored through three distinct intervals: $1.44-1.71$ GeV/c^2, $1.46-1.62$ GeV/c^2, and $1.45-1.75$ GeV/c^2. Secondly, the normalization range is varied with two ranges: $1.85-2.0$ GeV/c^2 and $1.65-1.75$ GeV/c^2. The residual background variation is then explored, considering polynomial of orders 3 and 4. The yield extraction method undergoes adjustment, transitioning from the default bin counting to the function integration method. Peak width parameters are varied, with the width set free in the default scenario and fixed to the PDG value (0.01573 GeV/c^2) for the systematic study, except in pp system where it's fixed in the default case and set free as the systematic variation. The width range is examined within $\pm 2\sigma$ for the default case and $\pm 1\sigma$ for the systematic study. Peak fitting functions are also varied, using Voigtian function in the default case and the Breit-Wigner function in the systematic study. In the default case, the mass resolution parameters are obtained using Gaussian fits, while in the systematic investigation, they are derived from Breit-Wigner fits. Finally, the number of events mixed for obtaining the mixed-event background undergoes two variations: 15 events mixed and 5 events mixed. Each variation is systematically analyzed to find its impact on the measured Λ^* yield. The average value of fractional systematic uncertainty due to signal extraction across all p_{T} bins is 8.6% for p–Pb system and 6.5% for pp system.

4.7.2 Systematics due to particle identification

The systematic uncertainty related to particle identification (PID) is assessed by exploring variations in particle selection criteria, which are based on $\mathrm{d}E/\mathrm{d}x$ measurements in the TPC and time-of-flight measurements in the TOF. In both the p–Pb and pp collision systems, three variations are considered. In the p–Pb system, the default PID cut is set at TPC 2σ TOF 3σ, while variations include TPC 3σ TOF 3σ, TPC 3.5σ TOF 3.5σ, and TPC 2.5σ TOF 2.5σ. In case of the pp system, the default PID cut is set at TPC 3σ TOF 3σ, with variations including TPC 2σ TOF 3σ, TPC 2.5σ TOF 3σ, and TPC 3.0σ TOF 3.5σ. The average fractional systematic uncertainty across all p_{T} bins is found to be 5.4% for the p–Pb system and 4.2% for the pp system.

4.7.3 Systematics due to track and event selection

Systematic uncertainties originating from track selection are calculated by varying one track cut at a time across different parameters. **A)** DCA_{xy} cut: The default setting is $DCA_{xy} < 7\sigma$, while a value of $DCA_{xy} < 4\sigma$ is explored for systematic study. **B)** DCA_z cut: The default criterion is $DCA_z <$ 2cm, with systematic variations including $DCA_z <$ 3cm and $DCA_z <$ 1cm. **C)** Crossed-rows cut: The default requirement is a minimum of 70 crossed rows in TPC, while systematic variations entail considering 60 and 80 crossed rows for the study. **D)** TPC χ^2 cut: The default limit for χ^2 / TPC is < 4, with systematic exploration involving χ^2 / TPC < 5 and χ^2 / TPC < 3. **E)** ITS χ^2 cut: The default threshold for χ^2 / ITS is < 36, whereas systematic variations examine χ^2 / ITS < 49 and χ^2 / ITS < 25. **F)** Crossed rows over findable clusters TPC cut: The default condition requires a ratio of crossed rows over findable clusters in TPC > 0.8, while systematic variations explore ratios of 0.7 and 0.9 for the study. **G)** z vertex cut: The default setting is $z < |10|$, with a systematic variation of $z < |8|$ considered for the study. In the p–Pb system, the n parameter distributions resulting from various track cuts meet the Barlow criteria, indicating consistency, and therefore are not factored into the total systematic uncertainty. However, the event selection criteria do not satisfy the Barlow checks, contributing 4.5% to the overall systematic uncertainty. Conversely, in the pp system, the average fractional systematic uncertainty attributed to variations in track selection cuts is 5%, while event selection variations pass the Barlow checks and are thus excluded from the total systematic uncertainty calculation.

4.7.4 Material budget and hadronic interaction

The systematic uncertainties associated with the Λ^* yield, due to the material budget and hadronic interaction cross section within the detector, have been observed to remain constant up to p_{T} = 3.5 GeV/c and are insignificant for higher p_{T}. These values are taken from Ref. [84].

4.7.5 Global tracking

The uncertainty associated with determining the global tracking efficiency (ITS-TPC matching uncertainty) is consistent across various p_{T} values, with a 2% uncertainty observed for a single charged particle. When two tracks from the decay daughters of Λ^* are combined for invariant-mass analysis, this uncertainty increases to 4%. These values are taken from Ref. [123].

4.7.6 Total systematic uncertainty

The total systematic uncertainty is determined by summing all sources in quadrature. Nevertheless, the systematic uncertainty obtained from this method can show localized variations due to the independent calculation of systematic uncertainties for signal extraction and particle identification (PID) within each p_{T} bin, which are themselves prone to fluctuations. To address this, a smoothing technique is applied as follows: For each p_{T} bin j, the uncertainty σ_j is averaged with those of adjacent bins $(j \pm 1)$ during each iterative step. Let σ_j^i and $\sigma_{j\pm1}^i$ denote the uncertainty at the jth, $(j+1)$th, and $(j-1)$th locations at step i, respectively. The revised uncertainty σ_j^{i+1} is then computed as the average of the neighboring bins' uncertainties, $(\sigma_{j-1}^i + \sigma_j^i + \sigma_{j+1}^i)/3$. In this analysis, a single iteration of the smoothing process is performed, leaving the first and last p_{T} bins. The left and right panels of Figure 4.12 illustrate the summary of various systematic errors for minimum-bias p–Pb collisions at $\sqrt{s_{\mathrm{NN}}}$ = 8.16 TeV and inelastic pp collisions at $\sqrt{s_{\mathrm{NN}}}$ = 8 TeV after the smoothing process, respectively. For p–Pb collisions at $\sqrt{s_{\mathrm{NN}}}$ = 8.16 TeV, the systematic uncertainty pertaining to signal extraction is independently determined for the minimum-bias as well as for four V0A multiplicity classes, while the systematic uncertainties associated with PID cuts and track cuts are consistent across both the minimum-bias and the multiplicity classes. Table 4.3 presents a summary of systematic uncertainties originating from different sources in minimum-bias p–Pb collisions at 8.16 TeV and in the inelastic pp collisions at $\sqrt{s_{\mathrm{NN}}}$ = 8 TeV.

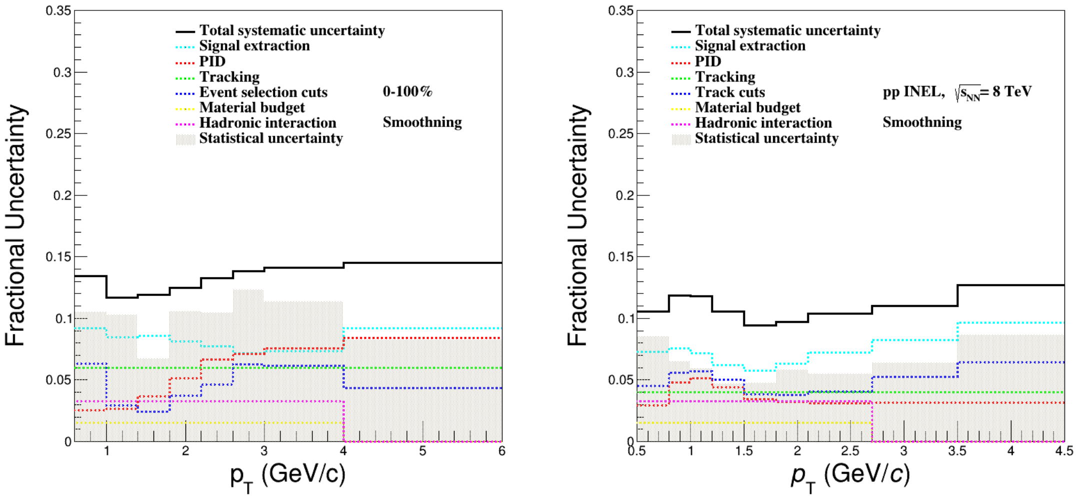

Figure 4.12: Total fractional systematic uncertainty after smoothening process due to various sources in minimum-bias p–Pb collisions at $\sqrt{s_{\mathrm{NN}}}$ = 8.16 TeV (left panel) and in the inelastic pp collisions at $\sqrt{s}$ = 8 TeV (right panel). The shaded gray area represents the total statistical uncertainty.

Table 4.3: Systematic uncertainties from various sources in minimum-bias p–Pb collisions at $\sqrt{s_{\rm NN}}$ = 8.16 TeV and inelastic pp collisions at $\sqrt{s_{\rm NN}}$ = 8 TeV.

Systematic source	p–Pb, 8.16 TeV	pp, 8 TeV
Signal extraction	8.6%	6.5%
Particle identification	5.4%	4.2%
Track and event cuts	4.5%	5.0%
Global tracking	4.0%	4.0%
Material budget	1.5% ($p_{\rm T}$ < 3.5 GeV/c)	1.4% ($p_{\rm T}$ < 3.5 GeV/c)
Hadronic interaction	3.3% ($p_{\rm T}$ < 3.5 GeV/c)	3.0% ($p_{\rm T}$ < 3.5 GeV/c)
Total	12.3%	11.0%

4.7.7 Uncorrelated systematic uncertainty

This section outlines the methodology used to evaluate the uncorrelated systematic uncertainty in the context of p–Pb collisions. We meticulously compared the $p_{\rm T}$ spectra for each systematic source across various multiplicity classes, noting deviations from the baseline (minimum-bias). A consistent shift in all multiplicity classes indicates a correlation in systematic errors. In contrast, if the data randomly varies around the baseline without a fixed pattern, the systematic error is considered uncorrelated. We compute uncorrelated systematic uncertainty solely for signal extraction sources, as uncertainties from PID cuts and track selection cuts are based on minimum-bias data across all multiplicity classes. Despite the full correlation of global tracking efficiency, systematic uncertainties related to the material budget and hadronic interactions remain independent of multiplicity classes but show a dependency on $p_{\rm T}$, making them partially correlated. Figure 4.13 presents the uncorrelated systematic uncertainty for various V0A multiplicity classes in p–Pb collisions at $\sqrt{s_{\rm NN}}$ =8.16 TeV.

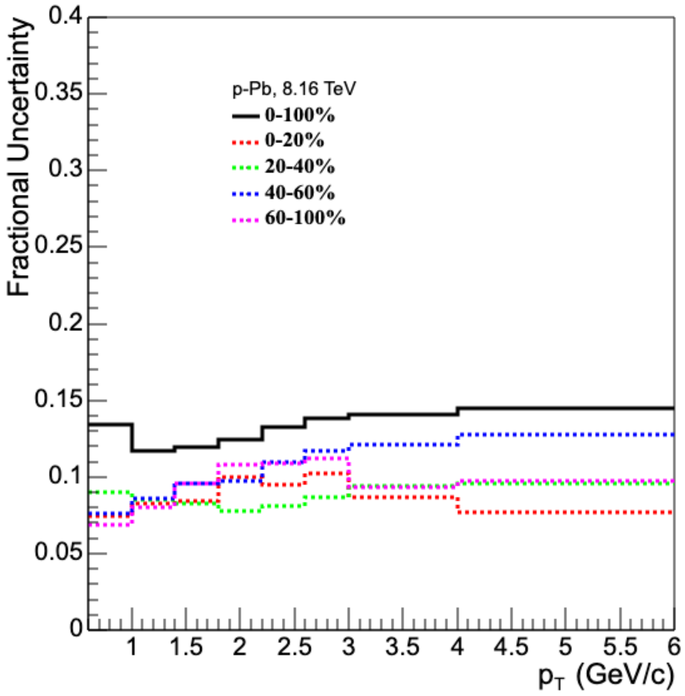

Figure 4.13: Uncorrelated systematic uncertainties for various multiplicity classes in p–Pb collisions at $\sqrt{s_{\mathrm{NN}}}$ = 8.16 TeV. Solid black line shows total systematic uncertainty for minimim-bias collisons.

4.8 Results and discussion

4.8.1 Transverse momentum spectra

The raw p_{T} spectra undergo corrections using factors for efficiency × acceptance, event loss, and signal loss. The systematic error applied to minimum-bias p–Pb collisions is specific to the minimum-bias case only. Each multiplicity class is associated with its own set of systematic errors. Figure 4.14 presents the corrected p_{T} spectra, complete with systematic and statistical errors, for non-single diffractive (NSD) and four V0A multiplicity classes in p–Pb collisions at $\sqrt{s_{\mathrm{NN}}}$ = 8.16 TeV, as well as for inelastic pp collisions at $\sqrt{s_{\mathrm{NN}}}$ = 8 TeV within the mid-rapidity range. The Λ^* p_{T} spectra in the p–Pb collisions undergo hardening with multiplicity. The corrected p_{T} spectra are fitted with the Levy-Tsallis function [130]. This function describes the exponential shape of the spectrum at low p_{T} and the power-law distribution at high p_{T}, quantified by the inverse slope parameter C and the exponent

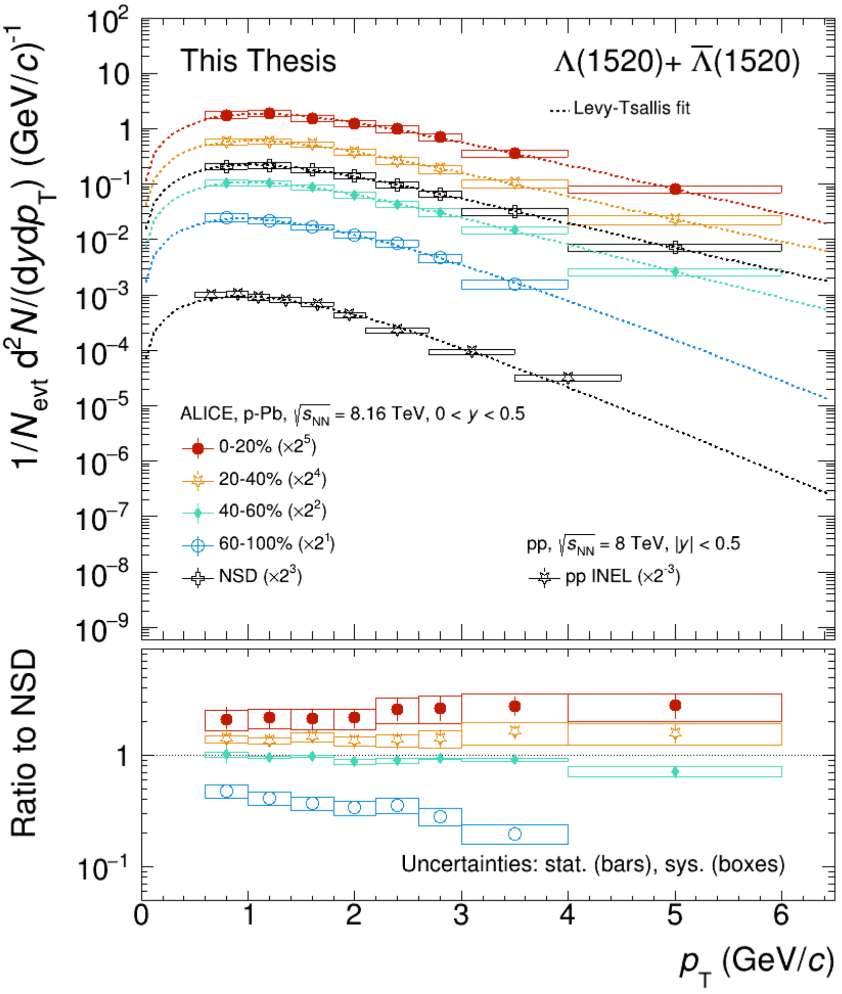

Figure 4.14: The corrected p_{T} spectra of Λ^* for NSD events and across four multiplicity intervals (0–20%, 20–40%, 40–60%, and 60–100%) in p–Pb collisions at $\sqrt{s_{\mathrm{NN}}}$ = 8.16 TeV, as well as for inelastic pp collisions at $\sqrt{s_{\mathrm{NN}}}$ = 8 TeV. The lower panel illustrates the ratio of p_{T} spectra in different multiplicity classes within p–Pb collisions to the minimum-bias spectra of the same collision system. Both statistical (bars) and systematic (boxes) errors are presented.

parameter n, respectively.

$$\frac{d^2N}{dydp_{\mathrm{T}}} = p_{\mathrm{T}} \times \frac{dN}{dy} \times \frac{(n-1)(n-2)}{nC[nC+m(n-2)]}[1+\frac{m_T-m}{nT}]^{-n} \tag{4.14}$$

where, m and m_T are the mass and transverse mass of Λ^*. The function gives a good description of the data in the full measured range of p_{T} of Λ^*. The dependence of the Λ^* p_{T} spectra on energy has been observed by measuring the ratio of the p_{T} spectra at $\sqrt{s_{\mathrm{NN}}}$ = 8.16 TeV to those at $\sqrt{s_{\mathrm{NN}}}$ = 5.02 TeV [84] for NSD and different V0A multiplicity classes in p–Pb collisions, and for inelastic pp collisions at $\sqrt{s_{\mathrm{NN}}}$ = 8 TeV relative to the p_{T} spectra

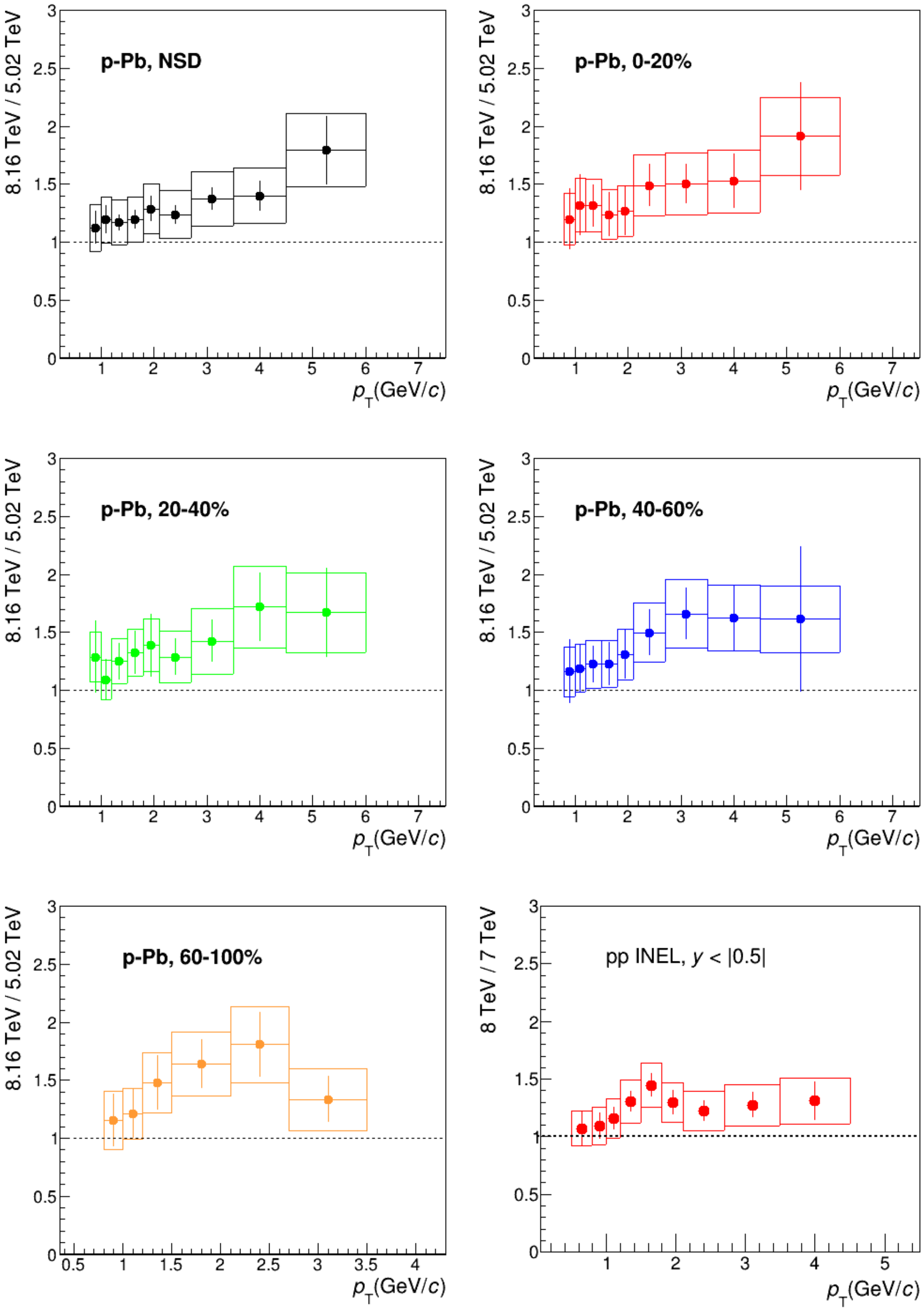

Figure 4.15: The p_T spectral ratios of Λ^* for NSD and four V0A multiplicity classes in p–Pb collisions at $\sqrt{s_{NN}}$ = 8.16 TeV are compared to those at $\sqrt{s_{NN}}$ = 5.02 TeV, along with the spectral ratio of Λ^* in pp collisions at 8 TeV versus 7 TeV. A dotted line at unity provides visual guidance. The errors are represented by bars for statistical errors and boxes for systematic errors.

at $\sqrt{s_{\mathrm{NN}}}$ = 7 TeV [84], as shown in Figure 4.15. The spectral ratios exhibit energy dependence, particularly noticeable at high p_{T}, while the ratio at low p_{T} remains close to unity within statistical or systematic errors for the p–Pb and pp collisions. This phenomenon is consistent across minimum-bias events and all analyzed multiplicity classes, indicating that particle production in the hard-scattering region depends on the energy of the colliding system. Figure 4.16 illustrates the comparison of the Λ^* p_{T} spectrum in the NSD event class

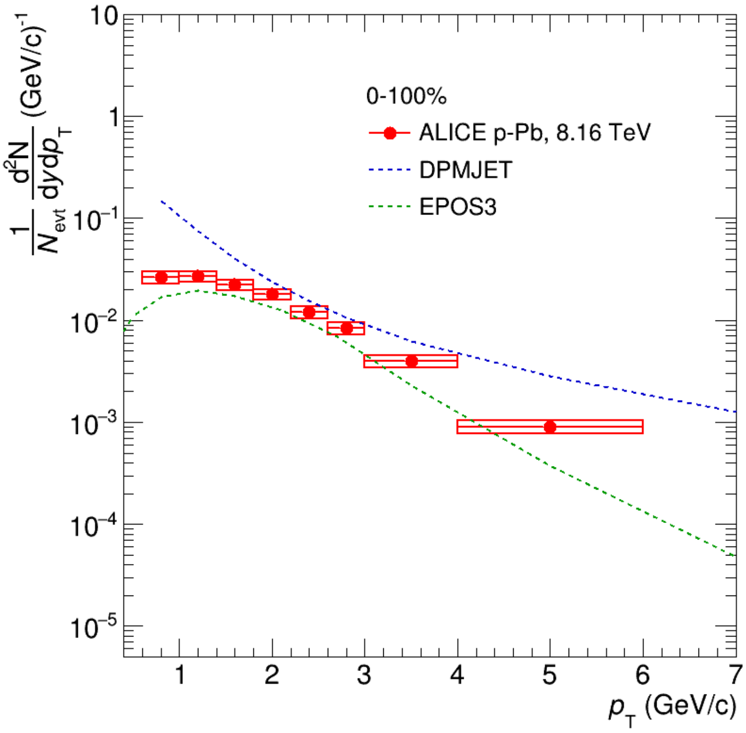

Figure 4.16: The Λ^* p_{T} spectra, measured in the mid-rapidity range for p–Pb collisions at $\sqrt{s_{\mathrm{NN}}}$ = 8.16 TeV, is compared to the predictions from EPOS3 [131] and DPMJET [132] models. The statistical and systematic uncertainties are shown as bars and boxes, respectively.

with predictions from the EPOS3 [131] and DPMJET [132] models. The EPOS3 model is based on partons and employs the Gribov-Regge multiple-scattering framework, where scatterings are depicted as pomerons analogous to parton ladders. These ladders evolve into strings or flux tubes that are initially split into core and corona components. The core, with its high density, undergoes collective hadronization, whereas the low-density, high-momentum corona does not. In contrast, DPMJET is a dual-parton model inspired by QCD and uses the Gribov-Glauber approach, treating soft and hard scatterings distinctly. The DPMJET model overestimated the data, while EPOS3 underestimated it in all p_{T} ranges.

However, EPOS3 accurately captures the spectral shape throughout the p_{T} range.

4.8.2 Integrated yield and mean transverse momentum

The p_{T}-integrated yield ($\mathrm{d}N/\mathrm{d}y$) is determined by integrating the spectrum within the measured range and extrapolating it to zero p_{T} and higher p_{T} by fitting the measured spectra with the Levy-Tsallis parametrization [130]. The integrated yield ($\mathrm{d}N/\mathrm{d}y$) and mean p_{T} ($\langle p_{\mathrm{T}}\rangle$) are computed using the `YieldMean.C` macro in the `ALICE/PWGLF/SPECTRA` module of the AliRoot software. The final values and statistical uncertainties are obtained from Levy-Tsallis fits performed on spectra considering statistical uncertainties and data points within the fit regions. Systematic uncertainties consist of two components: one originating from the systematic uncertainties of the measured spectra and the other from extrapolating the spectra to unmeasured regions. The first component of systematic uncertainties is evaluated by re-fitting the data while adjusting the points within the errors, assuming that they are fully uncorrelated in all p_{T} bins. The maximum deviation from the default value is designated as uncertainty. The second component of systematic uncertainties is determined by fitting the measured spectra with various functions such as the m_{T}-exponential, the p_{T}-exponential, Boltzmann-Gibbs blast wave and taking the standard deviation from all fits as the systematic uncertainty due to extrapolation. The systematic uncertainty originating

Table 4.4: The $\mathrm{d}N/\mathrm{d}y$ and $\langle p_{\mathrm{T}}\rangle$ values for Λ^{*} in NSD and four multiplicity classes in p–Pb collisions at $\sqrt{s_{\mathrm{NN}}} = 8.16$ TeV, and for inelastic pp collisions at $\sqrt{s} = 8$ TeV. The percentage contribution due to extrapolation is provided in brackets.

Multiplicity(%)	$dN/dy \pm$ stat $\pm$ sys (extr.)	$< p_{\mathrm{T}} > \pm$ stat $\pm$ sys (extr.)
0–20	$0.13 \pm 0.006 \pm 0.018(14.7\%)$	$1.8 \pm 0.043 \pm 0.08(7.4\%)$
20–40	$0.083 \pm 0.004 \pm 0.010(13.1\%)$	$1.7 \pm 0.047 \pm 0.076(8.0\%)$
40–60	$0.056 \pm 0.003 \pm 0.0075(13.3\%)$	$1.6 \pm 0.045 \pm 0.067(9.1\%)$
60–100	$0.022 \pm 0.001 \pm 0.0036(18.7\%)$	$1.42 \pm 0.03 \pm 0.068(11.7\%)$
NSD	$0.059 \pm 0.001 \pm 0.0075(13.6\%)$	$1.66 \pm 0.02 \pm 0.067(9.6\%)$
pp, INEL	$0.014 \pm 0.0003 \pm 0.0017(10.0\%)$	$1.31 \pm 0.015 \pm 0.046(6.0\%)$

from extrapolation is combined in quadrature with the uncertainty from the measured region to determine the final systematic uncertainty of the yield. The computed values of $\mathrm{d}N/\mathrm{d}y$ and $\langle p_{\mathrm{T}}\rangle$, along with their statistical and systematic uncertainties, are given in Table 4.4.

The Λ^* p_{T}-integrated yield ($\mathrm{d}N/\mathrm{d}y$) as a function of $\langle \mathrm{d}N_{\mathrm{ch}}/\mathrm{d}\eta \rangle_{|y|<0.5}$ is presented in the upper panel of Figure 4.17. These results are compared with other ALICE measurements in p–Pb collisions at $\sqrt{s_{\mathrm{NN}}} = 5.02$ TeV [84]. It is interesting to note that the integrated yield, although not explicitly shown for Pb–Pb collisions [83] in Figure 4.17, depends on charged particle multiplicity rather than the specific collision system and the collision energy. The integrated yield exhibits a smooth evolution as a function of multiplicity from pp to p–Pb collisions. Even for similar $\langle \mathrm{d}N_{\mathrm{ch}}/\mathrm{d}\eta \rangle_{|y|<0.5}$, these values remain consistent within uncertainties for different colliding systems and at various LHC energies. This observation indicates that event multiplicity serves as a common driver for hadron production, demonstrating a remarkable consistency across different colliding systems and energies at the LHC. The EPOS3 model with and without UrQMD, underestimated the data, although it follows a linear trend of increase with event multiplicity, similar to the observed ALICE data. The $\langle p_{\mathrm{T}}\rangle$ exhibits an increasing trend as a function of $\langle \mathrm{d}N_{\mathrm{ch}}/\mathrm{d}\eta \rangle_{|y|<0.5}$ as shown in the lower panel of Figure 4.17 which confirms the hardening of the p_{T} spectra of Λ^* with multiplicity. Although the $\langle p_{\mathrm{T}}\rangle$ results for Pb–Pb system are not shown explicitly, but a closer observation and comparison across all systems reveal an interesting pattern: the rate at which the mean p_{T} increases with multiplicity tends to decrease as the size of the colliding system increases. Specifically, the increase in $\langle p_{\mathrm{T}}\rangle$ is more rapid for pp and p–Pb compared to the Pb–Pb system [83]. Moreover, for common multiplicity values, the $\langle p_{\mathrm{T}}\rangle$ values in pp and p–Pb collisions surpass those observed in Pb–Pb collisions. This variation in $\langle p_{\mathrm{T}}\rangle$ values at comparable multiplicities across Pb–Pb, p–Pb, and pp collisions suggests differences in the geometry and dynamics of these collision systems and is related to the collective flow observed in large collision systems [83] compared to smaller collision systems.

The strong increase of $\langle p_{\mathrm{T}}\rangle$ with $\langle \mathrm{d}N_{\mathrm{ch}}/\mathrm{d}\eta \rangle_{|y|<0.5}$ in small collision systems can be further investigated by analyzing the measurements for $\langle p_{\mathrm{T}}\rangle$ from different models in pp

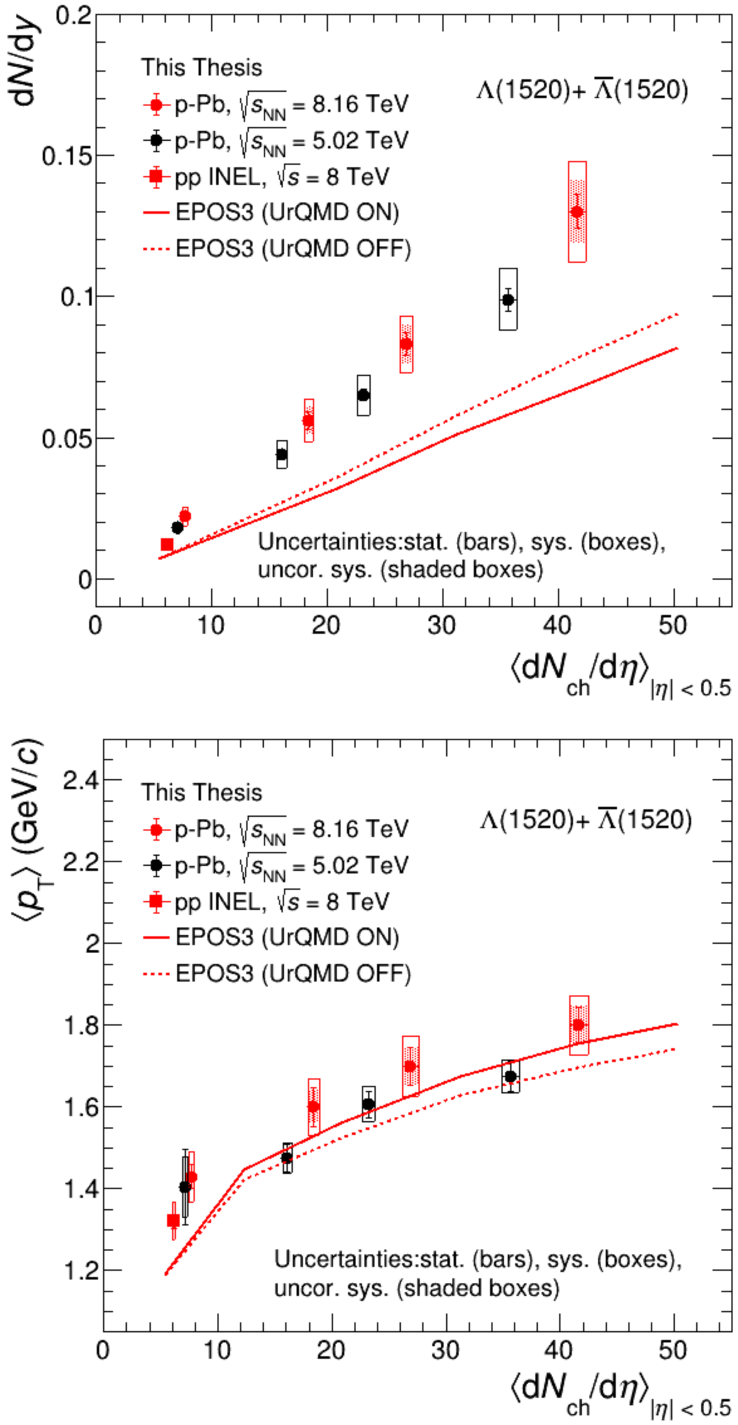

Figure 4.17: The p_T-integrated yield (dN/dy, upper panel) and average transverse momentum ($\langle p_T \rangle$, lower panel) as a function of charged particle pseudorapidity density for Λ^* in p–Pb collisions at $\sqrt{s_{NN}}$ = 8.16 TeV (round red markers) and $\sqrt{s_{NN}}$ = 5.02 TeV (black markers) [84], and for inelastic pp collisions at $\sqrt{s}$ = 8 TeV (square red markers). The solid and dotted lines represent the measurements in the p–Pb system at $\sqrt{s_{NN}}$ = 8.16 TeV from the EPOS3 with and without UrQMD, respectively. Statistical errors are represented by bars, systematic errors by boxes, and shaded boxes indicate uncorrelated errors.

and p–Pb collisions that incorporate processes like color reconnection between strings produced in multi-parton interactions, different string fragmentation processes, and the core-corona mechanism. It was observed in Ref. [133] that the PYTHIA8 model with color reconnection, which introduces a flow–like effect, and the EPOS-LHC model, which uses parameterized flow, are able to reproduce the increasing trend of $\langle p_{\mathrm{T}} \rangle$ of strange hadrons as a function of multiplicity in pp collisions at $\sqrt{s}$ = 13 TeV. The predictions of $\langle p_{\mathrm{T}} \rangle$ of Λ^* from the EPOS3 model in p–Pb collisions at $\sqrt{s_{\mathrm{NN}}}$ = 8.16 TeV describe the data very well throughout the multiplicity range.

4.8.3 Nuclear modification factor

The p–Pb collisions provide a good test to check whether the suppression observed in high p_{T} region in Pb–Pb collisions is due to the hot partonic QCD medium or due to cold nuclear matter (CNM) effects. This can be studied by the nuclear modification factor defined as:

$$R_{pPb}(p_{\mathrm{T}}) = \frac{d^2N_{pPb}/dydp_T}{\langle N_{\mathrm{Coll}} \rangle . d^2N/dydp_T} \tag{4.15}$$

where the numerator represents the measured spectral yield in p–Pb collisions, the denominator includes $\langle N_{\mathrm{Coll}} \rangle$ = 7.118 [134], and the measured spectral yields in inelastic pp collisions.

Due to the fact that the measured hadron spectra in inelastic pp collisions are not available at $\sqrt{s_{\mathrm{NN}}}$ = 8.16 TeV, the reference p_{T} spectra is obtained using the simulation approach of the p_{T} spectrum from the EPOS3 model and the p_{T} spectrum from ALICE data in the closest beam energies at $\sqrt{s_{\mathrm{NN}}}$ = 8 TeV. The reference p_{T} spectrum at $\sqrt{s_{\mathrm{NN}}}$ = 8.16 TeV is calculated using the p_{T} spectrum at $\sqrt{s_{\mathrm{NN}}}$ = 8 TeV scaled with a correction factor. The correction factor is calculated as the ratio of the p_{T} spectrum at $\sqrt{s_{\mathrm{NN}}}$ = 8.16 TeV to the p_{T} spectrum at $\sqrt{s_{\mathrm{NN}}}$ = 8 TeV, obtained from EPOS3 shown in Figure 4.18. The total systematic error in the reference pp spectra obtained is calculated by taking the quadrature sum of the systematic uncertainty from the measured p_{T} spectra at $\sqrt{s_{\mathrm{NN}}}$ = 8 TeV and the difference of the reference p_{T} spectra with the measured p_{T} spectra at $\sqrt{s_{\mathrm{NN}}}$ = 8 TeV. Fig-

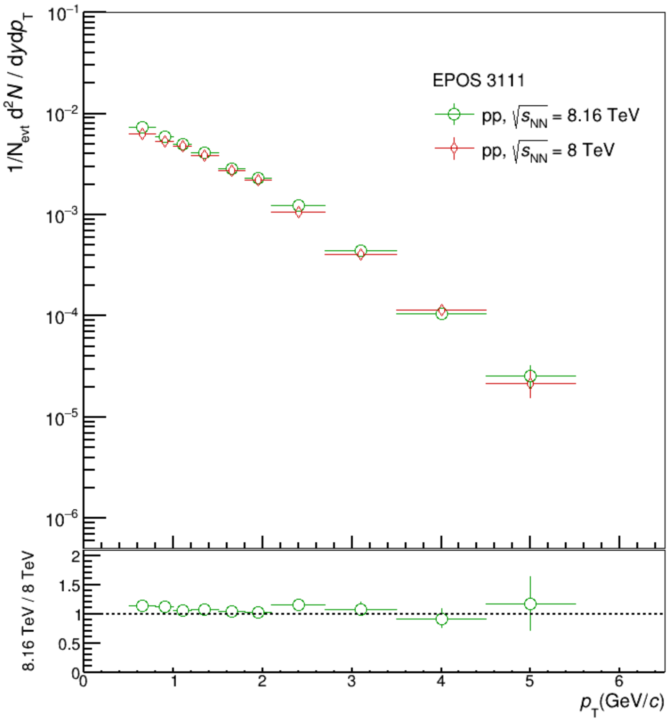

Figure 4.18: The Λ^* p_T spectra measured in pp collision at $\sqrt{s}$ = 8.16 TeV and $\sqrt{s}$ = 8 TeV from EPOS3 model (top panel) and their ratio (bottom panel) which serves as the correction factor for R_{pPb} measurements.

ure 4.19 shows the particle species dependence of the nuclear modification factors in p–Pb collisions at 8.16 TeV. The left panel of Figure 4.19 includes the nuclear modification factor for K^{*0} [123] and K^0_S [135] while the right panel includes nuclear modification factors for Λ [135] and Λ^* as a function of p_T in p–Pb collisions at $\sqrt{s_{NN}}$ = 8.16 TeV. We compare R_{pPb} of different baryons and mesons to check the mass dependence of particle production and to investigate the mechanisms involved in the production of baryons and mesons. At low p_T (< 2 GeV/c), R_{pPb} is less than unity for all hadrons. At intermediate p_T (2−8 GeV/c), R_{pPb} of the baryons shows a Cronin-like enhancement [136, 137]. In particular, resonances experience greater suppression in the low p_T regime compared to stable particles, reflecting the influence of later-stage hadronic interactions of the decay daughters of these resonances in p–Pb collisions. At high p_T (> 8 GeV/c), the R_{pPb} values of all particles are consistent with unity within the uncertainties in the collisions of p–Pb at $\sqrt{s_{NN}}$ = 8.16 TeV suggesting that there is no modification in R_{pPb} due to the effects of cold nuclear matter for different species of particles. Thus, p–Pb collisions effectively disentangle hot and cold nuclear matter effects. Similar findings are also reported for π^0 meson with p_T up to 200 GeV/c in

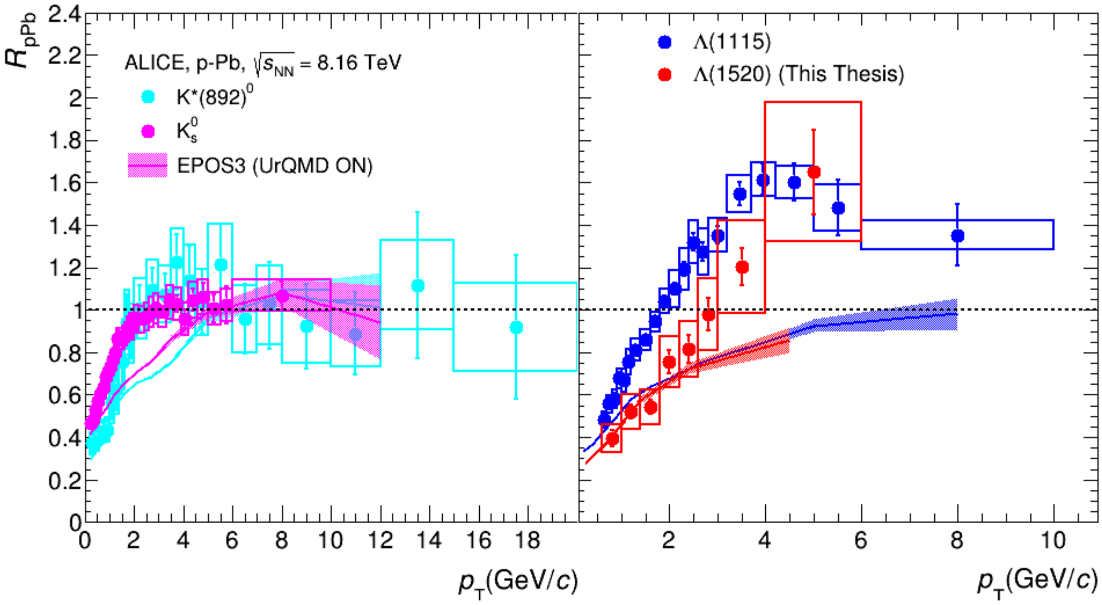

Figure 4.19: The left panel shows the R_{pPb} of K^{*0} [123] and $\mathrm{K}^0_{\mathrm{S}}$ [135], while the right panel depicts the R_{pPb} of Λ [135] and Λ^*, both as functions of p_{T} in p–Pb collisions at $\sqrt{s_{\mathrm{NN}}}$ = 8.16 TeV, with statistical and systematic uncertainties represented by vertical bars and boxes, respectively. The bands represent the measurements from EPOS3 with UrQMD.

p–Pb collisions at $\sqrt{s_{\mathrm{NN}}}$ = 8.16 TeV [138], for charged hadrons in p–Pb collisions at $\sqrt{s_{\mathrm{NN}}}$ = 5.02 TeV by ALICE [139, 140], and for strange hadrons by CMS in p–Pb collisions at $\sqrt{s_{\mathrm{NN}}}$ = 5.02 TeV [141] and by STAR in d–Au collisions at $\sqrt{s_{\mathrm{NN}}}$ = 200 GeV [142].

4.8.4 Resonance to stable particle yield ratio

We observe from the previous measurements in p–Pb collisions that the ratios of ρ^0 and K^{*0} to stable hadrons show suppression with increase in multiplicity, while no such suppression has been observed for ϕ resonance as it has a longer lifetime compared to other hadronic resonances [79, 123]. The ratios of Λ^* and K^{*0} to their corresponding ground state particles Λ and $\mathrm{K}^0_{\mathrm{S}}$ in p–Pb collision system at $\sqrt{s_{\mathrm{NN}}}$ = 8.16 TeV is measured and is shown in Figure 4.20. We observed no suppression or enhancement in the Λ^*/Λ yield ratio in p–Pb collisions at the highest available energy at LHC and these measurements confirm previous measurements at $\sqrt{s_{\mathrm{NN}}}$ = 5.02 TeV [84]. Conversely, $\mathrm{K}^{*0}/\mathrm{K}^0_{\mathrm{S}}$ yield ratio shows some decreasing trend with multiplicity. This provides hints for the formation of a hadronic phase in the p–Pb collision system but for a very brief time. The EPOS3 model provides a unique

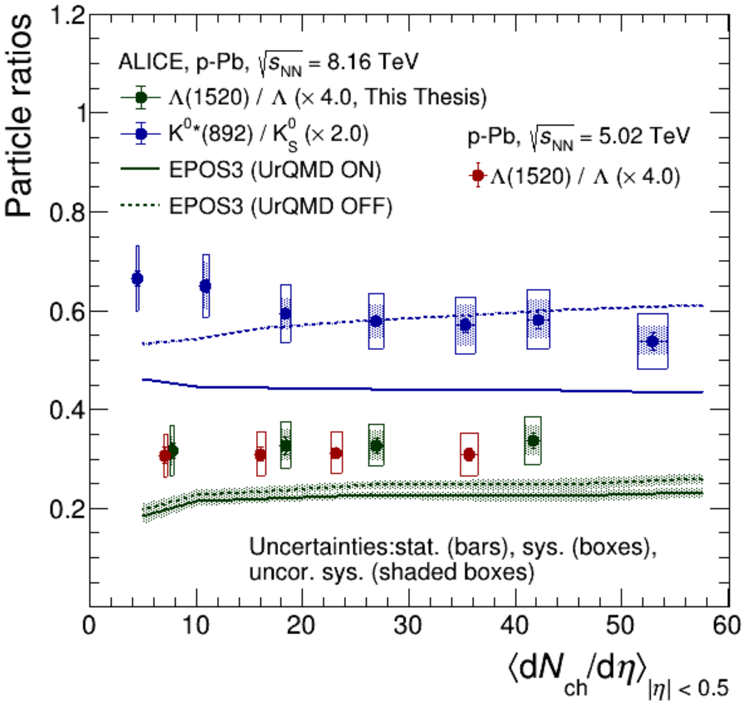

Figure 4.20: The p_T-integrated yield ratios for K^{*0}/K^0_S [123, 135] and Λ^*/Λ [135] are shown as a function of $\langle dN_{ch}/d\eta \rangle_{|\eta|<0.5}$. The Λ^*/Λ ratios are further compared with available data from p–Pb collisions at 5.02 TeV [84]. Measurements from the EPOS3 model, both with and without UrQMD, are included as well.

opportunity to understand these data measurements of resonance to non-resonance yield ratios due to its incorporation of later-stage hadronic interactions, which can be switched "ON" and "OFF" states during events generation to assess their impact on particle yields. Consequently, the calculation of these ratios has been performed using the EPOS3 model, both with and without final-state interactions. The EPOS3 with UrQMD "ON" and "OFF" predicts a consistent flat-ratio trend for the $\Lambda^*/\ \Lambda$ ratio similar to the data.

In contrast, the ratio for the K^{*0} resonance exhibits a decreasing trend with UrQMD "ON" while there is no such suppression when UrQMD is "OFF" and these measurements also align with the data. These observations indicate that the EPOS3 model predicts the existence of a hadronic phase in p–Pb collisions at $\sqrt{s_{NN}}$ = 8.16 TeV but for a very short time such that Λ^* decays after the hadronic phase ends and its daughters do not experience any rescattering effects in the hadronic gas. However, in case of decay daughters of the K^{*0} resonance, they undergo rescattering in the hadronic phase due to its short lifetime, which is comparable to the lifetime of the hadronic phase in p–Pb collisions at $\sqrt{s_{NN}}$ = 8.16 TeV.

Chapter 5

Strangeness and resonances in EPOS4

5.1 Introduction

High-energy heavy-ion collisions provide a unique opportunity to study the quark-gluon plasma (QGP), also called the fireball, a deconfined state of quarks and gluons created under extreme conditions of temperature and/or density [1]. This state of matter, believed to have existed shortly after the Big Bang, forms in the early stages of heavy-ion collisions and undergoes rapid expansion and cooling. As the fireball evolves and undergoes phase transitions, it becomes inaccessible for direct observation. In this context, the study of strange particles is particularly compelling. An enhancement in the production of strange quarks relative to ‘up’ and ‘down’ quarks is among the earliest proposed signatures of QGP formation in nuclear collisions [143, 144]. Strange quarks are less likely to form in purely hadronic interactions because of their relatively high mass and associated production energy threshold. However, in the high-temperature QGP phase, abundant gluons can facilitate the efficient production of strange quarks. This enhancement in the production of strange and multi-strange hadrons has been experimentally confirmed by ALICE in collisions Pb–Pb at $\sqrt{s_{\mathrm{NN}}}$ = 2.76 TeV, where a clear increase in the ratio of strange to non-strange particles was observed with increasing multiplicity of events [145]. Such findings strongly support the idea of the formation of QGP in heavy-ion collisions.

As the dense medium formed in these collisions continues to evolve, quarks and gluons recombine to form hadrons, resulting in a hadron resonance gas (HRG). The hadronic phase, which spans from chemical freeze-out (where inelastic collisions stop) to kinetic freeze-out (where elastic collisions cease), is investigated through the study of hadronic resonances. These resonances decay, and their decay particles can either rescatter or regenerate within the hadronic phase, thereby modifying the observed yields compared to those produced before the chemical freeze-out. The dominance of rescattering or regeneration can be explored by analyzing the yield ratios of resonances to longer-lived hadrons with similar quark content as a function of system size. To investigate hadronic resonance production and their interactions, various resonances with different lifetimes, valence-quark flavors, masses, and spins have been studied at LHC [68, 76, 76, 80, 84, 146, 147] and RHIC [86, 148, 149] energies. These studies provide insight into the dynamics of the hadronic phase and the modification of resonance yields in different collision systems.

Recent measurements show that the yields of short-lived resonances, such as ρ^0 (1.335 fm/c) and K^{*0} (4.16 fm/c), are significantly modified in the hadronic phase compared to longer-lived resonances like the ϕ meson (46.26 fm/c). This is attributed to the fact that short-lived resonances decay within the hadronic medium, where processes such as rescattering and regeneration affect their yields. In contrast, longer-lived resonances typically decay after the hadronic phase, when the medium has expanded sufficiently and the interactions are minimal, resulting in little or no yield modification [84, 146, 147]. For baryonic resonances, such as the $\Sigma^{*\pm}$ (5.0$-$5.5 fm/c) and Λ^* (12.54 fm/c), the studies in Pb–Pb collision system have shown modification of yield for Λ^* but not for $\Sigma^{*\pm}$, despite the latter having a shorter lifetime [83]. Interestingly, such studies in small collision systems indicate that there is no significant yield modification for these resonances [84].

To understand the dynamics of the modification of resonance production in the hadronic phase, various approaches have been carried out. One such approach is the use of the transport AMPT model that simulates the time evolution of the system through microscopic interactions between particles. This model accounts for processes such as scattering, regeneration, and decay of resonances during the hadronic phase [150]. Another approach involves the HRG model in partial chemical equilibrium (PCE). This model describes the dynamics of particle yields and reactions in the hadronic phase, capturing the interplay between resonance decay, regeneration, and freeze-out conditions [151]. Additionally, the SMASH model (Simulating Many Accelerated Strongly-interacting Hadrons) is a hadronic transport model designed to simulate the non-equilibrium dynamics of hadronic systems. It accounts for the hydrodynamic description with SMASH as a hadronic afterburner, modeling the evolution of the system after QGP transitions to a hadron-dominated medium [152]. The findings from experimental measurement and theoretical studies suggest that the final resonance yields are influenced not only by their lifetimes but also by additional factors, such as the duration of the hadronic phase, the interaction cross-section of decay daughters, the freeze-out temperature, and the mean free path of the resonances.

In this chapter, we present results of various strange and non-strange hadrons, including hadroinc resonances, at midrapidity ($|y| < 0.5$) for pp collisions at $\sqrt{s}$ = 13.6 TeV and Pb–Pb collisions at $\sqrt{s_{\mathrm{NN}}}$ = 5.36 TeV using the EPOS4 with UrQMD hadronic afterburner both ON and OFF. The terms “with UrQMD" and “without UrQMD" are used interchangeably to refer to simulations with UrQMD ON and UrQMD OFF, respectively, and may appear throughout this chapter. The inclusion of UrQMD (Ultra-relativistic Quantum Molecular Dynamics) enables detailed modeling of the hadronic phase by simulating its effects on the system. These effects can significantly alter key observables such as transverse momentum (p_{T}) spectra, particle yields, and yield ratios, as well as collective phenomena such as flow and particle correlations. By comparison of simulations with and without UrQMD with experimental data, the influence of the hadronic phase on resonance production has been explored. The study also examines how strangeness enhancement and baryon-to-meson ratios influence the production of hadronic resonances and multi-strange hadrons. This comparison provides valuable insights into the dynamics of the hadronic phase and its impact on final-state observables. The highest energies and finer high multiplicity events in small systems are chosen to improve upon previous studies [70, 153] and to offer opportunities for future comparisons with experimental measurements

Experimentally, hadronic resonances are reconstructed using the invariant-mass technique via the addition of 4-momenta of their decay daughters. The longer-lived decay daughters, such as charged pions, charged kaons, and (anti)protons, reach the detectors and are often identified through measurements of energy loss ($\mathrm{d}E/\mathrm{d}x$) in a Time Projection Chamber (TPC) and/or velocity in a Time-of-Flight (TOF) detector. The weakly decaying daughters, such as $\mathrm{K^0_S}$, Λ, Ξ and Ω can be selected based on their decay topologies, which puts further constraints. For this study, 5 million events were generated for pp collisions, both with and without UrQMD, while 1.5 million events were generated for Pb–Pb collisions under the same conditions. The events are divided into various multiplicity classes based on the number of charged particles present within the pseudorapidity ranges $-3.7 < \eta < -1.7$ and $2.8 < \eta < 5.1$. This method follows an approach similar to that used by the ALICE experiment for pp and Pb–Pb collisions in the Run 2 studies.

Particles are selected from the generated data according to their unique EPOS IDs, with weak decays disabled to ensure that only primary particles contribute to the final yield calculations. After selecting resonances based on their unique EPOS IDs, they are flagged as either reconstructible or non-reconstructible. When a resonance decays, the EPOS4 model tracks its decay daughters. If any of the decay daughters undergo elastic interactions that alter their momenta, the parent resonance is flagged as non-reconstructible. As a result, the resonance is not included in the final yield measurements. This ensures that only resonances whose decay daughters have not undergone significant elastic scattering are counted, following a similar approach to experimental measurements, where resonance particles are reconstructed based on the momenta and trajectories of their decay products.

5.2 EPOS4 model: Overview and insights

EPOS4 is a general purpose scheme designed to study various observables in relativistic collisions of different systems, ranging from proton-proton to nucleus-nucleus, at energies from several GeV per nucleon to several TeV [154]. The key concept on which EPOS4 is based is parallel scattering. Unlike sequential scatterings, parallel scattering involves multiple parton-parton scatterings occurring simultaneously in high-energy collisions because of the extended reaction times of high-energy particle scatterings. This new approach also distinguishes between primary and secondary scatterings. Primary scatterings refer to parallel scatterings involving the initial nucleons (and their partonic constituents) occurring instantaneously at very high energies. The theoretical tool used here is the S-matrix theory, employing a particular form of the proton-proton scattering S-matrix (Gribov-Regge approach [155, 156, 157, 158]), which can be generalized for nucleus-nucleus collisions. Secondary scatterings refer to subsequent interactions of the string decay products, including a core-corona separation based on the string segments, followed by the formation, evolution, and decay of the core part.

Keeping energy-momentum conservation is crucial when dealing with multiple scatterings. While all event generators ensure this conservation, the theoretical approach varies. Historically, the Gribov-Regge (GR) theory incorporated multiple scatterings in an S-matrix framework, treating all scatterings equally without a specific order. However, this approach did not properly share energy-momentum among the scatterings, details of which can be found in [159, 160]. In a truly parallel scattering scenario, the initial energy-momentum must be fairly distributed among the multiple scatterings and the remnants of the projectile and target. This fair distribution is referred to as a “rigorous parallel scattering scenario," which, for pp scattering, uses integrands like:

$$\prod_{i=1}^{n+2} f_i(p_i) \times \delta\left(p_{\text{initial}} - \sum_{i=1}^{n+2} p_i\right) \tag{5.1}$$

where p is the four-momentum and n is the number of parallel scatterings. The diagram in Figure 5.1 depicts the rigorous parallel scattering scenario for multiple ($n = 3$) scatterings. Each scattering occurs independently, yet simultaneously, with energy-momentum conservation enforced globally through delta functions as in Equation 5.1. The “rigorous parallel scattering scenario" aims to introduce unbiased parallel scattering. However, this approach leads to violations of factorization and binary scaling in nucleus-nucleus (AA) collisions. Factorization refers to the separation of hard and soft processes in scattering, and binary scaling implies that AA collisions can be described as multiple nucleon-nucleon (NN) collisions. These violations indicate that something is missing in the parallel-scattering framework.

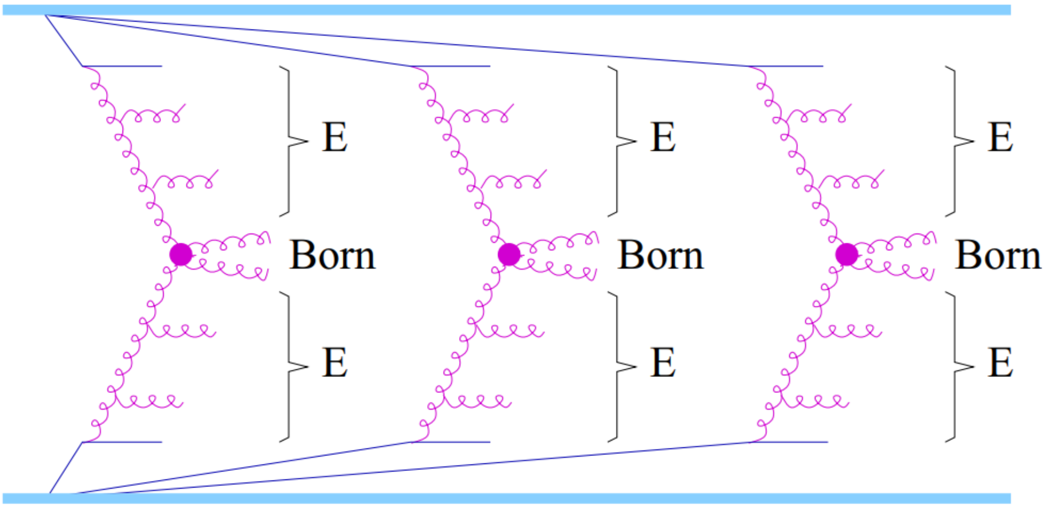

Figure 5.1: Rigorous parallel scattering scenario, for $n = 3$ parallel scatterings [161].

In high-energy collisions, partons (quarks and gluons) with very small momentum fractions $x \ll 1$ become significant. As parton distribution functions (PDFs) increase at small x, the parton density becomes large, rendering the linear DGLAP (Dokshitzer-Gribov-Lipatov-Altarelli-Parisi) evolution scheme [157, 162, 163] invalid. Instead, non-linear evolution, which includes gluon-gluon fusion, becomes important. This nonlinear evolution is referred to as "small x physics" or "saturation" [164, 165, 166, 167, 168]. Saturation effects result in the screening of low-p_{T} particle production below a "saturation scale." These effects are more pronounced in AA collisions due to the fusion of parton ladders from different nucleons [165, 166]. The introduction of a saturation scale provides a lower limit for the virtualities in the DGLAP evolution. This scale encapsulates the non-linear effects of parton interactions. By including a saturation scale, one can recover the factorization and binary scaling properties that are otherwise violated in the parallel scattering scenario. The diagrams in Figure 5.2 illustrate the non-linear effects and the introduction of saturation scales. These diagrams show how parton ladders, which initially evolve independently, eventually fuse, leading to nonlinear effects that are summarized by the saturation scale. The red ellipses highlight the regions where these non-linear effects are significant, and the replacement of these regions with saturation scales simplifies the treatment of these complex interactions. Although other models, such as Pythia/Angantyr [169, 170], do not explicitly include saturation, they introduce a sequence of NN scatterings to avoid overpro-

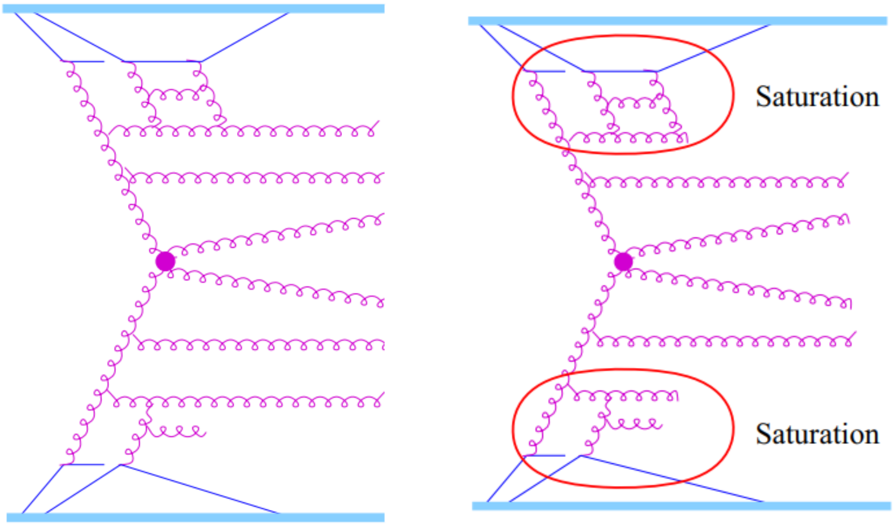

Figure 5.2: Illustrations of the nonlinear effects and the introduction of saturation scales in high-energy collisions. The diagram on the left panel shows how independent parton ladders eventually fuse, necessitating a saturation scale, while the diagram on the right panel highlights the regions (red ellipses) where nonlinear effects are significant and are replaced by saturation scales for simplification [161].

duction of charged particles in AA collisions. In contrast, EPOS4 incorporates a dynamic saturation scale to achieve similar effects. This difference highlights the unique approach of EPOS4 in treating multiple scatterings and saturation phenomena. The discussion emphasizes that saturation and factorization are interconnected concepts in high-energy physics. By understanding and implementing saturation scales, one can address the issues of energy sharing and maintain the desired properties of factorization and binary scaling. The diagrams inside the red ellipses in Fig. 5.2 are replaced by two scales, $Q^2_{\text{sat,proj}}$ and $Q^2_{\text{sat,targ}}$, which are equal in pp scattering. The final version of the ’rigorous parallel scattering scenario’ in EPOS4 is sketched in Figure 5.3, where there is still the DGLAP evolution for each of the scatterings, but one introduces saturation scales.

This was the story of "primary scatterings," which occur instantaneously at $t = 0$ in EPOS4, where the S-Matrix approach is used. Now we move on to the "secondary scatterings." In the EPOS framework, a core-corona procedure [131, 171, 172] is used, where strings at a given proper time are divided into "string segments." These segments are categorized into "core" and "corona" based on their energy loss as they traverse through matter composed of other segments. Corona segments can escape, while core segments lose all

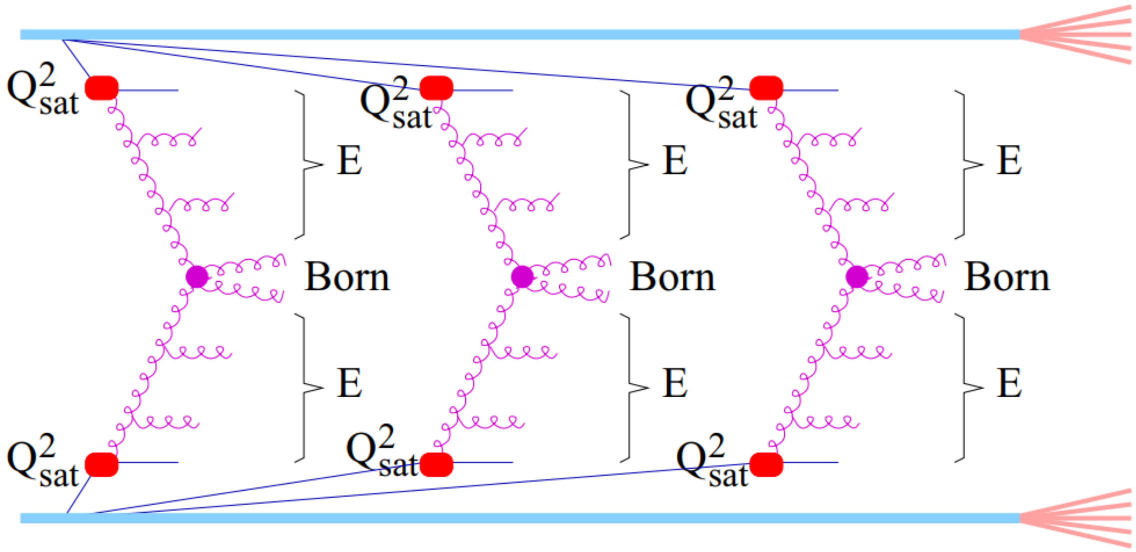

Figure 5.3: Rigorous parallel scattering scenario, for $n = 3$ parallel scatterings, including nonlinear effects via saturation scales. The red symbols should remind one that the parts of the diagram representing nonlinear effects are replaced by simply using saturation scales [161].

their energy and form the "core," serving as the initial condition for hydrodynamic evolution. This evolution continues until the energy density falls below a critical value, marking the hadronization point where the fluid decays into hadrons.

EPOS4 introduces a new approach to handling the energy-momentum flow through the freeze-out hypersurface [154], allowing the definition of an effective invariant mass that decays into hadrons. These hadrons are then Lorentz boosted according to the flow velocities at the freeze-out hypersurface. EPOS4 also incorporates new and efficient methods for the microcanonical procedure [154], ensuring the conservation of energy-momentum and flavors throughout primary and secondary interactions.

To summarize the above discussion, the "full" EPOS4 scheme comprises:

1. Primary interactions, based on an S-matrix approach for parallel scatterings,
2. Secondary interactions, consisting of:
    (a) Core-corona separation procedure,
    (b) Hydrodynamic evolution and microcanonical hadronization,
    (c) Hadronic afterburner (UrQMD [173, 174])

Thus, EPOS4 is a suitable model for discussing strangeness production and studying the hadronic phase through resonance production yields, as it distinguishes primary and secondary scatterings, which play a key role in these phenomena, allowing us to play with various tunes of the model and observe their effects on final hadron yields and their ratios.

5.3 Results and discussion

5.3.1 Transverse momentum spectra

To study how the hadronic phase affects resonance production, analyzing the shape of the p_{T} spectra can reveal insights into their production dynamics and interactions. The K^{*0} and ϕ mesons serve as excellent candidates for these investigations due to their comparable masses, but markedly different lifetimes: K^{*0} has a much shorter lifetime of around 4.16 fm/c, whereas the ϕ meson is more stable with a lifetime of roughly 46.2 fm/c, which is almost ten times longer. The upper panels of Figure 5.4 show the p_{T} spectra for K^{*0} (left)

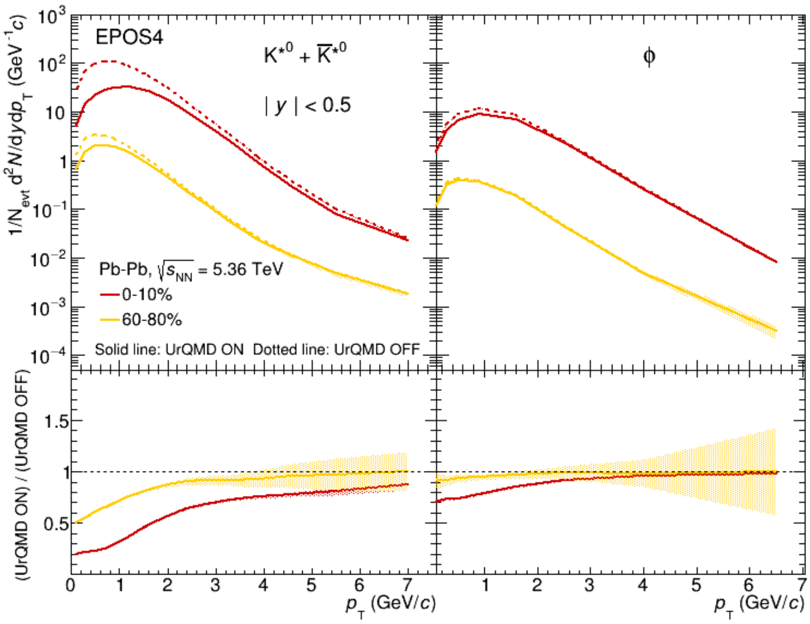

Figure 5.4: **Upper panel:** The p_{T} distributions of K^{*0} and ϕ resonances at midrapidity for central (0–10%) and peripheral (60–80%) Pb–Pb collisions at $\sqrt{s_{\mathrm{NN}}}$ = 5.36 TeV using EPOS4 with both UrQMD ON and OFF tunes. Solid lines depict UrQMD ON measurements, while dotted lines indicate UrQMD OFF measurements. **Lower panel:** The ratio of p_{T}-differential yields for K^{*0} and ϕ between UrQMD ON and OFF tunes. Statistical uncertainties in the measurements are shown by the bands.

and ϕ (right) using EPOS4 with UrQMD ON (solid lines) and OFF (dotted lines) for 0–10% and 60–80% centrality classes at midrapidity ($|y| < 0.5$) in Pb–Pb collisions at $\sqrt{s_{\mathrm{NN}}}$ = 5.36 TeV. The lower panels illustrate the ratios that compare the p_{T} spectra with UrQMD ON to those with URQMD OFF. A significant difference is observed at low p_{T} for K^{*0} in the UrQMD ON vs. OFF scenario, with a greater impact in central (0–10%, red lines) compared to peripheral (60–80%, yellow lines) collisions. Similarly, Figure 5.5 presents these ratios for pp collisions in the multiplicity classes 0–1% (red) and 70–100% (cyan) at $\sqrt{s}$ = 13.6 TeV. A comparable suppression at low p_{T} is observed in high-multiplicity (0–1%) pp collisions for K^{*0} versus ϕ. This suppression in high-multiplicity pp collisions is similar in magnitude to that in peripheral Pb–Pb collisions, as the multiplicity in high-multiplicity pp collisions approaches those found in peripheral Pb–Pb collisions. In the most central Pb–Pb collisions, a significant suppression is observed, which is similar to previous findings from ALICE measurements at LHC energies [78]. This indicates that the decay products of the short-lived K^{*0} experience rescattering within the hadronic phase, especially noticeable at

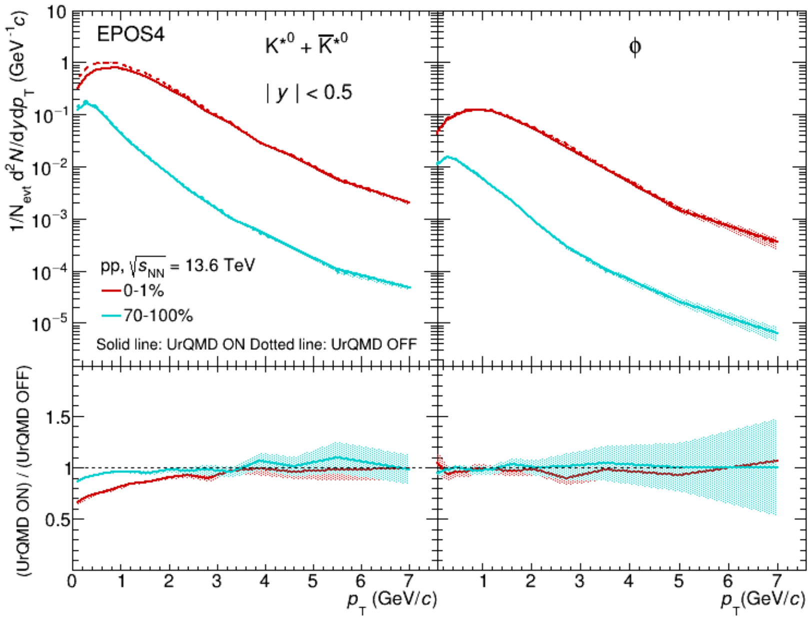

Figure 5.5: **Upper panel:** The p_{T} spectra of K^{*0} and ϕ resonances in the midrapidity region for high multiplicity (0–1%) and low multiplicity (70–100%) in pp collisions at $\sqrt{s}$ = 13.6 TeV, using EPOS4 with UrQMD ON and UrQMD OFF settings. The solid lines denote measurements when UrQMD is ON, whereas the dotted lines indicate measurements with UrQMD OFF. **Lower panel:** The p_{T}-differential yield ratios for K^{*0} and ϕ with UrQMD ON compared to UrQMD OFF settings. The bands illustrate the statistical uncertainties associated with the measurements.

low p_T in central Pb–Pb collisions and in high-multiplicity pp collisions. In contrast, at high p_T and in low-multiplicity events, the ratios tend toward unity. Comparatively, the ϕ shows a milder effect, which is anticipated due to its longer lifetime. This shows that the EPOS4 model with UrQMD effectively simulates the influence of the hadronic phase on resonance production.

To further explore the impact of the hadronic phase, Figure 5.6 illustrates the ratio of p_T spectra for various hadronic resonances with lifetimes between 1 and 47 fm/c, both with UrQMD ON and OFF, in central 0–10% Pb–Pb collisions at $\sqrt{s_{NN}}$ = 5.36 TeV. The data reveal a consistent suppression trend ordered as $\rho^0 < \Delta^{++} < \mathrm{K}^{*0} < \Sigma^{*\pm} \sim \Lambda^* < \Xi^{*0} < \phi$, where suppression intensifies with shorter resonance lifetimes. However, for Λ^* and $\Sigma^{*\pm}$ baryons, the suppression observed is similar despite their different lifetimes, suggesting that factors beyond resonance lifetime affect the yield modifications of heavier baryonic resonances in the hadronic phase. The low-p_T (non-perturbative QCD) region of the p_T

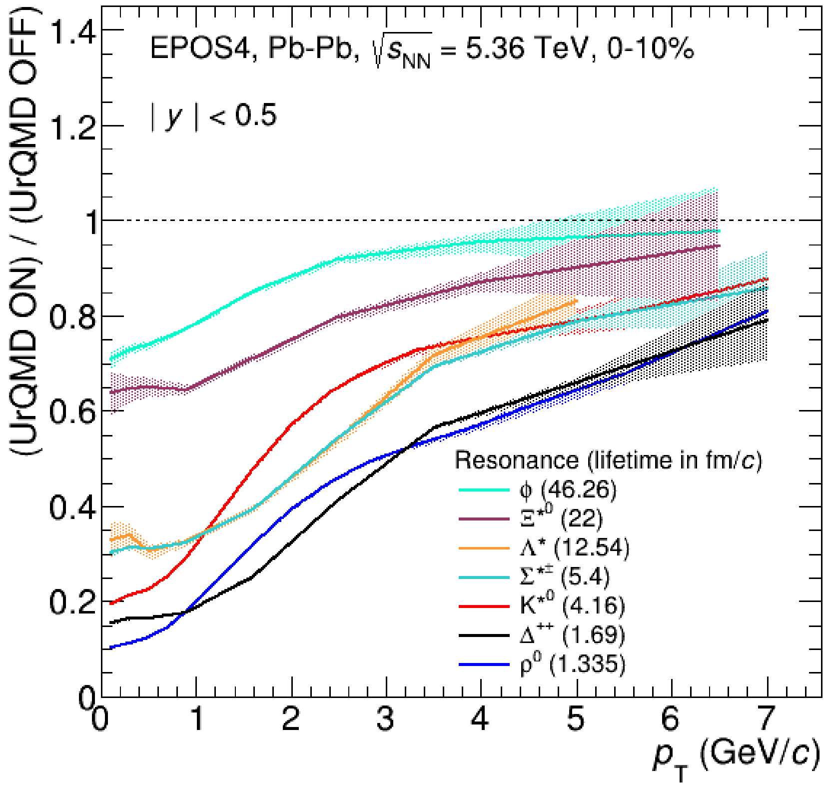

Figure 5.6: The p_T-differential spectra of hadronic resonances in central (0-10%) Pb–Pb collisions with UrQMD are compared to the spectra obtained without UrQMD using EPOS4. The bands in the data indicate the statistical uncertainty.

spectra is important for understanding production dynamics, as processes such as rescattering, regeneration, strangeness enhancement, radial flow, and baryon-to-meson ratios can significantly impact the shape of the p_{T} spectra and hadron interactions. Particle ratios serve as effective tools to differentiate these processes. Specifically: (a) resonance-to-stable hadron yield ratios offer insight into the p_{T} distributions of hadrons with similar quark content but varying masses; and (b) baryon-to-meson yield ratios enable comparisons of hadrons with similar masses but different baryon numbers and quark structures. To quantify the p_{T}-dependence of the rescattering effect, the upper panels of Figure 5.7 illustrate the p_{T}-differential ratios $\mathrm{K}^{*0}/\mathrm{K}$ (left) and ϕ/K (right) in central (0–10%) and peripheral (60–80%) Pb–Pb collisions at $\sqrt{s_{\mathrm{NN}}}$ = 5.36 TeV, along with high multiplicity (0-1%) pp collisions at $\sqrt{s}$ = 13.6 TeV using the UrQMD hadronic afterburner. The lower panels show the comparison of p_{T}-differential yield ratios for central and peripheral Pb–Pb collisions against high-multiplicity pp collisions. In pp and Pb–Pb collisions, despite being at different energies, particle yields are observed to depend primarily on the charged-particle multiplicity rather than solely on the collision energy, as demonstrated by ALICE measurements [78, 83]. Consequently, the highest multiplicity classes of pp collisions are chosen as the reference point, providing a suitable baseline for comparing peripheral Pb–Pb collisions and offering further insights into their dynamics. The double ratio of $\mathrm{K}^{*0}/\mathrm{K}$ shows suppression at low-p_{T}, especially in central collisions compared to peripheral ones. This suppression is due to rescattering effects that influence K^{*0} production, and the strangeness effects are neutralized with the use of the $\mathrm{K}^{*0}/\mathrm{K}$ ratio. In contrast, no significant suppression or centrality dependence is detected for the ϕ/K ratio. In peripheral Pb–Pb collisions and high-multiplicity pp collisions, p_{T}-differential yield ratios are similar. This similarity implies that hadron production processes in peripheral Pb–Pb and high-multiplicity pp collisions may have similar characteristics. Similarly, Figure 5.8 illustrates the p_{T}-differential yield ratios for various hadronic resonances at centrality 0–10% (left) and peripheral 60–80% (right) in Pb–Pb collisions at $\sqrt{s_{\mathrm{NN}}}$ = 5.36 TeV to high-multiplicity pp collisions. At low p_{T}, these ratios follow a specific sequence: $\Lambda^{*}/\Lambda < \rho^{0}/\pi < \mathrm{K}^{*0}/\mathrm{K} < \Xi^{*0}/\Xi^{-} \approx \Sigma^{*\pm}/\Lambda < \Delta^{++}/\mathrm{p} < \phi/\mathrm{K}$. Despite the longer lifetime of Λ^{*}, it suffers large suppression

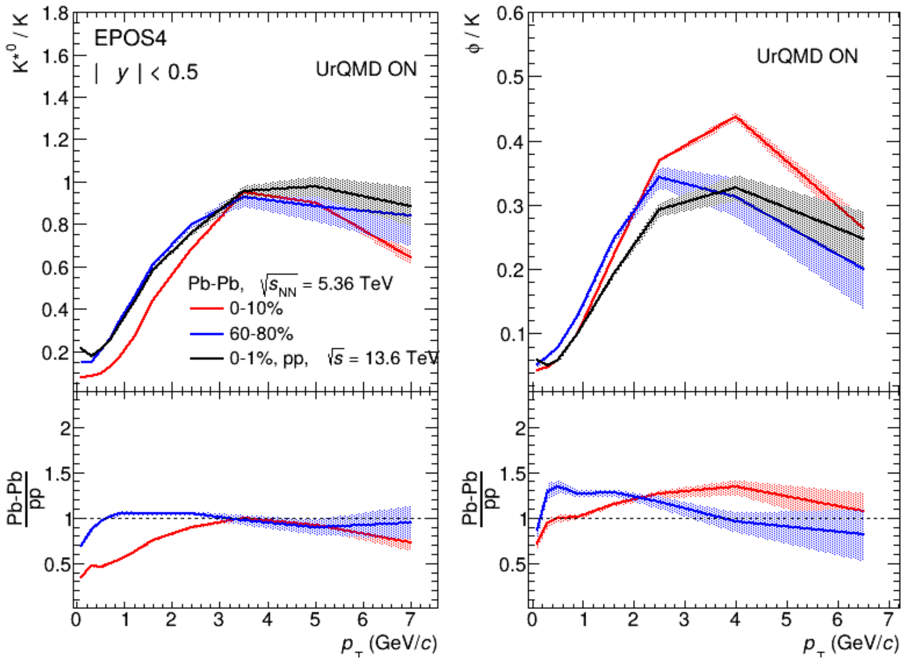

Figure 5.7: **Upper panel:** The $p_{\rm T}$-differential ratios $\mathrm{K}^{*0}/\mathrm{K}$ (left) and ϕ/K (right) in the central (0–10%) and peripheral (60–80%) Pb–Pb collisions at $\sqrt{s_{\rm NN}}$ = 5.36 TeV, as well as in the high multiplicity (0-1%) pp collisions at $\sqrt{s}$ = 13.6 TeV with UrQMD. **Lower panel:** The comparison of $p_{\rm T}$-differential ratios in the central and peripheral Pb–Pb collisions to the high multiplicity pp collisions. The bands in the measurements represent statistical uncertainty.

compared to other resonances having shorter lifetimes, a pattern also observed in the $p_{\rm T}$-integrated yield ratios for the most central Pb–Pb collisions (explored in Section 5.3.4). However, in peripheral Pb–Pb collisions, these ratios approach unity, indicating minimal impact of resonance lifetimes on the ratios.

5.3.2 Baryon-to-meson ratios

The study of particle ratios, specifically baryon-to-meson ratios, is important to interpret mass-dependent radial flow and to understand the production mechanisms of baryons and mesons. This section discusses the baryon-to-meson ratios of various hadrons, including resonances like K^{*0}, ϕ, Λ^*, and $\Sigma^{*\pm}$, using calculations from EPOS4 with and without UrQMD. EPOS4 with UrQMD captures a clear mass-dependent enhancement at low to intermediate $p_{\rm T}$ in the ratios of baryons (Λ, Λ^*, and $\Sigma^{*\pm}$) to $\mathrm{K}^0_{\rm S}$ for the most central Pb–Pb collisions, as shown in Figure 5.9. Similar features are seen in the ratios of p/π and $\Lambda/\mathrm{K}^0_{\rm S}$ for light-flavor hadrons in central Pb–Pb collisions, consistent with observations reported

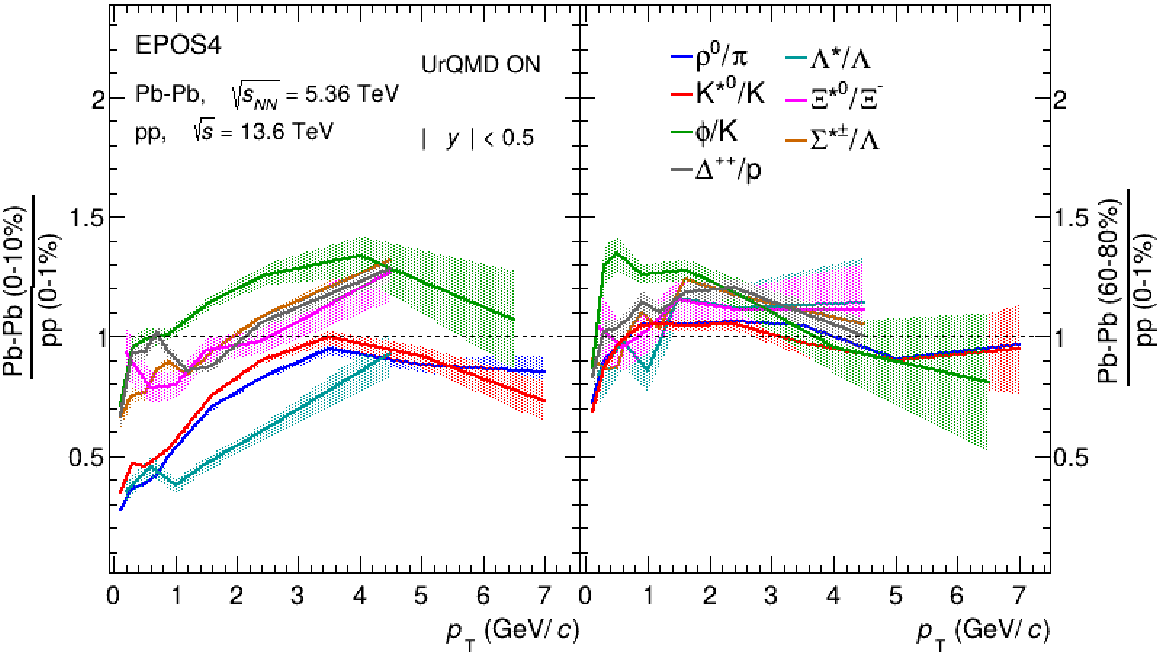

Figure 5.8: The p_{T}-differential ratios ρ^0/π, $\mathrm{K}^{*0}/\mathrm{K}$, ϕ/K, Δ^{++}/p, Λ^*/Λ, Ξ^{*0}/Ξ^- and $\Sigma^{*\pm}/\Lambda$ are compared for central (0–10%, left) and peripheral (60–80%, right) Pb–Pb collisions at $\sqrt{s_{\mathrm{NN}}}$ = 5.36 TeV against high multiplicity (0-1%) pp collisions at $\sqrt{s}$ = 13.6 TeV, analyzed using UrQMD. The statistical uncertainty in the measurements is indicated by the bands.

by the ALICE Collaboration in Ref. [175, 176]. Moreover, the enhancement decreases, and the peak position shifts toward high-p_{T} region with increasing baryon masses. An alternative explanation is that quark recombination drives baryon-to-meson enhancement. The production of baryons is favored because the combination of three quarks to form a baryon is more probable than the formation of a meson through a quark-antiquark pair [177]. To distinguish whether the enhancement at intermediate p_{T} arises due to recombination or radial flow, we examine the baryon-to-meson ratios involving baryons and mesons with similar masses, such as p/ϕ and p/K^{*0} using EPOS4 with and without UrQMD and compared them with the ALICE measurements as shown in Figure 5.10. However, the p/ϕ ratio from ALICE data shows a rather p_{T}-independent effect up to 3 GeV/c, and EPOS4 shows a similar flat trend with UrQMD ON up to p_{T} ($<$ 1.5 GeV/c). At high-p_{T}, both data and model results show a similar decreasing trend for all particle species that suggests that a common fragmentation mechanism plays an important role, while the model overestimates the data. Although EPOS4 with UrQMD ON describes the p/π ratio for stable hadrons,

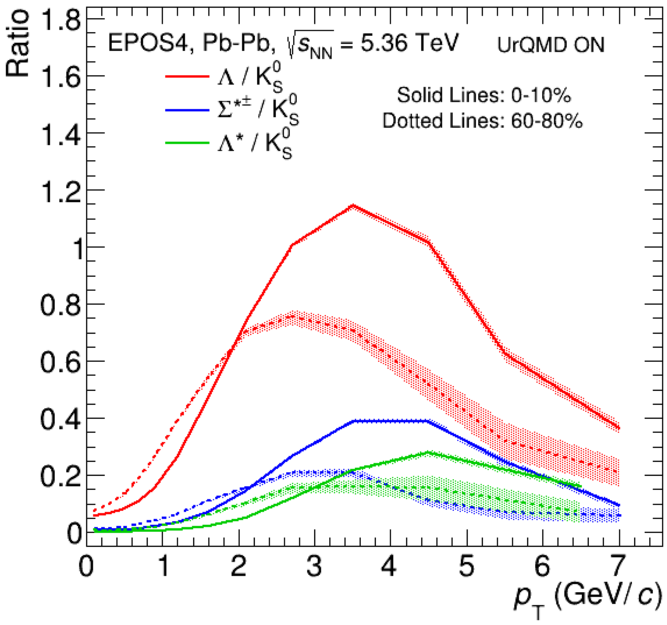

Figure 5.9: The p_T-differential ratios Λ/K^0_S, $\Sigma^{*\pm}/K^0_S$, and Λ^*/K^0_S in central (0–10%, solid lines) and peripheral (60–80%, dotted lines) Pb–Pb collisions at $\sqrt{s_{NN}}$ = 5.36 TeV, simulated using EPOS4 with UrQMD. The shaded bands represent statistical uncertainties in the measurements.

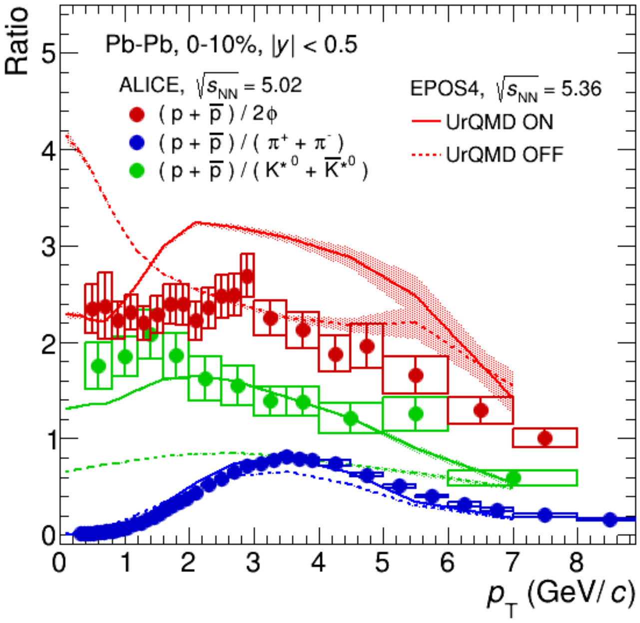

Figure 5.10: The p_T-differential ratios p/ϕ, p/π and p/K^{*0} in the central Pb–Pb collisions with ALICE at $\sqrt{s_{NN}}$ = 5.02 TeV (markers) and using EPOS4 model with UrQMD (solid lines) and without UrQMD (dotted lines) at $\sqrt{s_{NN}}$ = 5.36 TeV. The bars and boxes in the ALICE measurements represent statistical and systematic uncertainties, respectively. The shaded area in the model calculations represent statistical uncertainty.

EPOS4 with UrQMD OFF fails to capture the exact enhancement trend in the intermediate p_{T} region. Furthermore, the results from EPOS4 with UrQMD OFF do not describe the measured ratios when one of the particles involved is a resonance.

The p/K^{*0} ratio from the ALICE measurements shows a slight decreasing trend, which is similarly supported by the model results. This behavior is expected, as the K^{*0} spectral shape is modified due to hadronic phase effects that dominate in the low p_{T} region. At high p_{T}, the proton, K^{*0} and ϕ show a similar decreasing trend. The EPOS4 describes the p/K^{*0} ratio qualitatively similar to the data but underestimated at low p_{T}. This indicates that although protons K^{*0}, ϕ have a different quark content, the mass of hadrons and the hadronic phase effect on short-lived resonances play an important role in determining the spectral shapes.

5.3.3 Average transverse momentum

The $\langle p_{\mathrm{T}} \rangle$ of various hadronic resonances as a function of average charged-particle multiplicity is shown in Fig. 5.11 for midrapidty in pp collisions at $\sqrt{s}$ = 13.6 TeV and in Pb–Pb collisions at $\sqrt{s_{\mathrm{NN}}}$ = 5.36 TeV. These calculations are obtained using EPOS4 with and without UrQMD hadronic afterburner. The results are also compared with measurements from the ALICE Collaboration for pp collisions at $\sqrt{s}$ = 13 TeV and 2.76 TeV [76, 146, 147] and Pb–Pb collisions at $\sqrt{s_{\mathrm{NN}}}$ = 5.02 TeV and 2.76 TeV [80, 146, 179], when available. The $\langle p_{\mathrm{T}} \rangle$ increases with increasing charged-particle multiplicity and mass of hadron species. The steeper rise in $\langle p_{\mathrm{T}} \rangle$ for pp collisions compared to Pb–Pb collisions is well reproduced by EPOS4, showing a similar behavior to that observed in the data. The EPOS4 model generally reproduces the observed $\langle p_{\mathrm{T}} \rangle$ trends in Pb–Pb collisions, demonstrating good agreement with experimental data across various centralities. In contrast, for pp collisions, EPOS4 tends to slightly underestimate the $\langle p_{\mathrm{T}} \rangle$ values, particularly at higher multiplicities. Activating the hadronic cascade (UrQMD ON) usually leads to an increase in $\langle p_{\mathrm{T}} \rangle$, improving the consistency of the model with measured data. This enhancement reflects the significant role of hadronic rescattering in modifying the p_{T} spectra during the later stages of collision evolution. The $\langle p_{\mathrm{T}} \rangle$ values for short-lived resonances such as ρ^0, K^{*0} show sig-

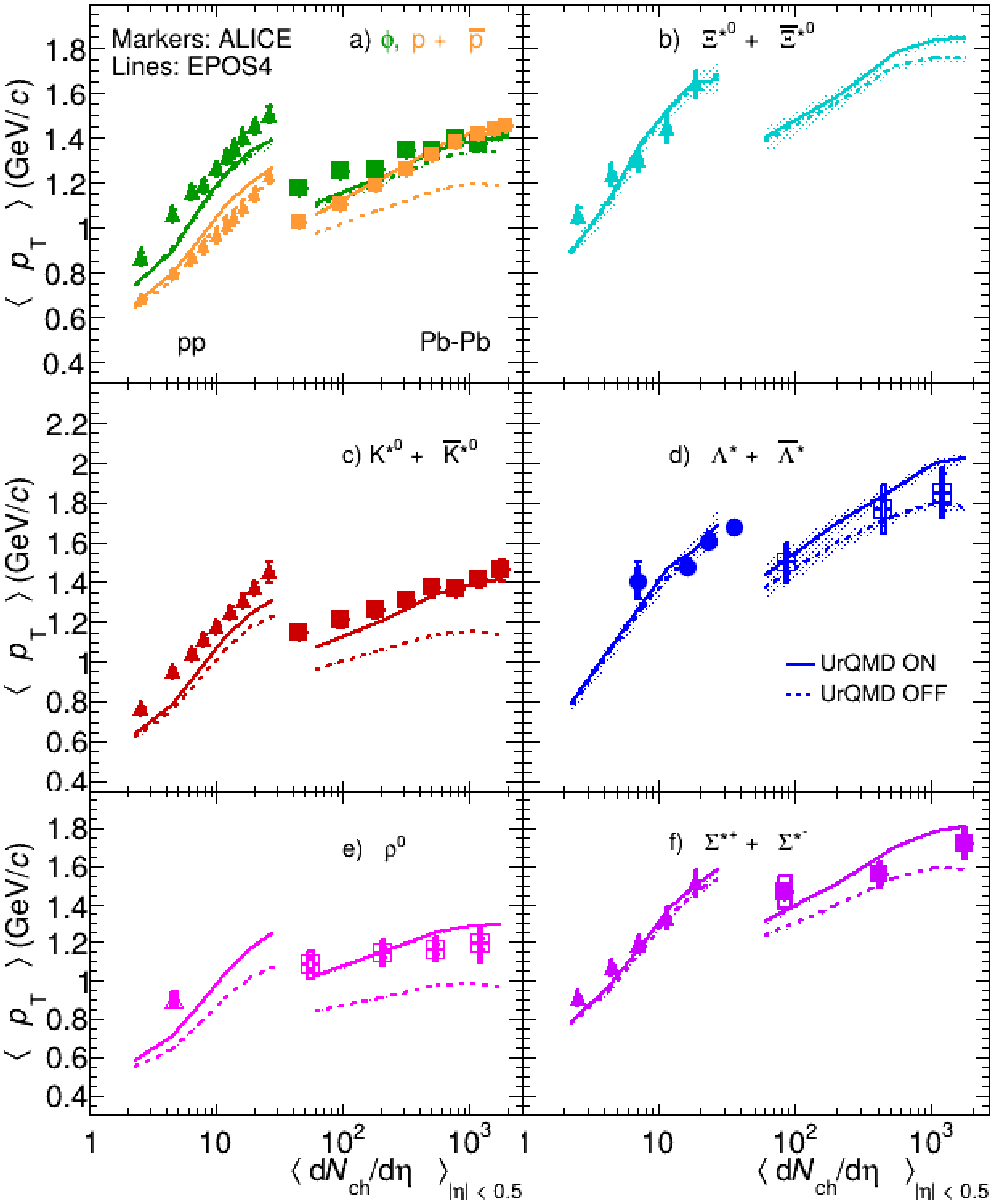

Figure 5.11: Average transverse momentum of protons, mesonic resonances (ρ^0, K^{*0}, and ϕ) and baryonic resonances ($\Sigma^{*\pm}$, Λ^* Ξ^{*0}) as a function of charged-particle multiplicity density at intermediate-rapidity. Markers indicate ALICE measurements in pp system at $\sqrt{s}$ = 2.76 TeV (open triangles) [76] and $\sqrt{s}$ = 13 TeV (solid triangles) [146, 147, 178], in p–Pb system at $\sqrt{s_{\mathrm{NN}}}$ = 5.02 TeV (soild circles) [84], and in Pb–Pb system at $\sqrt{s_{\mathrm{NN}}}$ = 2.76 TeV (open squares) [76, 83] and $\sqrt{s_{\mathrm{NN}}}$ = 5.02 TeV (soild squares) [78, 80, 175]. The lines represent EPOS4 predictions for pp collisions at $\sqrt{s}$ = 13.6 TeV and for Pb–Pb collisions at $\sqrt{s_{\mathrm{NN}}}$ =5.36 TeV with UrQMD (solid lines) and without UrQMD (dotted lines). The statistical and systematic uncertanities in the ALICE data are represented by bars and boxes, respectively while the statistical uncertainty in the model measurements are represented by bands.

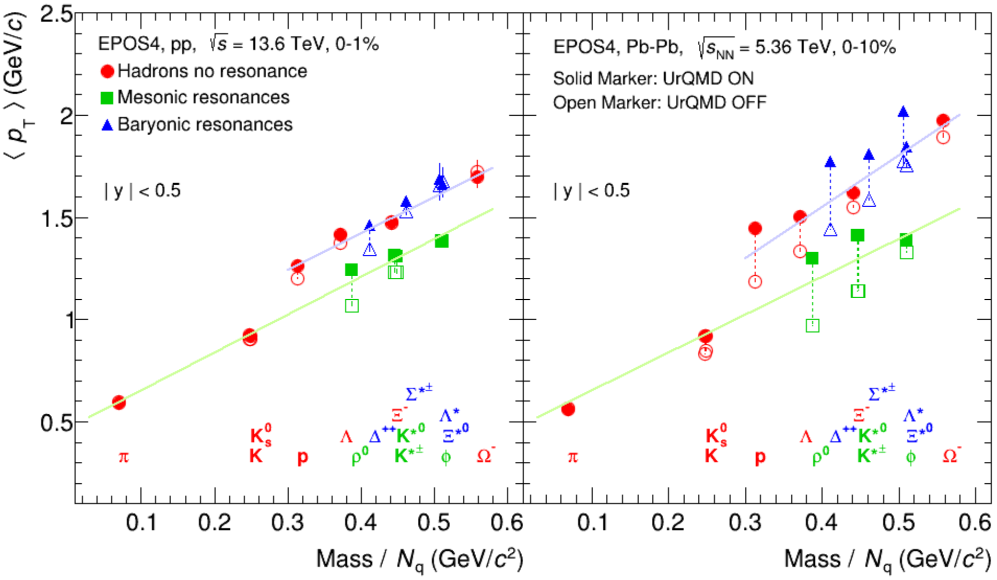

Figure 5.12: The average transverse momentum of hadrons in the midrapidity region plotted as a function of the hadron mass, scaled by the number of valence quarks, in high multiplicity (0-1%) pp collisions at $\sqrt{s}$ = 13.6 TeV (left panel) and in central (0-10%) Pb–Pb collisions at $\sqrt{s_{\mathrm{NN}}}$ = 5.36 TeV (right panel) using the EPOS4 model with UrQMD (solid markers) and without UrQMD (open markers). The green and blue lines represent linear functions. The statistical uncertainty in the measurements is represented by bars.

nificant changes between with and without UrQMD for Pb–Pb collisions, whereas the effect is less pronounced for pp collisions. For the ϕ-meson, the difference in $\langle p_{\mathrm{T}} \rangle$ between the two cases (with and without UrQMD) is smaller because its decay daughters interact less with the hadronic medium due to its longer lifetime. The change in $\langle p_{\mathrm{T}} \rangle$ can be attributed to modifications in the spectral shape, as shown in Figures 5.4 and 5.5. For short-lived resonances, their decay daughters undergo substantial hadronic interactions in the hadronic phase, leading to pronounced modifications. This effect is strongest in central Pb–Pb collisions and decreases with lower multiplicity, consistent with the shorter hadronic phase lifetimes discussed later in Section 5.3.5. For baryonic resonances such as $\Sigma^{*\pm}$, Λ^{*}, and Ξ^{*0}, no significant change in $\langle p_{\mathrm{T}} \rangle$ is observed for small systems (up to $\langle \mathrm{d}N_{\mathrm{ch}}/\mathrm{d}\eta \rangle_{|\eta|<0.5} \sim 35$). However, in Pb–Pb collisions, both the spectral shape and the $\langle p_{\mathrm{T}} \rangle$ values exhibit significant modifications due to the extended hadronic phase. Particles with similar masses, such as the proton and the ϕ-meson, show comparable $\langle p_{\mathrm{T}} \rangle$ values in central Pb–Pb collisions, as reported by ALICE measurements [78, 175]. This observation aligns with expectations from hydrodynamical models, which predict that $\langle p_{\mathrm{T}} \rangle$ depends mainly on particle mass in such collisions. The calculations of the EPOS4 model also support this trend.

The $\langle p_{\mathrm{T}} \rangle$ value of the proton shows a slight difference between the simulations with and without UrQMD, suggesting that feed-down contributions from resonance decays are necessary to accurately describe the proton p_{T} spectrum. In contrast, the ϕ-meson momentum spectrum is negligibly affected by the hadronic phase due to its longer lifetime and lower interaction cross-section with the hadronic gas (in Figure 5.10, p_{T}-differential p/ϕ from EPOS4 shows a flat behavior at low p_{T} as seen in the data and overestimates after p_{T} > 2 GeV/c).

The $\langle p_{\mathrm{T}} \rangle$ as a function of reduced mass (Mass/N_{q}), where the mass of hadron is scaled by the number of valence quarks, is calculated for various light-flavor hadrons, including resonances for high multiplicity (0-1%) pp collisions at $\sqrt{s}$ = 13.6 TeV and central (0-10%) Pb–Pb collisions at $\sqrt{s_{\mathrm{NN}}}$ = 5.36 TeV using the EPOS4 model, both with and without UrQMD, as shown in Figure 5.12. The $\langle p_{\mathrm{T}} \rangle$ follows a linear trend with increasing mass. Baryons and mesons are grouping separately and exhibit parallel trends to each other. Stable mesons (red markers) and mesonic resonances (green markers) are observed to generally follow a linear trend, aligning closely with the linear fit function represented by the green line for both UrQMD ON and OFF. However, the resonances ρ^0, K^{*0}, K$^{*\pm}$, and Δ^{++} slightly deviate from the linear trend, with different values observed between UrQMD ON and OFF. This deviation is expected due to the finite hadronic phase in high-multiplicity (0–1%) pp collisions, which leads to the modification of the spectral shape of short-lived resonances. Similarly, the observed deviation from the linear function increases for Pb–Pb collisions compared to pp collisions. Hadronic resonances such as ρ^0, K^{*0}, K$^{*\pm}$, Δ^{++}, $\Sigma^{\pm}$, and Λ^* show significant deviations from the expected linear trend due to the larger size of the system. The value of $\langle p_{\mathrm{T}} \rangle$ is higher for short-lived resonances when UrQMD is ON compared to when it is OFF for most central collisions Pb–Pb. This indicates that the rescattering effect leads to an increased value of $\langle p_{\mathrm{T}} \rangle$. Furthermore, for stable hadrons such as the proton and Λ, the $\langle p_{\mathrm{T}} \rangle$ values deviate from the linear trend and differ between the cases with UrQMD ON and OFF. This indicates that the spectral shape and $\langle p_{\mathrm{T}} \rangle$ of protons and Λ are modified in the hadronic phase due to contributions from the decay of higher resonance states, since they are likely decay daughters.

5.3.4 Resonance to non-resonance yield ratios

Figure 5.13 presents the resonance-to-stable-hadron yield ratios as a function of charged-particle multiplicity at midrapidity ($\langle \mathrm{d}N_{\mathrm{ch}}/\mathrm{d}\eta \rangle_{|\eta|<0.5}$) for pp and Pb–Pb collisions at LHC energies. Recent measurements of the ρ^0/π and K^{*0}/K ratios show a decreasing trend with increasing multiplicity. These ratios have been investigated using the EPOS4 model, both with and without the UrQMD hadronic afterburner. A significant difference is observed between the predictions of the model with and without UrQMD, with the difference being more pronounced in central Pb–Pb collisions compared to pp collisions. Furthermore, this difference is more significant for resonances with shorter lifetimes compared to those with longer lifetimes. The EPOS4 model, with the UrQMD hadronic afterburner enabled, successfully captures the characteristics of particle production and qualitatively describes the behavior observed in the data. The K^{*0} and ϕ resonances are ideal candidates for these ratios because they have similar masses and contain strange quarks, while differing by lifetimes of an order of magnitude of 10. The ratios are chosen in such a way that the strangeness effect on the production yield is canceled out, allowing for a more direct comparison of resonance yields relative to stable hadrons. Suppression in the $\mathrm{K}^{*0}/\mathrm{K}$ ratio suggests that the decay daughters of the resonance undergo re-scattering processes in the hadronic phase, resulting in a modified final yield of the resonance compared to what was originally produced before chemical freeze-out. This suppression becomes more pronounced with increasing system size. The observed suppression in the $\mathrm{K}^{*0}/\mathrm{K}$ ratio, compared to the ϕ/K ratio in small to large collision systems, supports the idea that the shorter lifetime of K^{*0} plays a significant role in modifying the resonance yield in the hadronic phase. Similarly, the short-lived ρ^0/π ratio also shows suppression with increasing multiplicity. Observations from both data and model results indicate that re-scattering effects dominate over regeneration in the hadronic phase for short-lived mesonic resonances.

Similarly, Figure 5.13 (right) shows the ratios of baryonic resonances to stable hadrons as a function of $\mathrm{d}N_{\mathrm{ch}}/\mathrm{d}\eta$ at midrapidity. The Ξ^{*0}/Ξ^- ratio increases with multiplicity,

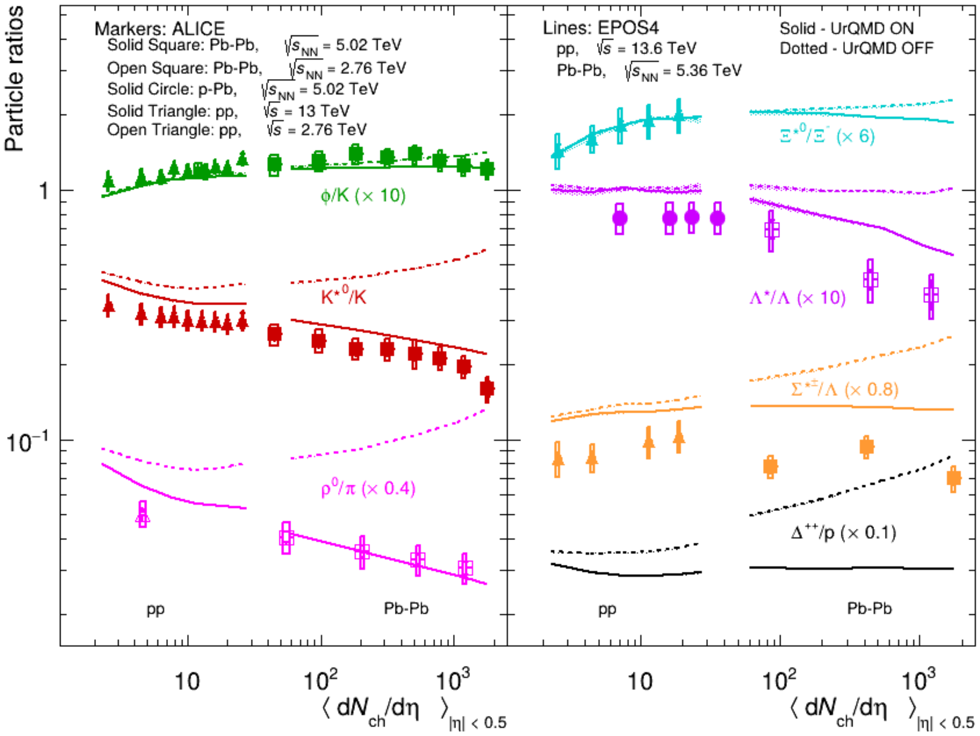

Figure 5.13: Left panel shows the ratios of mesonic resonances to stable mesons yield while the right panel shows the ratios of baryonic resonances to stable baryons yield. Different markers represent ALICE results in pp collisions at $\sqrt{s_{NN}}$ = 13 TeV (solid triangles) [146, 147] and $\sqrt{s_{NN}}$ = 2.76 TeV (open triangles) [76], p–Pb collisions at $\sqrt{s_{NN}}$ = 5.02 TeV (solid circles) [84], Pb–Pb collisions at $\sqrt{s_{NN}}$ = 2.76 TeV (open squares) [76] and $\sqrt{s_{NN}}$ = 5.02 TeV (solid squares) [68, 80]. The statistical and systematic uncertainties in the data are represented by bars and boxes, respectively. The lines represent predictions from EPOS4 in pp collisions at $\sqrt{s_{NN}}$ = 13.6 TeV and in Pb–Pb collisions at $\sqrt{s_{NN}}$ = 5.36 TeV with UrQMD (solid) and without UrQMD (dotted). The shaded area indicates the statistical uncertainty in the model calculations.

whereas the Λ^*/Λ and Σ^*/Λ ratios show no significant change with multiplicity in pp collisions. In Pb–Pb collisions, the Λ^*/Λ ratio decreases with increasing multiplicity, while the Ξ^{*0}/Ξ^- and $\Sigma^{*\pm}/\Lambda$ ratios remain largely unaffected, despite the fact that $\Sigma^{*\pm}$ has a shorter lifetime compared to Λ^*. This behavior may be attributed to the fact that the decay daughters of these resonances undergo regeneration and rescattering through (pseudo)-elastic interactions in the hadronic phase. In the case of $\Sigma^{*\pm}$, the regeneration and rescattering effects are expected to cancel each other out, resulting in minimal changes in the yield with increasing system size. In contrast, the decreasing trend of the Λ^*/Λ ratio with multiplicity is driven primarily by rescattering effects. However, recent studies reported in Ref. [152] suggest that the mean free path of resonances also plays a significant role in modifying the final yield. The Ξ^{*0}/Ξ^{-} also show a weak dependence with multiplicity due to a longer lifetime compared to Λ^{*}. For the resonance Δ^{++}, it is observed that Δ^{++}/ p shows a flat behavior with multiplicity for Pb–Pb collisions, while the same ratios exhibit a decreasing trend for pp collisions. Based on experimental data and model calculations, baryonic resonances exhibit distinct behaviors in pp and Pb–Pb collisions. This indicates that the modification of the final reconstructed resonance yields in the hadronic phase is not solely determined by the resonance lifetime. Other factors, such as the mean free path of resonances, the duration of the hadronic phase, the cross section of the decay products, and the chemical freeze-out temperature, also play a significant role.

5.3.5 Lifetime of hadronic phase

The suppression of short-lived resonances is seen in both the ALICE data and the results from EPOS4 with UrQMD. The suppression in the resonance to stable hadron yield is probably caused by the rescattering of decay products of resonances in the hadronic phase. These ratios act as useful tools for estimating the timespan between chemical and kinetic freeze-outs using the exponential decay law, under the following assumptions:

i) Negligible regeneration effects.

ii) Simultaneous freeze-out for all particle species. The relation is given by:

$$[h^{*}/h]_{kinetic} = [h^{*}/h]_{chemical} \times e^{-\tau/\tau_{h^{*}}} \tag{5.2}$$

where $[h^{*}/h]_{kinetic}$ denotes the ratio of resonance to stable hadron yield at kinetic freeze-out, $\tau_{h^{*}}$ is the lifetime of the resonance particle in its rest frame and τ is the timespan of the hadronic phase. Under these assumptions, all resonance particles decaying before kinetic freeze-out are lost due to rescattering of their decay daughters in the hadronic gas, with no regeneration of resonances through elastic scattering. Thus, the estimated time duration is considered as the lower limit for the timespan between chemical and kinetic freeze-outs.

For this calculation, it is further assumed that no hadronic phase forms in pp collisions due to the small system size. Therefore, the yield ratio in minimum bias pp collisions

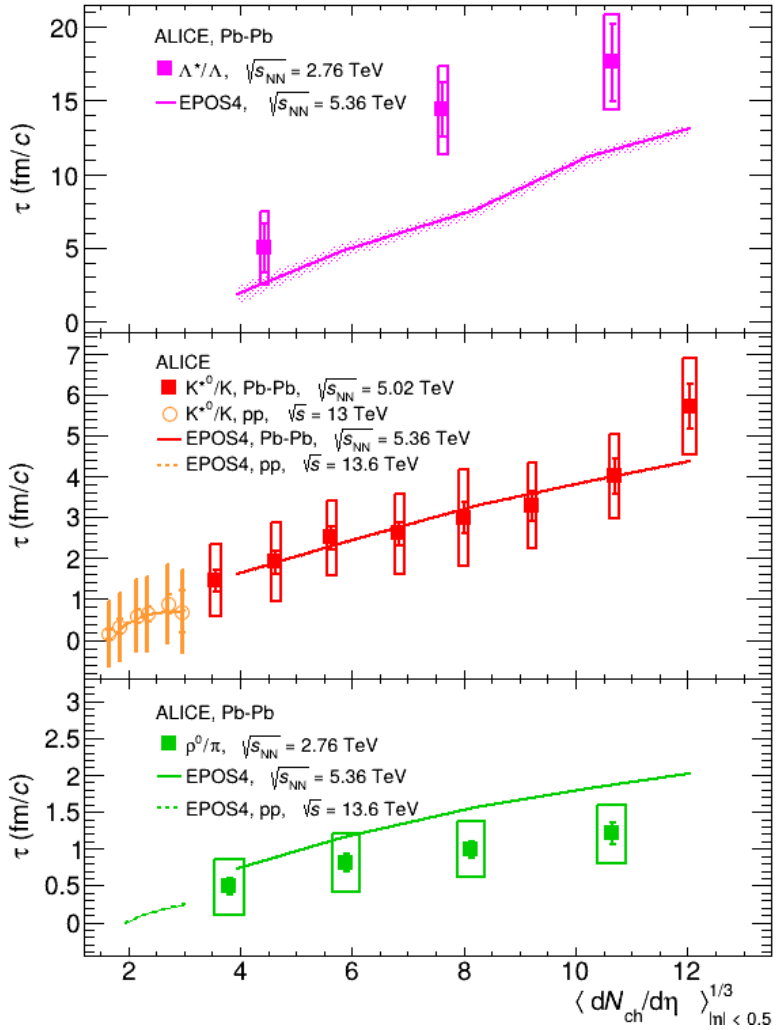

Figure 5.14: Lower limit on the lifetime of the hadronic phase between chemical and kinetic freeze-outs in Pb–Pb collisions across different V0M multiplicity classes, obtained from yield ratios: Λ^*/Λ at $\sqrt{s_{\rm NN}}$ = 2.76 TeV (magenta markers) [83], $\mathrm{K}^{*0}/\mathrm{K}$ at $\sqrt{s_{\rm NN}}$ = 5.02 TeV (red markers) [68], and ρ^0/π at $\sqrt{s_{\rm NN}}$ = 2.76 TeV (green markers) [76]. EPOS4 predictions for Pb–Pb collisions at $\sqrt{s_{\rm NN}}$ = 5.36 TeV are shown as lines, with shaded areas representing statistical uncertainties. Statistical and systematic uncertainties in the ALICE data are depicted by bars and boxes, respectively. The figure also includes ALICE measurements of $\mathrm{K}^{*0}/\mathrm{K}$ in pp collisions at $\sqrt{s} = 13$ TeV (orange markers) [146] and EPOS4 predictions for pp at $\sqrt{s} = 13.6$ TeV (orange line), highlighting the system size dependence of the hadronic phase lifetime.

is used as a proxy for $[h^{*}/h]_{chemical}$. A Lorentz boost factor is also applied in the calculation of τ because the lifetime of resonance is dilated when transitioning from the rest frame of the resonance to the laboratory reference frame. This factor is approximated as $\sqrt{1+(\langle p_{\mathrm{T}}\rangle/mc)^{2}}$, where $\langle p_{\mathrm{T}}\rangle$ is the average transverse momentum and m is the rest mass of the resonance particle. The methodology used to estimate τ is the same as discussed in Ref. [68]. The results for the estimated duration of the hadronic phase (τ) as a function of $\langle dN_{ch}/d\eta\rangle^{1/3}$ from ALICE measurements and EPOS4 with UrQMD using resonances (ρ^{0}, K^{*0} and Λ^{*}) at LHC energies for pp and Pb–Pb collisions, are shown in Figure 5.14. An increasing trend in the lifetime of hadronic phase is observed for these resonances in both data and model, corresponding to the decreasing yield ratios (as shown in Figure 5.13) as a function of system size. This trend is expected, as a larger system size at a fixed chemical freeze-out leads to a decrease in the kinetic freeze-out temperature, thereby a longer timespan exists between chemical and kinetic freeze-outs. This pattern is consistent with the simultaneous blast-wave fits of the identified particle p_{T} distributions [175]. The timespan of the hadronic phase calculated from the ρ^{0}/π, $\mathrm{K}^{*0}/\mathrm{K}$ ratios, are lower than that from the Λ^{*}/Λ ratio. The model predictions for estimation of τ using the Λ^{*}/Λ ratios underestimate the data, whereas ρ^{0}/π overestimate the data. Although the experimental data and model predictions are obtained at slightly different energies, the comparison reveals only minor differences. Since particle production is primarily driven by charged-particle multiplicity, the dependence on collision energy is expected to be weak or negligible. However, the model predictions for $\mathrm{K}^{*0}/\mathrm{K}$ ratio are in good agreement with the data. Contrary to the expectation of a common hadronic phase duration for all resonances, different values are found for the ρ^{0}, K^{*0}, and Λ^{*} yields, with longer-lived resonances showing longer timescales. The observed different values in the time duration of the hadronic phase across different species may be attributed to additional factors beyond rescattering, which also contribute to the final modification of resonance yields. These factors are not accounted for in the simple exponential decay model, as described in Eq. 5.2. If regeneration is significant, the estimated duration from the yield ratios represents the timescale between delayed resonance production (caused by regeneration) and kinetic freeze-out. This duration reflects a lower limit for the actual hadronic-phase duration. To find the exact duration, the delay from regeneration needs to be added to this estimate. Recently hydrodynamics based SMASH model calculation suggest that mean free path of resonances also play an important role in the final yield of resonances [152]. Similar studies in particularly at high multiplicity pp collisions also play huge interest for better understanding of the microscopic origin of resonance suppression. The EPOS4 model results for K^{*0} with UrQMD in high-multiplicity pp collisions also show a nonzero hadronic phase duration, approximately matching the value in peripheral Pb–Pb collisions, thus highlighting the system size dependence of the hadronic phase lifetime, as shown in Figure 5.14.

5.3.6 Strangeness enhancement

The relative yield ratios of various hadrons to pions serve as a key observable to understand the origin of strangeness production and the hadronization mechanism. Figure 5.15 shows the yield ratios of protons, K^0_S and multi-strange baryons (left), along with hadronic resonances (right), normalized to pions as a function of charged-particle multiplicity for pp to Pb–Pb collisions at LHC energies. The results from EPOS4 with and without UrQMD are represented by solid and dotted lines, respectively, and are compared with the available measurements from the ALICE Collaboration [80, 83, 133, 146, 147, 175, 176, 178, 180]. The yield ratios exhibit a smooth evolution with multiplicity from pp to Pb–Pb collisions, whereas $\langle p_T \rangle$ shows a discontinuous pattern with multiplicity, as observed in Figure 5.11. This behavior can be understood as different saturation effects with multiplicity is expected for pp and Pb–Pb collisions. The saturation scale increases with multiplicity for pp collisions, whereas in Pb–Pb collisions, the saturation scale shows a more modest increase, as discussed in [154]. The observed enhancement in the production rates of strange hadrons relative to pions is primarily driven by the strange-quark content of the hadrons rather than their mass. This effect appears to be more pronounced for heavier baryons containing strange quarks in pp collisions. For Pb–Pb collisions, the ratios attain a saturation trend for hadrons that contain strange quark at higher multiplicities. This behavior indicates that their production reaches a chemical equilibrium in central Pb–Pb collisions. The saturation

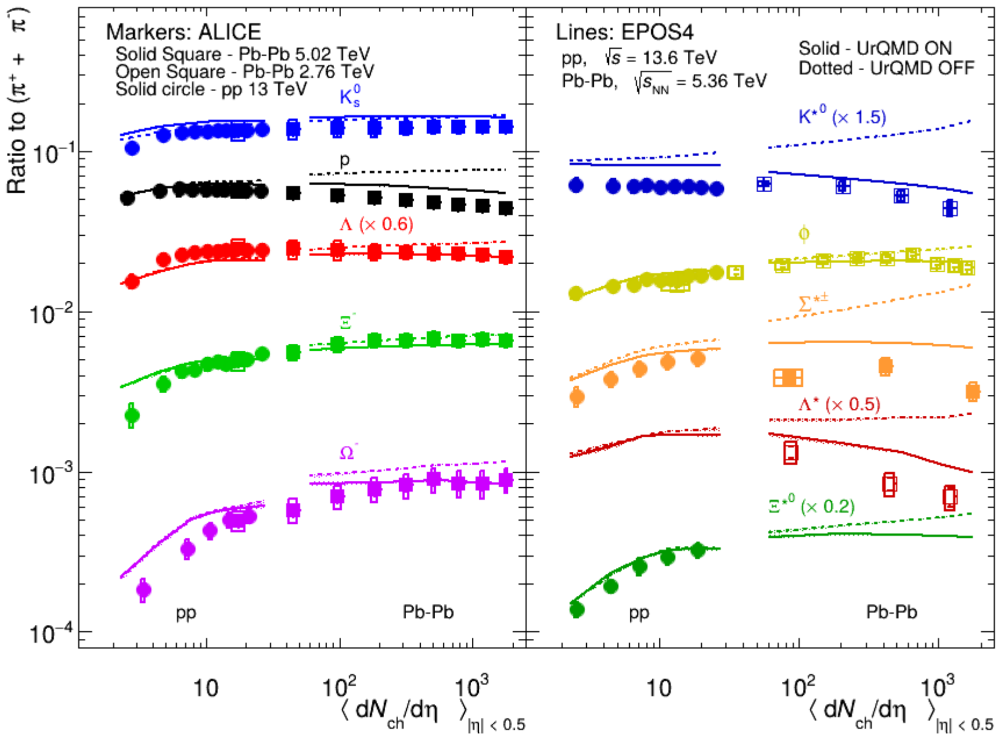

Figure 5.15: Left panel shows the ratios of proton, strange and multi-strange hadrons while the right panel shows the ratios of hadronic resonances, normalized to pions yield. Different markers represent ALICE results in pp collisions at $\sqrt{s_{\mathrm{NN}}}$ = 13 TeV (solid circles) [133, 146, 147, 176, 178] and Pb–Pb collisions at $\sqrt{s_{\mathrm{NN}}}$ = 2.76 TeV (open squares) [83, 180] and $\sqrt{s_{\mathrm{NN}}}$ = 5.02 TeV (solid squares) [80, 175]. The statistical and systematic uncertainties in the data are represented by bars and boxes, respectively. The lines represent predictions from EPOS4 in pp collisions at $\sqrt{s_{\mathrm{NN}}}$ = 13.6 TeV and in Pb–Pb collisions at $\sqrt{s_{\mathrm{NN}}}$ = 5.36 TeV with UrQMD (solid) and without UrQMD (dotted). The shaded area indicates the statistical uncertainty in the model calculations.

reflects the system reach thermalized environment, where the production of strange and multi-strange hadrons becomes independent of further increases in multiplicity for central heavy-ion collisions at LHC energies. The EPOS4 model incorporates the microcanonical ensemble (MCE) framework which reproduces the observed behavior in the experimental data. However, when the system gets very small, one gets a reduction in heavy particle production due to the microcanonical treatment of strange particle production which imposes constraints on energy and flavor conservation. This effect becomes more pronounced with increasing particle mass and is observed most significantly for Ω and Ξ baryons in pp collisions.The model results show a small difference with and without UrQMD tune for multi-strange hadrons for Pb–Pb collisions, whereas there is no significant difference for pp collisions.

Further, the same ratios to pion for hadronic resonances that content strange quarks of short-lived resonances (ρ, K^{*0} and Λ^{*}) show suppression behavior in central Pb–Pb collisions. The results with and without UrQMD show significantly different behavior. This indicates that the rescattering effect is dominant over the strangeness enhancement. The ϕ-meson shows a weak enhancement trend, except in the most central Pb–Pb collisions, where the measurements reveal a decreasing trend. A similar behavior is observed in the results with UrQMD. Future measurements will provide further constraints for understanding this behavior.

The yield ratios of protons to pions show a decreasing trend at the highest multiplicities in Pb–Pb collisions, with a similar behavior observed in both the data and the predictions of the EPOS4 model using UrQMD, although the model results overestimate the measurements. This suppression is attributed to baryon-antibaryon annihilation at large multiplicities, which reduces the proton yield. However, the effects of baryon-antibaryon annihilation appear less pronounced for strange baryons such as the Λ, Ξ^{-} and Ω^{-} at high multiplicities in Pb–Pb collisions. To further understand the production of non-strange and strange baryons in Pb–Pb collisions, the yield ratios of Λ, Ξ^{-} and Ω^{-} to protons, as a function of charged-particle multiplicity and normalized to the values measured in inelastic pp collisions, have been calculated using EPOS4 with UrQMD predictions. The results are shown in Figure 5.16. The ratios for Δ^{++} show flat behavior with multiplicity for Pb–Pb collisions, as expected, since Δ^{++} has no strange content and no hadronic phase effects are observed, as discussed in Figure 5.16. Similarly, the same ratios for Λ,Ξ^{-} and Ω^{-} increase with multiplicity, with the rate of enhancement rising according to the strange-quark content of the hadrons. This behavior can be understood as a competitive interplay between strangeness production and baryon-antibaryon annihilation processes, which influence multi-strange baryon production in the high-multiplicity environment of Pb–Pb collisions at LHC energies. The stepper rise in the slope of the ratios is observed in pp collisions. Future experimental measurements of these ratios at the LHC will provide deeper insight, helping to distinguish between the effects of strangeness production and baryon-antibaryon annihila-

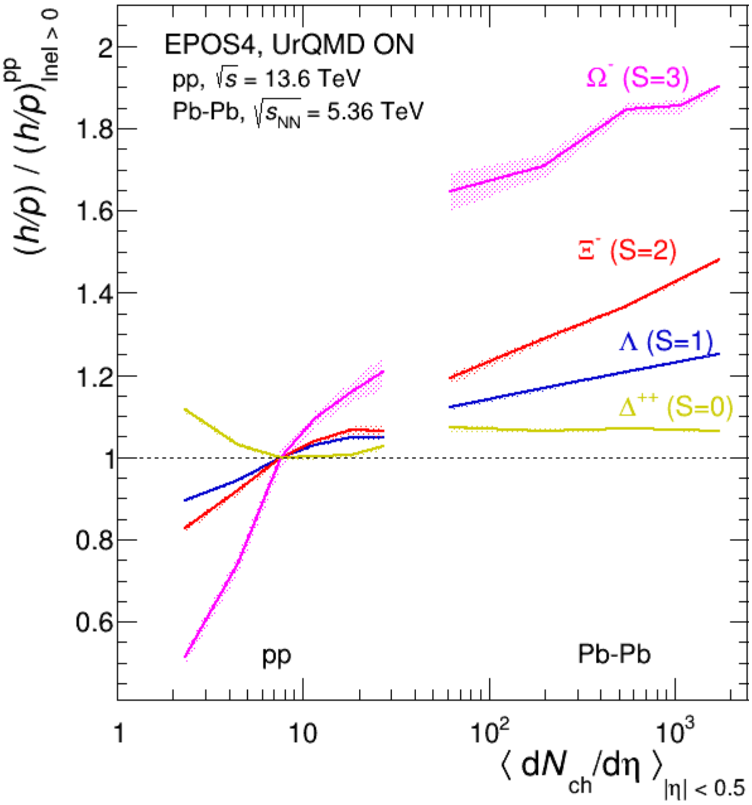

Figure 5.16: Particle yield ratios to proton, normalized to the values measured inelastic pp collisions, as predicted by the EPOS4 model with UrQMD. The results are shown for Δ^{++} and multi-strange baryons in Pb–Pb collisions at $\sqrt{s_{\mathrm{NN}}}$ = 5.36 TeV and in pp collisions at $\sqrt{s}$ =13.6 TeV. The bands in the measurements represent statistical uncertainty.

tion. This observation suggests that the net suppression in the most central Pb–Pb collisions depends on the modification of hadron yields due to combined contributions from various processes, such as strangeness production, baryon-antibaryon annihilation, and hadronic phase effects.

Chapter 6

Summary and conclusion

The Standard Model of particle physics stands as a monumental achievement in the history of physics. This model unifies three of the four fundamental forces of nature: the electromagnetic force, the weak nuclear force, and the strong nuclear force. The electromagnetic force governs the attraction between electrons and the nucleus, holding electrons in their atomic shells due to the opposite charges of electrons and protons. The weak nuclear force plays a crucial role in the stability of atomic nuclei by enabling the decay of neutrons into protons, beta particles, and neutrinos, thus maintaining a stable neutron-to-proton ratio in nuclei. The strong interaction manifests itself in two distinct ways. The first is the force that binds protons and neutrons together within the nucleus, overcoming the electromagnetic repulsion between protons. The second type of strong interaction is more fundamental, which occurs between quarks within nucleons, where quarks are bound so tightly that free quarks are never observed in nature. When enough energy is applied to separate quarks within a nucleon, this energy creates new quark-antiquark pairs which immediately bind together, preventing the isolation of a single quark. However, the gravitational force is not yet included in the Standard Model. Research is ongoing in this field, and we hope to one day see gravity incorporated into the Standard Model alongside the other fundamental forces.

Quantum Chromodynamics (QCD) is the theoretical framework within the Standard Model that explains the interactions among quarks. In QCD, quarks are bound together by exchanging particles called gluons, which act as the force carriers for the strong interaction.

QCD introduces the concept of color charges, analogous to electric charges in Quantum Electrodynamics (QED). Quarks and gluons carry these color charges, which come in three types: red, blue, and green—though these do not have a relation to visible colors. Only color-neutral hadron states are possible, a principle known as color confinement, which explains why quarks are never found free in nature. QCD also predicts a phenomenon called asymptotic freedom, where at extremely high energy densities, quarks and gluons are the only degrees of freedom. This state, known as quark-gluon plasma (QGP), can be recreated in the laboratory by colliding nuclei at relativistic speeds, as done at the Relativistic Heavy Ion Collider (RHIC) at Brookhaven National Laboratory (BNL) and the Large Hadron Collider (LHC) at CERN. The QGP exists only for a brief time, making it impossible to observe directly. Instead, its formation is confirmed through various signatures. These signatures include measuring the medium's temperature from direct-photon production yields, observing an enhancement in strange-quark production which leads to a higher yield of strange hadrons, detecting suppression of J/ψ particles due to interactions within the QGP, and chiral-symmetry restoration in the QGP medium. Each of these signatures supports the existence of QGP and reinforces the evidence provided by the others.

As the medium created in relativistic heavy-ion collisions expands, its temperature decreases, causing the asymptotically free quarks to recombine into mesons and baryons, collectively known as hadrons. During this phase, there is a mixed state of quarks and hadrons, where inelastic interactions produce new hadrons. As the system continues to expand, the remaining quarks also combine, and the production of new hadrons ceases, marking the chemical freeze-out. However, particles still interact elastically, altering their momenta. Further expansion leads to the kinetic freeze-out, where elastic interactions stop as particles move too far apart. The interval between chemical and kinetic freeze-out is known as the hadronic phase, during which only hadronic gas exists, and hadrons interact elastically. The duration of this phase depends on the size of the colliding system and the centrality of the collision. To understand the properties of the hadronic phase, we studied particles formed at or before chemical freeze-out with lifetimes comparable to the lifetime of the hadronic phase. Hadronic resonances, such as ρ^0, K^{*0}, $\Sigma^{*\pm}$, Λ^*, Ξ^{*0}, and ϕ, serve this purpose. These resonances decay within the hadronic phase, and their yields are modified by the rescattering or regeneration of their decay daughters. Studies with ALICE and STAR have shown that the ρ^0/π and $\mathrm{K}^{*0}/\mathrm{K}$ yield ratios decrease with multiplicity in both small and large systems, while the Λ^*/Λ ratio decreases only in large collision systems. The ϕ/π ratio, however, remains unaffected by multiplicity, likely due to the longer lifetime of ϕ compared to the time span of hadronic phase. Given that the lifetime of Λ^* falls between those of K^{*0} and ϕ, studying its production yield in p–Pb collisions at the highest LHC energy available in the p–Pb system is particularly interesting.

The production yield of Λ^* resonance is studied in the mid-rapidity region for p–Pb collisions in $\sqrt{s_{\mathrm{NN}}} = 8.16$ TeV in the NSD class and in four V0A multiplicity classes, and in the inelastic pp collisions at $\sqrt{s} = 8$ TeV using the ALICE detector. The analysis is based on approximately 35 million p–Pb events and 58 million pp events, after applying event selection cuts. The Λ^* resonance is reconstructed via its decay channel pK^- ($\bar{\mathrm{p}}\mathrm{K}^+$) using the invariant mass technique. The identification of its decay daughters, protons and kaons, is performed using the Time Projection Chamber (TPC) and Time-Of-Flight (TOF) detectors in ALICE. The TPC identifies particles through specific energy loss ($\mathrm{d}E/\mathrm{d}x$), while the TOF uses time-of-flight information. The invariant mass distribution (M_{inv}) is obtained by combining the four-momenta of primary protons and kaons with opposite charges from the same event. These distributions are combined to obtain the total signal for Λ^* and its anti-particle. A significant combinatorial background, due to protons and kaons that do not originate from $\Lambda(1520)$, is estimated using the event-mixing technique and subtracted from the signal. The invariant mass distributions are then fitted with a Voigtian function, which combines a Breit-Wigner distribution (for the signal peak) and a Gaussian function (accounting for mass resolution), along with a second-order polynomial for the residual background. The raw yield of $\Lambda(1520)$ is determined using the bin counting method, with function integration used for systematic studies. The raw spectra are normalized by dividing by the number of events in each multiplicity class (N_{evt}), detector efficiency and acceptance ($A \times \varepsilon_{\mathrm{rec}}$), branching ratio and the rapidity window factor (dy). The resulting spectra, after applying these corrections, are referred to as corrected spectra or transverse momentum

(p_{T}) spectra of $\Lambda(1520)$.

In this study, the p_{T} spectra, p_{T}-integrated yield ($\mathrm{d}N/\mathrm{d}y$), the average p_{T} ($\langle p_{\mathrm{T}}\rangle$), the resonance-to-stable particle yield ratio and the nuclear modification factor (R_{pPb}) for $\Lambda(1520)$ are measured. The p_{T} spectra of Λ^{*} in various V0A multiplicity classes for the p–Pb system show a hardening with increasing multiplicity, similar to the behavior observed for other hadrons. Both $\mathrm{d}N/\mathrm{d}y$ and $\langle p_{\mathrm{T}}\rangle$ increase with multiplicity, indicating that the yield and $\langle p_{\mathrm{T}}\rangle$ of Λ^{*} are influenced by the multiplicity of collisions. Comparison with published results at lower energy in the p–Pb system shows consistency in both energies across common multiplicity regions, suggesting that particle production is driven primarily by event multiplicity rather than collision energy, and this observation is similar to what has been observed for other resonances. The R_{pPb} of Λ^{*} shows a Cronin-like enhancement in the mid-p_{T} region, similar to that seen in the Λ baryon but absent in mesons such as K^{*0} and $\mathrm{K}^{0}_{\mathrm{S}}$, indicating different production mechanisms for baryons and mesons. At low p_{T}, the R_{pPb} is below unity for all particles, suggesting energy loss while traversing the medium in the p–Pb system. At high p_{T}, the R_{pPb} approaches unity for all particles, indicating that there is no significant modification due to the effects of cold nuclear matter. The resonance to non-resonance ratios in the p–Pb system at $\sqrt{s_{\mathrm{NN}}}$ = 8.16 TeV show that Λ^{*}/Λ remains flat, while $\mathrm{K}^{*0}/\mathrm{K}$ shows a slight decreasing trend, indicating the formation of a hadronic phase in the p–Pb system at this energy, but its lifetime is very short so that it does not significantly affect the yield of Λ^{*}. Furthermore, the Λ^{*}/Λ ratios at $\sqrt{s_{\mathrm{NN}}}$ = 8.16 and 5.02 TeV in the p–Pb system are consistent within uncertainties. The predictions of the EPOS3 model for R_{pPb} show a trend similar to the data in the low and high p_{T} regions, but they do not capture the Cronin-like enhancement in the mid-p_{T} region. The EPOS3 model shows a slight increasing trend with multiplicity for Λ^{*}/Λ ratio while it shows a slight decreasing trend for $\mathrm{K}^{*0}/\mathrm{K}$ when final state interactions are enabled.

To further explore the mechanisms of hadron production and the properties of the hadronic phase, we used EPOS4, a hydrodynamical model, to calculate particle yields and various ratios in pp collisions at $\sqrt{s}$ = 13.6 TeV and Pb–Pb collisions at $\sqrt{s_{\mathrm{NN}}}$ = 5.36 TeV, chosen as the latest energies recorded at the LHC. EPOS4, an extension of EPOS3, incorporates new approaches to multiple scatterings and saturation phenomena. In our study, p_{T}-differential spectra ratios of various hadrons were calculated across different event multiplicity classes, defined in the same way as in the ALICE measurements for Run 2 data. The $\langle p_{\mathrm{T}} \rangle$ has been analyzed as a function of both the charged-particle multiplicity and the hadron mass that is scaled to the number of valence quarks. The EPOS4 model qualitatively describes the ALICE data in both pp and Pb–Pb collisions and accurately captures the mass ordering of $\langle p_{\mathrm{T}} \rangle$, particularly in the most central Pb–Pb collisions for particles which have comparable masses such as the proton and ϕ. The $\langle p_{\mathrm{T}} \rangle$ exhibits a linear trend with the hadron mass, scaled to the number of valence quarks. Moreover, we observe a departure from this linear trend for resonances with short lifetimes, the deviation being more pronounced in the Pb–Pb system relative to the pp system.

The model study further examines baryon-to-meson ratios to understand mass-dependent radial flow and baryon/meson production mechanisms. Using calculations from EPOS4, both with and without UrQMD, we observed a mass-dependent enhancement at low- to intermediate-p_{T} in central collisions, which is similar to the findings of the ALICE Collaboration. This enhancement shifts towards higher-p_{T} regions with increasing baryon mass. Quark recombination may explain the enhancement; however, the influence of radial flow is considered by comparing similar-mass particle ratios. EPOS4 with UrQMD accurately describes the p/π ratio but failed to describe the p/K^{*0} ratio at low-p_{T} and the p/ϕ ratio at intermediate-p_{T}. In high-p_{T} regions, a consistent decreasing trend suggests that a common fragmentation mechanism is at play. The results indicate significant effects from the hadronic phase and quark content differences on the spectral shapes, particularly influencing low-p_{T} regions in the measured data.

The model predictions for resonance-to-stable particle yield ratios qualitatively match ALICE results when final-state interactions (UrQMD) are included, highlighting the importance of these interactions in modifying hadronic resonance spectra. The study also estimates the lifetime of the hadronic phase using resonance yield ratios to stable particles in EPOS4, observing that the lifetime increases with the centrality of Pb–Pb collisions, consistent with the expected decrease in kinetic freeze-out temperature as the size of the system increases.

The EPOS4 predictions for strange-to-pion yield ratios exhibit a qualitatively similar trend to the ALICE data, showing an increase with multiplicity in pp collisions and saturation at chemical equilibrium in central Pb–Pb collisions. EPOS4 with UrQMD aligns well with experimental observations but shows slight deviations, particularly in multi-strange hadron production. Suppression of hadronic resonances in central collisions is driven by rescattering effects, outweighing strangeness enhancement. Proton-to-pion ratios decrease at high multiplicities in heavy-ion collisions, primarily due to baryon-antibaryon annihilation. This interplay between strangeness production and baryon-antibaryon annihilation significantly influences baryon yields at high multiplicities.

Bibliography

[1] J. W. Harris and B. Muller, Ann. Rev. Nucl. Part. Sci. **46**, 71 (1996), hep-ph/9602235.

[2] G. Aad et al. (ATLAS), Physics Letters B **716**, 1 (2012).

[3] S. Chatrchyan et al. (CMS), Phys. Lett. B **716**, 30 (2012), 1207.7235.

[4] P. W. Higgs, Phys. Rev. Lett. **13**, 508 (1964).

[5] E. Rutherford, Phil. Mag. Ser. 6 **21**, 669 (1911).

[6] E. Rutherford, Phil. Mag. Ser. 6 **37**, 581 (1919).

[7] J. Chadwick, Nature **129**, 312 (1932).

[8] E. D. Bloom et al., Phys. Rev. Lett. **23**, 930 (1969).

[9] M. Breidenbach, J. I. Friedman, H. W. Kendall, E. D. Bloom, D. H. Coward, H. C. DeStaebler, J. Drees, L. W. Mo, and R. E. Taylor, Phys. Rev. Lett. **23**, 935 (1969).

[10] W. J. Marciano and H. Pagels, Phys. Rept. **36**, 137 (1978).

[11] R. Brandelik et al. (TASSO), Phys. Lett. B **86**, 243 (1979).

[12] J. Woithe, G. J. Wiener, and F. F. Van der Veken, Phys. Educ. **52**, 034001 (2017).

[13] S. Bethke, Prog. Part. Nucl. Phys. **58**, 351 (2007), hep-ex/0606035.

[14] M. Gockeler, R. Horsley, A. C. Irving, D. Pleiter, P. E. L. Rakow, G. Schierholz, and H. Stuben, Phys. Rev. D **73**, 014513 (2006), hep-ph/0502212.

[15] D. J. Gross and F. Wilczek, Phys. Rev. Lett. **30**, 1343 (1973).

[16] D. J. Gross and F. Wilczek, Phys. Rev. D **8**, 3633 (1973).

[17] H. D. Politzer, Phys. Rev. Lett. **30**, 1346 (1973).

[18] A. Herráez, R. Hanson, and L. Glasser, J. Chem. Education **86**, 566 (2009).

[19] T. D. Lee and G. C. Wick, Phys. Rev. D **9**, 2291 (1974).

[20] J. C. Collins and M. J. Perry, Phys. Rev. Lett. **34**, 1353 (1975).

[21] H.-T. Ding, F. Karsch, and S. Mukherjee, Int. J. Mod. Phys. E **24**, 1530007 (2015), `1504.05274`.

[22] F. Karsch, Prog. Theor. Phys. Suppl. **153**, 106 (2004), `hep-lat/0401031`.

[23] R. C. Hwa and X. N. Wang, eds., *Quark-gluon plasma 3*, vol. 3 (World Scientific, Singapore, 2004), ISBN 978-981-238-077-7, 978-981-4488-08-2.

[24] R. V. Gavai and S. Gupta, Phys. Rev. D **71**, 114014 (2005), `hep-lat/0412035`.

[25] F. Karsch, Nucl. Phys. A **698**, 199 (2002), `hep-ph/0103314`.

[26] Y. Aoki, G. Endrodi, Z. Fodor, S. D. Katz, and K. K. Szabo, Nature **443**, 675 (2006), `hep-lat/0611014`.

[27] S. Ejiri, Phys. Rev. D **78**, 074507 (2008), `0804.3227`.

[28] D. H. Rischke, Prog. Part. Nucl. Phys. **52**, 197 (2004), `nucl-th/0305030`.

[29] A. Pandav, D. Mallick, and B. Mohanty, Prog. Part. Nucl. Phys. **125**, 103960 (2022), `2203.07817`.

[30] F. Gelis, E. Iancu, J. Jalilian-Marian, and R. Venugopalan, Ann. Rev. Nucl. Part. Sci. **60**, 463 (2010), `1002.0333`.

[31] F. Gelis, Int. J. Mod. Phys. A **28**, 1330001 (2013), `1211.3327`.

[32] A. Rothkopf, Phys. Rept. **858**, 1 (2020), `1912.02253`.

[33] J. Rafelski and B. Muller, Phys. Rev. Lett. **48**, 1066 (1982), [Erratum: Phys.Rev.Lett. 56, 2334 (1986)].

[34] P. Koch, B. Muller, and J. Rafelski, Phys. Rept. **142**, 167 (1986).

[35] M. Petrán, J. Letessier, V. Petráček, and J. Rafelski, Phys. Rev. C **88**, 034907 (2013), `1303.2098`.

[36] E. Andersen et al. (WA97), Phys. Lett. B **449**, 401 (1999).

[37] F. Antinori et al. (NA57), J. Phys. G **32**, 427 (2006), `nucl-ex/0601021`.

[38] B. I. Abelev et al. (STAR), Phys. Rev. C **77**, 044908 (2008), `0705.2511`.

[39] F. Becattini, J. Manninen, and M. Gazdzicki, Phys. Rev. C **73**, 044905 (2006), `hep-ph/0511092`.

[40] F. Becattini, E. Grossi, M. Bleicher, J. Steinheimer, and R. Stock, Phys. Rev. C **90**, 054907 (2014), `1405.0710`.

[41] L. Adamczyk et al. (STAR), Phys. Rev. C **96**, 044904 (2017), `1701.07065`.

[42] J. Adam et al. (ALICE), Nature Phys. **13**, 535 (2017), `1606.07424`.

[43] T. Matsui and H. Satz, Phys. Lett. B **178**, 416 (1986).

[44] E. Braaten, S. Fleming, and T. C. Yuan, Ann. Rev. Nucl. Part. Sci. **46**, 197 (1996), `hep-ph/9602374`.

[45] R. L. Thews, M. Schroedter, and J. Rafelski, Phys. Rev. C **63**, 054905 (2001), `hep-ph/0007323`.

[46] P. Braun-Munzinger and J. Stachel, Phys. Lett. B **490**, 196 (2000), `nucl-th/0007059`.

[47] M. C. Abreu et al. (NA38), Phys. Lett. B **449**, 128 (1999).

[48] M. C. Abreu et al. (NA50), Phys. Lett. B **477**, 28 (2000).

[49] B. Alessandro et al. (NA50), Eur. Phys. J. C **39**, 335 (2005), `hep-ex/0412036`.

[50] R. Arnaldi et al. (NA60), Conf. Proc. C **060726**, 430 (2006), `0706.4361`.

[51] L. Kluberg and H. Satz, *Color Deconfinement and Charmonium Production in Nuclear Collisions* (Springer, 2010), `0901.3831`.

[52] R. Arnaldi et al. (NA60), Eur. Phys. J. C **59**, 607 (2009), `0810.3204`.

[53] Z. Ye (for the STAR collaboration), Talk at the Quark Matter 2022.

[54] V. Khachatryan (PHENIX), PoS **CPOD2017**, 079 (2018).

[55] J. Adam et al. (ALICE), Phys. Lett. B **754**, 235 (2016), `1509.07324`.

[56] J. Beringer et al. (Particle Data Group), Phys. Rev. D **86**, 010001 (2012).

[57] A. Bazavov et al., Phys. Rev. D **85**, 054503 (2012), `1111.1710`.

[58] A. I. Bochkarev and M. E. Shaposhnikov, Nucl. Phys. B **268**, 220 (1986).

[59] C. A. Dominguez and M. Loewe, Phys. Lett. B **233**, 201 (1989).

[60] R. Arnaldi et al. (NA60), Phys. Rev. Lett. **96**, 162302 (2006), `nucl-ex/0605007`.

[61] R. Arnaldi et al. (NA60), Phys. Rev. Lett. **100**, 022302 (2008), `0711.1816`.

[62] R. Arnaldi et al. (NA60), Eur. Phys. J. C **61**, 711 (2009), `0812.3053`.

[63] R. Arnaldi et al. (NA60), Phys. Rev. Lett. **102**, 222301 (2009), `0812.3100`.

[64] R. Rapp and J. Wambach, Adv. Nucl. Phys. **25**, 1 (2000), `hep-ph/9909229`.

[65] A. Adare et al. (PHENIX), Phys. Rev. C **93**, 014904 (2016), `1509.04667`.

[66] L. Adamczyk et al. (STAR), Phys. Rev. C **92**, 024912 (2015), `1504.01317`.

[67] S. Acharya et al. (ALICE), JHEP **06**, 024 (2023), `2204.11732`.

[68] S. Acharya et al. (ALICE), Phys. Lett. B **802**, 135225 (2020), `1910.14419`.

[69] S. Singha, B. Mohanty, and Z.-W. Lin, Int. J. Mod. Phys. E **24**, 1550041 (2015), `1505.02342`.

[70] A. G. Knospe, C. Markert, K. Werner, J. Steinheimer, and M. Bleicher, Phys. Rev. C **93**, 014911 (2016), `1509.07895`.

[71] A. Andronic, P. Braun-Munzinger, and J. Stachel, Phys. Lett. B **673**, 142 (2009), [Erratum: Phys.Lett.B 678, 516 (2009)], `0812.1186`.

[72] J. Cleymans and K. Redlich, Phys. Rev. C **60**, 054908 (1999), `nucl-th/9903063`.

[73] S. Chatterjee, S. Das, L. Kumar, D. Mishra, B. Mohanty, R. Sahoo, and N. Sharma, Adv. High Energy Phys. **2015**, 349013 (2015).

[74] D. Sahu, S. Tripathy, G. S. Pradhan, and R. Sahoo, Phys. Rev. C **101**, 014902 (2020), `1909.05788`.

[75] M. Tanabashi et al. (Particle Data Group), Phys. Rev. D **98**, 030001 (2018).

[76] S. Acharya et al. (ALICE), Phys. Rev. C **99**, 064901 (2019), `1805.04365`.

[77] V. Raibov, https://alice-notes.web.cern.ch/node/832.

[78] S. Acharya et al. (ALICE), Phys. Rev. C **106**, 034907 (2022), `2106.13113`.

[79] S. Acharya et al. (ALICE), Eur. Phys. J. C **83**, 540 (2023), `2204.10263`.

[80] S. Acharya et al. (ALICE), Eur. Phys. J. C **83**, 351 (2023), `2205.13998`.

[81] B. B. Abelev et al. (ALICE), Eur. Phys. J. C **75**, 1 (2015), `1406.3206`.

[82] D. Adamova et al. (ALICE), Eur. Phys. J. C **77**, 389 (2017), `1701.07797`.

[83] S. Acharya et al. (ALICE), Phys. Rev. C **99**, 024905 (2019), `1805.04361`.

[84] S. Acharya et al. (ALICE), Eur. Phys. J. C **80**, 160 (2020), `1909.00486`.

[85] J. Song, https://alice-notes.web.cern.ch/node/560.

[86] L. Gaudichet (STAR), J. Phys. G **30**, S549 (2004), `nucl-ex/0307013`.

[87] S. Acharya et al. (ALICE), Phys. Rev. Lett. **125**, 012301 (2020), `1910.14408`.

[88] A. Accardi et al., in *3rd Workshop on Hard Probes in Heavy Ion Collisions: 3rd Plenary Meeting* (2004), `hep-ph/0308248`.

[89] D. Perkins, *Introduction to High Energy Physics* (Cambridge University Press, 2000).

[90] J. Adam et al. (ALICE), Phys. Lett. B **772**, 567 (2017), `1612.08966`.

[91] R. L. Workman and Others (Particle Data Group), PTEP **2022**, 083C01 (2022).

[92] E. Mobs (2016), general Photo, URL `https://cds.cern.ch/record/2197559`.

[93] B. Lindstrom et al., Phys. Rev. Accel. Beams **23**, 081001 (2020), `2005.04520`.

[94] A. Collaboration (2017), figure Repository, URL `https://alice-figure.web.cern.ch/node/11218`.

[95] B. B. Abelev et al. (ALICE), Int. J. Mod. Phys. A **29**, 1430044 (2014), `1402.4476`.

[96] A. Tauro, *ALICE Schematics*, CERN Document Server (2017), aLICE-PHO-SKE2017-001, URL `https://cds.cern.ch/record/2263642`.

[97] A. Collaboration (2019), figure Repository, URL `https://alice-figure.web.cern.ch/node/16718`.

[98] J. Alme et al., Nucl. Instrum. Meth. A **622**, 316 (2010), `1001.1950`.

[99] A. Collaboration (2019), figure Repository, URL `https://alice-figure.web.cern.ch/node/16725`.

[100] A. Andronic (ALICE TRD), Nucl. Instrum. Meth. A **522**, 40 (2004), `physics/0402131`.

[101] C. Adler et al. (ALICE), Nucl. Instrum. Meth. A **552**, 364 (2005).

[102] S. Acharya et al. (ALICE), Nucl. Instrum. Meth. A **881**, 88 (2018), `1709.02743`.

[103] A. Akindinov et al., Eur. Phys. J. Plus **128**, 44 (2013).

[104] A. Collaboration (2019), figure Repository, URL https://alice-figure.web.cern.ch/node/16722.

[105] ALICE Collaboration, Tech. Rep. CERN-LHCC-2006-014, CERN-LHCC (2006), URL http://cdsweb.cern.ch/record/932676.

[106] ALICE Collaboration, Tech. Rep. 99-4, CERN/LHCC (1999), URL https://edms.cern.ch/document/398934/1.

[107] ALICE Collaboration, Tech. Rep. CERN-LHCC-98-019, CERN (1998), URL http://cdsweb.cern.ch/record/381431.

[108] ALICE Collaboration, Tech. Rep. CERN-LHCC-99-032, CERN (1999), URL http://cdsweb.cern.ch/record/451099.

[109] ALICE Collaboration, Tech. Rep. CERN-LHCC-2003-038, CERN (2003), URL http://cdsweb.cern.ch/record/642177.

[110] ALICE Collaboration, Tech. Rep., CERN (2004), URL http://cds.cern.ch/record/781854.

[111] E. Abbas et al. (ALICE), JINST **8**, P10016 (2013), 1306.3130.

[112] A. Collaboration, Tech. Rep. CERN-LHCC-2003-062, CERN (2004), URL https://cds.cern.ch/record/684651.

[113] A. Gheata (ALICE), PoS **ACAT08**, 028 (2008).

[114] R. Brun and F. Rademakers, Nucl. Instrum. Meth. A **389**, 81 (1997).

[115] R. Brun, F. Bruyant, F. Carminati, S. Giani, M. Maire, A. McPherson, G. Patrick, and L. Urban (1994).

[116] I. J. M. Huancco, J. Phys. Conf. Ser. **1143**, 012011 (2018).

[117] A. Fasso et al., eConf **C0303241**, MOMT004 (2003), physics/0306162.

[118] T. Sjostrand, S. Mrenna, and P. Z. Skands, JHEP **05**, 026 (2006), hep-ph/0603175.

[119] B. P. Kersevan and E. Richter-Was, Comput. Phys. Commun. **184**, 919 (2013), hep-ph/0405247.

[120] X.-N. Wang and M. Gyulassy, Phys. Rev. D **44**, 3501 (1991).

[121] S. Roesler, R. Engel, and J. Ranft, in *International Conference on Advanced Monte Carlo for Radiation Physics, Particle Transport Simulation and Applications (MC 2000)* (2000), pp. 1033–1038, hep-ph/0012252.

[122] Y. Pei, S. Biswas, D. S. Fussell, and K. Pingali, Commun. ACM **62**, 122–133 (2019), ISSN 0001-0782, URL https://doi.org/10.1145/3363294.

[123] S. Acharya et al. (ALICE), Phys. Rev. C **107**, 055201 (2023), 2110.10042.

[124] M. L. Miller, K. Reygers, S. J. Sanders, and P. Steinberg, Ann. Rev. Nucl. Part. Sci. **57**, 205 (2007), nucl-ex/0701025.

[125] C. Loizides, J. Kamin, and D. d'Enterria, Phys. Rev. C **97**, 054910 (2018), [Erratum: Phys.Rev.C 99, 019901 (2019)], 1710.07098.

[126] S. Acharya et al. (ALICE), Eur. Phys. J. C **79**, 307 (2019), 1812.01312.

[127] W. Blum, W. Riegler, and L. Rolandi, *Particle detection with drift chambers; 2nd ed.* (Springer, Berlin, 2008), URL https://cds.cern.ch/record/1105920.

[128] S. Acharya et al. (ALICE), Phys. Rev. C **102**, 024912 (2020), 1910.14410.

[129] R. Barlow, in *Conference on Advanced Statistical Techniques in Particle Physics* (2002), pp. 134–144, hep-ex/0207026.

[130] C. Tsallis, J. Statist. Phys. **52**, 479 (1988).

[131] K. Werner, B. Guiot, I. Karpenko, and T. Pierog, Phys. Rev. C **89**, 064903 (2014), 1312.1233.

[132] M. Gyulassy and X.-N. Wang, Comput. Phys. Commun. **83**, 307 (1994), nucl-th/9502021.

[133] S. Acharya et al. (ALICE), Eur. Phys. J. C **80**, 167 (2020), 1908.01861.

[134] *Centrality determination in heavy ion collisions (ALICE Collaboration, ALICE-PUBLIC-2018-011)* (2018).

[135] ALICE Collaboration, *Analysis Note*, ALICE Analysis Note (2021), https://alice-notes.web.cern.ch/node/1191.

[136] D. Kharzeev, Y. V. Kovchegov, and K. Tuchin, Phys. Rev. D **68**, 094013 (2003), hep-ph/0307037.

[137] A. H. Rezaeian and Z. Lu, Nucl. Phys. A **826**, 198 (2009), 0810.4942.

[138] S. Acharya et al. (ALICE), Phys. Lett. B **827**, 136943 (2022), 2104.03116.

[139] J. Adam et al. (ALICE), Phys. Lett. B **760**, 720 (2016), 1601.03658.

[140] S. Acharya et al. (ALICE), JHEP **11**, 013 (2018), 1802.09145.

[141] A. M. Sirunyan et al. (CMS), Phys. Rev. C **101**, 064906 (2020), 1910.04812.

[142] B. I. Abelev et al. (STAR), Phys. Rev. C **78**, 044906 (2008), 0801.0450.

[143] P. Koch, J. Rafelski, and W. Greiner, Physics Letters B **123**, 151 (1983), ISSN 0370-2693.

[144] P. Koch, B. Müller, and J. Rafelski, Physics Reports **142**, 167 (1986), ISSN 0370-1573.

[145] B. Abelev et al., Physics Letters B **728**, 216 (2014), ISSN 0370-2693.

[146] S. Acharya et al. (ALICE), Phys. Lett. B **807**, 135501 (2020), 1910.14397.

[147] S. Acharya et al. (ALICE), JHEP **05**, 317 (2024), 2308.16116.

[148] B. I. Abelev et al. (STAR), Phys. Rev. Lett. **97**, 132301 (2006), nucl-ex/0604019.

[149] J. Adams et al. (STAR), Phys. Rev. C **71**, 064902 (2005), nucl-ex/0412019.

[150] Z.-W. Lin, C. M. Ko, B.-A. Li, B. Zhang, and S. Pal, Phys. Rev. C **72**, 064901 (2005), nucl-th/0411110.

[151] A. Motornenko, V. Vovchenko, C. Greiner, and H. Stoecker, Phys. Rev. C **102**, 024909 (2020), 1908.11730.

[152] D. Oliinychenko and C. Shen, arXiv preprint (2021), [hep-ph], 2105.07539.

[153] A. G. Knospe, C. Markert, K. Werner, J. Steinheimer, and M. Bleicher, Phys. Rev. C **104**, 054907 (2021), 2102.06797.

[154] K. Werner, Phys. Rev. C **109**, 014910 (2024), 2306.10277.

[155] V. N. Gribov, Zh. Eksp. Teor. Fiz. **53**, 654 (1967).

[156] V. N. Gribov, Sov. Phys. JETP **29**, 483 (1969).

[157] V. N. Gribov and L. N. Lipatov, Sov. J. Nucl. Phys. **15**, 438 (1972).

[158] V. A. Abramovsky, V. N. Gribov, and O. V. Kancheli, Yad. Fiz. **18**, 595 (1973).

[159] K. Werner, H. J. Drescher, S. Ostapchenko, and T. Pierog, Acta Phys. Hung. A **15**, 215 (2002), hep-ph/0107170.

[160] V. A. Abramovsky and G. G. Leptoukh, Sov. J. Nucl. Phys. **55**, 903 (1992).

[161] K. Werner, Phys. Rev. C **108**, 064903 (2023), 2301.12517.

[162] G. Altarelli and G. Parisi, Nucl. Phys. B **126**, 298 (1977).

[163] Y. L. Dokshitzer, Sov. Phys. JETP **46**, 641 (1977).

[164] L. V. Gribov, E. M. Levin, and M. G. Ryskin, Phys. Rept. **100**, 1 (1983).

[165] L. D. McLerran and R. Venugopalan, Phys. Rev. D **49**, 3352 (1994), hep-ph/9311205.

[166] L. D. McLerran and R. Venugopalan, Phys. Rev. D **49**, 2233 (1994), hep-ph/9309289.

[167] A. Kovner, L. D. McLerran, and H. Weigert, Phys. Rev. D **52**, 3809 (1995), hep-ph/9505320.

[168] Y. V. Kovchegov, Phys. Rev. D **54**, 5463 (1996), hep-ph/9605446.

[169] C. Bierlich, G. Gustafson, L. Lönnblad, and H. Shah, JHEP **10**, 134 (2018), 1806.10820.

[170] C. Bierlich, S. Chakraborty, G. Gustafson, and L. Lönnblad, Phys. Lett. B **835**, 137571 (2022), 2205.11170.

[171] K. Werner, Phys. Rev. Lett. **98**, 152301 (2007), 0704.1270.

[172] K. Werner, I. Karpenko, T. Pierog, M. Bleicher, and K. Mikhailov, Phys. Rev. C **82**, 044904 (2010), 1004.0805.

[173] S. A. Bass et al., Prog. Part. Nucl. Phys. **41**, 255 (1998), nucl-th/9803035.

[174] M. Bleicher et al., J. Phys. G **25**, 1859 (1999), hep-ph/9909407.

[175] S. Acharya et al. (ALICE), Phys. Rev. C **101**, 044907 (2020), 1910.07678.

[176] S. Acharya et al. (ALICE), Eur. Phys. J. C **81**, 256 (2021), 2005.11120.

[177] R. J. Fries, B. Muller, C. Nonaka, and S. A. Bass, Phys. Rev. Lett. **90**, 202303 (2003), nucl-th/0301087.

[178] S. Acharya et al. (ALICE), Eur. Phys. J. C **80**, 693 (2020), 2003.02394.

[179] J. Adam et al. (ALICE), Eur. Phys. J. C **76**, 245 (2016), 1601.07868.

[180] B. B. Abelev et al. (ALICE), Phys. Rev. C **91**, 024609 (2015), 1404.0495.

Appendix

A Datasets and run numbers

The p–Pb data sample at $\sqrt{s_{\rm NN}}$ = 8.16 TeV, classified as ESD (Event Summary Data), was processed in pass1. This data was gathered in 2016 during Run II from the LHC16r period. During pass1 processing, three separate reconstructions were executed:

- pass1_CEN_wSDD: all events in the CENT cluster, i.e. with SDD in the readout, reconstructed including SDD in the tracking
- pass1_CENT_woSDD: all events in the CENT cluster, i.e. with SDD in the readout, reconstructed excluding SDD from the tracking
- pass1_FAST: all events that are only in the in the FAST cluster (and not in the CENT), i.e. without SDD in the readout

To increase the statistics and have a sample with the best possible tracking performance, we used CENT_wSDD and FAST [source: CERN Twiki]. The run numbers for these two productions include:

1. LHC16r_pass1_CENT_wSDD: 266318, 266317, 266316, 266305, 266304, 266300, 266299, 266296, 266208, 266197, 266196, 266193, 266190, 266189, 266187, 266117, 266086, 266085, 266084, 266083, 266081, 266076, 266074, 266034, 265797, 265795, 265789, 265788, 265756, 265754, 265746, 265744, 265742, 265741, 265714, 265713, 265709, 265705, 265701, 265700, 265698, 265697, 265607, 265596, 265594.

2. LHC16r_pass1_FAST: 266316, 266317, 266318.

The p–Pb Monte-Carlo data is sourced from the period LHC17l7a2_cent and LHC17l7a2_fast1 (DPMJET) with the same run numbers as the experimental data.

The pp data sample at $\sqrt{s_{\mathrm{NN}}}$ = 8 TeV, also formatted in ESD, collected in 2012 (Run I) during the pass2 processing across 7 different periods is used, and these are:

1. LHC12a: 176661, 176701, 176704, 176707, 176710, 176715, 176730, 176749, 176752, 176753, 176849, 176854, 176859, 176924, 176926, 176927, 176929, 177011, 177148, 177157, 177160, 177167, 177173, 177180, 177182

2. LHC12b: 177477, 177496, 177497, 177501, 177580, 177592, 177597, 177601, 177612, 177620, 177624, 177671, 177679, 177680, 177681, 177682, 177798, 177799, 177802, 177804, 177805, 177810, 177858, 177860, 177861, 177864, 177866, 177869, 177938, 177942, 178018, 178024, 178025, 178026, 178028, 178029, 178030, 178031, 178052, 178053, 178163, 178167

3. LHC12c: 179569, 179571, 179584, 179585, 179591, 179618, 179621, 179638, 179639, 179796, 179802, 179803, 179806, 179837, 179858, 179859, 179916, 179917, 179918, 179919, 179920, 180000, 180042, 180044, 180127, 180129, 180130, 180131, 180132, 180133, 180195, 180199, 180200, 180201, 180230, 180500, 180501, 180507, 180510, 180512, 180515, 180517, 180561, 180562, 180564, 180566, 180567, 180569, 180716, 180717, 180719, 180720, 181617, 181618, 181619, 181620, 181652, 181694, 181698, 181701, 181703, 182017, 182018, 182022, 182023, 182106, 182110, 182111, 182207, 182289, 182295, 182297, 182299, 182300, 182302, 182322, 182323, 182324, 182325, 182509, 182513, 182624, 182635, 182684, 182686, 182687, 182691, 182692, 182724, 182725, 182728, 182729, 182730, 182740, 182741, 182744

4. LHC12d: 183913, 183916, 183932, 183933, 183934, 183935, 183936, 183937, 183938, 183942, 183946, 184000, 184126, 184127, 184131, 184132, 184134, 184135, 184137, 184138, 184140, 184144, 184145, 184147, 184183, 184188, 184208, 184209, 184210, 184215, 184216, 184370, 184371, 184374, 184383,

184389, 184673, 184678, 184682, 184687, 184784, 184786, 184843, 184845, 184846, 184928, 184930, 184933, 184938, 184964, 184967, 184968, 184987, 184988, 184990, 185029, 185031, 185116, 185126, 185127, 185132, 185133, 185134, 185157, 185160, 185164, 185189, 185196, 185198, 185203, 185206, 185208, 185217, 185221, 185282, 185284, 185288, 185289, 185291, 185292, 185293, 185296, 185299, 185300, 185302, 185303, 185348, 185349, 185350, 185351, 185356, 185359, 185360, 185361, 185362, 185363, 185368, 185371, 185375, 185378, 185457, 185459, 185460, 185461, 185465, 185467, 185472, 185474, 185475, 185563, 185565, 185567, 185569, 185574, 185575, 185578, 185580, 185581, 185582, 185583, 185588, 185589, 185659, 185680, 185687, 185692, 185695, 185697, 185698, 185699, 185700, 185701, 185734, 185735, 185738, 185756, 185757, 185764, 185765, 185768, 185775, 185776, 185778, 185784, 185909, 185912, 185915, 185916, 186000, 186003, 186006, 186007, 186009, 186011, 186038, 186066, 186073, 186078, 186079, 186082, 186083, 186084, 186162, 186163, 186164, 186165, 186167, 186200, 186205, 186208, 186229, 186318, 186319, 186320

5. LHC12f: 186668, 186688, 186689, 186690, 186692, 186693, 186694, 186807, 186809, 186811, 186813, 186814, 186815, 186816, 186838, 186843, 186844, 186845, 186851, 186853, 186855, 186857, 186859, 186937, 186938, 186939, 186965, 186966, 186967, 186969, 186987, 186989, 186990, 186992, 186994, 187047, 187084, 187136, 187143, 187145, 187146, 187147, 187148, 187149, 187150, 187151, 187152, 187201, 187202, 187203, 187335, 187339, 187340, 187341, 187343, 187484, 187485, 187486, 187487, 187488, 187489, 187508, 187510, 187534, 187535, 187536, 187537, 187556, 187560, 187561, 187562, 187623, 187624, 187627, 187633, 187654, 187656, 187695, 187697, 187698, 187739, 187744, 187749, 187753, 187780, 187783, 187785, 187791, 187796, 187849, 188021, 188025, 188027, 188028, 188029, 188093, 188101, 188108, 188123

6. LHC12h: 189122, 189146, 189147, 189183, 189228, 189229, 189231, 189301,

189306, 189310, 189315, 189316, 189340, 189341, 189344, 189347, 189350, 189351, 189352, 189353, 189396, 189397, 189400, 189402, 189406, 189407, 189409, 189410, 189411, 189473, 189474, 189518, 189522, 189523, 189526, 189577, 189578, 189602, 189603, 189605, 189610, 189611, 189612, 189616, 189621, 189623, 189647, 189648, 189650, 189654, 189656, 189658, 189659, 189696, 189697, 189698, 189729, 189734, 189735, 189736, 189737, 190150, 190209, 190210, 190212, 190213, 190214, 190215, 190216, 190240, 190303, 190305, 190307, 190335, 190336, 190337, 190338, 190340, 190341, 190342, 190344, 190386, 190388, 190389, 190390, 190392, 190393, 190416, 190417, 190418, 190419, 190421, 190422, 190424, 190425, 190895, 190898, 190903, 190904, 190968, 190970, 190974, 190975, 190979, 190981, 190983, 190984, 191129, 191227, 191229, 191230, 191231, 191232, 191234, 191242, 191244, 191245, 191247, 191248, 191450, 191451, 192004, 192072, 192073, 192075, 192095, 192128, 192136, 192140, 192141, 192172, 192174, 192177, 192194, 192197, 192199, 192200, 192201, 192202, 192205, 192246, 192342, 192344, 192347, 192348, 192349, 192415, 192417, 192453, 192461, 192468, 192471, 192492, 192499, 192505, 192510, 192534, 192535, 192542, 192548, 192551, 192729, 192731, 192732

7. LHC12i: 192772, 192775, 192778, 192779, 192820, 192822, 192824, 193004, 193005, 193007, 193008, 193010, 193011, 193014, 193047, 193049, 193051, 193092, 193093, 193094, 193097, 193148, 193150, 193151, 193152, 193155, 193156, 193184, 193187, 193188, 193189, 193192, 193194, 193750, 193751, 193752, 193758, 193759, 193760, 193766

The corresponding Monte-Carlo productions used are LHC15h2a, LHC15h2b, LHC15h2c, LHC15h2d, LHC15h2f, LHC15h2h and LHC15h2i.

B Invariant mass of pK pairs before background subtraction

Figures B.1 - B.5 illustrate the invariant mass distribution plots for $\Lambda(1520)$ prior to mixed-event background subtraction across different p_{T} bins for p–Pb collisions at $\sqrt{s_{\mathrm{NN}}}$ = 8.16 TeV, presented for minimum bias and various multiplicity classes.

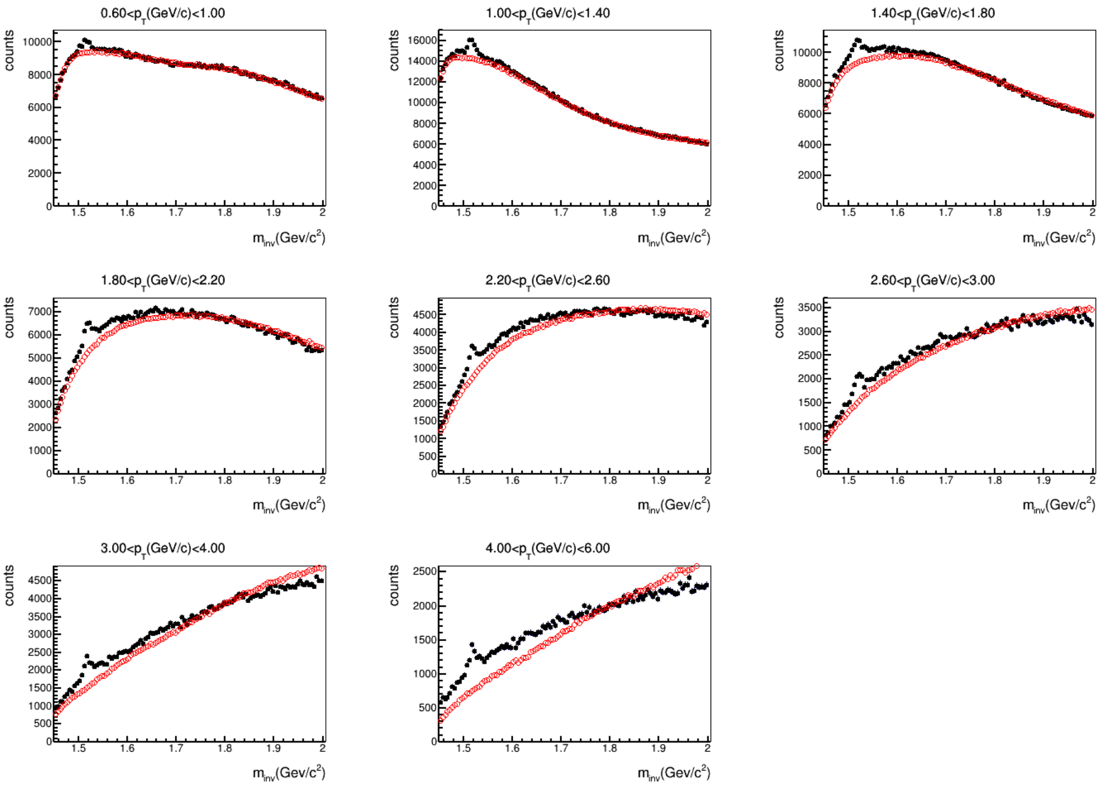

Figure B.1: Invariant mass distribution of pK pair before mixed event background subtraction for minimum bias $(0-100\%)$ p–Pb collisions at $\sqrt{s_{\mathrm{NN}}} = 8.16$ TeV. Black markers show (signal + background) and red markers show background.

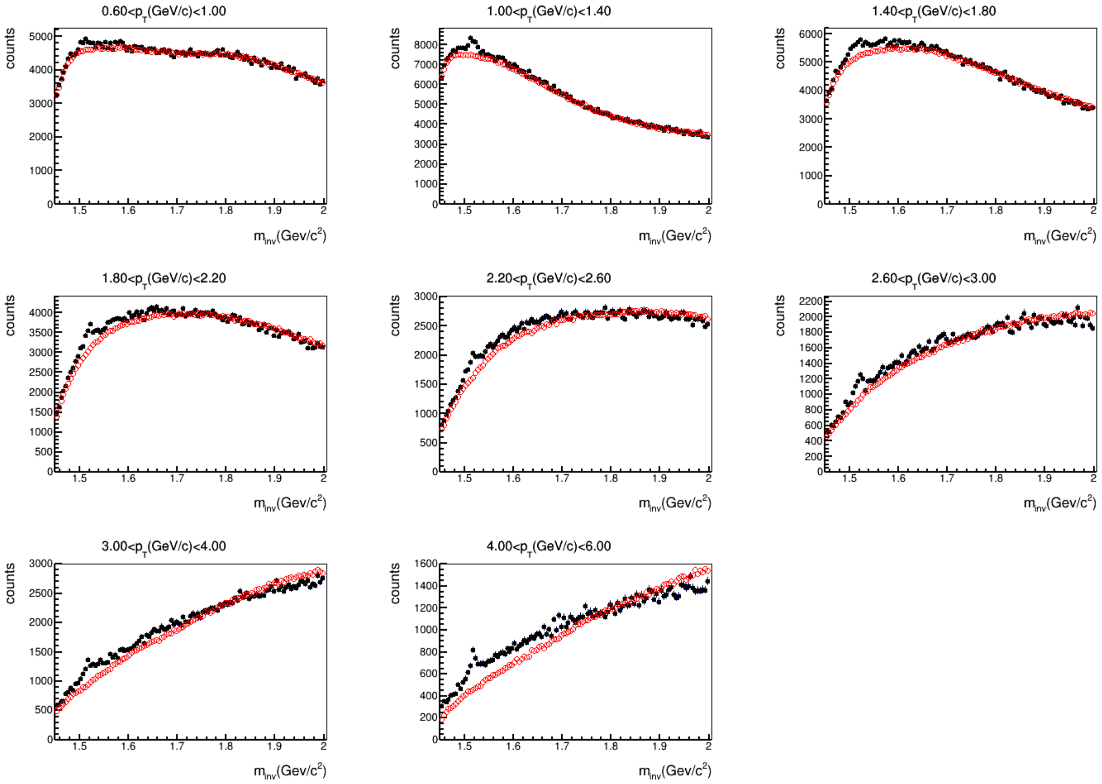

Figure B.2: Invariant mass distribution of pK pair before mixed event background subtraction for p–Pb collisions at $\sqrt{s_{\mathrm{NN}}} = 8.16$ TeV in the multiplicity class 0−20%. Black markers show (signal + background) and red markers show background.

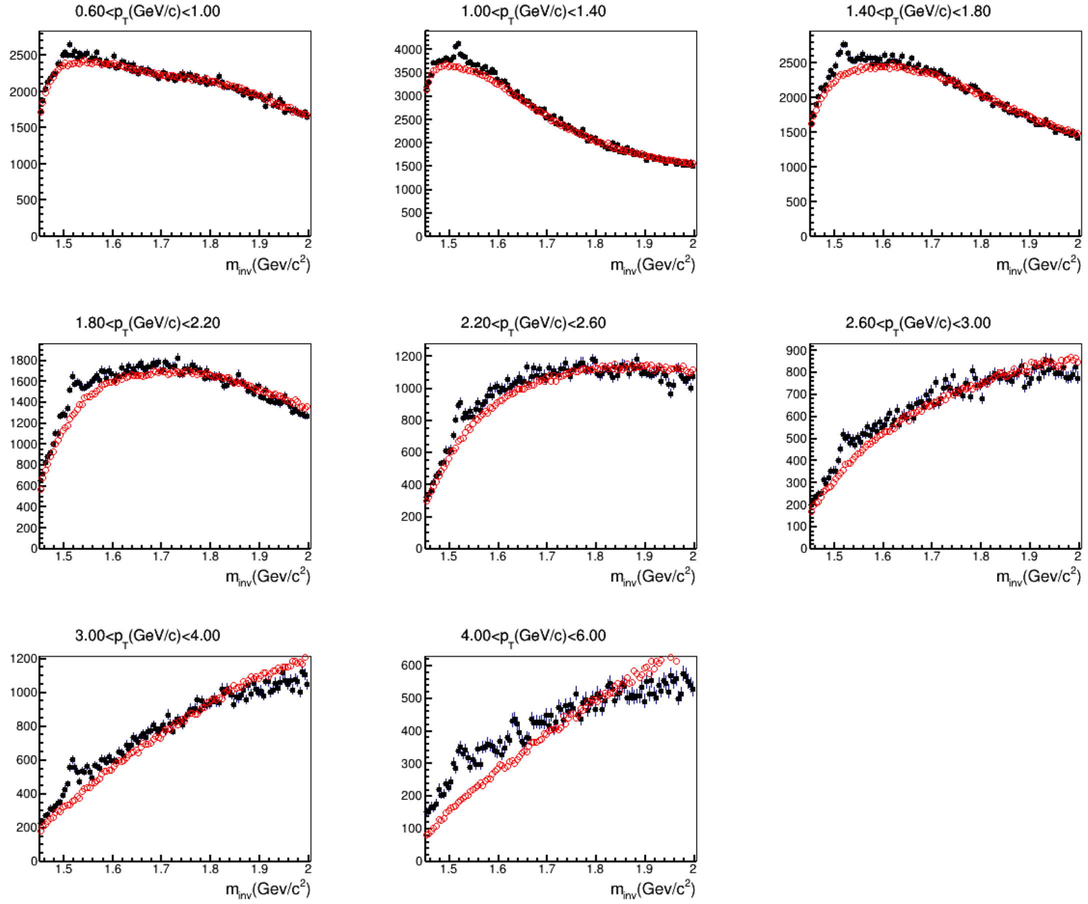

Figure B.3: Invariant mass distribution of pK pair before mixed event background subtraction for p–Pb collisions at $\sqrt{s_{\mathrm{NN}}}$ = 8.16 TeV in the multiplicity class 20−40%. Black markers show (signal + background) and red markers show background.

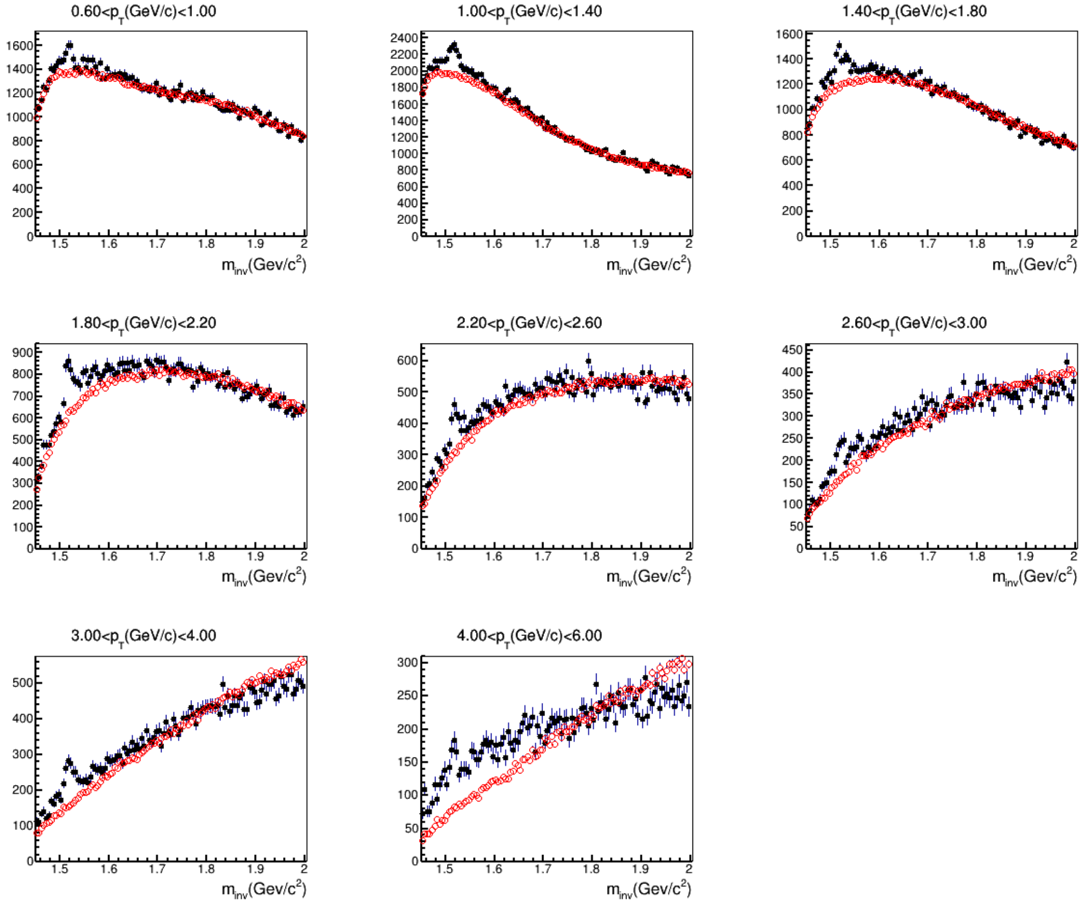

Figure B.4: Invariant mass distribution of pK pair before mixed event background subtraction for p–Pb collisions at $\sqrt{s_{\mathrm{NN}}}$ = 8.16 TeV in the multiplicity class 40−60%. Black markers show (signal + background) and red markers show background.

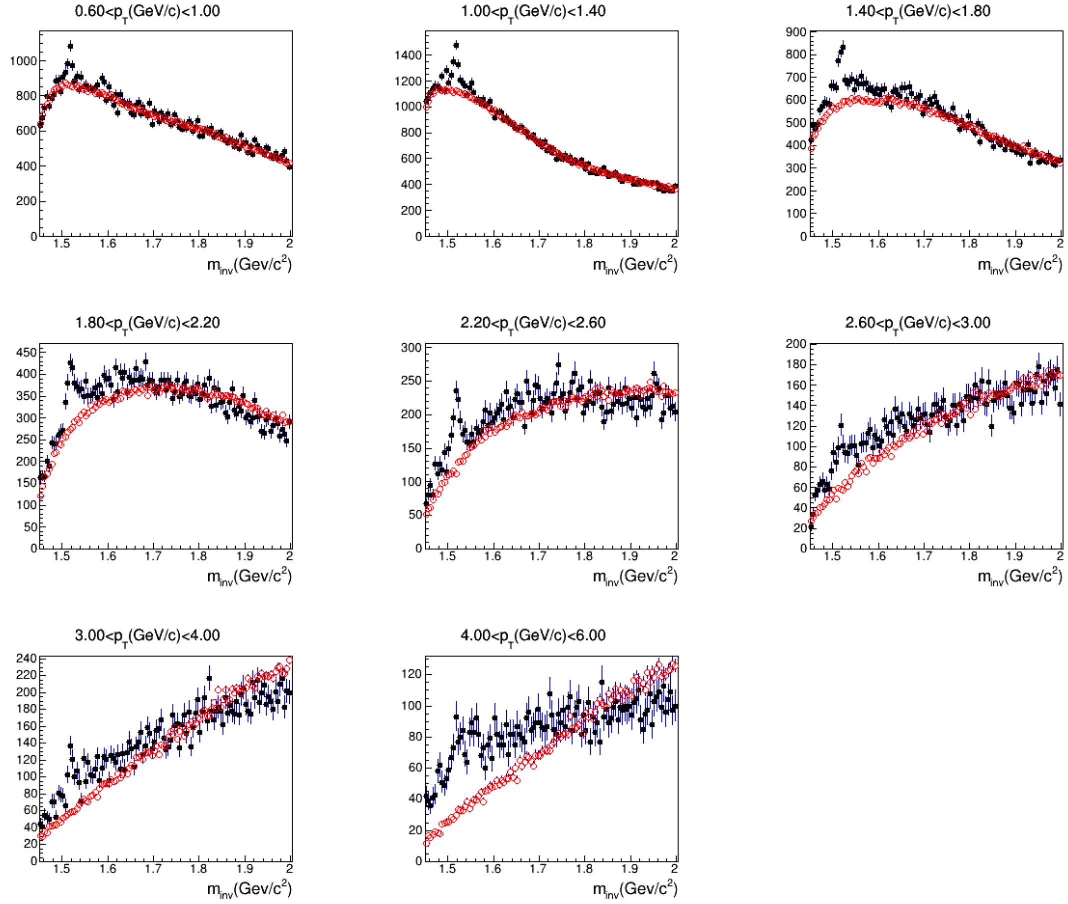

Figure B.5: Invariant mass distribution of pK pair before mixed event background subtraction for p–Pb collisions at $\sqrt{s_{\rm NN}}$ = 8.16 TeV in the multiplicity class 60−100%. Black markers show (signal + background) and red markers show background.

C Invariant mass of pK pairs after background subtraction

Figures C.1 - C.6 illustrate the invariant mass distribution plots for $\Lambda(1520)$ after mixed-event background subtraction across different p_{T} bins for p–Pb collisions at $\sqrt{s_{\mathrm{NN}}}$ = 8.16 TeV, presented for minimum bias and various multiplicity classes, and also in the inelastic pp collisions at $\sqrt{s}$ = 8 TeV.

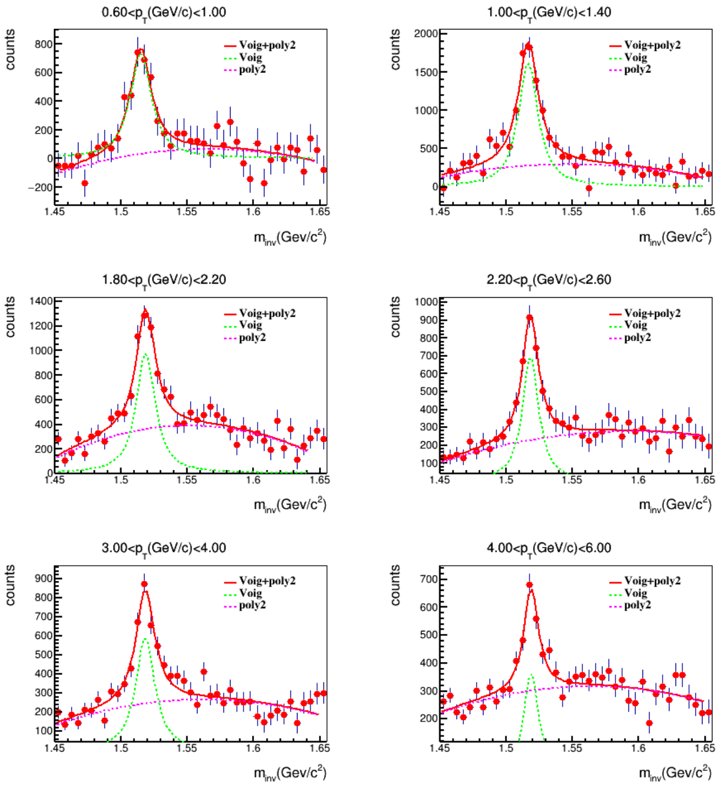

Figure C.1: Invariant mass distribution of pK pair after mixed event background subtraction for minimum bias (0−100%) p–Pb collisions at $\sqrt{s_{\mathrm{NN}}}$ = 8.16 TeV.

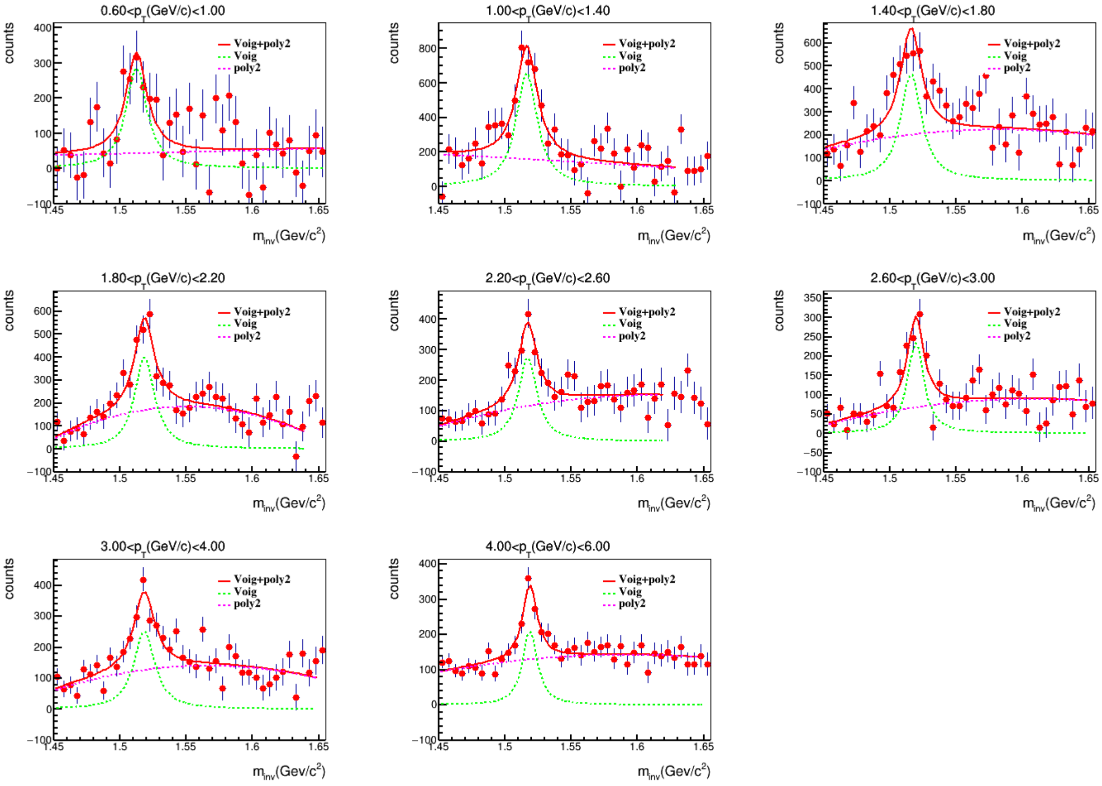

Figure C.2: Invariant mass distribution of pK pair after mixed event background subtraction for p–Pb collisions at $\sqrt{s_{\mathrm{NN}}}$ = 8.16 TeV in the multiplicity class 0−20%.

D The σ distributions of tracks in TPC and TOF

Figures D.1 and D.2 illustrate the sigma distribution of the tracks in the TPC and TOF for both data and Monte Carlo simulations, fitted with Gaussian distributions across various momentum bins in p–Pb collisions at $\sqrt{s_{\mathrm{NN}}}$ = 8.16 TeV. Figures D.3 and D.4 illustrate the mean and standard deviation derived from the Gaussian fits of the σ distributions.

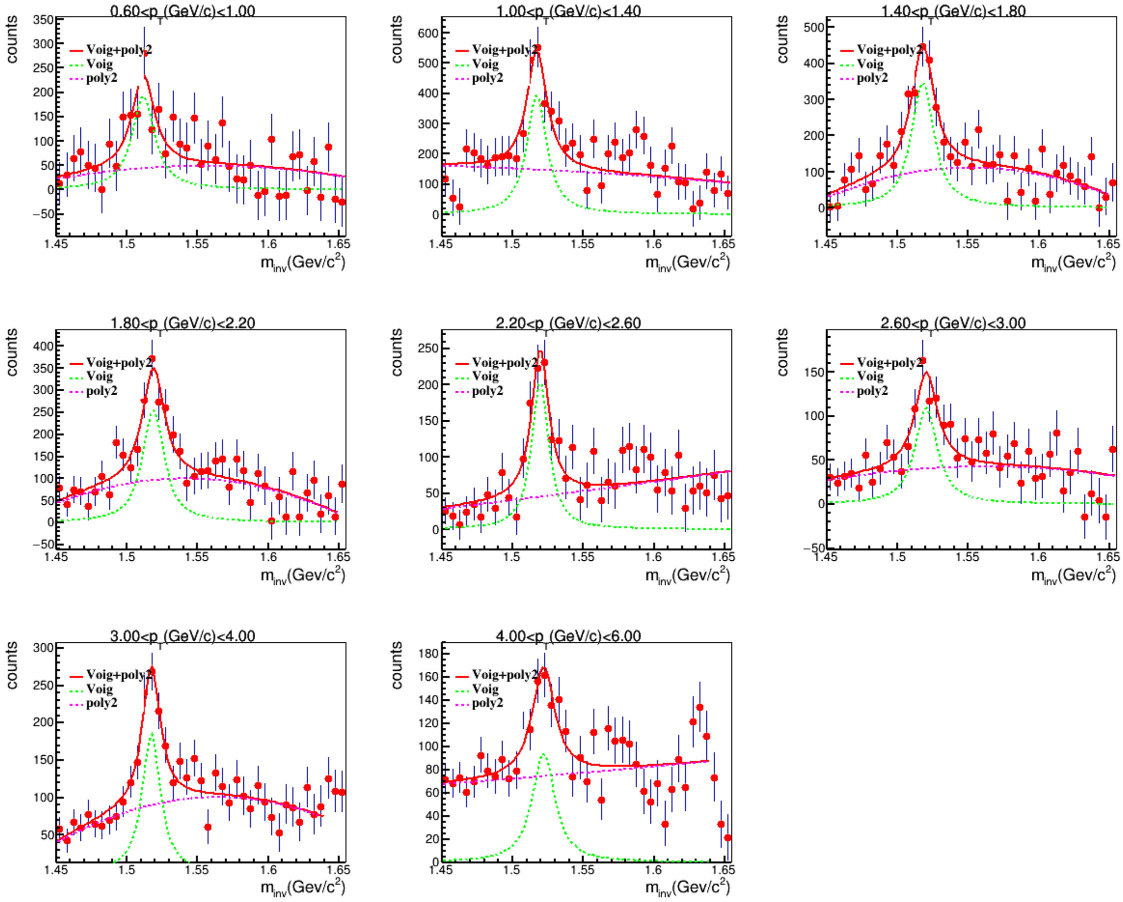

Figure C.3: Invariant mass distribution of pK pair after mixed event background subtraction for p–Pb collisions at $\sqrt{s_{\rm NN}}$ = 8.16 TeV in the multiplicity class 20−40%.

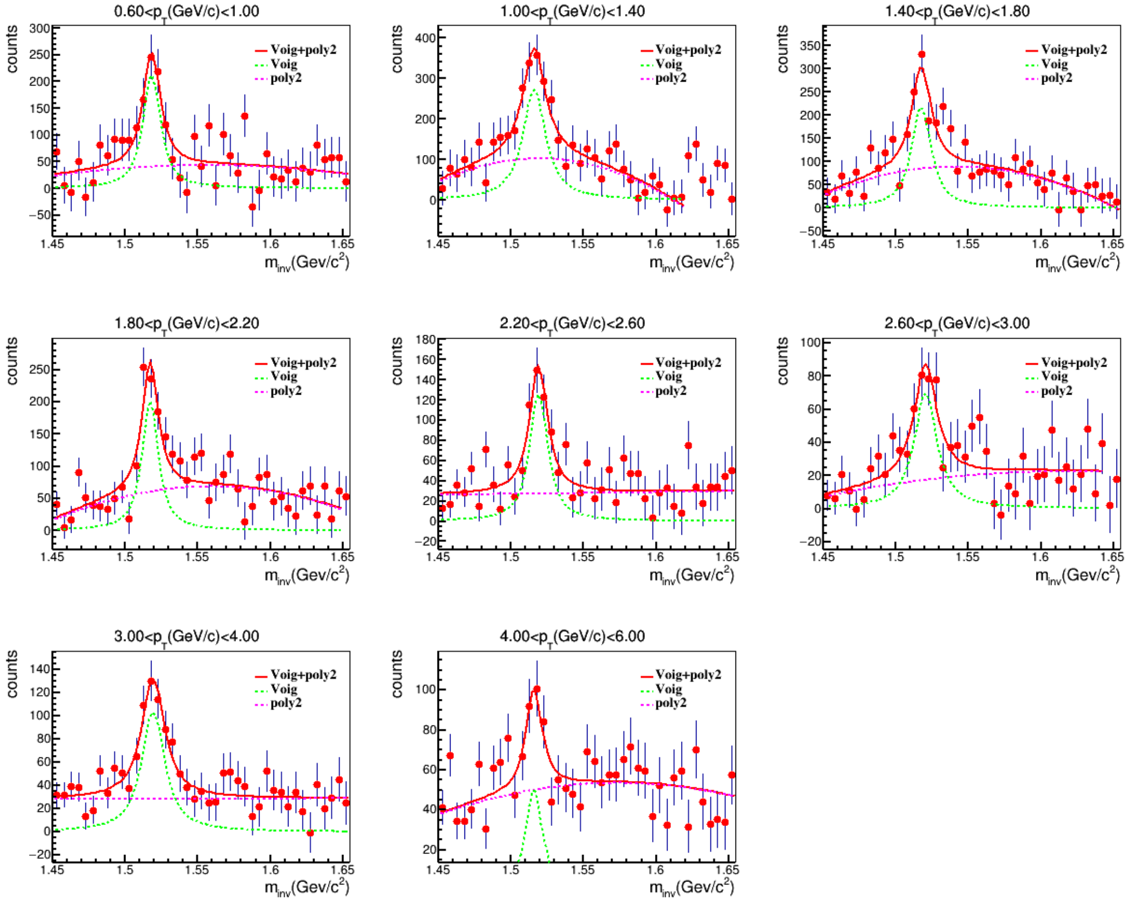

Figure C.4: Invariant mass distribution of pK pair after mixed event background subtraction for p–Pb collisions at $\sqrt{s_{\mathrm{NN}}}$ = 8.16 TeV in the multiplicity class 40−60%.

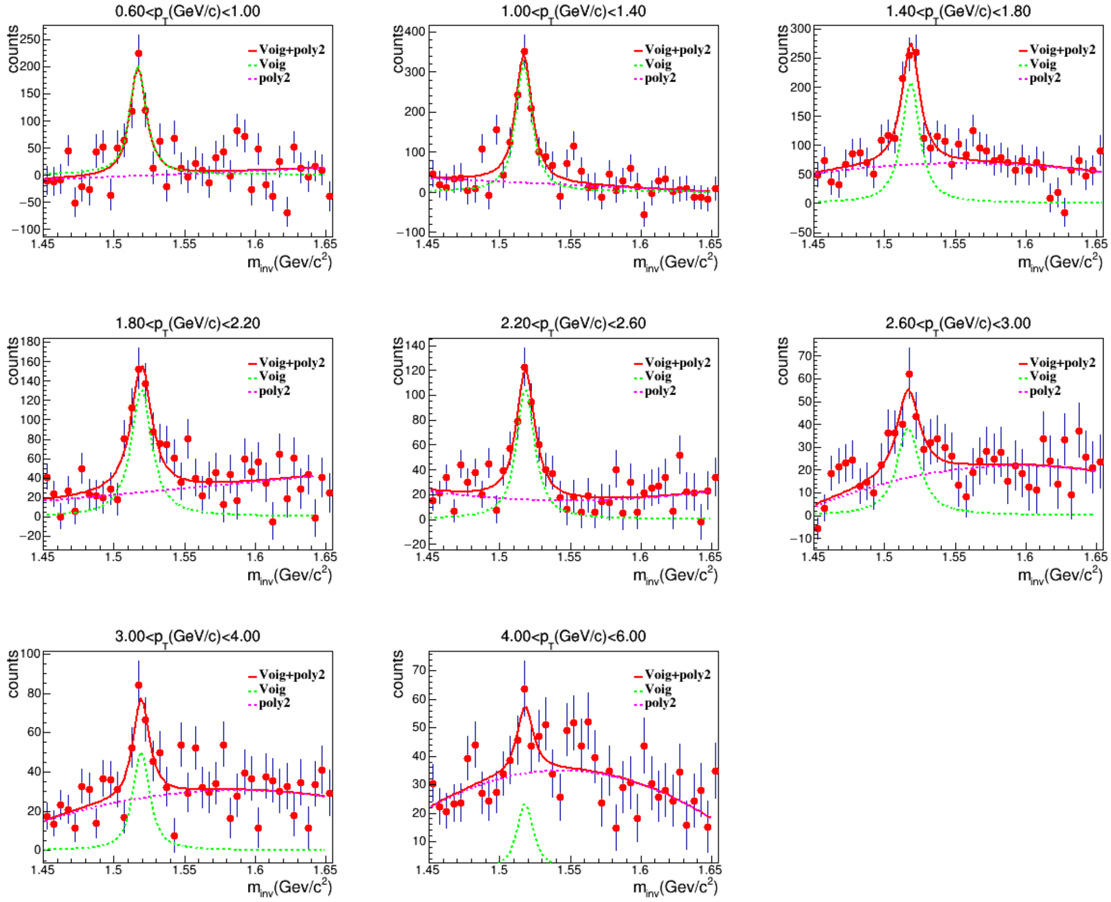

Figure C.5: Invariant mass distribution of pK pair after mixed event background subtraction for p–Pb collisions at $\sqrt{s_{\mathrm{NN}}} = 8.16$ TeV in the multiplicity class 60−100%.

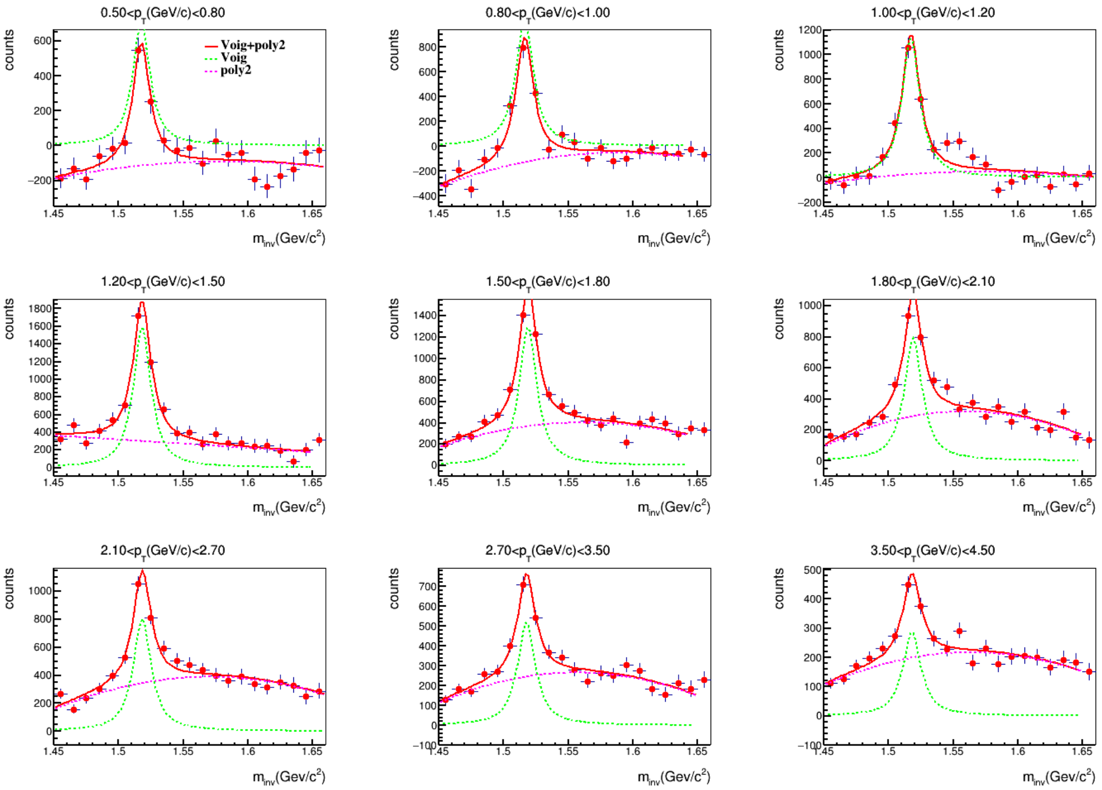

Figure C.6: Invariant mass distribution of pK pair after mixed event background subtraction for inelastic pp collisions at $\sqrt{s}$ = 8 TeV.

E Re-weighting efficiency

The iterative process involves the following steps:

1. Calculate the unweighted ε_{rec}.

2. Use this ε_{rec} to correct the measured $\Lambda(1520)$ p_{T} spectrum.

3. Fit the corrected $\Lambda(1520)$ spectra with the Levy-Tsallis function.

4. Utilize the fit to weight the MC-generated $\Lambda(1520)$ spectra. A p_{T} dependent weight is applied to both the generated and reconstructed $\Lambda(1520)$ spectra to align them with the fit, as illustrated in Figure E.1.

5. Obtain the weighted ε_{rec}.

6. Repeat steps 2-5 until the change in ε_{rec} is observed to be less than 0.1.

Typically, two iterations are sufficient for this reweighting procedure. After completion, the correction factor in ε_{rec} is derived as the ratio of the re-weighted ε_{rec} to the unweighted ε_{rec}, as demonstrated in Figures 1(c) and 1(d). This entire process can be implemented using the standard macro available in the resonance package:

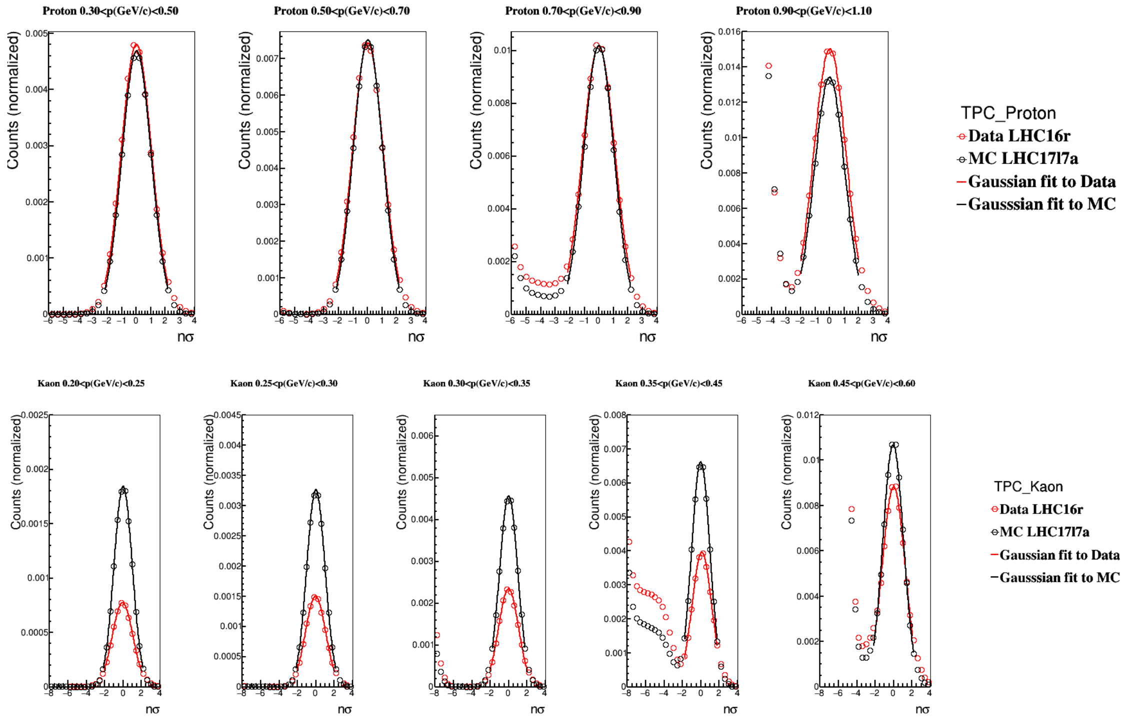

Figure D.1: The σ distribution of proton (upper panel) and kaon (lower panel) tracks from TPC in small p_{T} bins. Solid lines represent the Gaussian fits to the distributions. Red and black markers indicate data and MC, respectively.

/AliPhysics/PWGLF/RESONANCES/macros/utils/ReweightEfficiency.C

The net effect of this reweighting procedure is more pronounced at low p_{T} and negligible at high p_{T}, as shown in Figure 1(a) and 1(b) for CENT and FAST data in p−Pb collisions at $\sqrt{s_{\mathrm{NN}}} = 8.16$ TeV.

F Signal and event loss correction

The signal-loss correction factor for p–Pb collisions at $\sqrt{s_{\mathrm{NN}}} = 8.16$ TeV in $0-20\%$, $20-40\%$, $40-60\%$ and $60-100\%$ V0A multiplicity classes are shown in Figure F.1

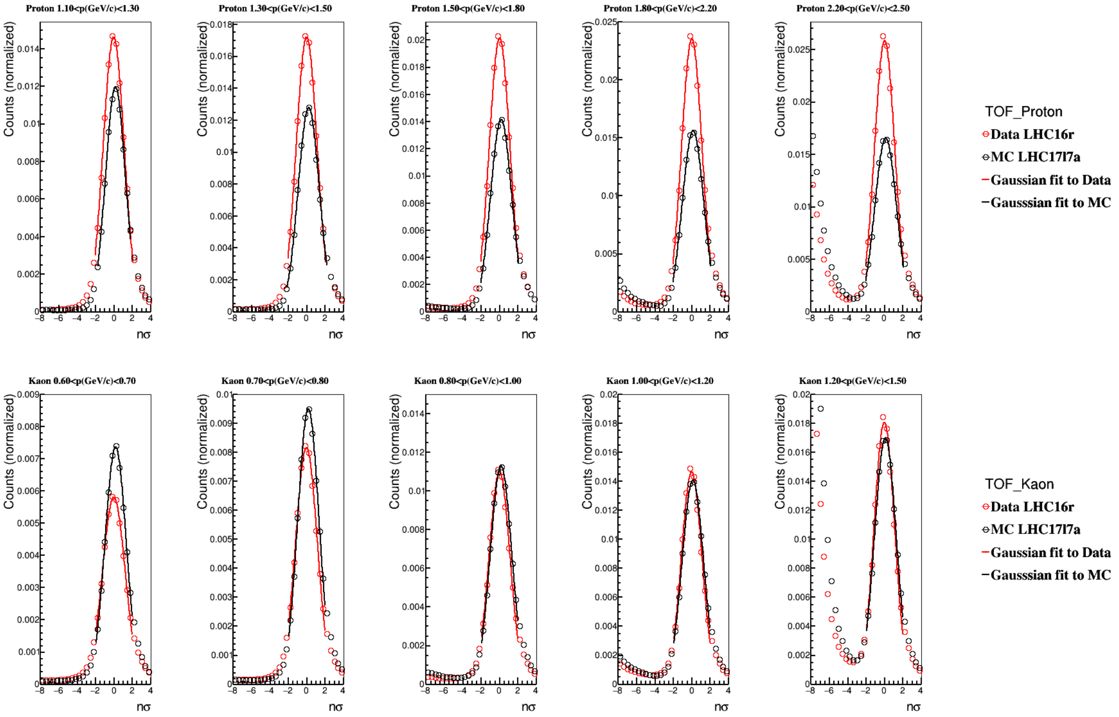

Figure D.2: The σ distribution of proton (shown in the upper panel) and kaon (depicted in the lower panel) tracks from TOF in narrow p_{T} intervals. The solid lines represent the Gaussian fit to these distributions. Data points are indicated with red markers whereas MC points are shown with black markers.

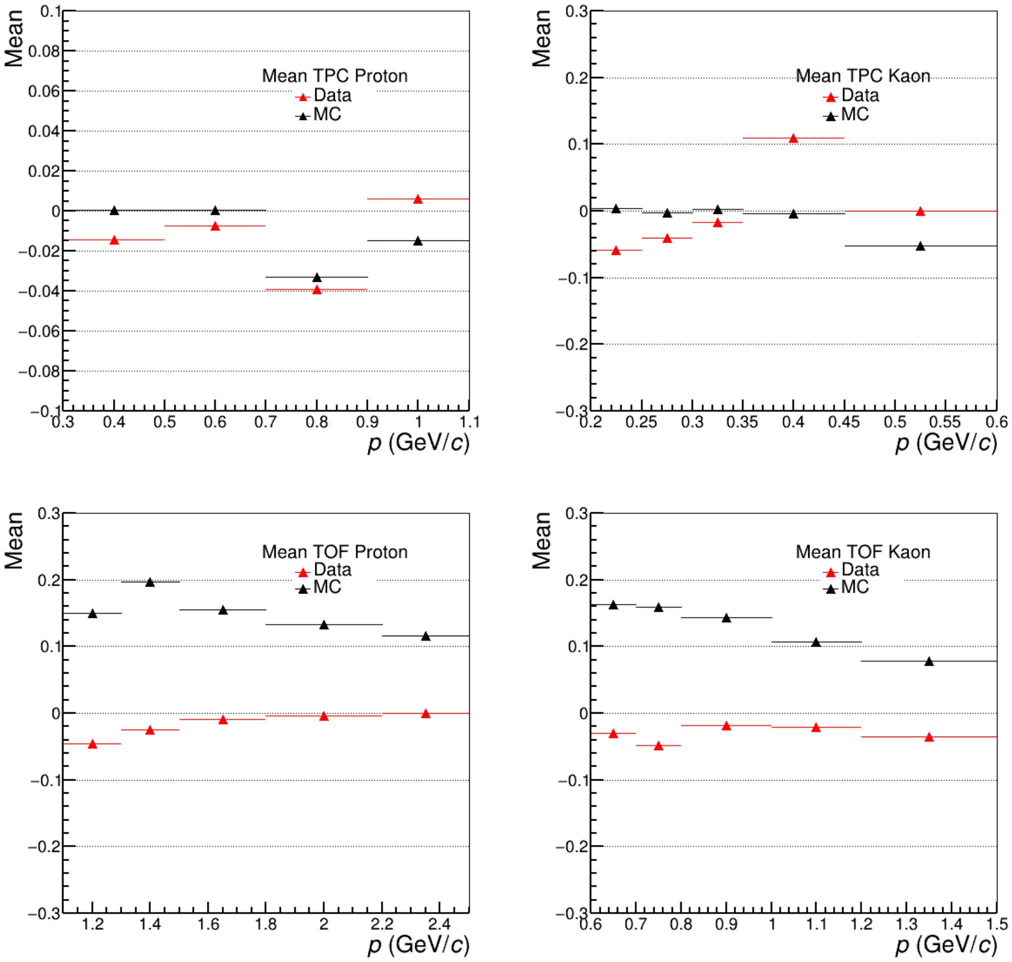

Figure D.3: Mean of the Gaussian fit of σ distributions of protons and kaons in TPC and TOF. Upper panel shows mean for protons(left) and kaons(right) in TPC while lower panel shows mean for protons(left) and kaons(right) in TOF.

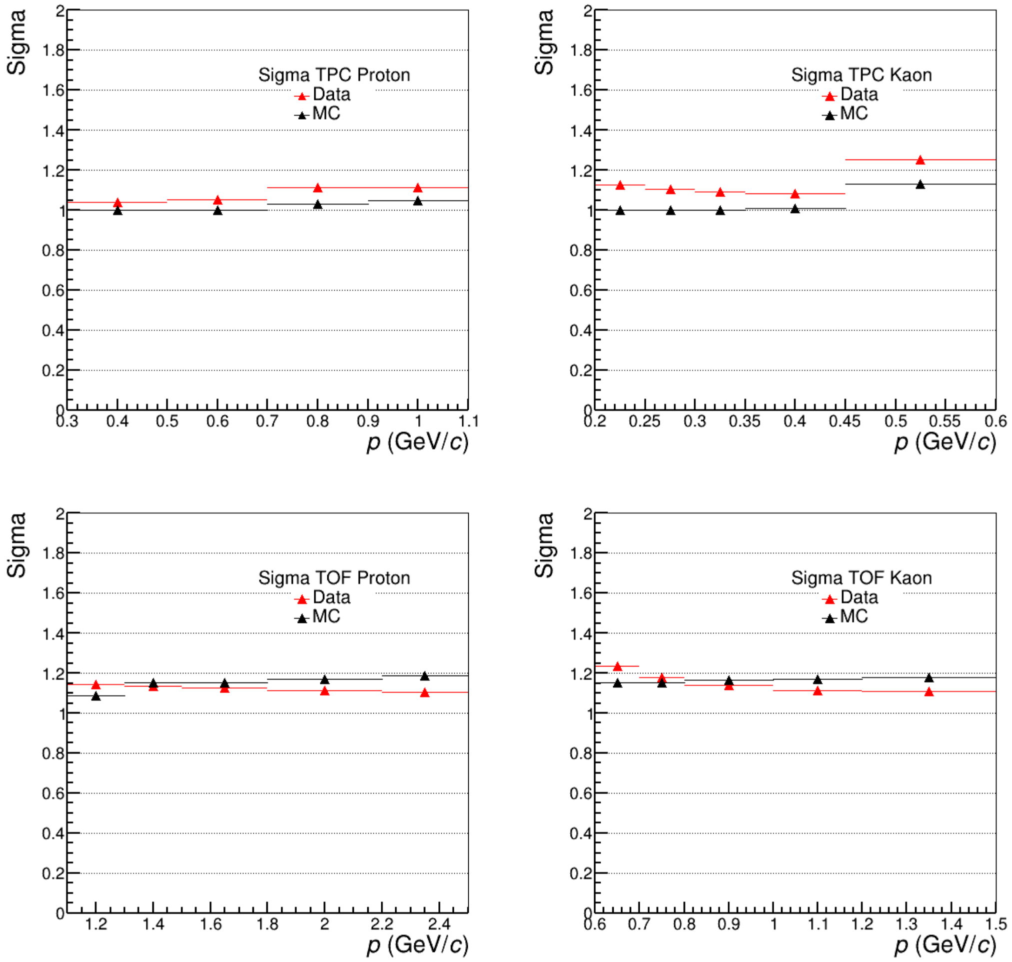

Figure D.4: Standard deviation of the Gaussian fit of σ distributions of protons and kaons in TPC and TOF. Upper panel shows standard deviation for protons(left) and kaons(right) in TPC while lower panel shows standard deviation for protons(left) and kaons(right) in TOF.

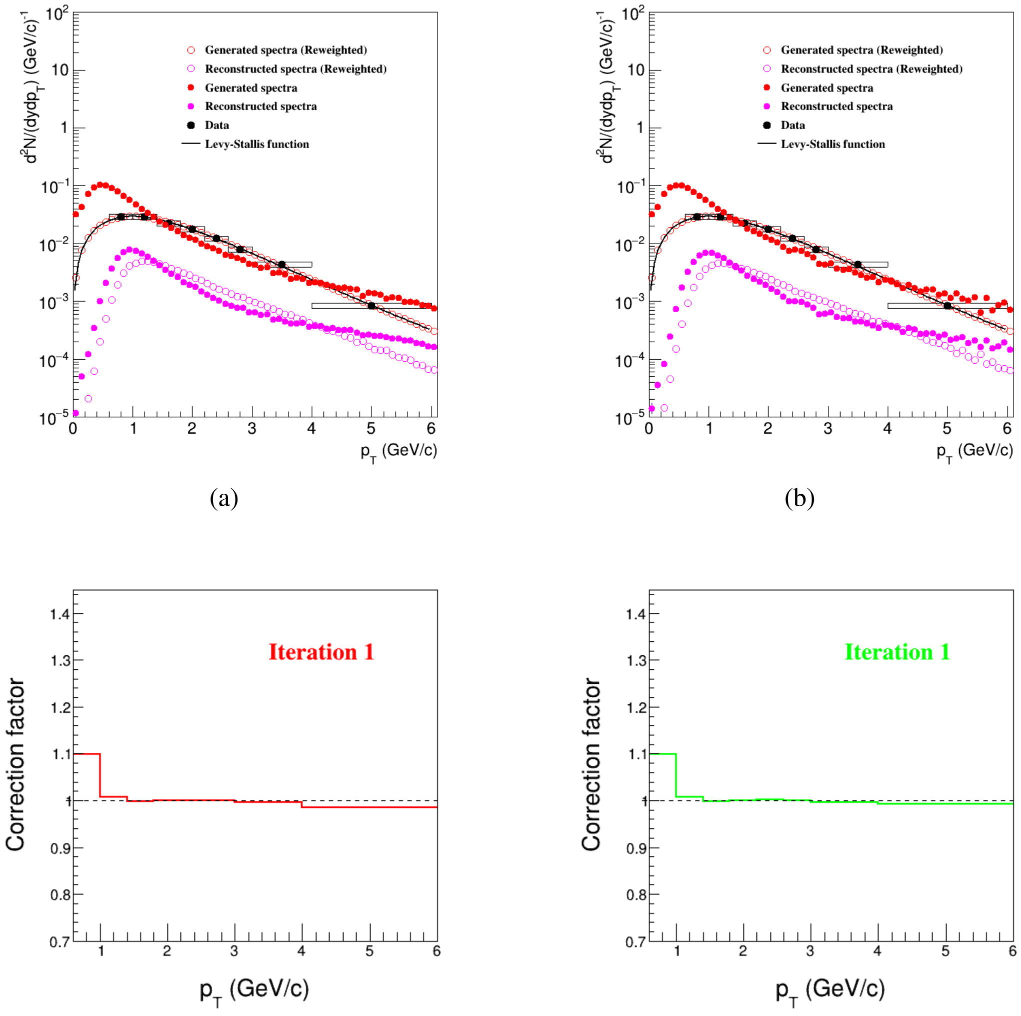

(a) (b)

(c) (d)

Figure E.1: (a) shows the generated and reconstructed spectra before (solid red and violet circles) and after (open red and violet circles) reweight for the CENT production and (b) shows the same for FAST production. (c) and (d) shows the correction factors for ε_{rec} for CENT and FAST productions, respectively in p−Pb collisions at $\sqrt{s_{\rm NN}}$ = 8.16 TeV.

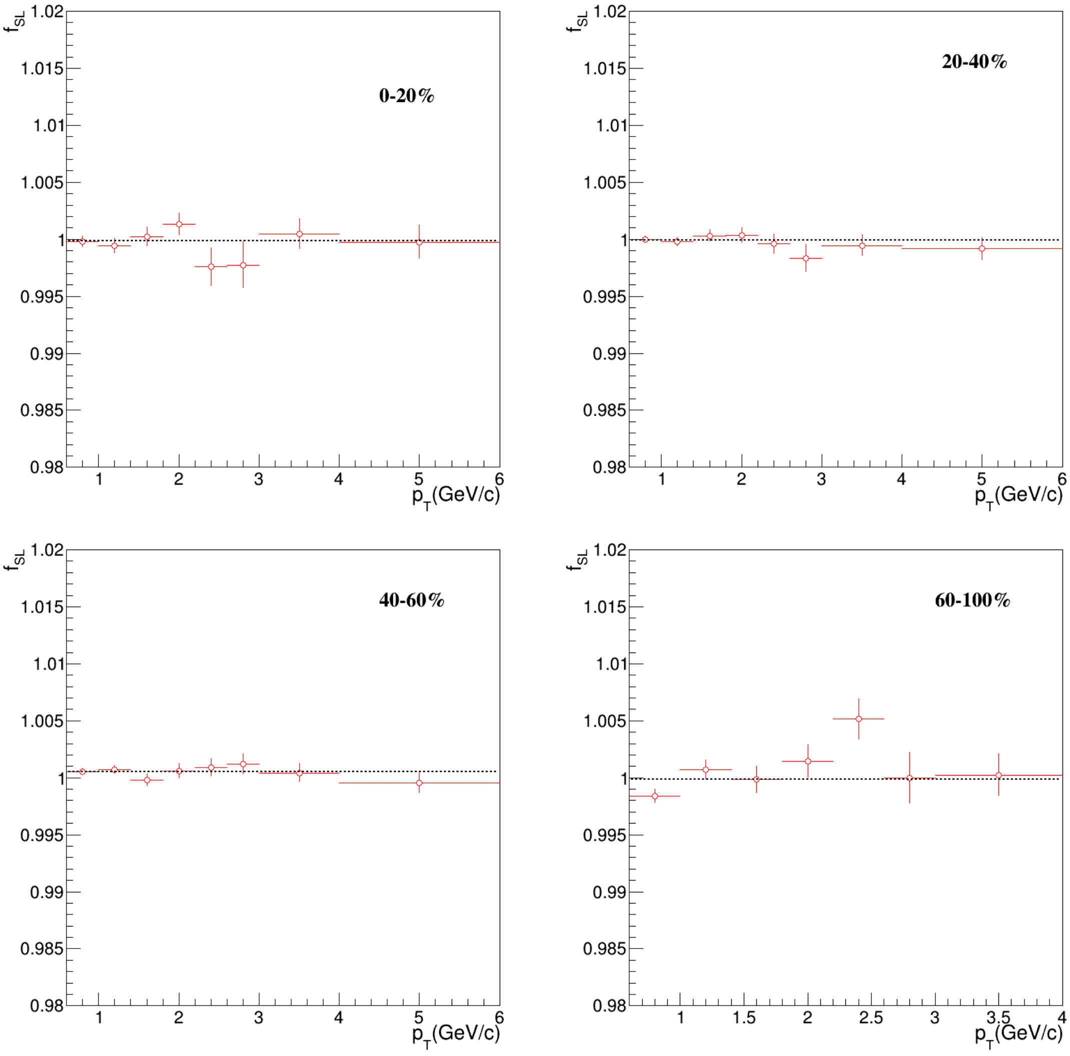

Figure F.1: Signal loss correction factors for minimum bias (0-100%) and various multiplicity classes in p–Pb collisions at $\sqrt{s_{NN}}$ = 8.16 TeV and for pp collisions at $\sqrt{s_{NN}}$ = 8 TeV. The dotted black line represents a constant fit function.

List of Publications and Presentations

Publications in Refereed Journals

1. Vikash Sumberia (for the ALICE Collaboration), System size and energy dependence of resonance production at ALICE, *EPJ Web Conf.*, 2022, **259**, 11004.
2. ALICE Collaboration, System-size dependence of the hadronic rescattering effect at energies available at the CERN Large Hadron Collider, *Phys.Rev.C*, 2024, **109**, 1, 014911.
3. ALICE Collaboration, Multiplicity and rapidity dependence of $\mathrm{K}^*(892)^0$ and $\phi(1020)$ production in p–Pb collisions at 5.02 TeV, *Eur.Phys.J.C*, 2023, **83**, 6, 540.
4. ALICE Collaboration, $\mathrm{K}^*(892)^0$ and $\phi(1020)$ production in p–Pb collisions at 8.16 TeV, *Phys.Rev.C*, 2023, **107**, 5, 055201.
5. ALICE Collaboration, Investigating strangeness enhancement in jet and medium via $\phi(1020)$ production in p–Pb collisions at $\sqrt{s_{\mathrm{NN}}}$ = 5.02 TeV, *Phys. Rev. C*, 2024, **110**, 6, 064912.
6. ALICE Collaboration, Observation of abnormal suppression of $\mathrm{f}_0(980)$ production in p–Pb collisions at $\sqrt{s_{\mathrm{NN}}}$ = 5.02 TeV, *Phys. Lett. B*, 2023, **853**, 138665
7. ALICE Collaboration, $\mathrm{K}(892)^{*\pm}$ resonance production in Pb–Pb collisions at $\sqrt{s_{\mathrm{NN}}}$ = 5.02 TeV, *Phys. Rev. C*, 2024, **109**, 4, 044902.
8. ALICE Collaboration, Multiplicity-dependent production of $\Sigma(1385)^{\pm}$ and $\Xi(1530)^0$ in pp collisions at $\sqrt{s}$ = 13 TeV, *JHEP*, 2024, **05**, 317.
9. ALICE Collaboration, $\mathrm{f}_0(980)$ production in inelastic pp collisions at $\sqrt{s} = 5.02$ TeV, *Phys. Lett. B*, 2023, *846*, 137644.
10. ALICE Collaboration, $\Sigma(1385)^{\pm}$ resonance production in Pb–Pb collisions at $\sqrt{s_{\mathrm{NN}}}$ = 5.02 TeV, *Eur. Phys. J. C*, 2023, **83**, 5, 351.

11. ALICE Collaboration, Multiplicity and rapidity dependence of $\mathrm{K}^{*}(\mathbf{892})^{0}$ and $\phi(\mathbf{1020})$ production in p–Pb collisions at $\sqrt{s_{\mathrm{NN}}} = 5.02$ TeV, *Eur. Phys. J. C*, 2023, **83**, 6, 540.

12. ALICE Collaboration, System-size dependence of the charged-particle pseudorapidity density at $\sqrt{s_{\mathrm{NN}}} = 5.02$ TeV for pp, p–Pb, and Pb–Pb collisions, *Phys. Lett. B*, 2023, **845**, 137730.

Conference Posters/Presentations

1. Vikash Sumberia, A review of yield suppression of hadronic resonances in heavy-ion collisions, 14^{th} *JK Science Congress*, University of Jammu, Jammu, India, Dec 20–22, 2019.

2. Vikash Sumberia, System size and energy dependence of resonance production at ALICE, *Strangeness in Quark Matter (SQM)*, BNL, USA , May 17–22, 2021.

3. Vikash Sumberia, Understanding the effect of system size and collision energy on the production of $\Lambda(1520)$ resonance with ALICE, 8^{th} *International Conference on Physics and Astrophysics of Quark-Gluon Plasma (ICPAQGP)*, Puri, Bhubneshwar, India, Feb 7–10, 2023.

4. Vikash Sumberia, Understanding hadron production mechanism in small collision systems using EPOS3 hydrodynamical model, *JK Science Congress for Women (JKSCW)*, University of Jammu, Jammu, India, Feb 11–13, 2024.

5. Vikash Sumberia and Dukhishyam Mallick, Probing the hadronic phase and strangeness production in high energy collisions with EPOS4 hydrodynamical model, *XXVI DAE-BRNS High Energy Physics Symposium*, BHU, Varanasi, India, Dec 19–23, 2024.